# Spectroscopic Characterisation of Mesoporous Materials

**Jennifer Helen Wall**

**PhD**

**University of York**

**Department of Chemistry**

**August 2011**

# Abstract

Commercially available inorganic solids and organically functionalised silicas and silica-polysaccharide composite materials synthesised in the laboratory were characterised by various techniques. These included direct infrared spectroscopic measurements, infrared and UV-visible probing techniques using probe molecules such as water, ammonia, $d_3$-actonitrile, aniline, Reichardt's dye and iodine and also by the application of the Knoevenagel condensation as a model reaction. As well as the information obtained about the surface activity of the solids, this review of techniques revealed the advantages and limitations of well-known and less frequently used methods. In particular, the use of iodine as a UV-visible probe molecule allowed the observation of differences between materials that are extremely difficult to analyse such as sodium carbonate and sodium acetate. However with current levels of knowledge about the electronic transitions of iodine adsorbed on surfaces, the results are not straight forward to interpret. The silica-polysaccharide composites also showed interesting properties, both in terms of their morphology and their chemistry and merit further study.

# Table of Contents

# Acknowledgements

I wish to thank Duncan Macquarrie for many valuable discussions and providing a great deal of helpful advice when things went wrong. I also wish to thank Richard Potterill for all his love and support.

# Declaration

I declare that I am the sole author of this thesis and that none of the material within it has been presented before in application for any other qualifications at this or any other institution. Nor has any of the material contained within this thesis been published in any format prior to this.

# Chapter 1: Introduction

## 1.1 Introduction

Porous solids are of great importance in chemical industries as adsorbents, heterogeneous catalysts and as catalyst supports. Probably the most well-known industries to rely heavily upon heterogeneous catalysts are those involved in petroleum refining. Demand for heterogeneous catalysts in this industry alone, according to a report entitled "Global Refinery Catalyst Market-Fcc, Htc, Hcc by Units, Geography, Ingredients & Applications (2010-2015)" by Research and Markets is forecast to reach US$3.4 billion in 2015 up from US$2.8 billion in 2009.[1] This is largely driven by the increased rate of production and consumption of petroleum based products, coupled with increasing environmental concerns and dwindling natural crude oil reserves.

Demands for heterogeneous catalysts and adsorbents are likely to increase in the fine chemicals and pharmaceutical industries also, as the European REACH regulations come into force. These regulations require that the majority of substances on the European market in quantities greater than 1 tonne per year be registered. This means that their hazards and environmental impact must be assessed and particularly hazardous materials are restricted. Disposal of waste is also becoming increasingly restricted and expensive. Particularly in the pharmaceutical industry, the waste to product ratio is about 25-100 kilos of waste for each kilo of product. Up to 80% of that waste is solvent and much of that is used in separation and purification of the final product.[2] Therefore, the use of heterogeneous catalysts, that can be easily separated from the reaction mixture by filtration and then recycled and adsorbents that can purify solvents for recycling will be extremely valuable.

The increasing demand for efficient catalysts and adsorbents has led to a great surge in the range of materials being developed. As well as the vast array of inorganic materials; metal oxides,[3] doped metal oxides,[4] metal phosphates[5] and so on, there has been a great deal of interest in the production of inorganic-organic hybrid materials.[6] These include; materials grafted with organic moieties (often silica)[7] metal-organic frameworks (MOFs)[8] and periodic mesoporous organosilicas (PMOs).[9]

Solid macrostructures are more difficult to characterise than soluble molecules. Solid-state NMR, infrared and UV-visible spectroscopy give much broader signals and are less useful for obtaining information about the surface, which may differ from the bulk but is where most of the activity usually occurs. This is due to the much greater mass of the bulk material compared to that of the surface and therefore much stronger signals.[10] Other useful techniques such as gas and liquid chromatography and mass spectrometry are not generally applicable. However, inverse phase gas chromatography has been used in some cases to characterise the properties of reverse phases, using standard volatile species such as n-alkanes and polar solvents such as acetone, chlorobenzene, tetrahydrofuran etc.[11] For obvious reasons this technique has been mainly used to study chromatographic stationary phases and since packing of the columns is fairly specialised, this is not a technique suited to many laboratories.

Some insight into solid morphology can be obtained by electron microscopy and porosimetry techniques. However, for transmission electron microscopy, the conditions under which the materials are studied are very harsh and using scanning electron microscopy, only relatively low resolution images can be obtained. Porosimetry techniques in conjunction with theoretical treatments such as those of Brunauer, Emmett and Teller (BET) are frequently used for determining surface area and pore size, volume and to some extent shape. These can be useful but a number of assumptions are used in the calculations that are not always justified and the

isotherms are usually recorded at 77K, which is not usually the operating temperature of the materials.[12]

To assess surface chemistry of solid materials and hence their behaviour as catalysts and adsorbents it is often more informative to use indirect spectroscopic probing techniques. These involve the adsorption of small molecules onto the surface of the material of interest and then observing the changes in the spectrum of the material, the small molecule or both, that are induced by this adsorption. In order to obtain relevant information from probing techniques a careful choice of probe molecules is required. There are a number of criteria that have been proposed for the study of the acid-base properties of heterogeneous catalysts by Knözinger[13] and Paukshtis and Yurchenko[14] that can be extended to other techniques. These are:

1. The probe molecule must induce an observable change in the spectrum of either the surface or the probe molecule itself when it is adsorbed onto the material

2. For studying surface acidity a probe molecule with predominantly basic properties should be used and *vice versa*

3. If studying a particular reaction, either the relevant reactant should be used or a molecule of similar size and reactivity

## 1.2 Monitoring the Formation of Porous Structures

The discovery by Beck and co-workers at the Mobil Corporation of the M41S family of ordered silicate/aluminosilicate mesoporous materials[15] sparked a great deal of interest in these materials. Prior to their discovery, the area of ordered materials with molecular sieve properties was dominated by zeolites (crystalline aluminosilicates). Traditional zeolites have pore

sizes in the micropore region (< 2nm in diameter).[16] The first zeotype material to have a larger pore diameter than this was the molecular sieve $AlPO_4$-8 discovered by Wilson and co-workers in 1982,[17] though its structure was not solved until 1990.[18] It was the first zeotype material to have 14-membered rings rather than the traditional twelve. Other materials were later found such as VPI-5 (18-membered rings)[19] and cloverite (openings made up of 20-tetrahedrally coordinated atoms in a clover-leaf shape)[20]. However, none of these ultra large pore molecular sieves have found significant applications either due to their poor stability or weak acidity.

Hence, the discovery of the M41S family of materials was a major breakthrough. For the first time, materials could be synthesised easily with pore sizes in the mesopore range (2-50nm). The sizes of the pores can also be tuned by careful selection of reaction conditions. These materials are made by addition of a silica source to a solution of molecules capable of forming liquid-crystal mesophases. In the original works this was a long chain alkylammonium cationic species.[15a,15c] More recently, Tanev and co-workers developed a method using a long-chain neutral amine under mild conditions.[21] The mechanism of the formation of these materials has a been a subject of much debate and there are a number of works in which techniques such as X-ray diffraction,[22] electron paramagnetic resonance (EPR),[23] NMR[22a,24] and infrared spectroscopy[25] are used in attempts to determine this.

One of the most frequently studied of these materials is MCM-41, which has a hexagonal pore structure.[15a] The range of pore sizes that can be formed in this material are shown in the TEM images by Beck and co-workers in figure 1.[15a] It was originally proposed that these structures were formed from either monomeric silicon containing species such as tetraethyl orthosilicate (TEOS) or short chain oligomers in sodium silicate solution in a surfactant solution by a liquid crystal templating mechanism, shown

schematically in figure 2. They proposed 2 possible pathways; (1) the surfactant molecules form a hexagonal mesophase with the polar head groups on the outside. The length of the hydrocarbon "tail" of the surfactant molecule determines the diameter of the cylinders formed. Then, the silicate species occupy the spaces between the cylinders. Or pathway (2) randomly ordered rod-like micelles interact with the anionic silicate species by Coulombic interactions to produce several monolayers of silicate encapsulation around the external surfaces of the micelles. These species then spontaneously pack into a highly ordered mesophase with an energetically favourable hexagonal arrangement accompanied by silicate condensation. In both cases the final calcination step burns off the surfactant template leaving just the silicate walls.[15a]

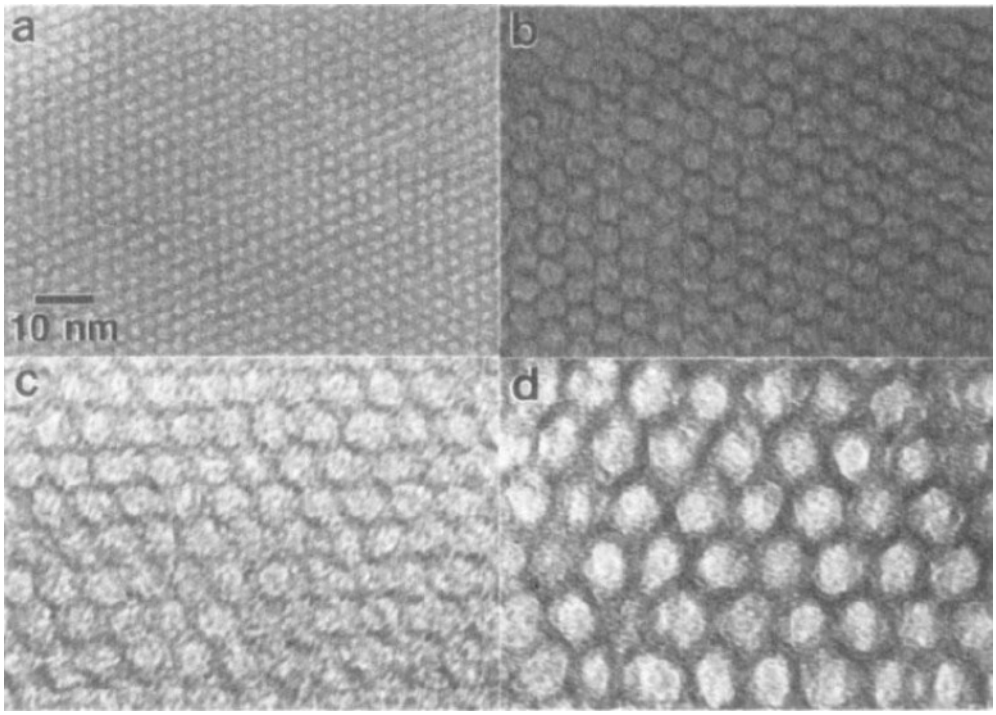


**Figure 1: TEM images of MCM-41 with average pore sizes (a) 20, (b) 40, (c) 65 and (d) 100 Å**

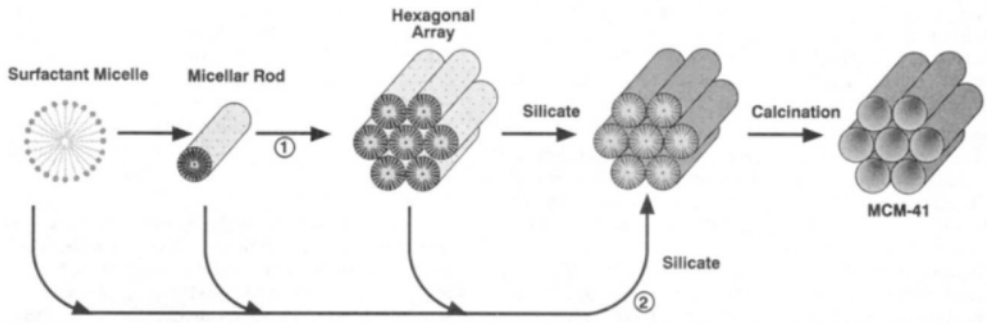


**Figure 2: The two possible pathways proposed by Beck and co-workers for the mechanism of formation of MCM-41[15a]**

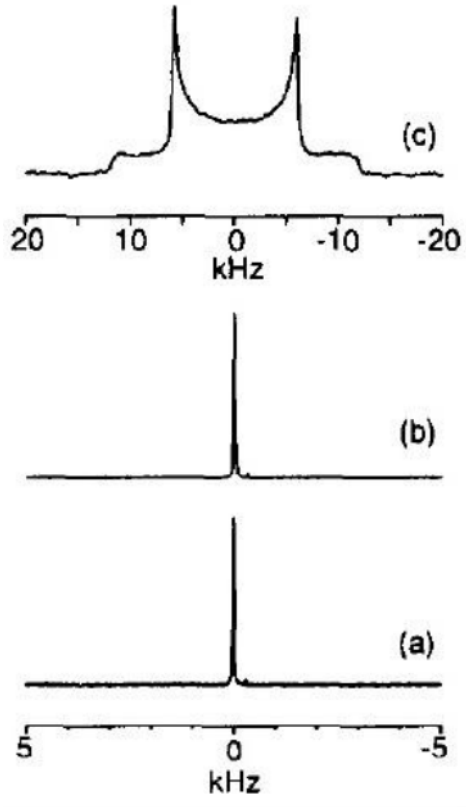


**Figure 3:[15]N NMR spectra of aqueous surfactant solutions. a) spherical micelles (7 wt%), b) rod-like micelles (17 wt%) and c) hexagonal liquid-crystalline phase (38 wt%)**

More recent studies seem to favour pathway (2). Chen and co-workers used X-ray powder diffraction, $^{29}$Si NMR and *in situ* $^{15}$N NMR to study formation of MCM-41. Their results from *in situ* $^{15}$N NMR measurements

shown in figures 3 and 4 indicate no evidence of a hexagonal mesophase in the reaction mixture (figure 4) that produced an MCM-41 powder diffraction pattern and hence this cannot be the structure-directing agent.[22a]

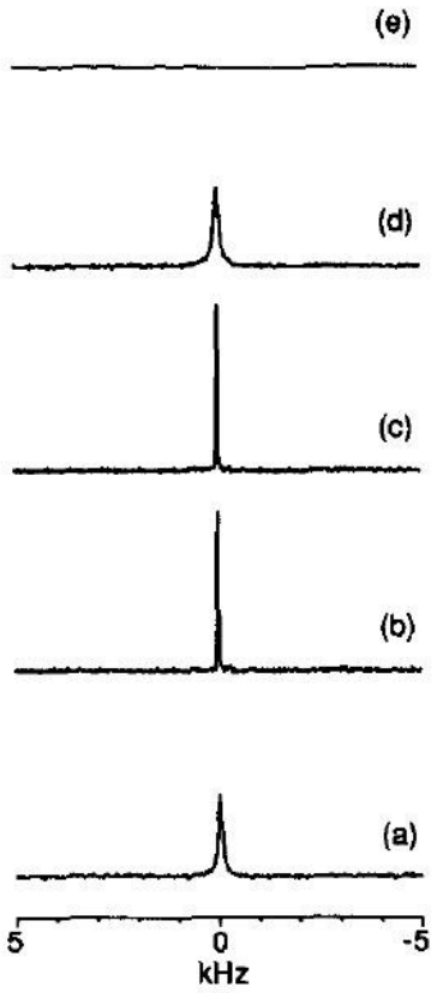


**Figure 4: *In situ* $^{15}$N NMR spectra of a) unheated synthesis gel, b) synthesis gel at 95˚C after heating for 1hr, c) synthesis gel at 95˚C after heating for 24hrs, d) wet solid product at 22˚C and e) solid product dried under ambient conditions**

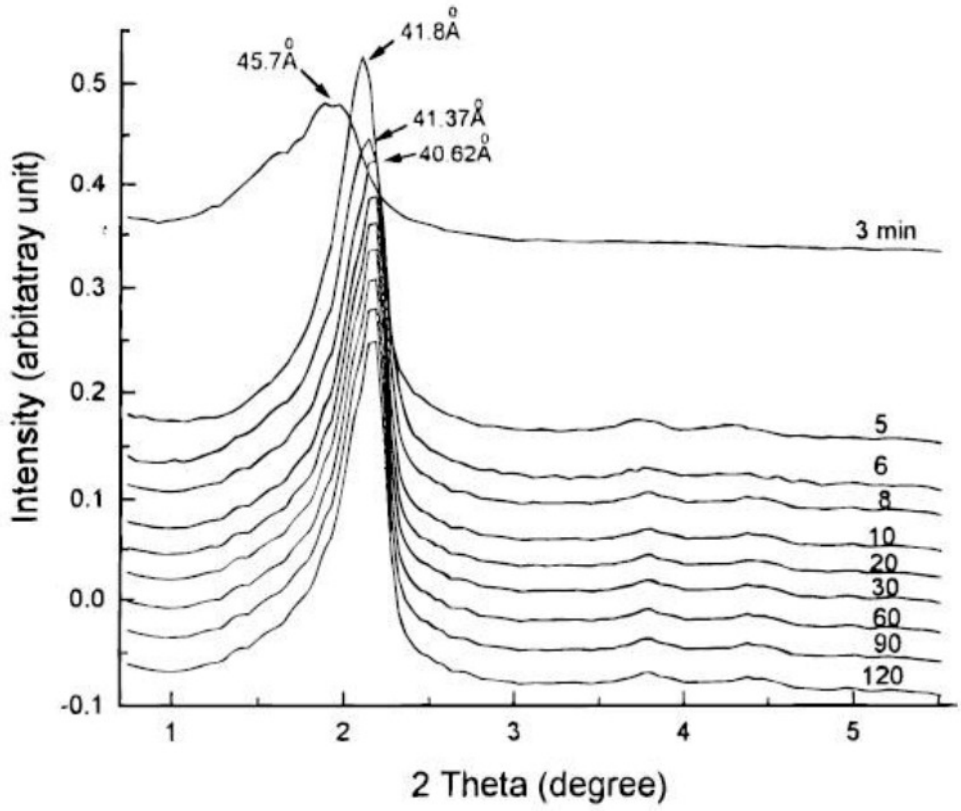


**Figure 5: XRD patterns for MCM-41 solid recorded at various times after the addition of TEOS to the starting surfactant solution[23b]**

The XRD patterns in figure 5 show that the hexagonal structure is beginning to appear after only 3 minutes reaction time. The peak shifts and gets narrower as further condensation of the silicate walls occurs. [23b]

*In situ* studies have also been carried out using electron paramagnetic resonance (EPR) by adding a stable radical species (a spin probe) to the reaction mixture.[23b,26] 4-(*N*,*N*-dimethyl-*N*-hexadecyl)-ammonium-2,2,6,6-tetramethyl piperidinyloxy iodide (CAT 16) is one such spin probe molecule. As shown in figure 6 its structure is very similar to that of the surfactant cetyltrimethylammonium bromide (or chloride) and so it is incorporated into the micelles along with the surfactant.

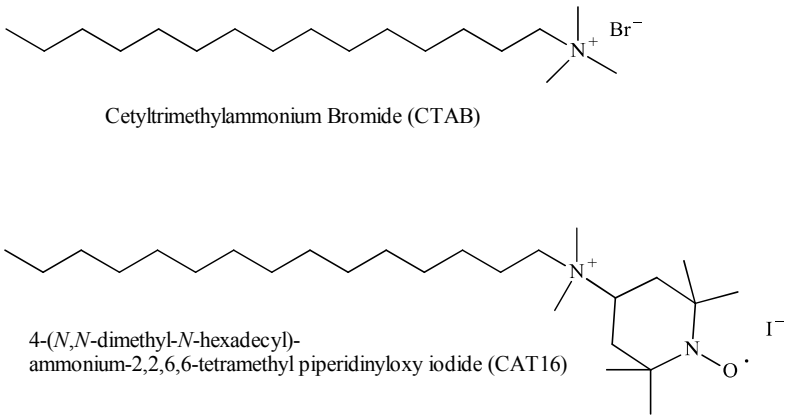


**Figure 6: Comparison of the surfactant CTAB and the spin probe CAT 16**

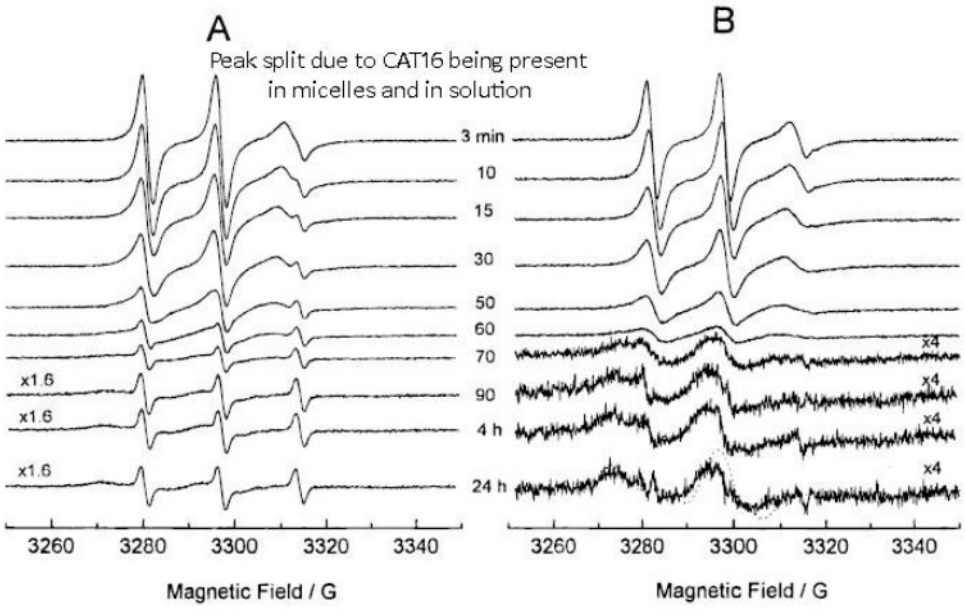


**Figure 7: A) EPR Spectra of MCM-41 reaction mixture containing CAT16 and B) the same spectra minus the aqueous component[23b]**

The high-field peak is a single sharp peak when CAT 16 is in aqueous solution. In the presence of the CTAB surfactant the peak is split as seen in the short reaction times in figure 7: A). This represents CAT 16 being present in the aqueous component and in the micelles and exchanging slowly on the EPR timescale. During the conversion, the aqueous component remains practically unchanged, whereas the micelle component

gradually broadens until it converts completely into the rigid line shape. The conversion lasts about 2.5 hours, after which time the spectra do not change. Subtracting the aqueous component in B) shows the line broadening more clearly.

It can be seen from the above data and has been found by other workers, e.g. Holmes *et al* using in situ infrared spectroscopy[25a] that there are two stages to the formation of MCM-41. 1. A rapid conversion to an ordered hexagonal mesophase when the silica source and surfactant are mixed and 2. a slow condensation step that increasingly cross-links the silicate to produce the final structure. It has been shown that in the original conditions used by Beck and co-workers, the concentration of quaternary alkylammonium chloride (or bromide) (usually cetyltrimethylammonium chloride/bromide) surfactant used as a template is below the critical micelle concentration. An ion exchange occurs between the surfactant and the negatively charged silica oligmers, with the concentration of the resultant $[CH_3(CH_2)_{14}CH_2N(CH_3)_3]^+ [Si_yO_x]^{n-}$ being above the critical micelle concentration. This leads to self-assembly of the rods.

Monnier *et al*[27] identified three essential phenomena for formation of a surfactant-silica mesostructure: i) multidentate binding of silicate oligomers to the surfactant, ii) preferential silicate polymerisation in the interface region and iii) charge density matching between the surfactant and the silicate. They however propose a slightly different formation mechanism to the liquid crystal templating mechanism proposed above. In their study they used a relatively low surfactant concentration and low temperatures. They observed that the formation of a lamellar phase before the formation of the hexagonal phase that produced MCM-41, as shown in figure 8.

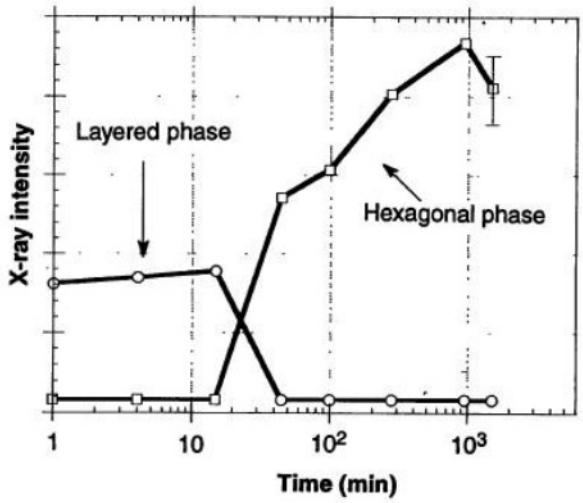


**Figure 8: Time evolution intensity of X-ray diffraction features associated with layered and hexagonal M41S mesostructures**[27]

In this mechanism, small silica oligomers bind in a multidentate fashion around the surfactant cations. This leads to a very strong interaction between them. These species can then further polymerise to form very large ligands. These multidentate surfactant-silicate ligands lead to a lamellar biphase governed by the optimal head group area ($A_0$). As the silicate polymerisation proceeds, the average head group area (A) of the surfactant assembly increases to decrease of the charge density of the larger silicate polyanions. This encourages corrugation of the silicate layers and ultimately results in the precipitation of the hexagonal mesophase.[27]

It can be seen from the preceding discussion that no single mechanism can be applied to the formation of M41S materials. The mechanism of formation is strongly influenced by the chosen reaction conditions.

## 1.3 The Use of Infrared Spectroscopy to Characterise the Surface Properties of Silica and Other Metal Oxides

Infrared spectroscopy is a widely used technique for studying the surface chemistry of solid materials. The majority of these studies have focussed on surface hydroxyl groups, particularly for metal oxides.[3b,28] The widespread use of these materials in industry as catalysts and adsorbents combined with the fact that the surface-species can be easily observed in infrared spectra even at low concentrations have made them popular choices for study.

Under ambient conditions, the surface of silica is covered with a variety of different silanol (SiOH) groups. These create a highly hydrophilic surface and there is a high concentration of adsorbed water. The concentration of adsorbed water depends upon the method of producing the silica and hence its surface properties. Burneau *et al*, in their study on the dehydration-rehydration of silica surfaces; found that for silica samples evacuated under vacuum at room temperature then placed in an atmosphere of 52% humidity, they adsorbed between 2.2% water by weight for Aerosil 200 (a fumed or "pyrogenic" silica) and 10.1% for a silica gel.[29] This difference in affinity for adsorption of water is mainly due to the number and type of surface silanol groups present. In mid-infrared (IR) spectra, the OH stretching vibrations of silanol groups are in the region 3800-2500 $cm^{-1}$. Figure 9 shows the mid-IR spectra of the silica samples mentioned above along with a precipitated silica, Zeosil 175 MP. The sharp peak at 3747$cm^{-1}$ is assigned to free isolated silanols and the broad band below that corresponds to a range of hydrogen-bonded silanol and water species.[29] Figure 10 shows the different silanol structures that may be present on a silica surface (without adsorbed molecular water). Free isolated silanol species are defined as those that have no other silanol groups within hydrogen bonding distance. Also shown in that figure are siloxane groups,

vicinal silanols (those that are close enough to each other to form hydrogen bonds) .and geminal and triple silanol groups which may be internally hydrogen-bonded.

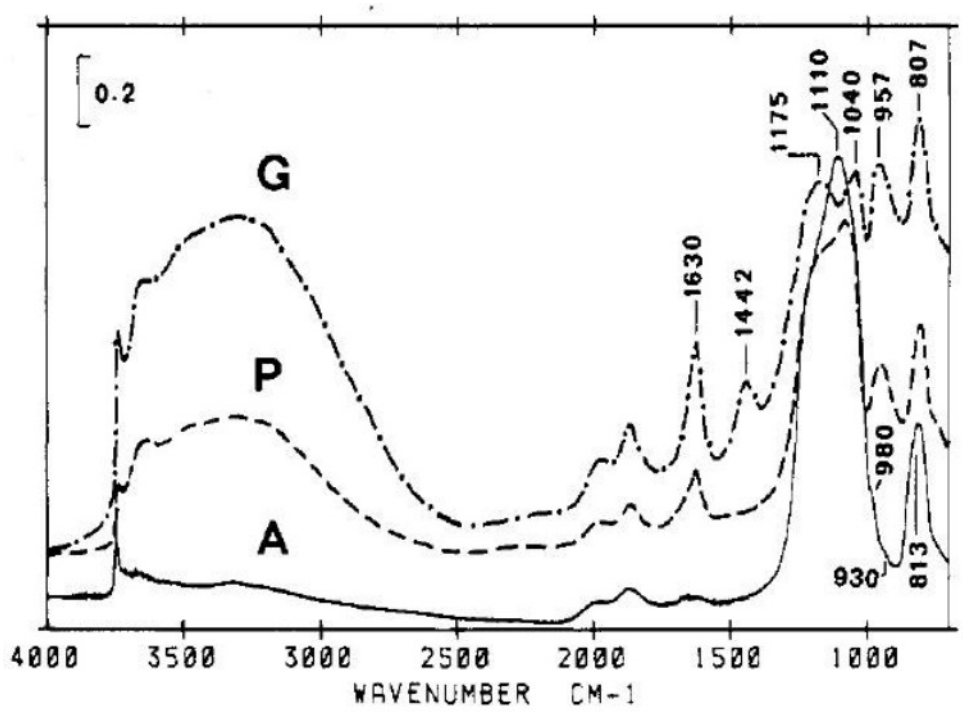


**Figure 9: Mid-IR spectra at room temperature of Aerosil 200 (A), Zeosil 175 MP (P) and silica gel (G)**

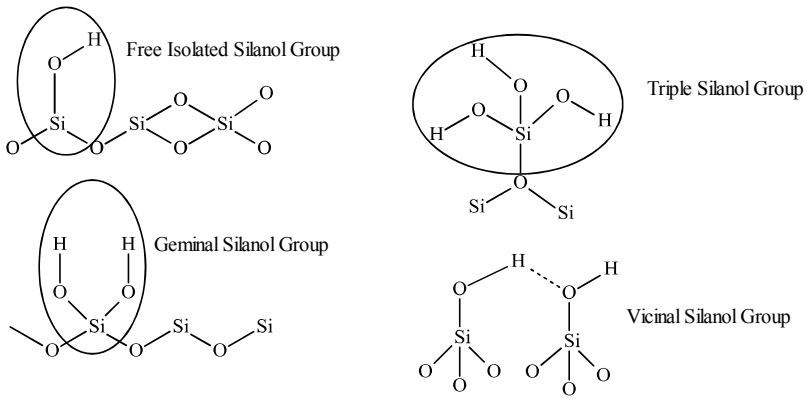


**Figure 10: Possible "free" silanol structures present on silica surfaces**

The band relating to the OH stretches of each of these groups shifts in position from the free isolated silanol at the highest wavenumber, to hydrogen-bonded vicinal silanol groups at the lowest wavenumber. It is very challenging to distinguish between isolated, geminal and triple silanol groups in infrared spectra. Davis and co-workers used Pearson VII bands to attempt to deconvolute the broad band at around 3650-2500cm$^{-1}$ for silica samples hydrated and dehydrated at different temperatures.[30] They required 8 Pearson VII bands to properly fit the broad band in hydrated silica samples. Tekeia *et al* generated silica surfaces that possessed only geminal or triple surface silanols by treatment of surface hydroxyls with trichloromethylsilane (geminal silanols created) or silicon tetrachloride (triple silanols created) followed by reaction of the chlorine groups with water.[31] They found that the position the IR bands for these generated groups shifted by only 2 and 3cm$^{-1}$ respectively from the peak position for an isolated silanol. Whereas the full-width at half maximum for the isolated silanol for a sample treated at 1073K is approximately 5cm$^{-1}$. Hence on a surface with more than one type of silanol group they cannot be distinguished.

Not only does the type of silica sample determine the concentration and type of surface hydroxyl groups but the temperature at which the sample is heated prior to use is a very important factor. Figures 11 and 12 are from a study carried out by Van Roosmalen on the dehydration/rehydration of silica aerogel samples.[32] They show that as the degassing temperature increases, the first band to disappear is at the lowest wavenumber and represents adsorbed water. Then in figure 12, curve B a slightly more defined band is observed representing hydrogen bonded silanol species (this band was previously masked by the water band). Finally, at high temperatures as seen in figure 11 the relatively narrow band associated with free isolated silanol groups is the main residual band. The hydrogen-bonded silanol groups are now only represented by the tailing of this band to low frequency in the subtraction spectra shown in figure 12.

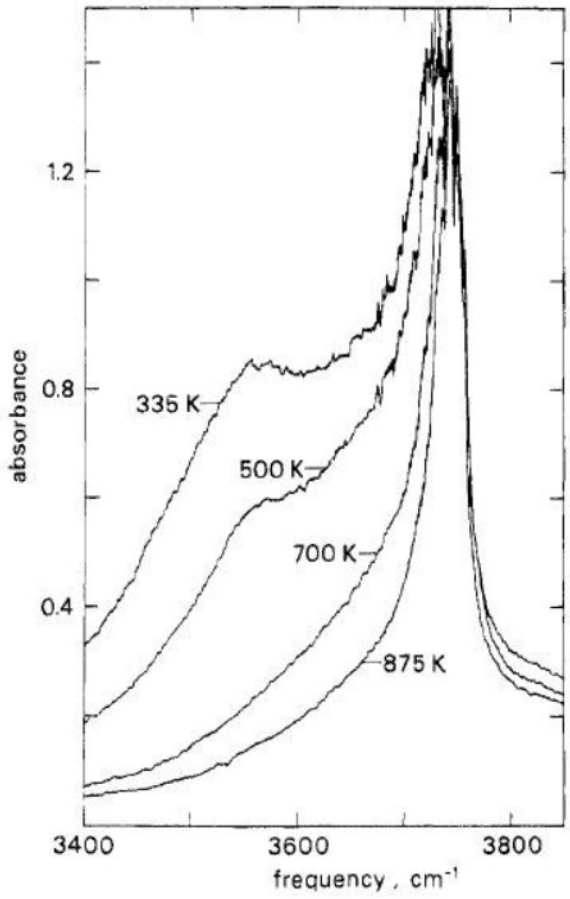


**Figure 11: Infrared spectra of a hydrated silica gel degassed under vacuum at the temperatures shown on the spectra**

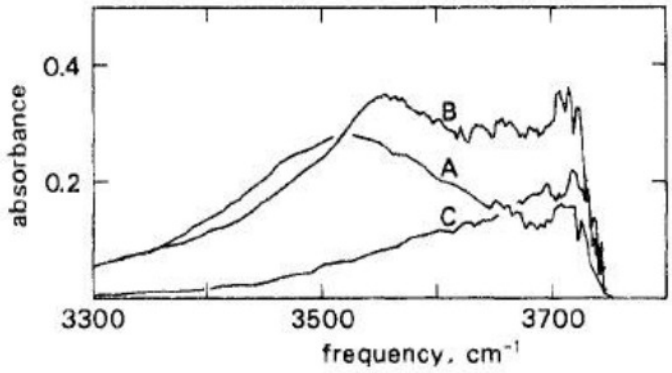


**Figure 12: Infrared spectra of the differences between the curves in figure 11. A: 335-500K, B: 500-700K, C: 700-875K**

In order to help overcome the difficulties associated with overlap of OH stretches from water and silanol groups in mid-IR studies of surface

hydroxyls Perry *et al* studied near-IR spectra in their investigation of the hydration/dehydration of porous sol-gel silica glasses.[33] Figure 13 shows the near-IR spectra of silica samples dehydrated at 180˚C and 1000˚C and then exposed to ambient conditions for the times given. Table 1 lists the relevant peak assignments.

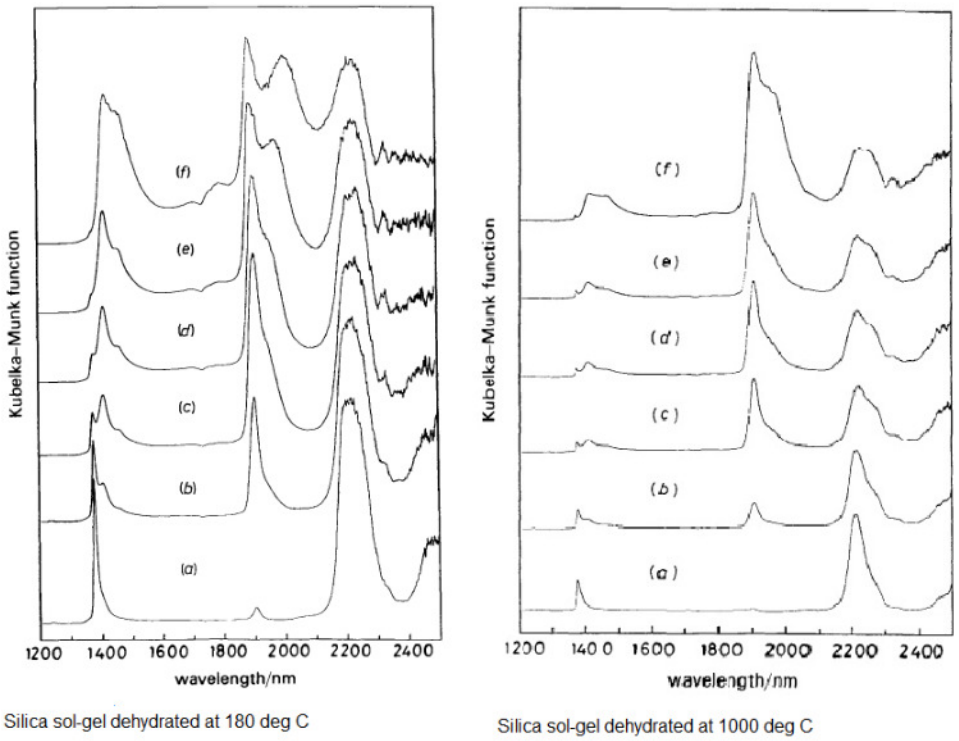


**Figure 13: Reflectance near-IR spectra showing the 1st overtone region of silica sol-gel glasses heated to 180˚C and 1000˚C and then exposed to ambient conditions for times: (a) t=0hr, (b) t=0.5hr, (c) t=1hr, (d) t= hrs, (e) t=4hrs, (f) t=72hrs**

**Table 1: Table showing the peak assignments for the near-IR spectra of a hydrated silica gel surface[33]**

| Peak Position/ nm | Peak Position/ $cm^{-1}$ | Peak Assignment |
|---|---|---|
| 2270 | 4405 | $\nu_{OH}$ (SiOH) + $\nu_s$(SiOSi) (H) |
| 2192 | 4562 | $\nu_{OH}$ (SiOH) + $\nu_s$(SiOSi) (F)[a] |
| 1950 | 5128 | $\nu_{OH}$ + $\delta_{OH}$ (S'$_1$, S'$_2$) (adsorbed $H_2O$) |
| 1892 | 5285 | $\nu_{OH}$ + $\delta_{OH}$ (S'$_0$) (adsorbed $H_2O$) |
| 1455 | 6873 | $2\nu_{OH}$(S'$_1$, S'$_2$) (adsorbed $H_2O$) |
| 1400 | 7143 | $2\nu_{OH}$(S'$_0$) (adsorbed $H_2O$) |
| 1400 | 7143 | 2νOH(SiOH) (H) |
| 1365 | 7326 | 2νOH SiOH (F) |

S'$_0$, ($S_0$) = monomeric; S'$_1$, ($S_1$) = partially hydrogen-bonded, S'$_2$, ($S_2$) = fully hydrogen-bonded; F= free; H = hydrogen-bonded

[a]Burneau and Carteret in their near-IR and computational study on the SiOH groups of silica surfaces assign this band to a combination of the OH stretch of SiOH with a SiOH bending mode.[34] This band also splits in to two when infrared spectra are recorded at low temperature, Zarubin attributed this to Fermi resonance splitting.[35]

Whatever the precise assignment of the two lowest frequency bands it can be seen from the near-IR reflectance spectra that heating the sample to

1000˚C removes almost all of the surface hydroxyl species leaving only bands related to free SiOH groups. Whereas heating to 180˚C leaves many hydrogen bonded silanol groups intact. The generally accepted mechanism for the dehydration of silica surfaces upon heating is shown in figure 14.

-

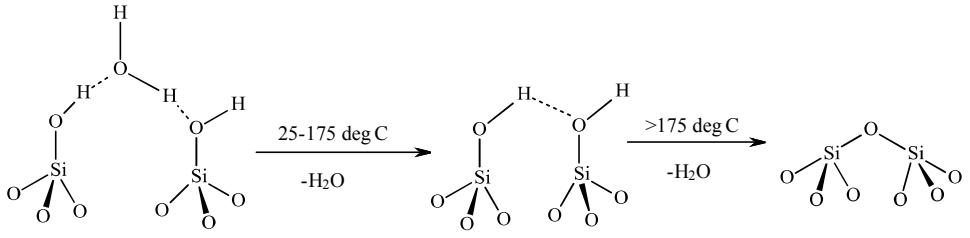


**Figure 14: The reactions occurring during thermal dehydration of a silica surface[36]**

The fact that there are so few silanol groups remaining on the silica surface after dehydration at 1000˚C and formation of siloxane groups shown in figure 14 explains why the surface takes a long time to rehydrate. Adsorption of water onto isolated silanol groups has shown to be a unfavourable interaction[29] as the siloxane groups are hydrophobic. In more hydrated silica samples, bands from the adsorbed water combination bands and the hydrogen bonded SiOH stretch overtone still overlap making assignments even in the near-IR difficult.

Because of these difficulties, several groups have used $D_2O$ adsorption to help identify the bands associated with adsorbed water on silica surfaces.[32,34,37] More interesting however from the point of view of the surface reactivity of silica based materials, are their surface acidity and basicity rather than their hydrophilicity. Classic infrared probe molecules for studying surface acidity are ammonia, aliphatic amines, pyridine, nitriles, benzene and substituted benzene and carbon monoxide.[28] Probes for surface basicity include carbon monoxide, carbon dioxide, sulphur dioxide, chloroform (and deuterated chloroform) and hydrogen chloride.[3b]

There is no single "perfect" infrared probe for surface acidity or basicity. For instance, $NH_3$ is a good probe for probing the acidity of micropores due to its small size, however the resulting infrared spectra may be complex and difficult to analyse. On sites of sufficient acidity $NH_3$ is protonated to $NH_4^+$ and the symmetry of this species may be perturbed possibly resulting in several bands in the infrared spectrum.[38] Although this protonation provides valuable information about the strength of the surface acid sites, the multiplicity of the bands may lead to confusion when assigning spectra. Also on certain surfaces (such as highly dehydroxylated silica) or when $NH_3$ is adsorbed onto a surface at high temperature $NH_3$ may dissociate to give Si-$NH_2$ groups.[39]

Nitriles are weak bases and generally are not protonated even on highly acidic sites but the CN stretch position shifts with hydrogen-bonding to surfaces. Also, the advantage of using this band to probe the strength of surface hydrogen-bonding is that it is well separated from most other resonances. Acetonitrile is a popular choice again because of its small size; however the deuterated analogue should be used to prevent complications from Fermi resonance and care must be taken because it may react with some surfaces.[40]

Usually, several different probe molecules are used to gain a fuller picture of the surface chemistry, for example, Gil *et al* used $NH_3$, pyridine, deuterated acetontrile and pivalonitrile $(CH_3)_3CCN$) to compare the surface properties of two different zeolites (SSZ-33 and SSZ-35).[41] SSZ-33 possesses a channel system made up of intersecting 12-MR (MR= member ring) and 10-MR pores. SSZ-35 has a uniform 1-dimensional 10-MR channel system, which periodically opens out into wide, shallow cavities with 18-MR openings.

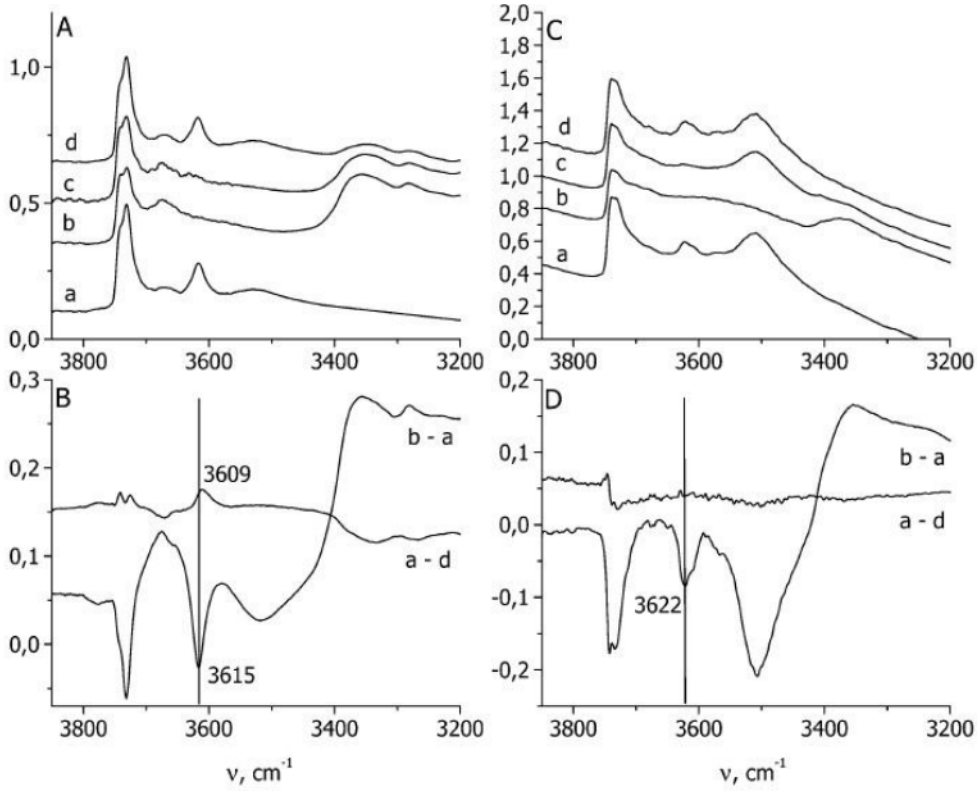


**Figure 15: The affects of $NH_3$ adsorption (at 150°C) of the OH stretch region of the IR spectra of SSZ-33 (A and B) and SSZ-35 (C and D). Key: a= spectra of samples before $NH_3$ adsorption, b= after 20 mins desorption at 150˚C (removal of weakly bound $NH_3$), c= after 20 mins desorption at 250˚C and d= after 20 mins desorption at 350˚C.**

It can be seen from figure 15 B and D (b-a) difference spectra that all the OH groups interact with ammonia. For SSZ-33, the increase in intensity of the band at around 3670cm$^{-1}$ suggests that a fraction of the Si-OH groups (3744cm$^{-1}$ and 3732cm$^{-1}$) are hydrogen-bonding to $NH_3$, resulting in a decrease in stretching frequency. The fact that these interactions are observed even after desorption at 250°C (see figure 15 A) led to the assignment of these as Si-OH groups hydrogen-bonding with $NH_4^+$ ions chemisorbed onto nearby Lewis or Brönsted sites. For both zeolites the acid sites (bridging Si-OH-Al species) are assigned to the bands at around 3620 cm$^{-1}$ "free" and 3500 cm$^{-1}$ "disturbed" by multiple interactions.[42] For SSZ-35 both of these species are restored more or less simultaneously but in SSZ-33 there is some heterogeneity. A band at 3609cm$^{-1}$ remains even after desorption at 350°C, indicating chemisorption onto the most acidic sites.

The results from pyridine adsorption were similar but pyridine can distinguish between Lewis and Brönsted sites.

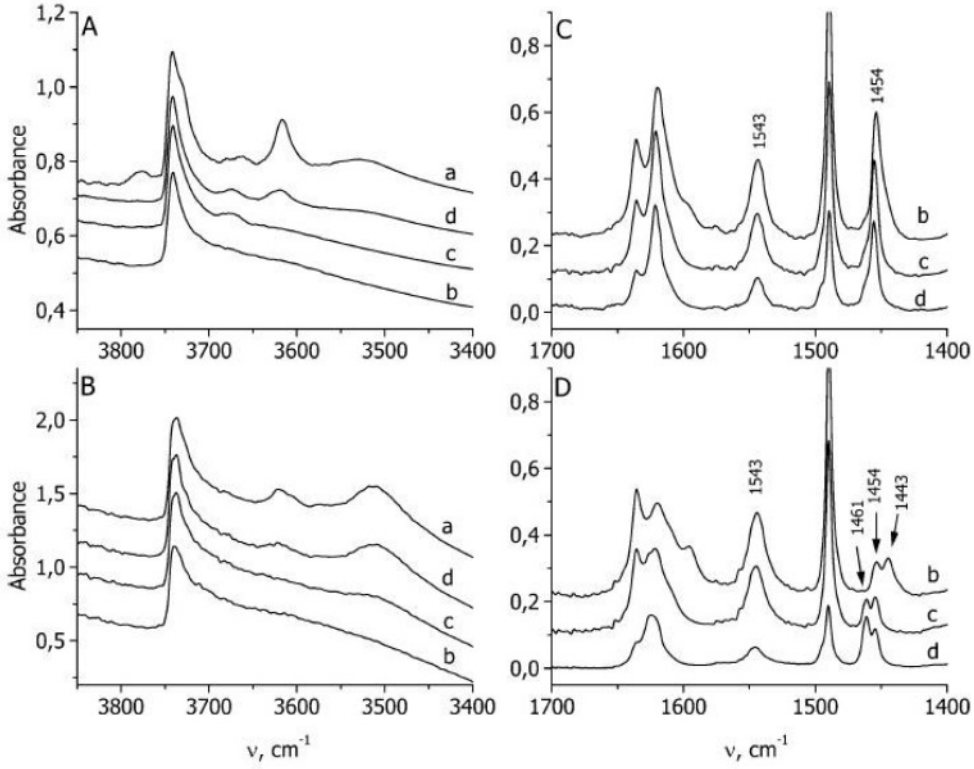


**Figure 16: Pyridine adsorption on SSZ-33 (A and C) and SSZ-35 (B and D) at 170C. Key: a= activated sample, b= after 20 mins desorption at 170°C, c= after 20 mins desorption at 250°C (SSZ-33) and 450°C (SSZ-35) and d= after 20 mins desorption at 550° C**

The band at 1543 $cm^{-1}$ in figure 16 C and D represents the pyridinium ion ($PyH^+$), pyridine adsorbed onto a Brönsted acid site. The single band at 1454$cm^{-1}$ for SSZ-33 and the 3 bands in the same region for SSZ-35 represent pyridine adsorbed on a Lewis acid site (PyL). The 1443 $cm^{-1}$ band is assigned to pyridine interacting with silanols and the two other bands either represent sites of differing Lewis acidity or one represents the true Lewis acid interaction and the other the formation of an iminium ion.[43] They showed with adsorption of $d_3$-acetonitrile that there are in fact 2 different Lewis acid sites, but either explanation is possible.

Pivalonitrile was chosen to distinguish between the acid sites located inside 10-MR and 12-MR channels in SSZ-33. The kinetic parameter for pivalonitrile is 0.6 nm, which should prevent it entering the 10-MR channels of dimensions 0.54×0.57 nm. Pivalonitrile however was observed to interact with almost all of the Brönsted sites, indicating that they are present inside 12-MR channels.

Other workers such as Morterra *et al* have studied acetonitrile adsorption on surfaces. They adsorbed acetonitrile onto different forms of zirconia and sulfated zirconia.[44] However, their resultant spectra are extremely complex due to a number of possible interactions and reactions that take place on the surfaces.

1. Coordinative interaction with $CH_3CN$ acting as a base (Surface Acid could be Brönsted or Lewis)

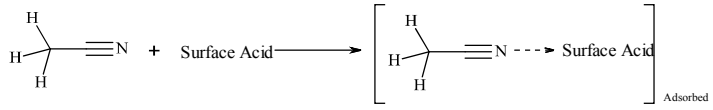


2. Π-type coordinative interaction with $CH_3CN$ acting as a base

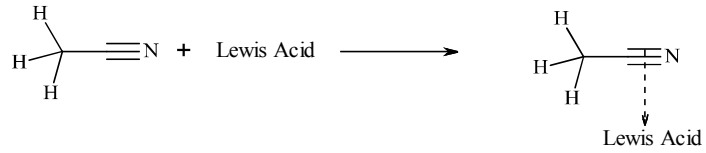


3. Carbanion formation with $CH_3CN$ acting as an acid

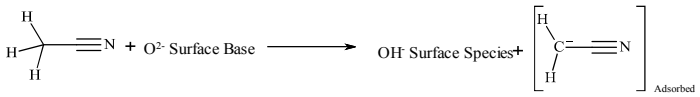


4. Hydrolytic formation of anionic acetamide species

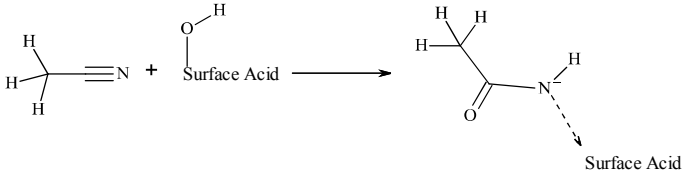


**Figure 17: Possible interactions of acetonitrile with metal oxide surfaces[44a]**

The occurrence of reaction 1 is monitored by the increase in spectral frequency of the νCN vibration. As mentioned previously, $CD_3CN$ is preferred for this because the νCN vibration is not perturbed by band doublings due to Fermi resonance. However, if using $d_3$-acetonitrile and reaction 3 occurs, the spectrum will be complicated by some deuterium exchange on surface hydroxyl species. This interaction is in competition with reaction 1. Interaction 2 is rarely observed and will result in a decrease

in spectra frequency of the νCN vibration. Reaction 4 has been shown to occur on transition aluminas[45] and on *m*-$ZrO_2$ systems.[44b] As many of 3 different types of the acetamide-type anions have been identified on *m*-$ZrO_2$. So obviously, some care is needed to be taken if acetonitrile is used as a probe molecule.

Camarota and co-workers studied the surface hydroxyl species in a phenylene-bridged periodic mesoporous organosilica using adsorbed ammonia and carbon monoxide.[46] The different hydroxyl species are shown in figure 18.

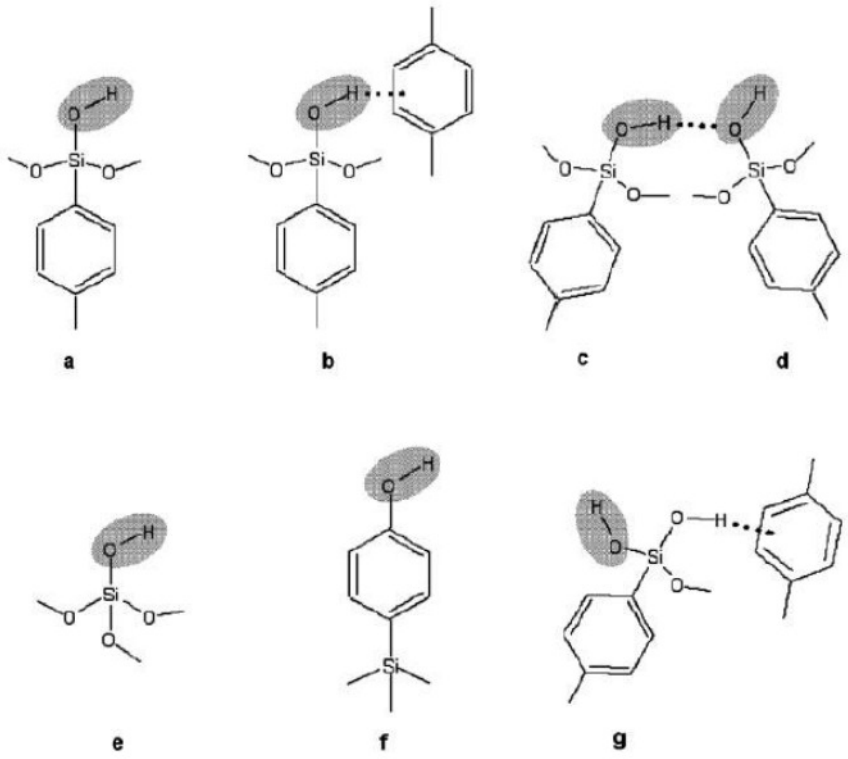


**Figure 18: The hydroxyl species found on the surface of phenylene-bridged peroidic mesoporous organosilica**

The changes to the OH stretching region of the IR spectra after adsorption of CO are shown in figure 19.

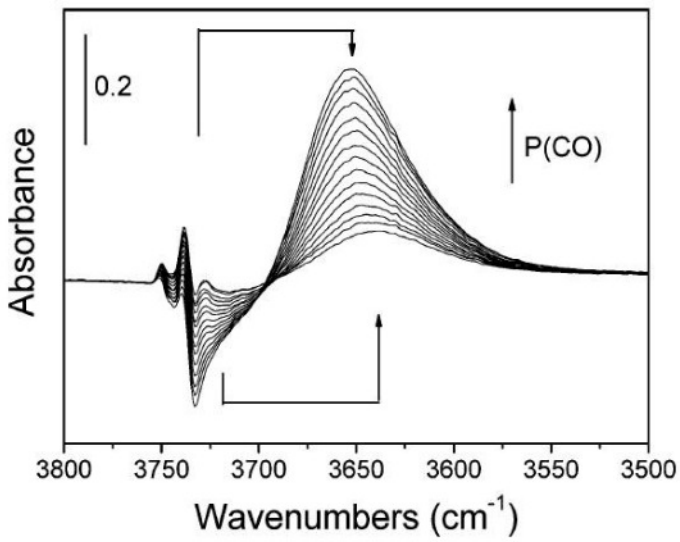


**Figure 19: Infrared difference spectra related to the interaction between CO and the organosilica in the pressure range 0.1-3570 Pa. The arrows show the shifts in SiOH stretching modes for species a and g[46]**

The positive band relates to silanol species hydrogen-bonding to CO, it is initially at 3640cm$^{-1}$ and shifts to 3655cm$^{-1}$ at higher coverage. This shift is due to CO adsorption on different SiOH species. The band at 3655cm$^{-1}$ is assigned to CO interacting with species a in figure 18 and the corresponding negative band is at 3730cm$^{-1}$.[47] Various studies using both computational calculations and data from infrared spectroscopy have demonstrated that CO interacts with acidic surface hydroxyl groups via a SiO-H---C≡O coordination.[48]

There is also a broader negative band at 3718cm$^{-1}$, which is eroded first. It is proposed that this represents the non-perturbed form of the hydrogen-bonded silanol absorbing at 3640cm$^{-1}$ and is assigned to species g. The shift in band position caused by hydrogen bonding is 78cm$^{-1}$, which is slightly larger than that for species a, ($\Delta\nu$SiOH = 73cm$^{-1}$). This, combined with the fact CO appears to interact with this group first indicates that it is slightly more acidic. The phenomenon of the acidity of a geminal silanol increasing in acidity when one of its OH groups is involved in hydrogen bonding has also been observed in silica.[49]

Surface basicity of metal oxides has been less frequently studied and the spectra of the available probe molecules are often complex when adsorbed on surfaces. For instance, $CO_2$ can form a number of different unidentate and polydentate structures.[50] HCl is a good probe for surface basicity but obviously there are handling difficulties associated with this molecule. $SO_2$ has been used by a few groups, however its behaviour with hydroxyl groups is not necessarily straightforward.[3b] $CDCl_3$ is a weak acid that was first proposed as a probe molecule for surface basicity by Paukshitis *et al*.[51] Pyrrole is a hydrogen-bond donating molecule that can be used to study surface basicity by measuring the IR shift of the νNH band.[3b]

Carbon dioxide is acidic and so adsorbs specifically onto basic sites of metal oxides, its adsorption onto alkaline zeolites has been widely studied. A band is generally observed at around 2360$cm^{-1}$, assigned to the $\nu_3$ stretching vibration, the degree of shift of this band to higher frequencies characterises the polarization strength of the cation. This interaction leads to a relaxation of the molecular symmetry and the appearance of a weak $\nu_1$ stretching mode band seen at 1380$cm^{-1}$.[52]

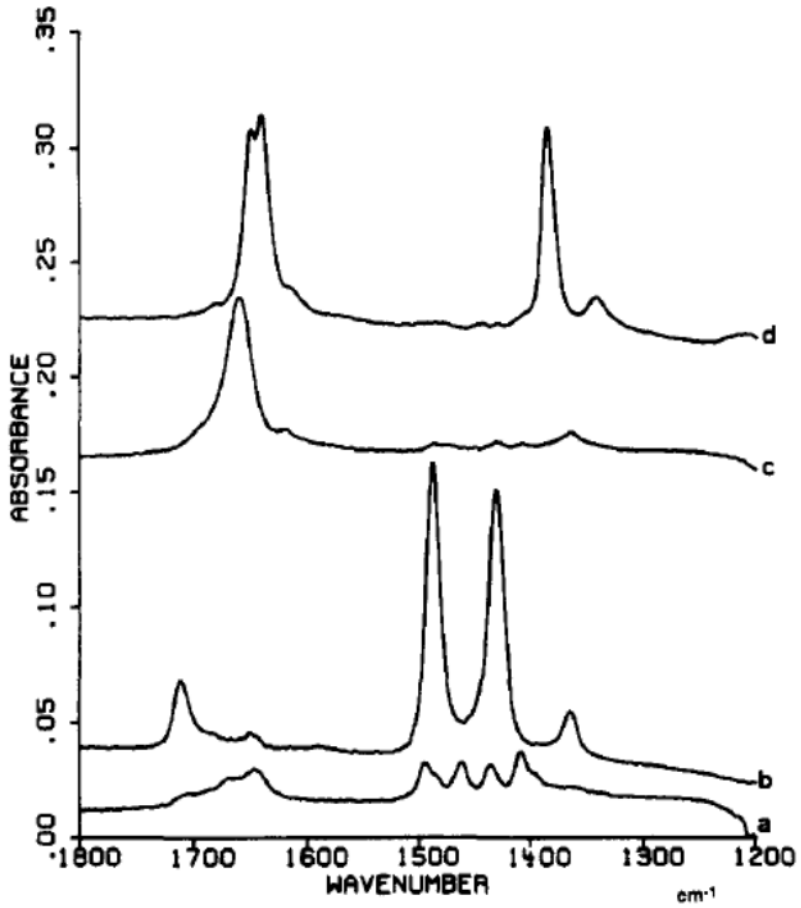


**Figure 20: IR spectra of chemisorbed species formed by $CO_2$ adsorption on X-type zeolites, a) LiX, b) NaX, c) KX and d) CsX**

$CO_2$ can also be chemisorbed onto zeolite surfaces forming carbonate species. The infrared spectra of these on several X-type zeolites are shown in figure 20. Jacobs *et al* particularly studied the case of NaX.[53]

The pair of bands at 1711cm$^{-1}$ and 1365cm$^{-1}$ is assigned to species 1 in figure 21, where $CO_2$ is bicoordinated to a framework Si or Al atom (labelled T) and a cation. This can be converted to species 2, characterised by bands at 1488cm$^{-1}$ and 1431cm$^{-1}$. As can be seen from figure 20, this conversion does not occur on CsX and no bands relating to carbonate species are observed for LiX. The formation of carbonate species indicates the presence $O^{2-}$ basic sites in alkaline zeolites (adsorption on hydroxyl groups leads to the formation of hydrogen carbonates).[54]

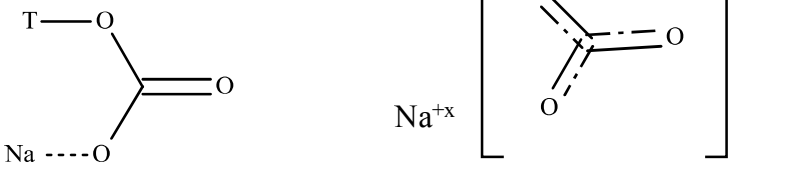


Species 1 Species 2

T= tetrahedrally coordinated metal (Si/Al)

**Figure 21: Species formed by chemisorption of $CO_2$ on NaX zeolite**

Sulphur dioxide is another probe for surface acidity, however its adsorption has mainly been studied on alumina, due the use of alumina as a catalyst for the Claus reaction used to remove sulphur from waste gas streams.[55]

$$2\ H_2S + SO_2 \rightleftharpoons 3/x\ S_x + 2\ H_2O$$

Lavalley and co-workers conducted infrared and gravimetric studies to try and deduce the mechanism of $SO_2$ adsorption on alumina. They found that after $CO_2$ adsorption on alumina to give hydrogen carbonate species, introduction of $SO_2$ removed the bands in the infrared spectrum characteristic of hydrogen carbonate species. Also that, pre-adsorption of $SO_2$ completely hinders the formation of hydrogen carbonate species when $CO_2$ is introduced.[56] This indicates that both species are adsorbed on the hydroxyl groups and since $SO_2$ is the stronger acid it will block these sites to $CO_2$.

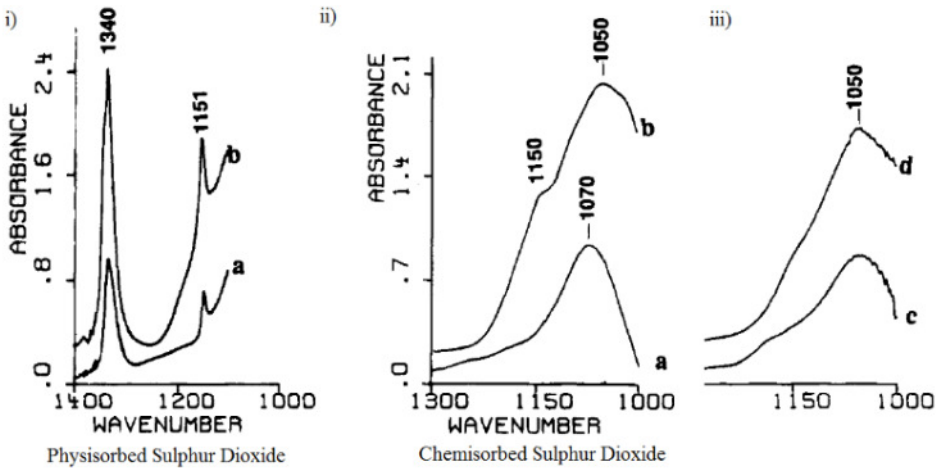


**Figure 22: Infrared spectra showing $SO_2$ physisorbed on alumina (left) and chemisorbed (right). a) $Al_2O_3$ (600), b) $Na/Al_2O_3$ (600), c) $Al_2O_3$ (350), d) $Na/Al_2O_3$ (350) (the number in brackets represents the activation temperature in°C)[57]**

In figure 22, the bands associated with physically adsorbed $SO_2$ are the antisymmetric (1340cm$^{-1}$) and symmetric (1151cm$^{-1}$) stretching vibrations. These are close to the positions for the gaseous species, indicating weak interactions. The bands in the spectra shown in figure 22 ii) and iii) represent sulphite species. It is clear that the more basic sodium impregnated alumina ($Na/Al_2O_3$) adsorbs more $SO_2$ than the bare alumina both physically and chemically. Also in this study $H_2S$ was adsorbed on the alumina samples pre-adsorbed with $SO_2$ and *vice versa*. It was found that since $SO_2$ was adsorbed more strongly onto the $Na/Al_2O_3$ it was less reactive with $H_2S$ than $SO_2$ adsorbed on bare alumina.[57]

Both $SO_2$ and $CDCl_3$ were used as infrared probes by Delsarte and co-workers to identify the basic sites on nitrided galloaluminophosphates used as catalysts for the Knoevenagel condensation.[5] The aim of the work was to test the hypothesis that the basic sites were due to the hydrogenated nitrogen species located at the surface after the nitridation treatment i.e. $NH_4^+$, $NH_3$, $–NH_2$ and –NH– groups and the exact nature of these groups.

Paukshitis *et a*l showed that the shift in the position of the CD stretching frequency can be used to determine the strength of the basic sites on metal oxides such as silica, alumina, MgO and CaO.[51] In this study on nitrided galloaluminophosphates it was found that the position and shape of this band differed between $CDCl_3$ adsorption on the $Al_{0.5}Ga_{0.5}PO_4$ precursor and the oxynitride form produced after $NH_3$ treatment as shown in figure 23.

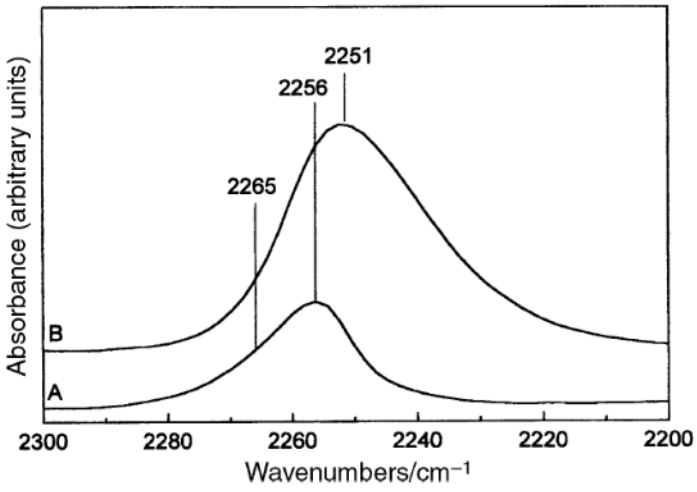


**Figure 23: The vCD band for $CDCl_3$ adsorbed on AlGaPO4 a) and oxynitride form b)**

In order to elucidate the exact nature of the adsorption sites for $CDCl_3$ on $AlGaPO_4$ and the nitrided form, subtraction spectra were calculated as shown in figure 24.

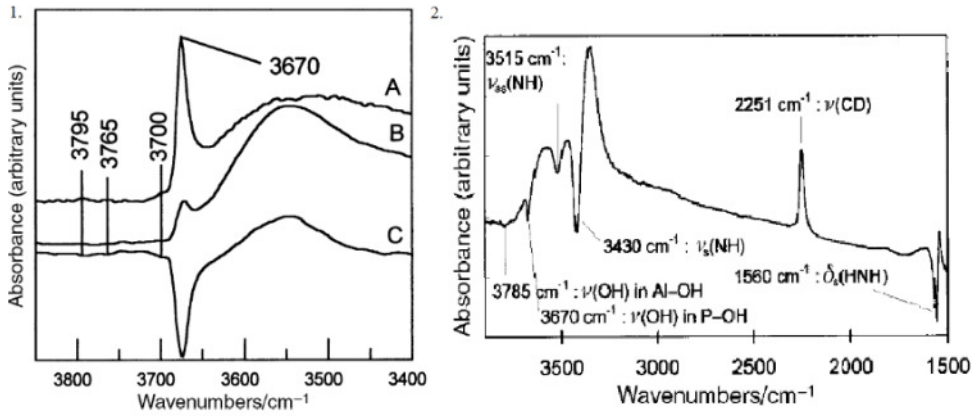


**Figure 24: Infrared spectra showing 1. Spectrum of the $AlGaPO_4$ precursor, a) before $CDCl_3$ adsorption, b) after $CDCl_3$ adsorption and c) subtraction spectrum. 2. Infrared subtraction spectrum showing $CDCl_3$ adsorption on the oxynitride form of $AlGaPO_4$**

It can be seen from figure 24: 1, that on the $AlGaPO_4$ sample, the $CDCl_3$ adsorption occurs on the OH groups. 1.c) shows perturbation of the bands at 3795$cm^{-1}$-νOH in tetrahedral Al-OH, 3765$cm^{-1}$- νOH in pentahedral Al-OH, 3700$cm^{-1}$- νOH in Ga-OH and 3670$cm^{-1}$-νOH in P-OH. On the oxynitride sample (2.) it can be seen that bands relating to νNH and δHNH for $–NH_2$ are perturbed by addition of $CDCl_3$. However the band at around 3300$cm^{-1}$ is not affected, this corresponds to –NH– groups. The same effect was also seen by them when $SO_2$ was adsorbed on the surface. Some $CDCl_3$ is also adsorbed on Al-OH but it is clear that the main sites for adsorption are $–NH_2$ groups. Whether these are attached to Al, Ga or P could not be determined.

Infrared spectroscopic probing techniques can provide a great deal of useful information about the interactions that take place when adsorbates are adsorbed onto a surface. These interactions can then provide information about the relative acidities or basicities of various surfaces. However, these techniques are most useful for studying specific systems or heterogeneously catalysed reactions. Often the behaviour of one probe molecule can be very different on different surfaces and the results are not always easily correlated. To gain a more complete picture infrared probing studies are

often used in conjunction with techniques such as temperature-programmed desorption[38] or model reactions as in the study by Delsarte.[5]

## 1.4 The Use of UV-Visible Spectroscopic Methods to Characterise Surface Properties

As discussed in the previous section, IR spectroscopic probing methods are only really suitable for the study of specific systems. For UV-visible probes however, attempts have been made to characterise a variety of solid surfaces according to some general parameters.[58] These parameters were developed to describe solvent-solute interactions[59] but have been extended to adsorbent-adsorbate interactions. They are based on the changes in the absorption maximum of a dye in dissolved in different solvents (or adsorbed on different surfaces). This is known as solvatochromism.

These parameters provide empirical measures of solvent or surface properties. They include Reichardt's $E_T(30)$ scale of solvent polarity[60] and Kamlet and Taft's linear solvation energy relationships that relate a number of different properties.[59]

The general Kamlet and Taft equation that can be used to describe the properties of any solvent is:

$$XYZ = (XYZ)_0 + m\delta_H^2 + a\alpha + b\beta + s(\pi^* + d\delta)$$

Where XYZ= measured value, $(XYZ)_0$ is the solute property of a reference medium i.e. a non-polar solvent, $\delta_H^2$ is a cavity term which relates to the Hildebrand solubility parameter, [61] $\alpha$ describes the hydrogen bond donating acidity, [62] $\beta$ describes the hydrogen bond accepting basicity[63] and $\pi^*$is the dipolarity/ polarizability of the solvents[64]. $\delta$ is a polarizability correction

term, which is 1 for aromatic, 0.5 for polyhalogenated and 0 for aliphatic solvents.[58e] m, a b, s and d are solvent independent correlation coefficients.

The Reichardt's $E_T(30)$ scale is based on the solvatochromic shift of the charge transfer transition of pyridinium-N-phenol betaine,[65] known now more commonly as Reichardt's dye. The transition is shown in figure 25.

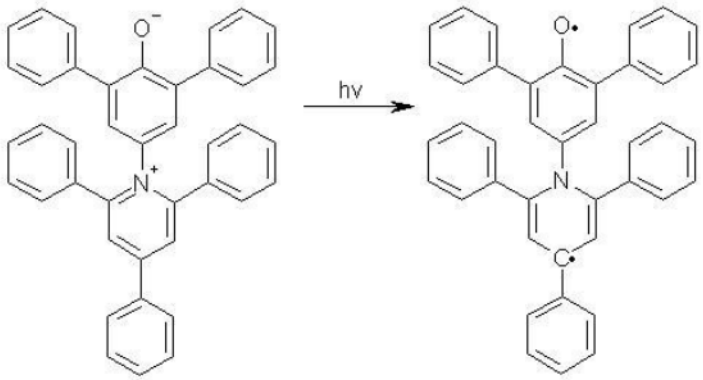


**Figure 25: The π-π* transition of Reichardt's dye used to calculate $E_T(30)$ values**

It has been found that $E_T(30)$ values can be expressed by a linear solvation energy relationship using the Kamlet and Taft parameters α and π* for well-behaved regular solvents. [66]

$E_T(30) = 31.2 + 15.2\ \alpha + 11.5\ \pi^*$ (a/s = 1.32)

This demonstrates that the $E_T(30)$ value for solvents contains contributions from the hydrogen bond donating acidity (60%) and dipolarity/polarizability values (40%). In fact Reichardt's dye is one of the dyes that may be used to calculate α values for protic solvents.[62] In order to calculate α and β values, pairs of indicator molecules, one which undergoes hydrogen bonding (either

as an acceptor or donator depending on whether α or β values are being calculated) and one that does not. For calculation of α values one such pair could be Reichardt's dye as the hydrogen bond acceptor and 4-nitroanisole as the non-hydrogen bonding substrate.[62] For calculation of β values, one possible pair is 4-nitroaniline as the hydrogen bond donor and N-N-diethylaniline as the non-hydrogen bonding substrate.[63] In a series of solvents of differing polarity but where hydrogen bonding is excluded the $\nu_{max}$ for the pairs of molecules should show linear correlation and in solvents which act as hydrogen bond donors or acceptors there should be significant displacement from the correlation line for the hydrogen bond donating or accepting indicator. It is this displacement that represents the α or β values. For these values and the other Kamlet and Taft values a great many different indicators and solvents have been tested and averaged values obtained and these are now a useful tool for predicting solvent behaviour.[59]

A great deal of work has been carried out by Spange and co-workers on using the solvatochromic comparison method to study the surface properties of silicas and modified silicas as well as alumina and silica-alumina samples. By the use of Reichardt's dye, shown in figure 25, a penta-tert-butyl substituted Reichardt's dye, $Fe(phen)_2(CN)_2$ and Michlers ketone, shown in figure 26 they established α and $\pi^*$ values for the surfaces and correlated them to $E_T(30)$ values.[58b,c,58e,f] The substituted Reichardt's dye is less basic than the original form, which makes it more suitable for the study of stronger acid surfaces. In acidic environments with pKa values lower than 6 the phenolate oxygen on the original Reichardt's dye becomes protonated, preventing the solvatochromic shift.[67] They found that in order to get good correlation between the $E_T(30)$ and α and π* values for silica and modified silicas a greater contribution from the α component was needed for acidic surfaces than for well-behaved regular solvents.[58b] This means that $E_T(30)$ values for silica are more a reflection of the acidity of the surface than the polarity.

$Fe(phen)_2(CN)_2$ is a probe more sensitive to the hydrogen-bond donating ability of the surrounding environment than to the polarizability/dipolarity and Michler's ketone is an indicator for polarizability/dipolarity. However, as for the α indicator $Fe(phen)_2(CN)_2$ the two parameters cannot be separated. [58e] More recently they reported the use of a novel solvatochromic dye shown in figure 27 that allowed the more or less exclusive measurement of π* values in hydrogen-bond donating environments.[58d]

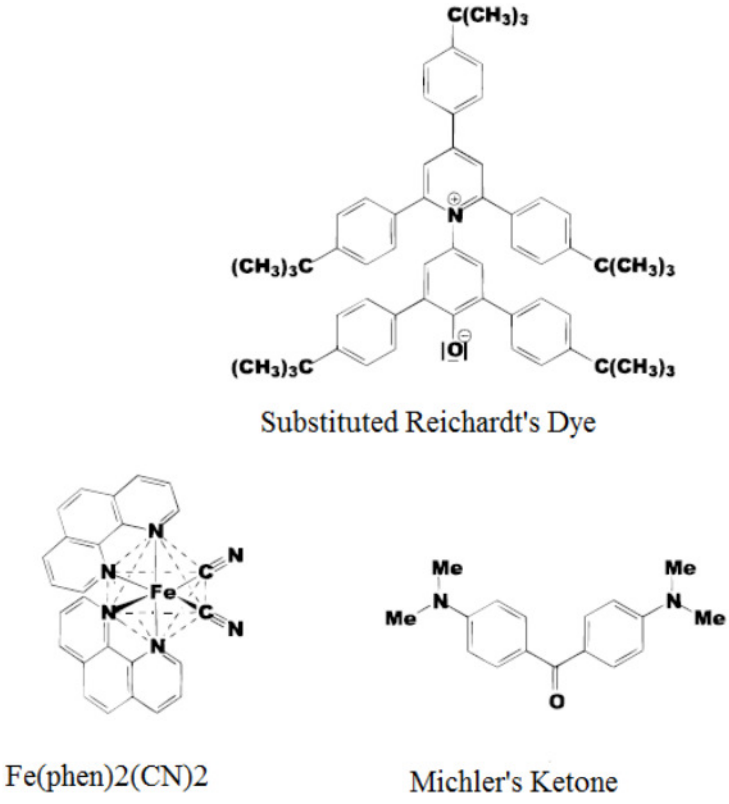


**Figure 26: Three of the indicators used by Spange *et al* for the calculation of $E_T(30)$, α and π* values for surfaces**

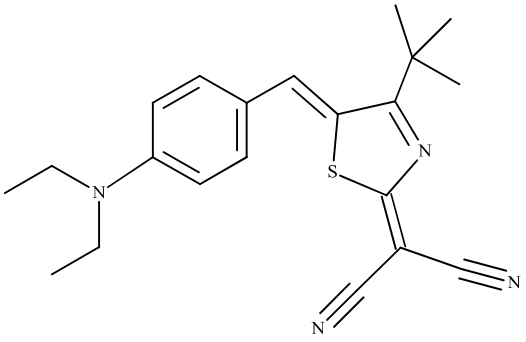


**Figure 27: Solvatochromic dye for evaluating π* parameters**

In one study, Spange *et al* compared the α, π* and $E_T(30)$ parameters of the external surface and inside the pores of an MCM-41 silica. Samples were made up with Reichardt's dye, $Fe(phen)_2(CN)_2$ or Michler's ketone encapsulated inside the pores during synthesis of the silica. The UV-vis spectra of the samples with the encapsulated indictors were then compared with those of MCM-41 with the indicator adsorbed on the external surface.[58f] $Fe(phen)_2(CN)_2$ was encapsulated inside the pores of sol-gel silica by mixing of the dye with methanol before mixing with tetramethoxysilane and water. The mixture was stirred to form a homogeneous and transparent sol before being dried under vacuum at 80˚C. The α value for this species was 1.55, whereas when it was adsorbed on the surface the α value was 1.05. This indicates that the internal pore environment is more acidic than the external surface. When Michler's ketone was adsorbed into the channels of MCM-41, two absorption maxima were found. One of these relates to an oxenium $[4\text{-}(CH_3)_2N(C_6H_4)]_2C^+O^-$ surface species. The formation of this species was due to the presence of rather acidic mobile protons within the pores. This is consistent with the observation that MCM-41 can directly initiate the cationic host-guest polymerization of electron-rich monomers such as vinyl ethers or N-vinylcarbazole.[58f]

Other groups have also used Reichardt's dye to obtain $E_T(30)$ (often converted to unitless $E_TN$ values) for chemically and thermally treated silica

samples. For instance, Tavener and co-workers showed that there was excellent correlation between the $E_T$N values for silica Kieselgel 60 heated to different temperatures and the weight loss by thermogravimetric analysis.[36,68] This is shown in figure 28. As discussed in section 1.3, when heated, a silica surface first loses adsorbed water, and then hydroxyl groups finally forming siloxane bridges and leaving just a few isolated silanol groups. This is a much less polar, much less hydrogen bond donating environment than that of the untreated silica, which shows a similar $E_T$N value to water because of its highly hydrated surface.

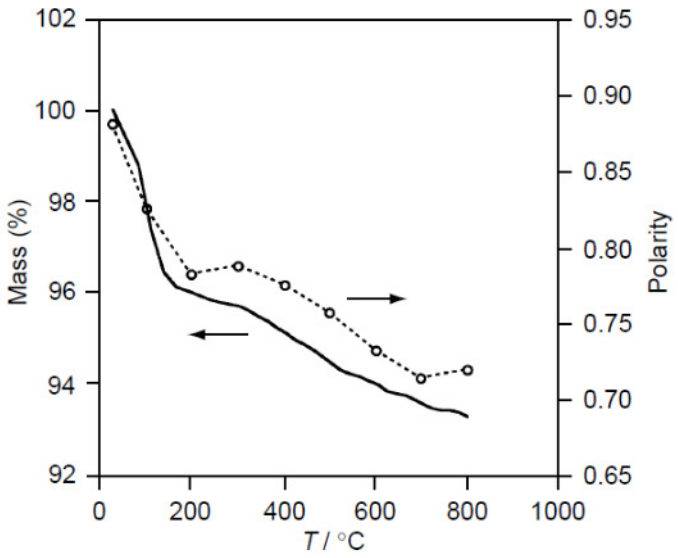


**Figure 28: Thermogravimetric analysis and the effect of thermal treatment on the polarity ($E_T$N) of Kieselgel 60 silica**

It is relatively easy to find probes to determine α and π* values for acidic surfaces, however it is not so easy to find suitable probes for the determination of β (hydrogen bond accepting) basicity values. Spange and co-workers used the indicator shown in figure 29, which was shown to adsorb preferentially on basic sites on silica and alumina samples and allowed sensible β values to be calculated from the $\nu_{max}$ positions measured.[58a]

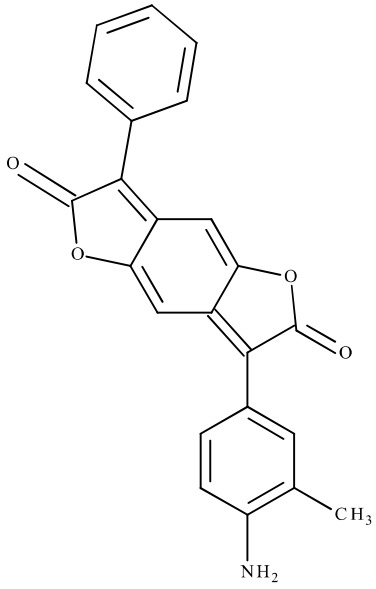


**Figure 29: An aminobenzofurandione dye used for probing the basicity of solid surfaces**

Another, rather simpler molecule that can be used for determining surface basicity is iodine. The electronic transition of interest for using iodine as a probe for surface basicity is shown in figure 30. This is the π*-σ* transition. Upon interaction with an electron donating environment the energy gap for this transition increases. This is observed as a decrease in wavelength of the $\nu_{max}$ in the visible region correlated with the strength of the basic site. [69]

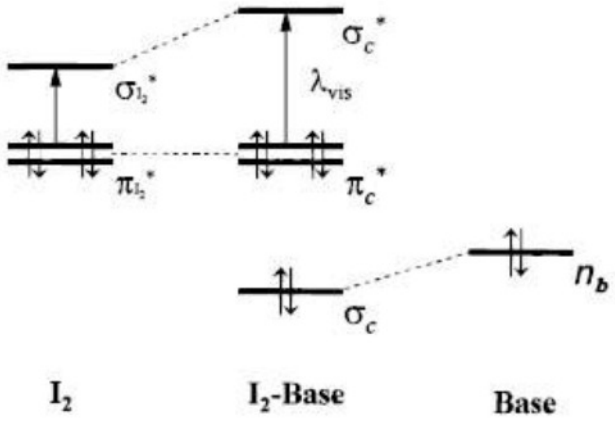


**Figure 30: The effect of an electron donating environment on the energy of the iodine π*-σ* transition**

UV-visible studies on solutions containing iodine have been carried out since the 1940's and a number of other bands besides the transition shown in figure 30 have been observed [70] Iodine is known to form donor acceptor complexes with many solvents. This produces a second band in the UV-region, which according to the classical description by Mulliken, corresponds to the transfer of an electron from the ground state of the complex (the HOMO of the donor molecule, with non-bonding character) to the LUMO of the acceptor, so that the excited state of the complex has purely ionic character[71]. This charge transfer band was first observed for iodine dissolved in aromatic solvents.[70b] The position of this band relates to the donor ionization potential.[72] Other bands may also be visible due to the dissociation of $I_2$ to give $I^+$ and $I^-$. The $I^-$ then reacts with another $I_2$ to give $I_3^-$.[73] The formation of $I_3^-$ has been found to occur on highly basic surface sites and though its band shows much larger shifts in peak position than those of the visible $I_2$ band, these shifts have not yet been reliably correlated to the surface properties.[74]

Despite these complications, iodine has been successfully used as a probe to rank the donor strength of basic oxygens in FAU-type zeolites.[69] As shown in figure 31 the long wavelength band for iodine is red shifted with increasing Si/Al concentration and blue shifts with increasing size of cation. Iodine was found to adsorb preferentially on the framework oxygen atoms away from the immediate vicinity of the cations. Therefore, adsorption of iodine showed that increasing the aluminium content and the size of the cation increases the donor strength of the framework.

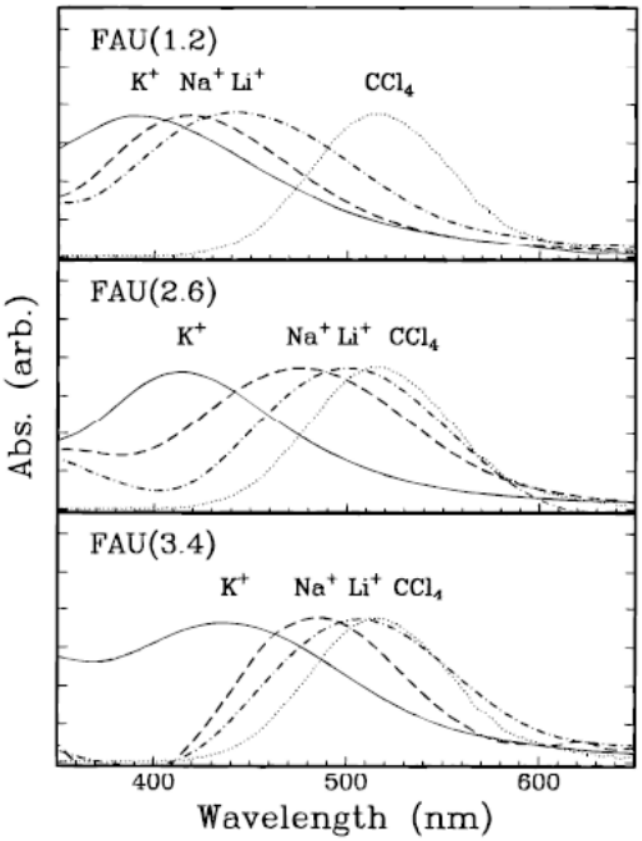


**Figure 31: Diffuse reflectance spectra (visible region) of iodine adsorbed on a series of FAU zeolites with different cation and Si/Al ratio (as indicated). For comparison, the absorption band of iodine in $CCl_4$ is shown in the dotted line.**

In the case of caesium impregnated X and Y-type zeolites, produced by decomposition of impregnated caesium acetate, $I_3^-$ was found to form irreversibly in the pores. This indicated the presence of highly basic sites. These particular zeolites were found to be the most active of the ion-exchanged zeolites tested by Doskocil *et al* for the formation of ethylene carbonate from carbon dioxide and ethylene oxide.[75]

Iodine has also been used by Camarota and co-workers to investigate the electron donating sites on ethane-bridged and phenylene bridged periodic mesoporous organosilicas (PMO).[74]

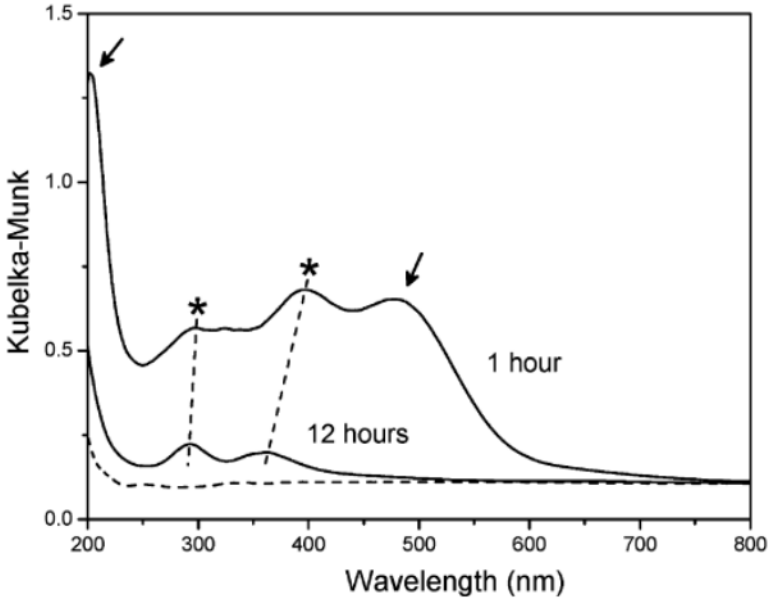


**Figure 32: UV-visible spectra of naked ethane-bridged PMO (dotted line) and ethane-bridged PMO contacted for 1 h with iodine and then outgassed at 293 K for 1and 12 h (solid lines).**

As can be seen from the UV-visible spectra shown in figure 32, the adsorption of $I_2$ onto ethane-bridged PMO gives rise to the $I_2$ visible transition at 478nm and the charge transfer band at around 200nm indicated by the arrows. These values are typical for the interaction of iodine with oxygenated bases, indicating that iodine is preferentially adsorbed on the oxygen atoms. The $\lambda_{max}$ at 478nm is at a higher energy than that on pure siliceous MCM-41 at 508nm.[75] This shows that the ethane-bridged PMO surface has a higher electron donating ability than that of pure silica due to the inductive effect of the aryl group. The bands marked with asterisks are due to the formation of $I_3^-$ on the surface and this species can be seen to be adsorbed onto the surface much more strongly than $I_2$.

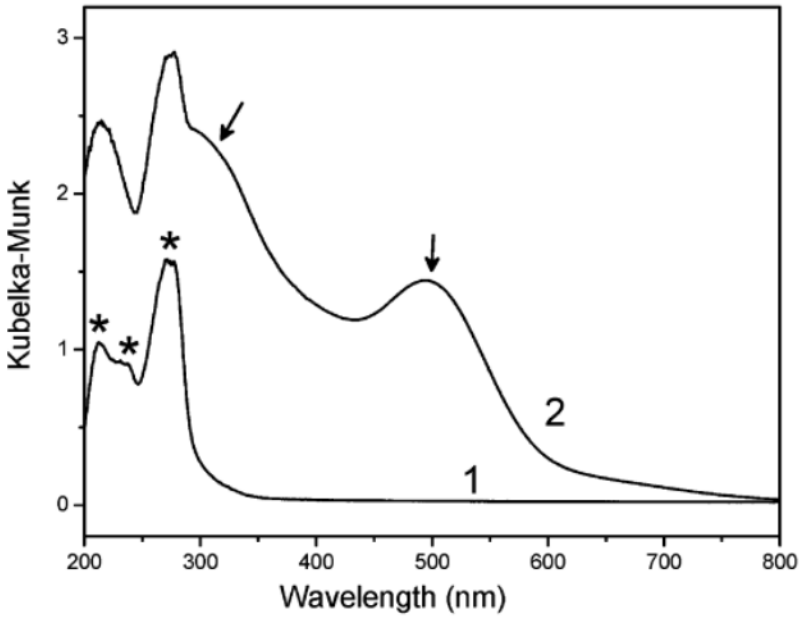


**Figure 33: UV-visible spectra of (1) naked phenylene-bridged PMO and (2) phenylene- bridged PMO after contact with iodine vapors for 1 h and successive outgassing at 293 K for 1 h.**

In figure 33, the asterisks on curve 1 represent absorption due to framework aromatic rings in phenylene bridged PMO. In curve 2 the values of $\lambda_{max}$ for the visible transition and charge transfer bands (the arrows) are at positions characteristic of iodine interacting with aromatic compounds. The $\lambda_{max}$ value for the visible transition for the phenylene-bridged PMO is 409nm, significantly higher than that for ethane-bridged PMO. The bands due to the aromatic rings are also seen to be perturbed after the adsorption of iodine. This indicates preferential adsorption of iodine on the aromatic groups, most likely due to the polarizability of these groups increasing the interaction strength. From this, it can be seen that framework aromatic rings in PMOs may play a role in surface phenomena such as adsorption and catalysis.

Though studies on UV-visible spectroscopic probing for the characterisation of surface sites are not as numerous as those for infrared probing, it can be seen that useful information about the likely interactions that will take place on a surface during reactions can be obtained. Through the use of the linear

solvation energy relationships the properties of surfaces can be compared to the much better known properties of solvents. This allows the behaviour of the surfaces to be predicted. Also, though not many indicators are available for the investigation of basic sites by UV spectroscopy, those that are known are generally larger than the probes for basic sites by infrared spectroscopy, such as $SO_2$, $CO_2$ and $CDCl_3$. These very small probes can access more or less all the sites on a surface, many of which may not be accessible to the intended reactants or adsorbants for the surface.

## 1.5 The Use of Model Reactions to Characterise the Surface Properties of Catalysts

The use of model reactions to study the acid-base properties of surfaces is another well-established technique. For obvious reasons it is mainly used to study materials intended as heterogeneous catalysts rather than adsorbents. Reaction systems are chosen such that either 1) the product is different depending on whether the catalyst surface shows predominantly acidic or basic characteristics or 2) the extent of reaction depends upon the how strongly basic or acidic the surface is.

Examples of type 1) reactions are: the dehydration or dehydrogenation reactions of alcohols including 1-phenylethanol[76], 2-propanol[77] and cyclohexanol.[78] Reactions of type 2) include: isomerisation of 3,3 dimethyl but-1-ene, or methylene cyclohexane for characterising surface acidity[78] and the Knoevenagel condensation with different reactants for evaluating surface basicity or acid-base cooperativity.[5,79]

The conversion of alcohols that can undergo dehydration or dehydrogenation reactions depending on the conditions is a well-known model reaction for testing the acid-base character of catalysts. For instance work by Di Cosimo *et al*[80] and Gervasini *et al*[81] indicated that 2-propanol is

dehydrated to propene on strong Brönsted acid sites by an $E_1$ mechanism. Whereas on amphoteric solids, 2-propanol is transformed to di-isopropylether and is transformed to propene on sites of dual-acid base strength in a concerted $E_2$ mechanism. However, dehydration can also take place on basic catalysts containing acid-base sites of imbalanced strength via an $E_{1cB}$ mechanism. Only on strongly basic catalysts is 2-propanol preferentially dehydrogenated to acetone.[82]

Díez and co-workers found in their work on the reactions of 2-propanol on $Mg_yAlO_x$ catalysts (of varying compositions) at 280˚C, that at low Al contents the formation of acetone was favoured and dehydration products were practically negligible. Whereas the formation rates of propene and di-isopropylether increased with increasing Al content. The formation rate of propene being three times faster on pure alumina than on $Mg_{0.2}AlO_x$- the most active mixed oxide catalyst.[80a]

The mechanisms of reaction of 2-propanol on magnesium rich $Mg_yAlO_x$ catalysts and aluminium rich $Mg_yAlO_x$ catalysts are shown in figure 34 and figure 35 respectively.

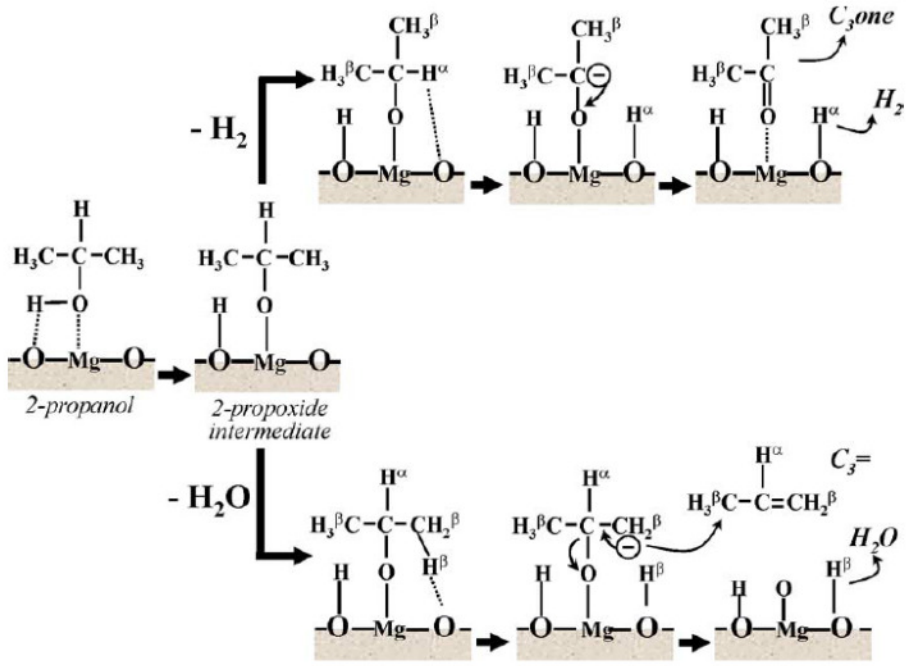


**Figure 34: Formation of acetone ($C_3$one) and propene ($C_3$=) via $E_{1cB}$ mechanisms on Mg-rich $Mg_yAlO_x$ catalysts**

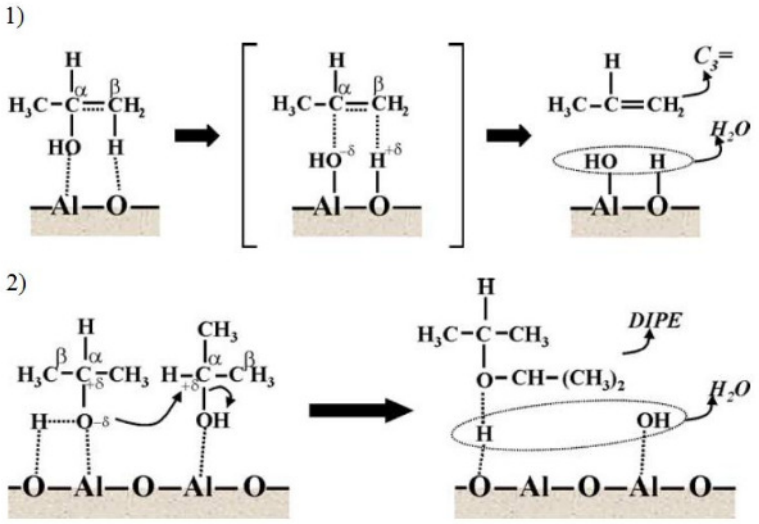


**Figure 35: 1) Formation of acetone ($C_3$one) and 2) formation of di-isopropylether (DIPE) on Al-rich $Mg_yAlO_x$ catalysts via $E_2$ type mechanisms**

The strength of acid sites on catalyst surfaces has been characterised by the isomerisation of 3,3-dimethylbutene (moderately strong acid sites) and methylene cyclohexane (weaker acid sites) The reaction schemes are shown

in figure 36. The two reactions were found to show the same orders of acidity for the different catalysts tested including, in order of decreasing acidity; silica-alumina, sulfated zirconia, with silica and ceria being only very weakly acidic. The ceria and silica samples were inactive in 3,3-dimethylbutene isomerisation. However, the two scales did not correlate for zirconia, which shows relatively high activity for methylene cyclohexane isomerisation. This was thought to be due to the presence of both Brönsted and Lewis acid sites, which may both contribute to the mechanism of reaction for this species.[78] Since these were high temperature vapour phase reactions, the presence of Lewis acid sites is possible.

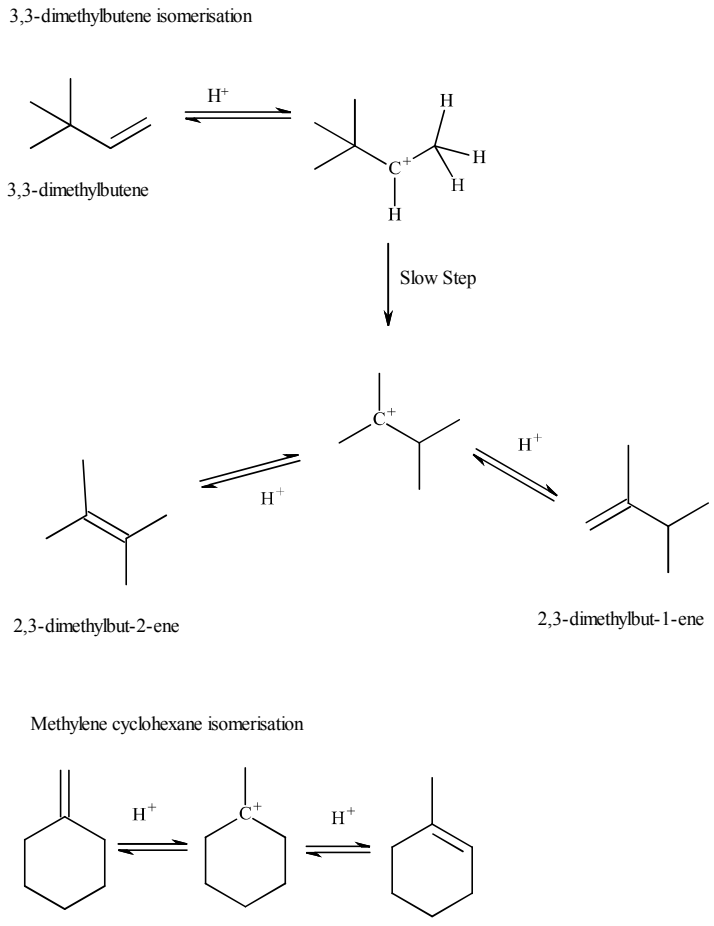


**Figure 36: Schemes for the acid catalysed isomerisation reactions of 3,3-dimethylbutene and methylene cyclohexane**

A number of heterogeneous catalysts have been developed for the Knoevenagel condensation and this reaction has become a test for the acid-base properties of catalysts.[5,7,79]

In their work on activated carbons exchanged with alkaline metal cations, López-González *et al* assumed a base-catalysed mechanism for the Knoevenagel condensation between benzaldehyde and methylenic compounds. The reaction steps for this are shown in figure 37.[79c]

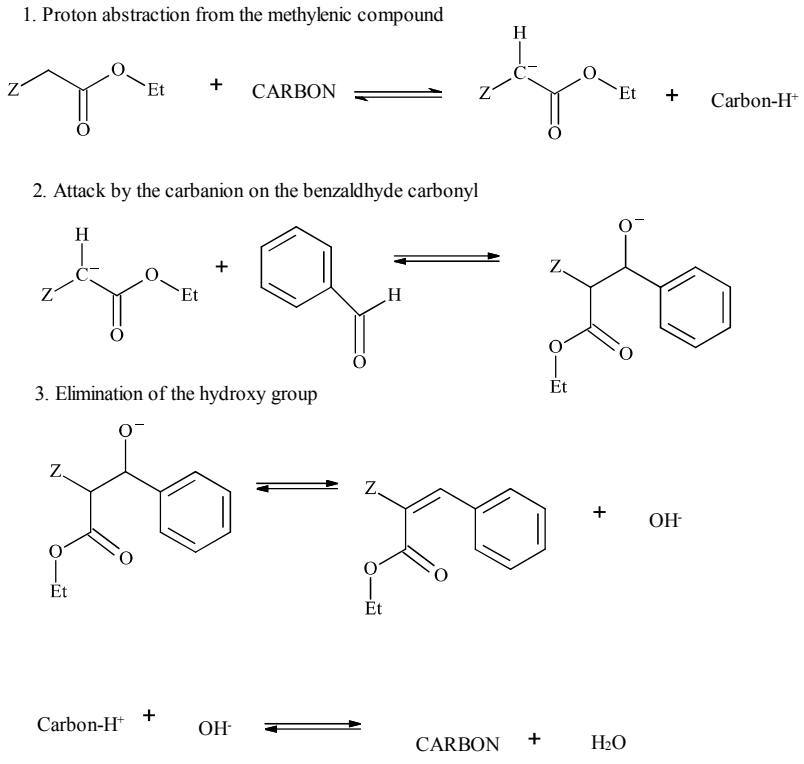


**Figure 37: The reaction sequence for the base catalysed Knoevenagel condensation on activated carbons**

The activated carbon sample that they used was a steam-activated commercial Norit carbon. The activation with steam, as well as enlarging the micropore structure also will cause oxidation of the surface carbon atoms. This will produce surface carbonyl, carboxyl and hydroxyl groups.[83] Though the paper by López-González *et al* did not specifically state the fact, it is assumed therefore, that the exchange takes place between the metal cation in the chloride salt that the added to the carbon and the hydrogen in surface hydroxyl groups. The presence of these groups will mean that the reactivity of these alkaline metal-exchanged carbons is somewhat similar to that of alkaline metal-exchanged zeolites and indeed the order of basicity for the different ions Na<K<Cs (ion exchanged carbons) mirrors that for alkaline metal-exchanged zeolites as measured by Doskocil *et al*[75] by iodine adsorption.

López-González *et al* found that the carbons samples exchanged with alkaline metal cations showed greater activity for the Knoevenagel condensation than the bare carbon sample and they correlated the increasing activity with decreasing polarization capacity (ion charge/ion radius) of the cation.[79c] However, in the studies on alkaline metal-exchanged zeolites, the basic sites were found to be framework oxygen atoms close to the metal cations and that increasing the electropositivity of the metal cation increased the donor strength of the framework oxygens.[69,75] Clearly in the case of activated carbons, the basic sites cannot be framework oxygens but perhaps they are the surface oxidation species created by the steam distillation in the vicinity of the metal cations. A search of the literature revealed little about the surface chemistry of these materials.

The use of the Knoevenagel condensation as a test reaction does not always give straightforward results. In their work on amine and imidazole functionalised silica samples Hruby and Shanks found that the reactivity of benzaldehyde with ethylcyanoacetate was enhanced by proximity of silanol groups to the active nitrogen containing groups. They proposed acid-base cooperative mechanisms for the reactions between the surface with the silanol groups donating a proton to activate the benzaldehyde.[79a] Further mechanistic discussion of this reaction is given in Chapter 6.

Model reactions can be useful methods for characterising the acid-base properties of solid catalyst surfaces. However as with the spectroscopic probing methods, careful selection of test reaction is needed in order that the desired surface properties are being studied. Care must be also be taken with results when cooperation between different types of site (e.g. Brönsted and Lewis) or acid-base cooperation mechanisms may operate on a surface.

## 1.6 Summary

As the previous discussion shows, a great deal of work has been carried out in attempts to understand the surface properties of solids. However, most of the studies have focussed on a few specific materials and probe molecules and there are no generally applicable techniques. There is still work to be done on establishing the limitations of many of the probing techniques. Also, only a few workers have tried to correlate data using different surface characterisation data such as UV-visible and infrared spectroscopic techniques and test reactions. In later chapters attempts will be made to correlate such data and again the limitations and difficulties with this will be established.

Silica-polysaccharide hybrid materials have been recently developed.[84] Their structural properties have been considered but their surface chemistry has not been studied. The application of some of the probing techniques discussed in this chapter to these materials should provide some interesting and valuable information about their surface properties and potential applications.

# Chapter 2: Experimental

## 2.1 Manufacture of Silica and Organically Functionalised Silica Samples

### Microporous Silica from "Water Glass"

Reference: Munoz-Aguado (1997)[85]

#### Materials

The silicate solution-crystal 0070 Silchem- K grade, weight ratio $SiO_2$: $Na_2O$ 3.3, Mean molecular ratio $SiO_2$: $Na_2O$ 3.41, Mean % $Na_2O$ 8.00, Mean % $SiO_2$ 26.4, Mean % solids 34.4 was obtained from INEOS Silicas.

Hydrochloric acid 2M was obtained from Fisher Scientific

#### Analytical Techniques

The progress of the gel formation was followed by attenuated total reflectance (ATR) Fourier Transform infrared spectroscopy (FT-IR) using a Brüker Vertex 70 Mid-infrared spectrometer fitted with a Specac Golden gate accessory.

#### Method

50 $cm^3$ of the sodium silicate solution was put into a 250 $cm^3$ conical flask fitted with a magnetic stirrer bar. With constant stirring, the 2M HCl was added until pH7 was reached (as tested by universal indicator paper). The gel was then aged with constant stirring for the first 24 hours and then left under static conditions for a further 34 days. Periodically the sample was stirred with a spatula and a small sample removed for IR analysis. After the

ageing process, the resultant gel was filtered on a sintered funnel and dried in air at room temperature on a glass plate. A portion of this dried sample was then heated in air in a furnace at a rate of 10˚C a minute up to 800˚C. The temperature was held at 800˚C for 1.5 hours and then allowed to cool down to room temperature.

## Mesoporous Silica from Tetraethyl orthosilicate and Organically Functionalised Derivatives

References: Tanev (1995),[21a] Macquarrie (2001)[7]

**Materials:**

Tetraethyl orthosilicate (TEOS), n-dodecylamine , 3-aminopropyl trimethoxysiliane purum ≥98.0%, hexamethyl disiloxane, (3-mercaptopropyl) trimethoxysilane and 1-pentanol were acquired from Aldrich. Ethanol, methanol 1-propanol and 2-propanol analytical reagent grade and acetone- laboratory grade, were acquired from Fisher Scientific.

**Method**

In the standard procedure, a solution of dodecylamine (0.0675 mol, 12.51g), ethanol (2.2725 mol, 104.69g, 133 $cm^3$) and deionised water (7.4 mol, 133.3g, 133.5 $cm^3$) was made up in a conical flask fitted with a magnetic stirrer bar.

Whilst stirring vigorously, TEOS (0.25 mol, 52.08g) was added. The reaction mixture was aged at ambient temperature for 18-29 hours and then dried by vacuum filtration using a sintered glass funnel. As in the case of the

microporous silica, the formation of the gel structure was followed by ATR FT-IR.

To remove the template, approximately 2g of the dried sample was stirred with about 200 $cm^3$ ethanol at reflux for 2 hours, before being filtered under vacuum and the washing repeated twice more. The resulting sample, designated hexagonal mesoporous silica (HMS) was again air dried on a glass plate at room temperature. Some portions of the washed silica were then calcined at a variety of temperatures as required.

The use of different solvents to wash the HMS samples was also tested. These solvents were methanol, 1-propanol, 2-propanol, acetone and 1-pentanol. The methods used were the reflux method described above or one of a number of alternative methods. These were ultrasound and microwave assisted extraction and use of FexIKA apparatus.

Ultrasound assisted extraction- Approximately 1g of HMS was mixed with about 100$cm^3$ solvent in a flask and then the flask was placed in an ultrasonic bath for 30 minutes. The silica was sucked dry by vacuum filtration as before, this was repeated twice more.

Microwave wash- About 0.1g of HMS was placed into a microwave tube with approximately 5$cm^3$ solvent and a magnetic stirrer bar. The sample was then heated in a CEM Discover microwave reactor for 5 minutes at 150W and then filtered as before. This was repeated once more.

FexIKA wash- This piece of apparatus simulates fluidised bed extraction. The solvent is heated in a vessel (the base vessel) positioned below the solid sample, which is separated from the base vessel by a filter. The solvent vapour penetrates the filter and condenses inside the extraction tube with the sample. The condensed solvent inside the extraction tube is heated to a rolling boil. During the next stage the solvent in the base vessel is cooled

and the steam pressure inside this vessel is lowered allowing solvent in the extraction tube to be drawn back into the base vessel. This heating-cooling cycle can be repeated. About 1g of HMS was placed in the vessel above the boiling solvent and the 250cm$^3$ flask was approximately half-filled with solvent. The heating and cooling cycle was programmed to repeat four times.

The removal of the dodecylamine template from the silica samples was followed by ATR FT-IR.

In order to manufacture the 3-aminopropyl functionalised silica (AMP-HMS) TEOS (18.72g, 0.09 mol) and 3-aminopropyl trimethoxysilane (1.79g, 0.01 mol) (9:1 molar ratio) were added separately but simultaneously over a few seconds to a stirred solution of n-dodecylamine (5.1g, 0.03 mol) in 50g ethanol and 50g water at ambient temperature. The reaction mixture was stirred for 18 hours and then the solid formed was filtered on a sintered glass funnel and sucked dry before being extracted with ethanol in a soxhlet apparatus for 8 hours. In order to do this, a soxhlet thimble was filled with the HMS sample and placed in the soxhlet above a 250cm$^3$ round-bottomed flask containing approximately 125cm$^3$ of ethanol and a magnetic stirrer bar. The resultant solid was dried in air at 120˚C for 16 hours.

For the trimethyl-functionalised “hydrophobic” silica, the same procedure as for the AMP-HMS was followed, except that the 3-aminopropyl trimethoxysilane was replaced by hexamethyl disiloxane (1.62g, 0.01 mol) and for the 3-mercapto functionalised silica the 3-aminopropyl trimethoxysilane was replaced by (3-mercapto) trimethoxysilane (1.96g, 0,01 mol).

# 2.2 Manufacture of Silica-Polysaccharide Hybrid Materials

References: Shchipunov (2003-2004)[84]

**Materials**

TEOS, alginic acid sodium salt and chitosan- low molecular weight (75-85% deacetylated) were all obtained from Aldrich. Carboxymethylcellulose sodium salt was obtained from Alfa Aesar, κ-carrageenan (potassium salt) was obtained from Fluka, ethanediol 99+%, acetone laboratory grade and 0.1M hydrochloric acid were obtained from Fisher Scientific.

**Method**

Firstly, the water soluble silicon source tetrakis(2-hydroxyethyl)orthosilicate (THEOS) was manufactured from TEOS.

30g (0.14mol) TEOS and 38g (0.61mol) ethanediol (an excess over the 1:4 TEOS:ethanediol molar ratio needed) were added to a round-bottomed flask fitted with a stirrer bar and condenser. With constant stirring the mixture was heated at reflux (~200˚C) for 24 hours. The ethanol was then distilled off. The un-reacted ethanediol (boiling point 197.3˚C) was left in the solution because its boiling point is too similar to that of THEOS (boiling point 200˚C) to successfully separate them.

To form the polysaccharide-silica hybrids (except for the silica/κ-carrageenan hybrid); 1g of the polysaccharide was stirred at room temperature in 89g of deionised water until the polysaccharide had dissolved. Then 10g of the THEOS/ethanediol solution was added and reaction mixture was stirred until a gel had formed. For the silica/κ-

carrageenan hybrid, the polysaccharide formed a gel in solution without the addition of THEOS. Addition of THEOS after this gel had formed resulted in an inhomogeneous silica/polysaccharide gel. Therefore the THEOS and κ-carrageenan were added simultaneously. In the case of the chitosan/ silica hybrid, in order to form the silica/polysaccharide gel the solution was acidified by the drop-wise addition of 0.1M hydrochloric acid from the initial pH of 7-8 to pH6.5 until a gel visibly began to form.

Once a gel was observed in the reaction vessel, it was sealed and left to age for 18 hours with stirring if the gel was sufficiently mobile or under static conditions in the case of κ-carrageenan/ silica which formed a solid gel after 1 hour.

After the ageing process, the hybrid materials were extracted with acetone using soxhlet apparatus. They were then dried under supercritical $CO_2$ using a Thar Technologies supercritical $CO_2$ rig operating at 50˚C, under 350 bar pressure and with a 10g $min^{-1}$ flow of $CO_2$ for 4 hours.

The silica/polysaccharide hybrids were analysed by nitrogen porosimetry using a Micrometrics ASAP 2010. Prior to the analysis the hybrids were degassed under vacuum ($p < 10^{-2}$ Pa) at 60˚C for at least 2 hours. The thermal properties of the materials were compared to those of the pure polysaccharides by thermogravimetric analysis. Simultaneous thermogravimetric/differential thermal analysis (TG/DTA) was carried out on a PL Thermal Sciences STA 625 using approximately 10mg of sample accurately weighed into an aluminium pan. An empty aluminium pan was used as a reference. The sample was then heated at a rate of 10˚C $min^{-1}$ under a 100ml $min^{-1}$ flow of either air or nitrogen.

# 2.3 Infrared Probing Techniques

## Infrared Spectra Recorded at the Green Chemistry Centre of Excellence, University of York

### Materials

Aniline 99%, diethylamine puriss p.a ≥95% (GC), fluorobenzene 99% and acetonitrile-*d3* 99.8% were purchased from Aldrich. Propanoic acid was purchased from FISONS Scientific Equipment and benzonitrile- 99% from AVOCADO Research Chemicals.

Silica Kieselgel 60 was purchased from Fluka, HMS was manufactured as described in section 2.1, zeolite ZSM-5 $SiO_2$:$Al_2O_3$ ratios 280 and 30 were obtained from RS Minerals. zirconia + 13% $Al_2O_3$ was obtained from Engelhard Exceptional Technologies. Aluminium oxide activated basic Brockmann Grade 1 was obtained from BDH Laboratory Supplies. 13x molecular sieve $SiO_2$: $Al_2O_3$ ratio= 2.8 ($Na^+$) was obtained from BDH Chemicals. Spectroscopic grade potassium bromide was obtained from Fisher Scientific.

Fourier Transform infrared spectra were recorded using a Brüker Equinox 55 infrared spectrometer fitted with an MCT cryo-detector operating in diffuse reflectance (DRIFTS) mode. Background spectra were recorded with 128 scans and the sample spectra with 64 scans at 2$cm^{-1}$ resolution from 8000$cm^{-1}$ to 600$cm^{-1}$. In most cases the samples were used undiluted but when dilution was required the sample was mixed with spectroscopic grade potassium bromide that had been previously finely ground in a pestle and mortar in an accurately weighed ratio 1:20 sample to KBr. Prior to use the KBr was kept in a low-temperature oven to limit water adsorption.

For the spectra recorded at elevated temperature, the infrared spectrometer was fitted with an environmental chamber accessory capable of heating the sample under vacuum or under a flow of gas. It was heated at a rate of 10˚C $min^{-1}$ until the desired temperature was reached under a 100ml $min^{-1}$ flow of nitrogen.

In order to adsorb the probe molecule onto the surface of interest, accurately weighed masses of the probe molecule and solid of interest were placed together in a glass sample vial and then this was sealed. The sealed vial was placed in an oven at 120˚C for approximately 30 seconds. Then the lid of the vial was tightened if necessary and the vial tapped against a desk or similar surface and shaken to make sure that the solid was free-flowing. The vial was then returned to the oven for a few seconds and then removed and allowed to cool to room temperature.

## Infrared Spectra Recorded at the Department of Materials Science and Chemical Engineering, Polytechnic University of Turin

### Materials

HMS, "hydrophobic" silica and AMP-silica (AMP-HMS ) were manufactured as described in section 2.1. SBA-15 was kindly donated by James Comerford and manufactured according to the procedure of Wang *et al*.[86] The acetone, $CO_2$, $NH_3$ and deionised water were those supplied by the laboratory.

Each of the silica samples was pressed into a thin self-supporting wafer and placed into a gold envelope. The HMS and SBA-15 samples in their envelopes underwent activation at 700˚C under air in a furnace before being allowed to cool sufficiently to enable them to be removed from the furnace. Prior to the infrared measurements being made, all the samples, in their

envelopes, were placed into the infrared cell and out-gassed under vacuum at 120˚C to remove residual water. The cell was then cooled to room temperature and sealed before being transferred to a vacuum line, set-up such that the window of the envelope containing the sample was in the infrared beam path whilst the cell was connected to the vacuum line. This allowed in-situ vapour adsorption/desorption.

The infrared measurements were recorded using a Brüker Equinox 55 FT-IR fitted with an MCT cryo-detector operating in absorbance mode at $2cm^{-1}$ resolution. 32 scans were recorded each time. The infrared spectrum of each out-gassed sample was recorded and then at increasing equilibrium pressure of the vapour after the cell was dosed with the probe gas. This continued until saturation was reached. Then the vapour was evacuated in a stepwise fashion from the cell, with infrared spectra being recorded after each evacuation until vacuum ($1*10^{-3}$ mbar) was reached. The final infrared spectrum of any irreversibly adsorbed species was then recorded.

In the case of acetone adsorption, after saturation of acetone vapour was reached inside the infrared cell, the cell was sealed and transferred back to the vacuum line upon which the out-gassing had taken place. The sealed cell was heated to 120˚C for 30 minutes before the expansion of the acetone vapour and accompanying infrared spectra were recorded.

## 2.4 UV-Visible Probing Techniques

**Materials**

Reichardt's dye 90%, iodine 99.8% A.C.S. reagent, butyl acetate, 2-methoxyethanol, chlorobenzene, ammonium Y zeolite, neutral activated Brockmann alumina grade 1, basic activated Brockmann alumina grade 1, zinc oxide, sodium hydrogen phosphate, octadecyl functionalised silica gel, (1-piperidino)propyl functionalised silica gel, κ-carrageenan (potassium

salt), sodium alginate, chitin, methylcellulose and chitosan were obtained from Aldrich.

Dichloromethane HPLC grade, concentrated sulphuric acid, xylene, dimethylformamide, calcium oxide, sodium carbonate (anhydrous), sodium hydrogen carbonate, sodium sulfate (anhydrous) and calcium carbonate were obtained from Fisher Scientific.

Zeolite ZSM-5 $SiO_2$:$Al_2O_3$ ratios = 30 , 80 and 280 were obtained from RS Minerals, 13x molecular sieve was obtained from BDH Chemicals, sodium acetate was obtained from Fisons Scientific Apparatus, silica Kieselgel 60 was obtained from Fluka and sodium carboxymethylcellulose was obtained from Alfa Aesar.

**Instrumentation**

All UV measurements were performed using a Jasco V-550 UV/Vis spectrometer. For the measurements in solution this was operated in absorbance mode with 1nm resolution. For the measurements on solids it was fitted with an ISV-469 solids unit operating in diffuse reflectance mode again with 1nm resolution.

**Preparation of Samples for UV-Visible Spectroscopy**

For the use of Reichardt's dye as a probe, a solution typically of 40 mg of dye dissolved in 100$cm^3$ dichloromethane was prepared. For each sample 10-20$cm^3$ of solution was accurately removed by pipette and added to 0.2-0.4g of solid powder in a round bottomed flask. The flask was swirled to evenly distribute the powder and solution and then the solvent removed on a rotary evaporator. The sample was then loaded into the cell for the UV-visible measurements.

To use iodine as a probe, a known mass of the solid surface of interest was placed in a sample vial. Several open vials with different solid surfaces were then placed in a vacuum dessicator with an open vial containing solid iodine. The dessicator was sealed and put under vacuum. After around 20 minutes under dynamic vacuum, the tap to the vacuum was closed and the dessicator left sealed for around 3 hours. The samples were then reweighed and the vials sealed until the UV-visible measurements were made, which was done as quickly as possible.

In order to conduct the controlled humidity studies the same set up as before using the vacuum dessicator was utilised. The solids basic activated Brockmann alumina, 13x molecular sieve, ZSM-5 $SiO_2$:$Al_2O_3$= 80, silica Kieselgel 60 and calcium oxide were selected for this study, they were used as supplied.

For a 10% humidity atmosphere a 64.8% sulphuric acid solution was made up and for a 50% humidity atmosphere a 55.9% sulphuric acid solution was made up according to the method of Wilson.[87] Before adding the iodine to the surfaces the mass change of the solids when exposed to the different atmospheres was checked. A known mass of each of the solids was accurately weighed into a separate sample vial. These open vials were then placed into the vacuum dessicator with an open beaker containing around 30$cm^3$ of the appropriate sulphuric acid solution. The dessicator was then sealed and put under vacuum as before. The samples were removed after the treatment and re-weighed. The experiment was then repeated with the inclusion of iodine in an open vial in the dessicator with the solids and the sulphuric acid solution and the UV-visible spectra were then run.

For all the samples, the spectrum of the bare solid was recorded before the addition of iodine. The spectrum of the bare solid was then subtracted from that of the surface/ solvent with adsorbed iodine to produce the spectra shown in the results.

For the spectra of iodine dissolved in the solvents; xylene, butyl acetate, dimethylformamide, chlorobenzene and 2-methoxyethanol iodine was dissolved in the solvent at a concentration of 1mg iodine to 10$cm^3$ solvent. Each solution was then placed in a UV-visible liquid cell and the pure solvent was used as the background.

## 2.5 Knoevenagel Condensation Model Reactions

### Materials

The solvents xylene, dimethylformamide, butyl acetate, chlorobenzene, dichloromethane and 2-methoxyethanol and the solids sodium hydrogen carbonate, calcium oxide, chitosan, 13x molecular sieve, silica Kieselgel 60, neutral activated Brockmann alumina and zeolite ZSM-5 $SiO_2$:$Al_2O_3$ = 80 were obtained as discussed in section 2.4. The 3-aminopropyl functionalised silica was manufactured according to the method given in section 2.1. The silica/κ-carrageenan, silica/sodium alginate and silica/sodium carboxymethylcellulose hybrid materials were manufactured according to the method given in section 2.2.

The ethylacetoacetate, benzaldehyde and dodecane were all purchased from Aldrich.

### Method

For the majority of the model reactions, 0.1g of the chosen catalyst was placed into a round-bottomed flask fitted with a magnetic stirrer bar. 5ml of xylene was then added. 460µl of benzaldehyde, 596µl of ethylacetoacetate and 227µl of dodecane were measured out using automatic pipettes of appropriate volume ranges and added to the flask. It was then fitted with a condenser and heated to140˚C. Several of these reactions were run simultaneous on a multi-point apparatus. For the purposes of comparison, a

blank reaction was also run with no solid catalyst. After 30 minutes and then either at 1 or 2 hour intervals thereafter up to 7 hours in some cases, a 30µl sample was removed from each reaction mixture using an automatic pipette and placed into a gas chromatography (GC) sample vial. From those reaction mixtures containing a solid the sample was filtered through a Pasteur pipette containing a cotton-wool plug into the GC vial. The samples were diluted with dichloromethane and GC traces were obtained.

The reactions carried out in different solvents followed the same method as that described for the reactions in xylene except that the reaction mixtures (without catalyst) using the same volumes of reactants were made up with 5ml of dimethylformamide, butyl acetate, chlorobenzene, dichloromethane or 2-methoxyethanol as well as that with xylene as a solvent for purposes of comparison. These reactions were run at 120˚C and a sample removed of the mixture as soon as the correct temperature was reached and then every hour for 7 hours for analysis by GC. They were then repeated with 0.1g of $NaHCO_3$ as a catalyst.

The GC measurements were carried out on a Varian 3800 GC fitted with a Phenom ZB-5-HT Inferno column- length-30m, width-250µl and stationary phase width-0.25µl. The injector temperature was set to 350˚C. The injection volume was 1µl with a split ratio of 50:1. The pressure was 22.35psi with a 115ml/min flow of carrier gas (He).

The start temperature was 60˚C and the ramp rate was 15˚C/min until the final temperature of 290˚C was reached. Then the oven was cooled. An FID detector was used.

The mass spectrometer used electron impact (EI) ionization.

The GC-MS measurements were carried out using a Perkin Elmer Claus 500 GC with a Perkin Elmer Claus 560 S mass spectrometer. The column used

was a DB5-HT column 30m by 250µl with a 0.25µl width of stationary phase. The injection volume was 0.5µl with a split ratio of 9:1. A 10ml/min flow of carrier gas (He) was used.

# Chapter 3: Formation of Porous Silica

## 3.1 Introduction

As part of this research project, a number of different silica, organically modified silica and silica-polysaccharide hybrid materials were manufactured under mild conditions to generate materials with regular porous structures and interesting surface properties. All of these silica gel structures are generated at low temperatures and no specialised apparatus is required (for detailed procedures see the experimental section). In this chapter, the development silica gel macrostructures of both microporous and mesoporous silica samples was followed by mid-IR spectroscopy.

The mesoporous silica manufactured had an MCM-41-like hexagonal structure (this sample is donated HMS). However instead of the traditional ionic surfactants a neutral amine template was used according to the method developed by Tanev.[21a] This template can be removed by washing the silica with a polar solvent and the effects of ultrasound and microwave assisted extraction and the use of different extraction solvents was studied.

## 3.2 The Use of Infrared Spectroscopy to Monitor the Development of Silica Gel Structures

There have been several attempts recorded in the literature to monitor the development of silica gel structures *in situ* by infrared spectroscopy[25] and silicon or nitrogen NMR.[24b,25a] The formation of a silica gel is quite complex, as discussed in Chapter 1.2. There are several processes that take place; 1) the hydrolysis of the silicon source, 2) the polymerisation of Si-OH groups and 3) cross-linking to form the gel structure. The main bands of

interest when monitoring the formation of the gel network are the framework Si-O bands in the 1200-1000cm$^{-1}$ region, the Si-OH band at 974cm$^{-1}$ and the Si-O band at 780cm$^{-1}$. The bands in the 1200-1000cm$^{-1}$ region in silica gel structures have been assigned to slightly different species by different authors.[25,88]

Holmes *et al*, in their *in situ* infrared studies on the formation of MCM-41 using TEOS, cetyltrimethylammonium chloride as a template and ammonia as a catalyst assigned these to so-called $Q_3$ and $Q_4$ silicon species, where the numbers 3 and 4 refer to the number of silicon atoms bonded via oxygen to a particular silicon atom.[25] These are pictured in figure 38 along with the positions of the relevant Si-O antisymmetric stretch frequencies. These are either external (on the surface of the silica) or internal (in the bulk material). In crystalline silica forms such as quartz, the $Q_4$ bands at 1100 and 1200cm$^{-1}$ are visible as distinct peaks rather than both appearing as a broad shoulder on the side of the band at around 1050cm$^{-1}$.[37b] The problem with the assignments of the bands in the 1000-1220cm$^{-1}$ region given by Holmes *et al*, is that for a highly hydrated silica gel in water, which is the case during the synthesis of a silica gel, there will be no such thing as an external $Q_4$ species. All the surface Si atoms will have at least one hydroxyl group. So, these assignments are unlikely to be strictly accurate.

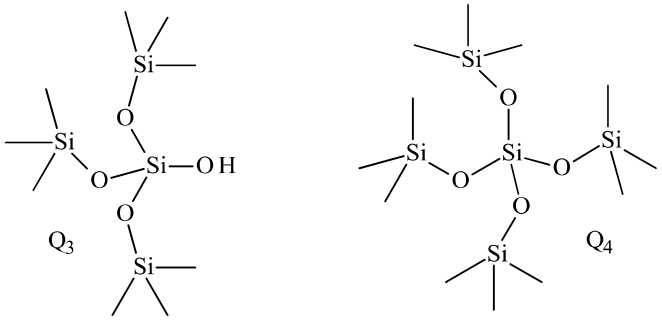


Internal Si-O: 1040-1060cm$^{-1}$
External Si-O : 1180 cm$^{-1}$

Internal Si-O: 1100cm$^{-1}$
External Si-O: 1220cm$^{-1}$

**Figure 38: Silicon Species Observable by Infrared Useful for the Monitoring of Silica Gel Structure Development**

The $Q_0$-$Q_2$ species (0-2 silicon atoms bonded via oxygen) distinguishable by silicon NMR but in infrared they are indistinguishable from other Si-O bands.

Rubio *et al* offer different assignments for these bands but these in some ways contradict other assignments in the literature for silica bands.[33,89] They assign the bands at 1200, 1147, 1100 and 1086cm$^{-1}$ to the Si-O-Si antisymmetric stretch in cyclic structures, the Si-O-Si antisymmetric stretch in linear structures, the Si-O-Si symmetric stretch in linear structures and the S-O-Si symmetric stretch in cyclic structures respectively. But as in the work by Holmes *et al*, they followed the evolution of the gel structures by the increasing intensity of the bands towards the high frequency end, in this case, the bands at 1200 and 1147cm$^{-1}$.

In the present study the gel formation of neutral-amine-templated mesoporous silica (HMS) and a microporous silica gel made by acidification of a sodium silicate solution were investigated by infrared spectroscopy. Both of these experiments were carried out at room temperature.

## Silica Gel Formation from "Water-Glass"

In the first experiment, sodium silicate solution (water glass) was acidified to approximately pH7 (determined by universal indicator papers) and stirred at room temperature until a gel was observed. It was then aged under static conditions for 5 weeks. Periodically the gel was stirred and a sample removed using a small spatula. An infrared spectrum of this sample was run using the ATR spectrometer as detailed in Chapter 2.1. The mid-IR spectra are shown in figure 39.

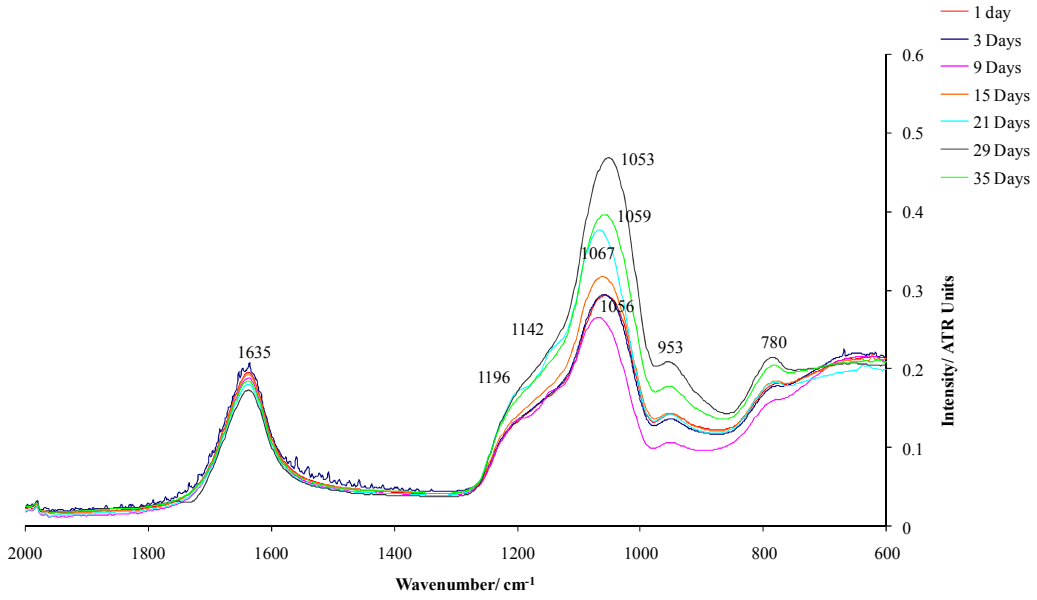


**Figure 39: The mid-IR region of ATR spectra showing the changes during silica gelation**

The infrared spectra of the dried and calcined samples are shown in figure 40 for the purposes of comparison.

The main features that can be observed in figure 39 during the gelation process are; an appearance and gradual increase in intensity of a band at

780cm$^{-1}$and an increase in intensity of all the bands in the 1200-1050cm$^{-1}$ region.

The band as 780cm$^{-1}$ is assigned to either the Si-O-Si symmetric stretch (Perry)[89] or a Si-O-Si bend in $SiO_2$ (Rubio).[90] In either case, the growth of this band indicates an increase in the number of Si-O-Si structures and therefore increasing polycondensation. This band shifts to 795cm$^{-1}$ in the dried and calcined samples shown in figure 40. This would indicate that these bonds shorten and strengthen during the drying process. However, this shifting pattern is not seen with the antisymmetric stretching band at between 1053 and 1067cm$^{-1}$ in figure 39. This shifts down to 1046cm$^{-1}$ in the dried sample and then up again to 1069cm$^{-1}$ in the 800˚C calcined sample shown in figure 40.

In the sample calcined at 800˚C this band increases sharply in intensity showing the condensation of Si-OH groups that occurs as silica is heated.

The band at 953cm$^{-1}$ assigned to the Si-OH stretch does not appear to change much in intensity or width during the gelation in solution. However, as the sample is dried this becomes much weaker relative to the band at 1046cm$^{-1}$. When the silica is calcined at high temperature, this band disappears entirely. This corroborates the evidence in the increase in intensity of the Si-O-Si band at 795cm$^{-1}$ that the Si-OH groups are condensed to Si-O-Si groups.

The bands in the 1200-1050cm$^{-1}$ region assigned to Si-O-Si stretches generally increase in intensity during the course of the gelation. Some of the spectra recorded after a fairly long gelation time such as that labelled 21 days show some structure in the 1200-1140cm$^{-1}$ shoulder region. This is again seen in figure 40 in the calcined sample with a band at 1198cm$^{-1}$. The band width of this region also decreases after drying the silica indicating an increase in the homogeneity of the Si-O-Si bands. This is to be expected

because when silica is heated at high temperature, the main species present are the $Q_4$ species.

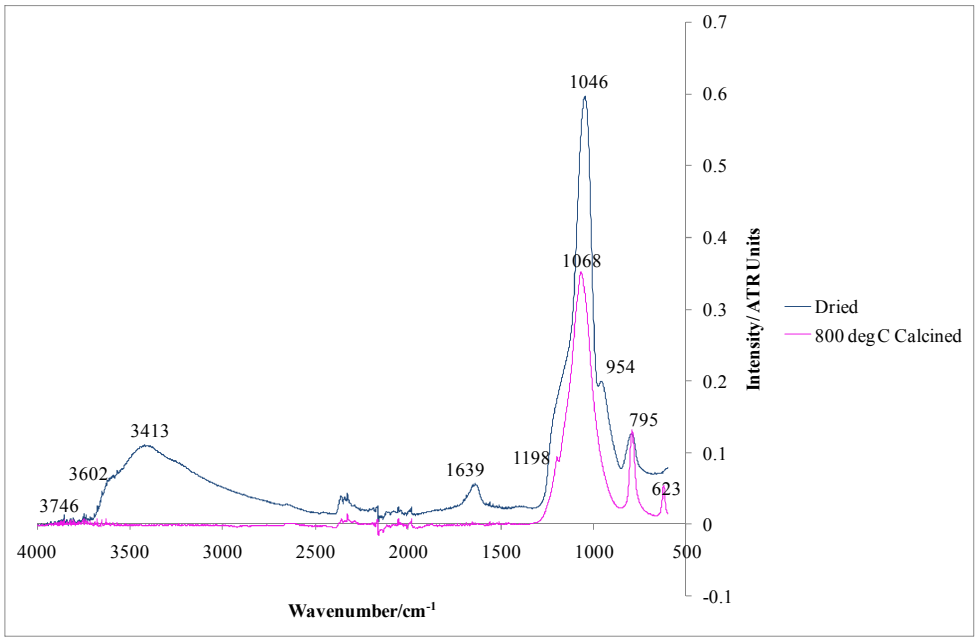


**Figure 40: ATR infrared spectra showing microporous silica air-dried at room temperature and calcined at 800˚C**

Another feature shown in figure 40, is the disappearance of the broad band in the 3650-3000cm$^{-1}$ region when the silica is calcined at 800˚C corresponding to the hydrogen-bonded-OH groups. Only a tiny peak remains at 3746cm$^{-1}$ corresponding to free isolated SiOH groups. This again shows the condensation of the SiOH groups.

The main point to note from these infrared spectra is that the silica gel formation does not stop until after the silica is dried and the structure changes during calcination.

## Silica Gel Formation from TEOS

The silicon source for the HMS silica was TEOS and for the purposes of comparison with the resultant silica gel the infrared spectrum of TEOS is shown in figure 41. The peak assignments are given in table 2.

**Table 2: Infrared peak assignments for TEOS**

| **Wavenumber/cm$^{-1}$** | **Peak Assignment (TEOS)[90-91]** |
|---|---|
| 787 | $SiO_4$ symmetric stretch [a] |
| 962 | $CH_3$ rocking |
| 1074 | C-O asymmetric stretch [b] |
| 1101 | C-O asymmetric stretch [b] |
| 1171 | $CH_3$ rocking [b] |
| 1298 | $CH_2$ twist [b] |
| 1369 | $CH_3$ symmetric deformation |
| 1394 | $CH_2$ wagging |
| 1446 | $CH_3$ asymmetric deformation |
| 1485 | $CH_2$ bend |
| 2893 | Symmetric C-H stretch $CH_2$ |
| 2932 | Asymmetric C-H stretch $CH_2$ |
| 2976 | Asymmetric C-H stretch $CH_3$ |

[a] This is an unusual peak assignment because the silica Si-O-Si symmetric stretch is in this position

[b] The Si-O-Si antisymmetric stretching bands of silica are normally also assigned to this region

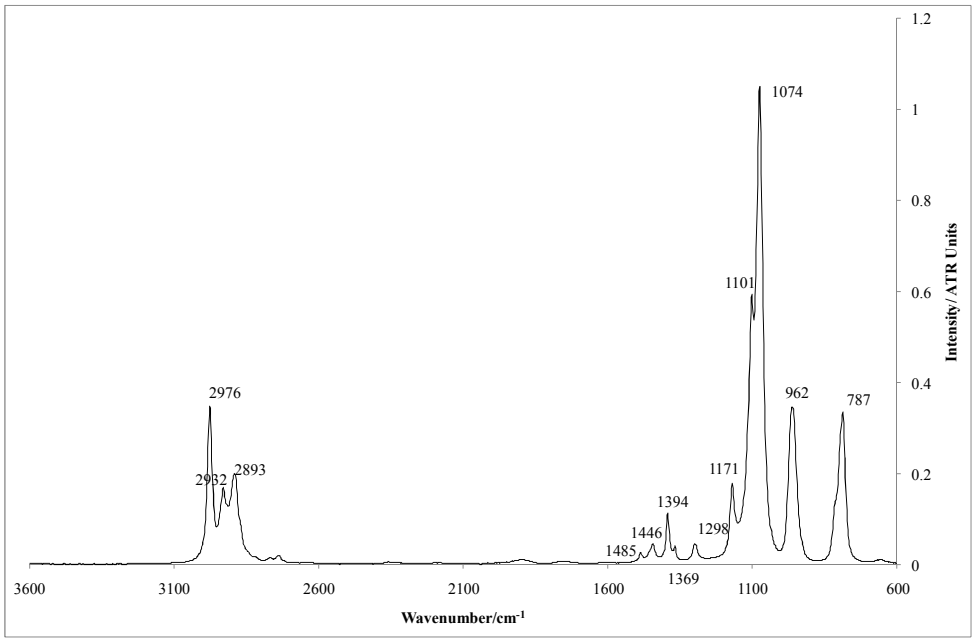


**Figure 41: ATR infrared spectrum of TEOS**

The development of a neutral amine templated HMS silica was followed over a reaction time of 29 hours. At each of the times listed in figures 42 and 43, the gel was stirred with a small spatula, a small sample removed from the reaction flask and placed on the golden gate accessory of the Brüker Vertex ATR spectrometer. 64 scans were recorded each time.

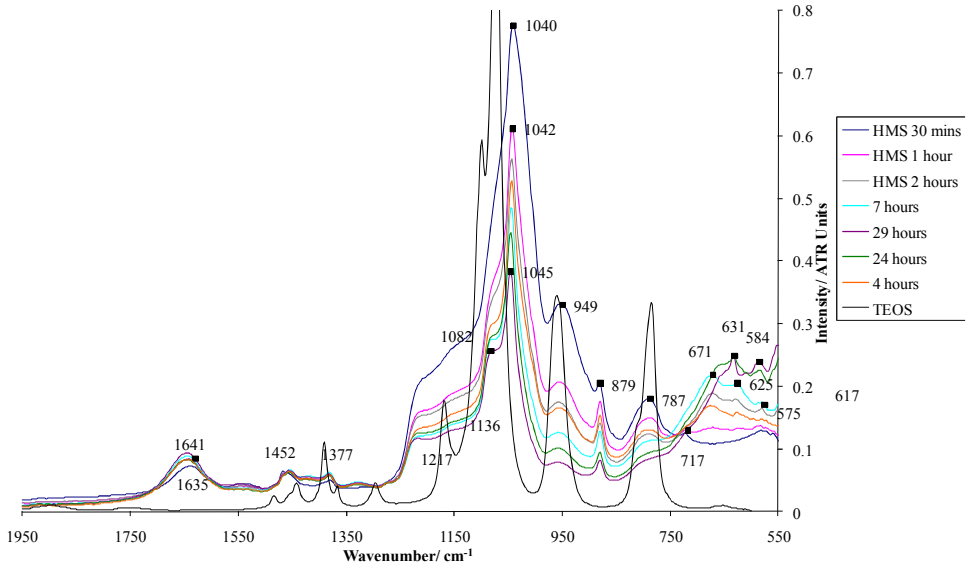


**Figure 42: ATR infrared spectra showing the Si-O region during the development of a HMS gel network**

The changes at the low frequency end of the infrared spectra are; the development of a series of bands in the 600-700cm$^{-1}$ region corresponding to the formation of carbonate species generated by reaction between the amine template and atmospheric $CO_2$.[92] Comparing figures 41 and 42, the band at 787cm$^{-1}$, which corresponds to the $SiO_4$ antisymmetric stretch of TEOS is seen to decrease in intensity quite rapidly and is barely visible by the end of the reaction time. The band at 962cm$^{-1}$ due to a $CH_3$ rocking mode does not appear in figure 42, though it may just be masked by the broad band that is present at 949cm$^{-1}$ due to the Si-OH stretch.

The band at 879cm$^{-1}$ that at 30 minutes is small, increases in intensity slightly and then decreases again by the end of the reaction (though it still remains intense) is assigned to a SiOH bending mode.[30] It is interesting to note that there is no equivalent band in either figure 39 or 40 for the microporous silica gel. This band at 879cm$^{-1}$ seems to be typical of TEOS since it is also not present in spectra of the dried samples shown in figure 42.

The assignment of the peaks in the 1220-1040cm$^{-1}$ is made extremely difficult by the fact that both the Si-O stretches and the C-O stretches from ethanol and TEOS all appear in this region. However, what can be seen is that there is a large change in peak width and intensity between 30 minutes and 1 hour and that no are no discernable changes after 7 hours. It is therefore expected that the gel forming reaction has completed by that time.

A significant shift from  can be seen in the water bending mode from 1635 to 1641cm$^{-1}$ between 30 minutes and 1 hour reaction time. This indicates an increase in the strength of the water hydrogen-bonding network parallel with the formation of the silica gel network.

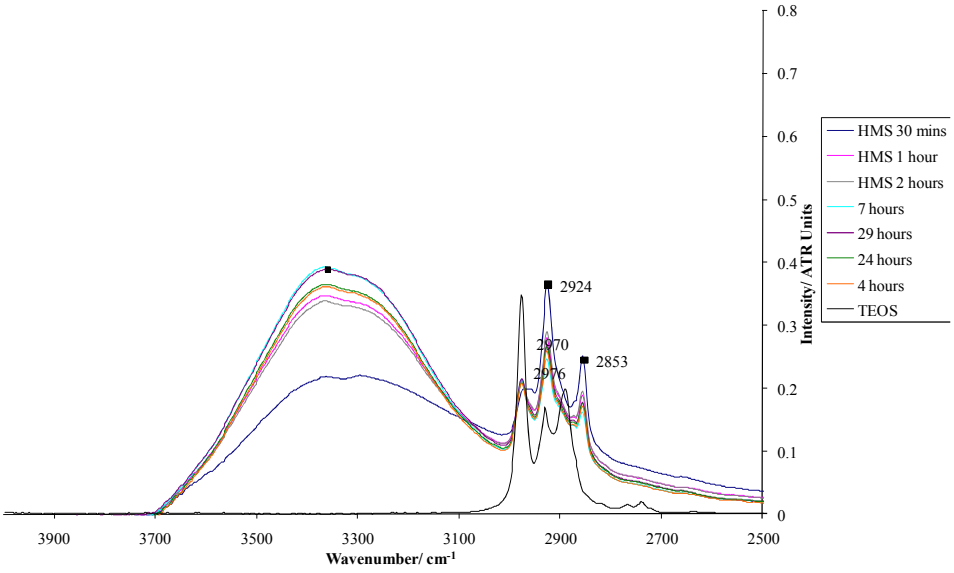


**Figure 43: ATR Infrared Spectra Showing the O-H and C-H Stretching Regions During the Development of a HMS Gel**

The C-H stretch and OH stretching bands in the 2980-2850cm$^{-1}$ and the 3700-3100cm$^{-1}$ regions do not show any real changes during the reaction time. The C-H stretches come from TEOS, ethanol and dodecylamine. The features in the OH stretch region are most likely Evans windows.

The dried and calcined at 700˚C samples are shown in the DRIFT spectra in figure 44 for the purposes of comparison.

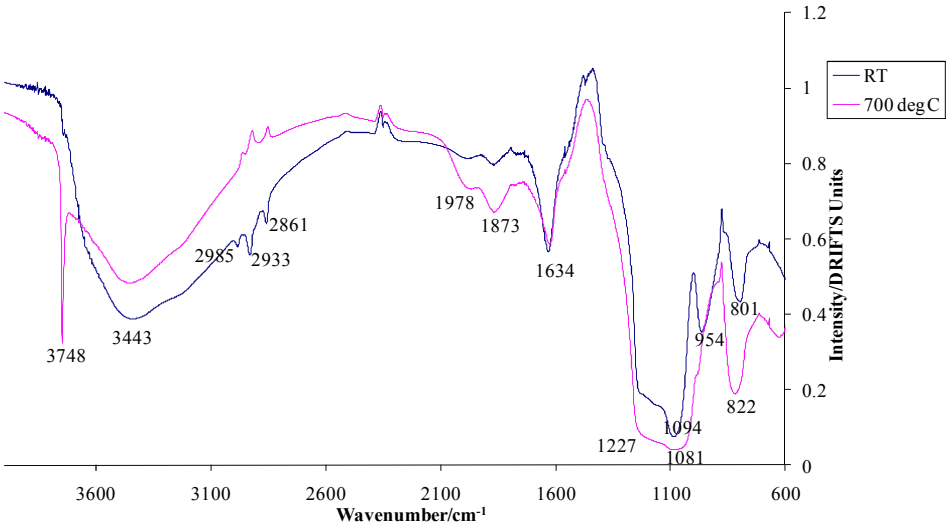


**Figure 44: DRIFT spectra using samples diluted with KBr of air dried and calcined HMS samples**

As with the microporous silica, calcination of the HMS causes the Si-O band at around 800cm$^{-1}$ to shift to higher frequency indicating a shortening and strengthening of the bonds. Also, the bands relating to SiOH at 954cm$^{-1}$ and around 3440cm$^{-1}$ decrease in intensity as the SiOH groups are condensed to Si-O-Si bridges. This is accompanied by the appearance of the free isolated SiOH band at 3748cm$^{-1}$.

Although the microporous silica was calcined at 800˚C rather than 700˚C and above 800˚C some surface restructuring begins to take place,[93] SiO-H stretching vibrations would be expected in the calcined sample in figure 40. So, this sample would appear to have a much lower level of surface hydroxylation that the HMS samples shown in figure 44.

By comparison of figures 42 and 44, it appears that the band at 1082cm$^{-1}$ that develops during the reaction corresponds to the silica Si-O bands. This seems to be fully present by 4 hours reaction time. But it is still unclear what species the other bands in that region actually represent.

Some information can be obtained by infrared spectroscopy about the formation of silica gel structures but particularly in the case of the HMS structure the presence of C-O bands in the same region as the pertinent Si-O bands make precise assignment of the peaks more or less impossible.

## 3.3 Extraction of the Dodecylamine Template from Hexagonal Mesoporous Silica

The HMS samples whose gelation was followed in section 3.2 were, as stated previously, formed using dodecylamine as a template. In the method described by Tanev[21a] and as detailed fully in the experimental section, the template was removed by washing with several portions of hot ethanol. Infrared spectra after this procedure indicated that in some cases the template was not fully removed and in others that a different pattern of bands relating to C-H groups could be observed in the sample even after drying. This raised two questions; 1) Could another method such as microwave or ultrasound assisted extraction improve the efficiency of the template removal? And 2) do these C-H groups correspond to residual solvent or reaction of the solvent with the surface?

The presence of organic groups on the silica samples was observed by ATR infrared spectroscopy.

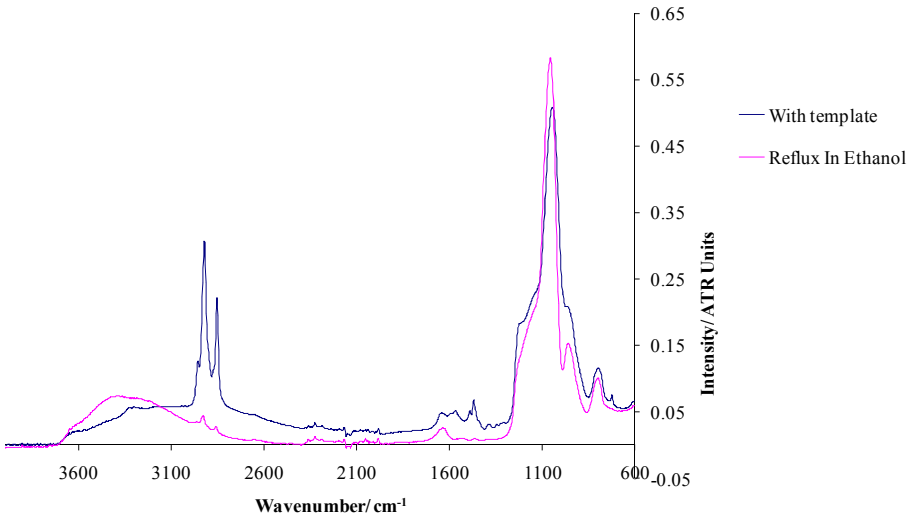


**Figure 45: ATR infrared spectra showing HMS with the dodecylamine template and after extraction 3 times with ethanol at reflux**

As can be seen from figure 45, the bands associated with the template are the weak N-H stretching vibrations at around 3340 and 3305cm$^{-1}$, the C-H stretching bands at 2850-2950 cm$^{-1}$ and the N-H and C-H deformation region at around 1400-1600cm$^{-1}$. After extraction with ethanol the bands relating to N-H vibrations are no longer visible and the C-H vibrations are much weaker. However a broad band appears in the region 3000-3700cm$^{-1}$ corresponding to hydrogen bonded OH stretches. This may indicate that this particular sample was not entirely dry when the infrared spectrum was obtained. Due to the comparative weakness of the remaining bands, the 1400-1600cm$^{-1}$ deformation was not considered further and the following spectra focussed on the C-H stretch region.

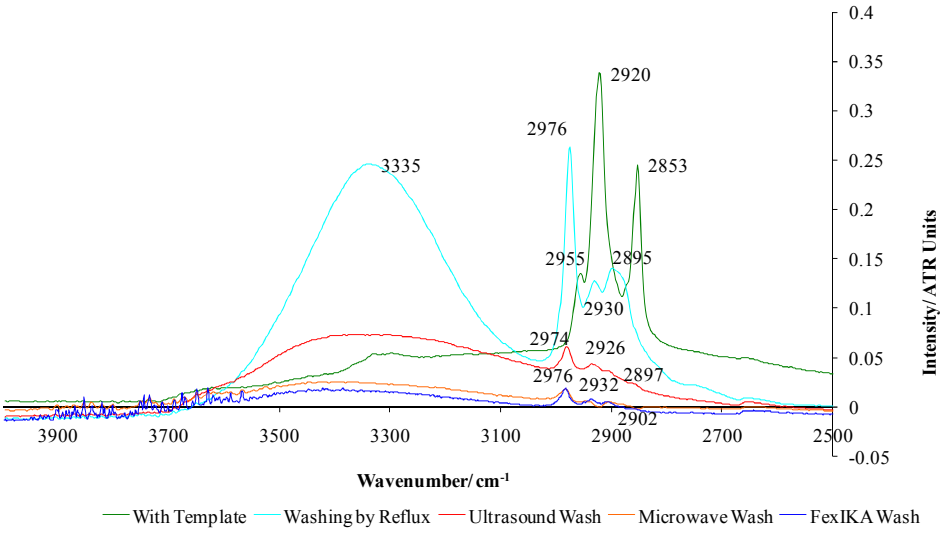


**Figure 46: ATR infrared spectra showing the OH and CH stretching region for HMS extracted by different methods using ethanol as the solvent**

For an explanation of the different washing techniques see Chapter 2.1.

As can be seen from figure 46, the C-H stretching vibrations relating to dodecylamine at 2955, 2920 and 2853cm$^{-1}$ are removed by the various washing techniques and are replaced by bands at 2975, 2930 and 2896cm$^{-1}$. These peak positions are characteristic of C-H stretching vibrations in ethanol.[90] All of the techniques remove the bands relating to dodecylamine but it is not clear whether the lower intensity of the C-H stretching bands in the spectra after the microwave and fexIKA washing of the silica is merely due to more efficient drying or more efficient removal of organic groups.

The extraction was then tried with a selection of other solvents; methanol, 1-propanol, 2-propanol, acetone and 1-pentanol. The relevant C-H stretching vibrations are given in table 3.

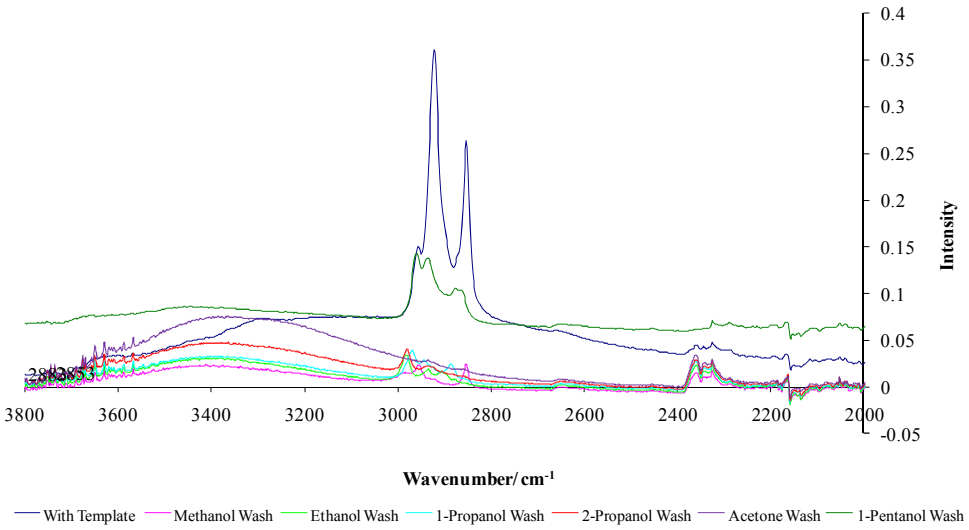


**Figure 47: ATR infrared spectra showing the OH and CH stretching region for HMS washed by microwave assisted extraction**

**Table 3: C-H stretching bands for the different solvents used to wash HMS by reflux**

| **Solvent** | **C-H stretch positions/cm$^{-1}$** | **Literature values/ cm$^{-1}$** |
|---|---|---|
| Methanol | 2988, 2957 and 2854 | 2999, 2959 and 2843 (monomer)[94] |
| Ethanol | 2981, 2936 and 2907 | 2974, 2930, 2892 (liquid)[90] |
| 1-Propanol | 2969, 2944 and 2887 | 2963, 2937 and 2878 (liquid)[95] |
| 2-Propanol | 2980 and 2937 second band possibly a doublet | 2987, 2982, 2975, 2968 and 2886.5 (Argon matrix)[96] 2980 and 2889 (vapour)[97] |
| Acetone | 2936 and 2859 (both very weak) | 3018, 2872 and 2937 (vapour) and 3004, 2964 and 2924 (liquid)[98] |
| 1-Pentanol | 2960, 2935, 2878 and 2864 (last two peaks are a doublet) | 2935 and 2870 (liquid)[99] |

As can be seen from table 3, the C-H stretching vibrations are very similar to the literature values for the solvents. This suggests that the organic groups are just residual solvent rather that silica-alkoxy groups.

If a silica-alkoxy bond is formed then this would be expected to be a strong bond. So, this was tested by taking one of the 1-propanol containing samples obtained by microwave extraction of the template in 1-propanol and then performing a single washing treatment by reflux and ultrasound in ethanol on different portions of this 1-propanol treated sample.

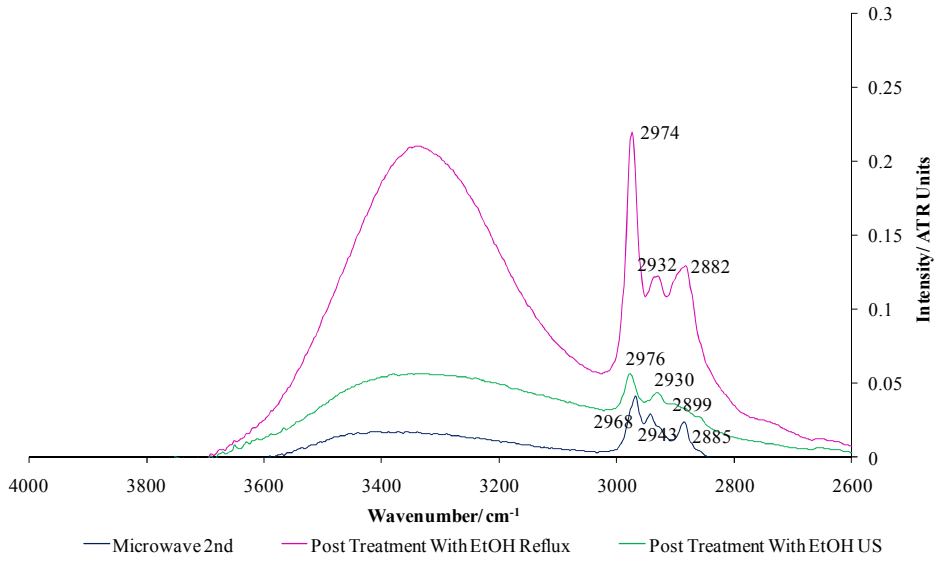


**Figure 48: ATR infrared spectra showing the C-H stretch region for HMS extracted in 1-propanol in the microwave followed by reflux or ultrasound (US) treatment with ethanol**

From figure 48, it appears that for the ethanol ultrasound washed sample (green) all the propoxy groups (blue) are replaced with ethoxy groups. However for the reflux wash, the peaks are so much larger that peaks for both ethoxy and propoxy groups may both be present. Some residual solvent is to be expected since the samples were just sucked dry by vacuum filtration and then left open to the air in the laboratory to dry further. A more effective test would be to take one of the samples washed with an

alcohol and then extract with a more inert solvent, such as hexane. However, it does seem that the C-H stretches relate simply to residual solvent rather than the products of surface reactions.

## 3.4 Conclusions

It was not possible to obtain much mechanistic information from the infrared study of the silica gel structure formation. The main points of interest were that drying and calcining the silica gel manufactured from water-glass had a much larger impact on the condensation of the SiOH groups than in the formation of the HMS structure. Secondly, the dramatic change in the water bending mode during the formation of the HMS gel, which is not something that been reported in the literature. The third point of interest is that the HMS gel formation has finished by 7 hours reaction time. This may well be due to the amine template also acting as a catalyst. It is known that the hydrolysis of silane esters is subject to general base catalysis.[100] Also, Chrzczonowicz proposed a mechanism for condensation of silanols by primary and secondary amines involving a nucleophilic attack on silicon followed by rapid attack of the dialkylsilanediol as shown in figure 49.[100-101]

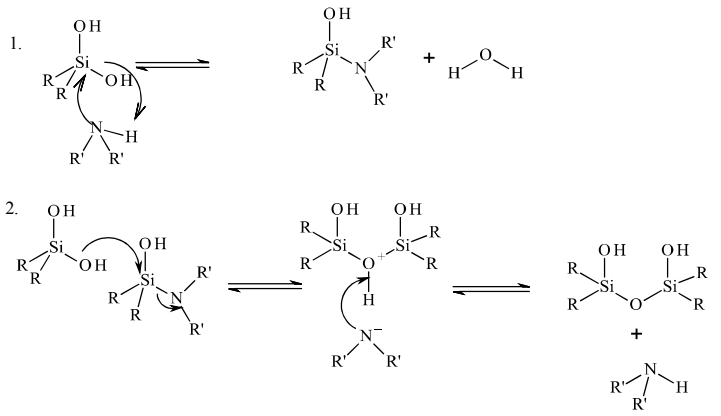

**Figure 49: Proposed reaction steps for amine catalysed condensation of silanols[100]**

Catalysis of silanol condensation by the amine template also means that thermal treatment is less crucial than in the formation of the microporous silica. This fits with the observation that the template can be removed at low temperature without the structure collapsing.

In the template removal processes it can be seen that the faster and lower-energy techniques of ultrasound and microwave assisted extraction are just as efficient at removing the template as extraction by solvent at reflux. However, work has not yet been carried out to determine whether or not the textural properties and surface area of these materials are preserved. It also seems that there is no significant reaction between the silica and the solvents used to extract the template. This means that the results of the template extraction step are highly reproducible.

# Chapter 4. Infrared Probing Techniques for Studying the Surface Chemistry of Metal Oxides and Organically Functionalised Silica

As covered in the introduction, infrared probing techniques are popular and well established methods for studying, in particular, the acid/base properties of surfaces.[3b,28] Many different species have been used as probe molecules. A small selection of these are used in this chapter to characterise the surface of silica samples activated under different conditions, silica surfaces functionalised with hydrophobic alkane groups and amines and a number of different metal oxides.

## 4.1 Survey of Several Different Probe Molecules for the Study of the Surface Chemistry of High Temperature Activated Silica Samples

As covered in the introduction, silica is a popular surface to study due to its widespread use in areas such as chromatography and catalysis. Compared to many metal oxide surfaces, it also has a relatively simple structure, made up of different silanol and siloxane structures. Also, it is quite simple to graft organic groups onto the surface or generate organically modified silica structures by a one-pot synthesis.[7,102]

The difficulties with studying this surface as will be seen from the following experiments are that the surface structure depends on the type of silica and the pretreatment conditions but samples can also vary between different batches. Also ideally the infrared spectra should be recorded as soon as the sample is cool enough to touch after the calcination treatment because the

surface dehydroxylation is reversible. This is especially crucial for pretreatment conditions below about 500˚C. After calcination above this temperature the reverse reaction to rehydroxylate the silica surface is slow. In this study an activation/ calcination temperature of 700˚C was used.

A number of different probe molecules with different properties were adsorbed onto the surface of a commercial sample of Kieselgel 60 and onto a hexagonal mesoporous silica produced by the neutral amine templating route detailed in the experimental section. These samples were then activated at 700˚C in air. Infrared spectra were recorded using the Brüker Equinox 55 IR operating in diffuse reflectance mode in the mid-IR and in some cases near-IR range as well. The desorption of some of these probes from the surface was studied by use of the environmental chamber accessory for the spectrometer. This accessory allows the heating of a sample *in situ* up to approximately 400˚C under a controlled atmosphere or vacuum. The probes chosen were diethylamine, aniline, propanoic acid, fluorobenzene and deuterated acetonitrile ($CD_3CN$).

The main property that the probe molecules used in this section have in common is that they are all liquids at room temperature. They were added to the silica sample in the liquid state before being heated in a sealed vessel to vaporise the liquid and ensure even coverage on the surface.

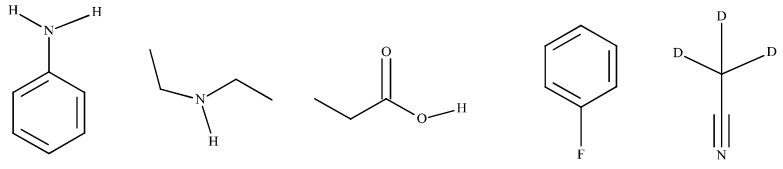


**Figure 50: Five different probe molecules used to study the surface properties of high temperature activated silica**

These molecules display a range of acidities and possible interactions with the surface. Diethylamine is the strongest base used and would be expected to interact with the surface hydroxyl groups (pKa~7) via a (SiO-H---N-H)

Brönsted type interaction. The aniline is also more basic than SiOH but is a weaker base than diethylamine so a weaker interaction would be expected. The propanoic acid is more acidic than the silanol groups and so would be expected to act as Brönsted acid on the silanol surface. Fluorobenzene would be expected to undergo a hydrogen bonding interaction with the silanol groups of the type (SiO-H---F-C). Both fluorobenzene and anilne may also interact through an OH---π cloud bond in a similar manner to that shown by the interaction of benzene with surface hydroxyl groups.[103] Acetonitrile-$d_3$ is a weak Lewis base and will interact with the silanol groups via a (C≡N---H-OSi). However, as will be seen later it can undergo more complex reactions on metal oxide surfaces that are more active than silica.

**Table 4: Peak Assignments for bands seen in the infrared spectra of high temperature activated silica**

| **Peak Position/ $cm^{-1}$** | **Assignment** |
|---|---|
| 810-820 | Si-O-Si symmetric stretch[89] |
| 974 | Si-OH stretch (usually a weak shoulder)[89] |
| 1090-1225 | Si-O-Si antisymmetric stretches (several species in this range)[89] |
| 1659 | Bending mode associated water (water picked up again after activation or trapped in internal "pocket")[29] |
| 1878 | Silica framework overtone/combination band |
| 1990 | Silica framework overtone/combination band |

| | |
|---|---|
| 3650 | Hydrogen bonded SiO-H stretch (weak)[89] |
| 3747 | Isolated terminal SiO-H stretch[89] |
| 4562 | SiO-H stretch + SiOH bend combination mode[89] (or SiO-H stretch + Si-O-Si symmetric stretch mode)[29] |
| 5280 | OH stretch + bending mode combination band associated water[89] |
| 7143 | Overtone SiO-H stretch hydrogen bonded silanol[89] |
| 7326 | Overtone SiO-H stretch free terminal silianol[89] |

## Diethylamine Adsorbed on Silica Kieselgel 60

Amines are popular probes for the study of surface acidity of metal oxides. Of the aliphatic amines, butylamine is probably the most frequently used.[104]

Diethylamine was chosen for this trial because it has been less well studied than many other amines. It a boiling point of 56˚C making it liquid when measuring it out by mass or volume onto the surface and then easy to vaporise in a low-temperature oven. It was also readily available in the laboratory.

In this study diethylamine was adsorbed from the liquid phase onto the silica Kieselgel 60 (K60) surface in a ratio of $6.01*10^{-4}$ moles probe to 1g silica K60. The sample was diluted in a 1:20 ratio of sample to KBr and heated in the environmental chamber under a 100 ml/min flow of $N_2$ up to 210˚C with spectra recorded every 30˚C.

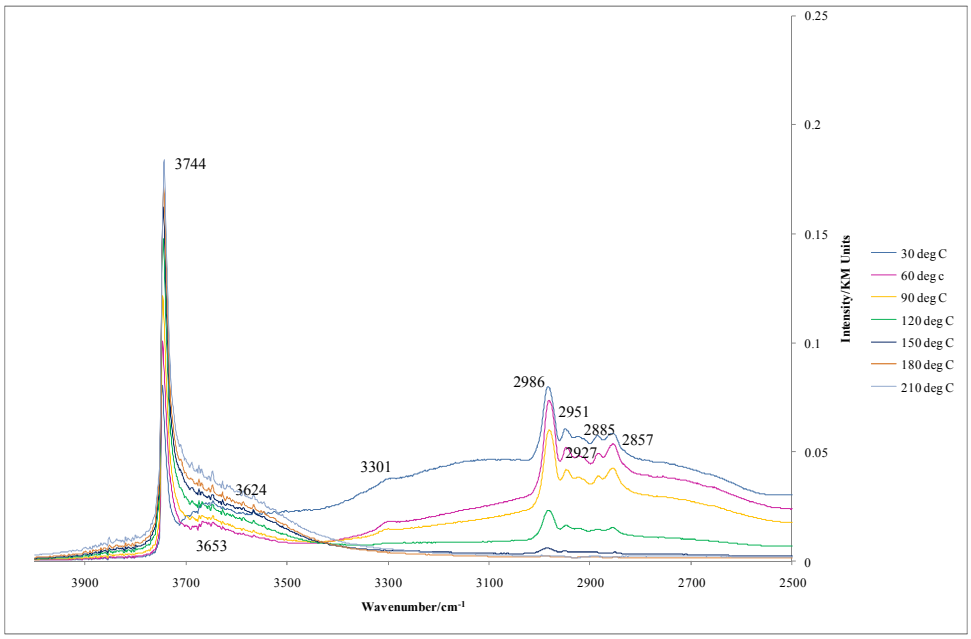


**Figure 51: Infrared spectra showing the high frequency region after adsorption of diethylamine onto silica K60 followed by heating under flowing nitrogen up to 210˚C**

Starting at low temperatures (corresponding to a high coverage of diethylamine) and heating to 210˚C the main changes relating to surface silanol species shown in figure 51 are: the increase in the intensity of the isolated SiO-H band at 3744cm$^{-1}$, the disappearance of the bands at 3653cm$^{-1}$ and approximately 3000cm$^{-1}$ relating to hydrogen-bonded SiOH hydroxyl groups and the formation of a new band as a shoulder on the side of the 3744cm$^{-1}$ band at around 3624cm$^{-1}$ also relating to hydrogen bonded SiOH groups. Unfortunately, in this particular experiment, the spectrum of the silica before the addition of diethylamine was not recorded. So, there is no way of telling whether the second hydrogen-bonded SiO-H stretching band was present in the original sample or was formed as a result of opening of siloxane bridges. The shift between the position of the isolated free silanol stretch and the broad stretch relating to the hydrogen bonded silanol groups (in this case the band at around 3000cm$^{-1}$) is correlated with the strength of the interaction between the probe and the surface.

The changes in bands relating to diethylamine are: the disappearance of the small feature at 3301cm$^{-1}$ corresponding to the N-H stretch and a number of bands in the region of 2986-2857cm$^{-1}$ relating to C-H stretching vibrations. The fact that these bands overlap with that relating to the hydrogen-bonded OH groups band is not ideal as it makes the centre of this band more difficult to pinpoint. No bands relating to N-H or C-H remain after the heating process indicating that the diethylamine is desorbed from the surface.

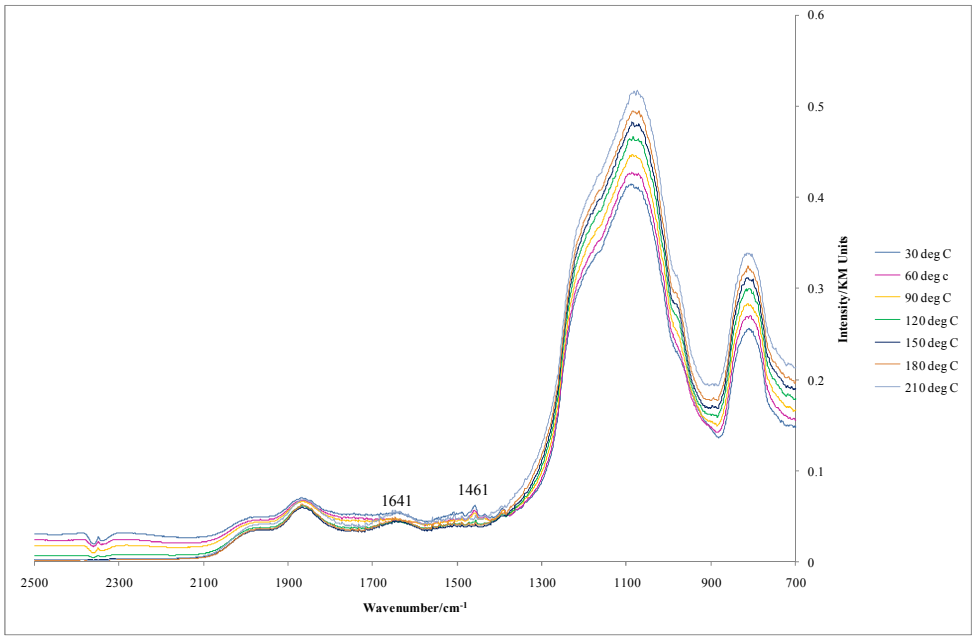


**Figure 52: Low frequency region of the infrared spectra recorded after adsorption of diethylamine onto silica K60 followed by desorption under flowing nitrogen up to 210˚C**

In figure 52, the band at 1461cm$^{-1}$ is assigned to a $CH_2$ wagging vibration of the amine. The band at 1641cm$^{-1}$ that also decreases in intensity with increasing temperature is assigned to the deformation mode of adsorbed water. It is in approximately the right region for an N-H deformation mode of an amine but this band for a secondary amine is usually very weak and at lower frequency.[105]

Diethylamine is a fairly strong base with a pKa of 10.7 compared with silanol groups at pKa~7.[106] However, it should be noted that these pKa

values are measure in water and do not necessarily correlate with the behaviour observed in the gas phase. The main reason for quoting them is that gas phase proton affinity values were not available for silanol groups. Based on the pKa values it would be expected that diethylamine would be able to abstract a proton from the silanol group. However, no conclusive evidence of this can be observed in the infrared spectra. Bands such as the $(CH_3CH_2)_2NH_2^+$ symmetric and antisymmetric stretches and an $NH_2$ bending band would be expected if significant proton abstraction did take place.[107] So, clearly in this case, the pKa values are not a good description for this system.

The effect on the near-infrared region of the spectrum of a 700˚C activated silica upon adsorption of diethylamine was studied using a neutral amine template mesoporous silica (HMS). In this study the concentration of adsorbed diethylamine was slightly higher at $1.20*10^{-3}$ moles probe/g silica and the effect of heating under flowing $N_2$ was not investigated. In order that the weak bands in the near-IR region could be observed, the sample was not diluted by KBr.

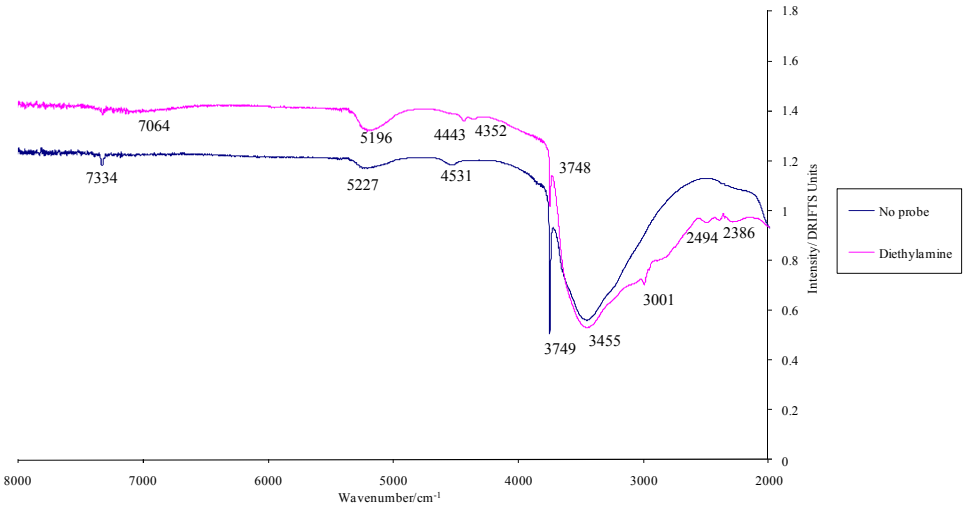


**Figure 53: Infrared spectra showing the OH stretch region and the 1st overtone region of 700˚C activated HMS and that sample with adsorbed diethylamine without KBr dilution**

By comparison of figures 51 and 53 it can be seen that when using DRIFTs techniques on undiluted samples, the positions of strong bands such as those for the N-H and C-H stretches can be shifted to lower frequency by a significant amount. Also, these bands can be observed to change shape. For strong bands the "correct" position is that given in the infrared spectrum of the diluted sample.

In the OH stretch 1$^{st}$ overtone region of figure 53 (7400-6900cm$^{-1}$) the changes upon diethylamine adsorption mirror those seen for the fundamental bands. The peak relating to the 1st overtone of the free isolated silanol stretch decreases in intensity and a new broad, weak band develops at around 7064cm$^{-1}$ corresponding to the 1$^{st}$ overtone of the hydrogen bonded OH stretches.

The two combination modes are also perturbed by the adsorption of diethylamine. The band at 5227cm$^{-1}$ is not listed in table 4 but it corresponds to a combination band of the v2+ v3 bending modes of

symmetrical ( i.e. similar perturbation on each hydroxyl) or weakly perturbed adsorbed water as might be expected for water adsorbing on isolated silanol groups.[29] After adsorption of diethylamine, this band shifts to lower frequency and becomes more intense. The new position of 5196cm$^{-1}$ is close to the position found by Burneau *et al* for water inside a cluster.[29] This indicates hydrogen bonding to multiple species.

As listed in table 4, the band at 4531cm$^{-1}$ is a combination band involving the SiO-H stretch. This band almost disappears after diethylamine adsorption and what is left is somewhat masked by the overtones for the C-H stretches at 4443cm$^{-1}$ and 4352cm$^{-1}$.

## Aniline Adsorbed on Silica Kieselgel 60

Due to the resonance effect of the aromatic ring aniline is much more acidic than diethylamine but it is still more basic than the silanol groups.

In this study, a sample made up of 3.29*10$^{-4}$ mols aniline/g silica K60 was diluted 1:20 with KBr and placed in the environmental chamber accessory of the Brüker Equinox 55 IR and heated under a 100ml/min flow of nitrogen up to 210˚C. Infrared spectra were recorded every 30˚C. In this experiment, the blank sample was also run under the same conditions. This allows the changes due only to aniline adsorption/desorption to be observed by subtracting the spectrum recorded of the bare silica from that of the sample with the adsorbed aniline at each temperature.

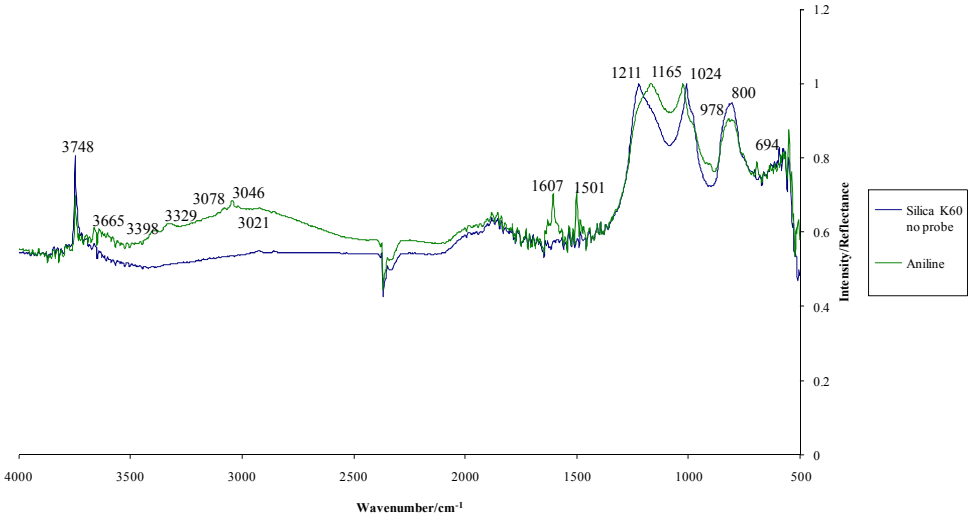


**Figure 54: Comparison of the infrared spectra of silica K60 activated at 700°C and the same sample with adsorbed aniline**

From figure 54, it is interesting to note that the bands relating to the Si-O-Si antisymmetric stretch between 1211cm$^{-1}$ and 1024cm$^{-1}$ are split into two rather than just being one broad asymmetrical band. The bands at 1211cm$^{-1}$and 1165cm$^{-1}$ in the aniline sample are, according to the assignments of Holmes *et al*[25] related to "external" Si-O-Si vibrations (i.e. those in the surface layer or just below the surface). The band at 1024cm$^{-1}$ that doesn't shift when aniline is adsorbed on the surface, is assigned to "internal" Si-O-Si vibrations (i.e. those below the surface of the silica).[25a] In this high temperature activated silica sample, the presence of surface Si-O-Si is possible, unlike in the hydrogel during synthesis as discussed in Chapter 3.2. Whether or not these external Si-O-Si groups exist, it is interesting to note that changes can occur to the Si-O-Si bonds when aniline is adsorbed on the surface.

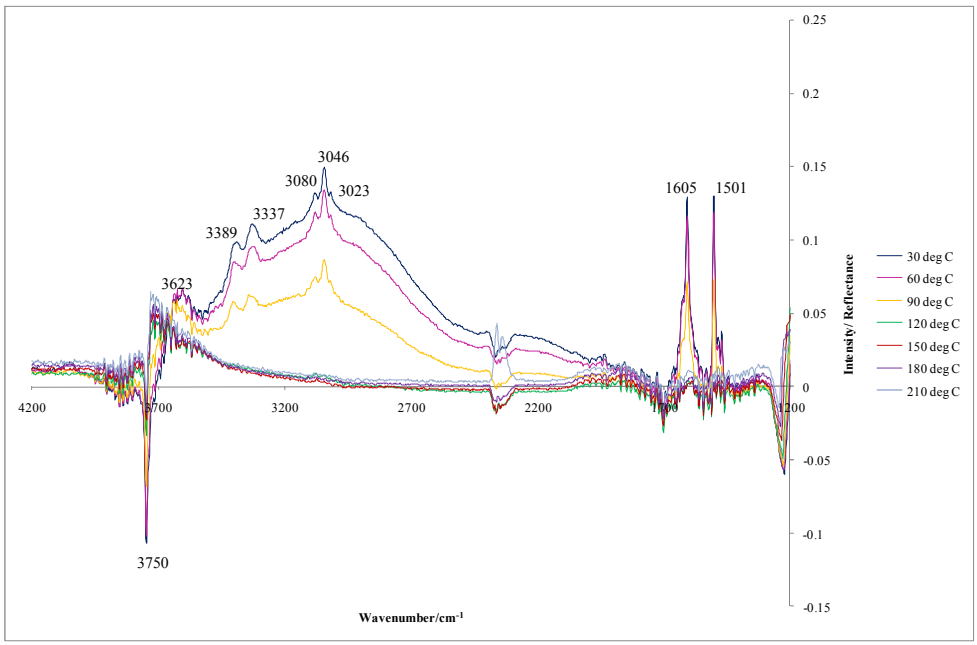


**Figure 55: Infrared subtraction spectra showing the changes after aniline adsorption onto 700˚C activated silica K60 and subsequent desorption under flowing $N_2$ up to 210˚C**

It can be clearly seen by the decrease in intensity of the band at 3750cm$^{-1}$ in figure 55, that aniline is adsorbed onto the isolated silanol groups. This band is gradually restored as the temperature is increased and the aniline desorbed. The positive bands that develop at high aniline coverage (30˚C line in figure 55) are bands due to the OH stretches of hydrogen-bonded SiOH groups at 3623cm$^{-1}$ and centred at around 3050cm$^{-1}$. There are no groups that absorb at around 1800cm$^{-1}$ that could have overtones in the 3600cm$^{-1}$ region. Overtones would be the most likely vibrations to interact via Fermi resonance with SiOH stretching vibrations. In the absence of these bands, it seems likely that the two different bands relating to hydrogen bonded OH stretches relate to genuinely different species.

As with diethylamine, aniline produces bands that overlap with OH stretching band envelope. These are assigned to the primary N-H stretching vibrations at 3389cm$^{-1}$ and 3327cm$^{-1}$, and the aromatic C-H stretching vibrations at 3080, 3046 and 3023cm$^{-1}$. The bands at 1605cm$^{-1}$ and

1501cm$^{-1}$ are assigned to $NH_2$ and C-H deformations respectively.[108]

Heating to above 150˚C can be seen to remove all the bands relating to aniline from the spectrum and therefore remove the aniline from the surface. However, the free isolated silanol band is not fully restored and a feature develops to the low frequency side, this indicates some ring opening of the siloxane bridges to form new vicinal silanol groups. This is most likely caused by residual water because no signs of strong chemisorption of aniline to the surface can be observed. However it is possible that the aniline could help to catalyse this reaction.

## Propanoic Acid Adsorbed on Silica Kieselgel 60 700˚C activation

In this study a sample was made up of 3.34*10$^{-4}$ moles propanoic acid/ g silica by the method detailed in Chapter 2.3. The infrared spectra were then recorded as for the aniline sample.

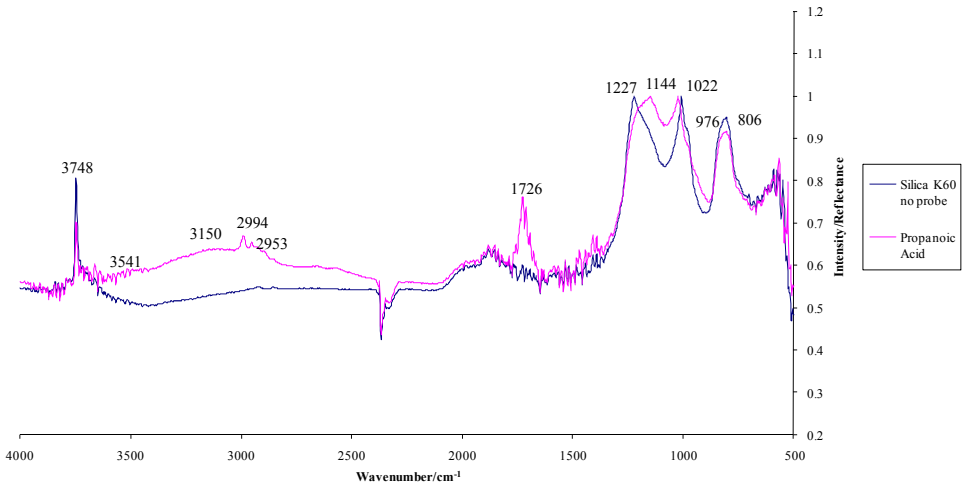


**Figure 56: Comparison of the mid-IR spectra of silica K60 700C activation and the same sample with adsorbed propanoic acid**

As shown by figure 56, the changes in the silica framework bands region upon propanoic acid adsorption are much the same as those for aniline adsorption in figure 54. Again a shift in one of the Si-O-Si antisymmetric stretching bands is observed, in this case from 1227-1144cm$^{-1}$ as is reduction in intensity of the Si-OH stretch at 976cm$^{-1}$. As before, the changes in the region above 1200cm$^{-1}$ are more easily observed in the subtraction spectra, shown in figure 57.

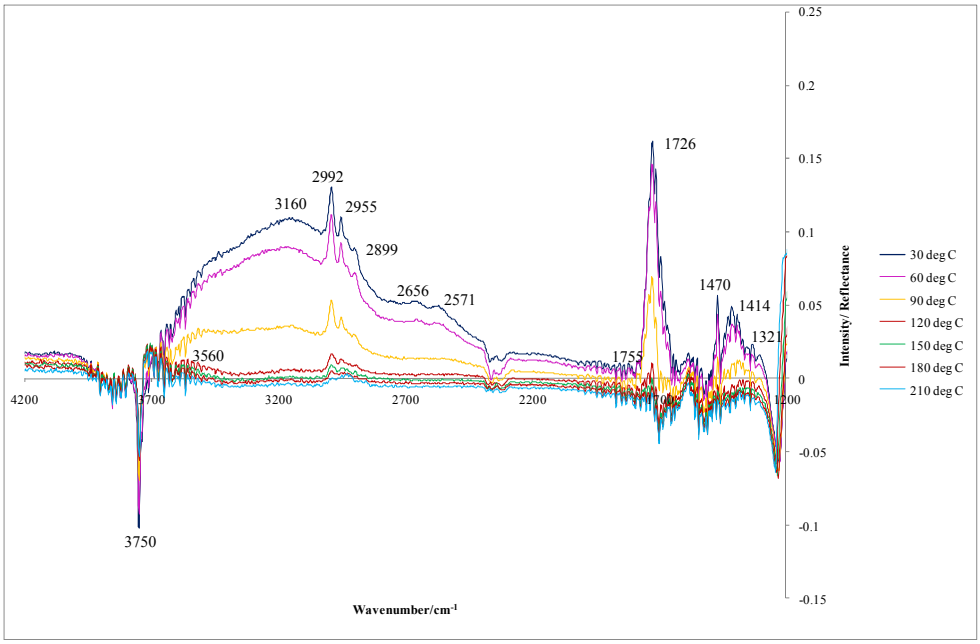


**Figure 57: Infrared subtraction spectra showing the changes after propanoic acid adsorption on silica K60 700˚C activation followed by desorption under flowing 100ml/min $N_2$ up to 210˚C**

As with the amine probes used, the adsorption of propanoic acid onto the silica surface causes a reduction in intensity of the free SiO-H stretch, this is not fully restored even at 210˚C. Also at high temperature a second band appears to the low frequency side of this band, related to hydrogen bonded SiOH groups. Again a broad band is formed due to hydrogen bonded OH groups this time centred at around 3160cm$^{-1}$. Though, this is slightly

complicated by the fact that both the hydrogen-bonded silanol OH stretch and the propanoic acid OH stretch occur in this region.

At high coverage (low temperatures) in figure 57, the bands in the 3000-2500cm$^{-1}$ region due to propanoic acid that can be observed are; the C-H stretches at 2992, 2955 and 2899cm$^{-1}$ and the overtone and combination bands for propanoic acid dimers at 2656 and 2571cm$^{-1}$. The structure of the dimer is shown in figure 58. Below 2000cm$^{-1}$ the band assignments are, the νC=O band of physisorbed propanoic acid at 1726cm$^{-1}$, the δC-H deformation peaks at 1470 and 1321cm$^{-1}$and the broad band at around 1414cm$^{-1}$ corresponds to the νC-O and δO-H bands.[109]

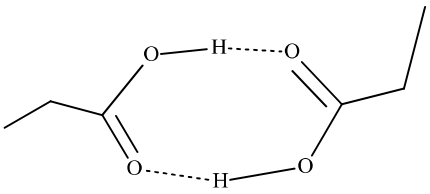


**Figure 58: The structure of the propanoic acid dimers formed at high concentration**

As the temperature is increased, in the 3700-2500cm$^{-1}$ region, the only bands that remain unrestored at the free νSiO-H band and a residual band at around 3560cm$^{-1}$ characteristic of hydrogen bonded SiOH groups. This is probably due to some chemisorbed propanoic acid remaining on the surface. The overtone and combination bands of the dimer disappear by around 90˚C, indicating that, by this temperature, propanoic acid is adsorbed on the surface as monomers. It is accompanied by a weak shoulder on the side of the 1726cm$^{-1}$ band at around 1755cm$^{-1}$ due to the νC=O band of chemisorbed propanoic acid, this remains at least until 180˚C.

## Fluorobenzene adsorbed on High Temperature Activated Silica

Fluorobenzene would be expected to interact with the silanol group via hydrogen bonding between the SiO-H group and either the F-C bond or the benzene ring via a π-type interaction. Flurobenzene was chosen as a probe molecule because the results from the infrared data could be compared with those from $^{19}F$ NMR data. However, very little $^{19}F$ NMR data was ever obtained due to serious instrumental problems and more work would be needed using that technique.

In this study, a sample was made up of $1.05*10^{-3}$ moles fluorobenzene/ g silica K60 700˚C activation. The sample was placed undiluted in the environmental chamber of the Brüker Equinox 55 IR and heated to 100˚C under a 100ml/min flow of nitrogen. Because the sample was studied undiluted, the region of most interest will be that above $2000cm^{-1}$, bands below that frequency generally saturate the signal.

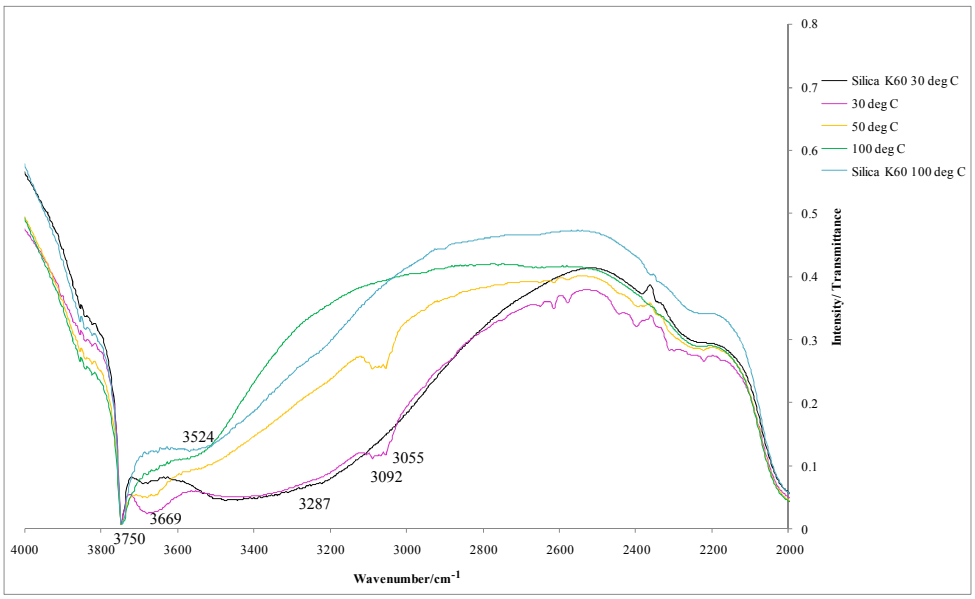


**Figure 59: OH stretch region fluorobenzene adsorbed on silica K60 700˚C activation followed by heating under 100ml/min $N_2$ up to 100˚C**

In the mid-IR region shown in figure 59, the adsorption of fluorobenzene onto this sample produces little change in the intensity of the free SiO-H stretch. The only real changes in the mid-IR region upon adsorption of fluorobenzene are the development of a band at 3669cm$^{-1}$ due to hydrogen bonded silanol groups and appearance of the doublet at 3092 and 3065cm$^{-1}$ due to the fluorobenzene C-H stretching vibrations. Unlike with the other probes, no new broad band due to strongly hydrogen bonded hydroxyl groups is observed. The band at 3669cm$^{-1}$ disappears at higher temperatures and for both samples with and without fluorobenzene a band appears at around 3525cm$^{-1}$. This corresponds to residual hydrogen-bonded silanol groups. This sample generally has a higher concentration of hydrogen-bonded silanol groups than the others. The higher concentration of adsorbed water may either be due to a longer time being allowed to elapse between the activation of the silica and the infrared spectra being run or alternatively to water being present in the fluorobenzene. No particular effort was made to exclude water from the fluorobenzene.

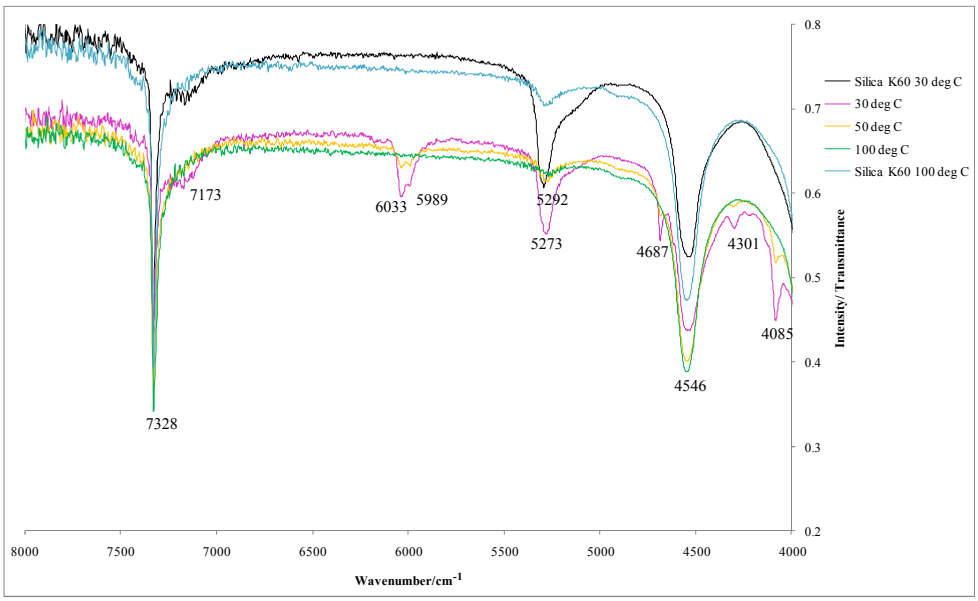


**Figure 60: Near-IR spectra comparing silica K60 700˚C activation with that sample with adsorbed fluorobenzene during heating to 100˚C under100ml/min flowing $N_2$**

Due to the number of different features present in the near-IR spectra in figure 60, the difference spectra were calculated by normalising the spectra to the same baseline intensity at around 5645cm$^{-1}$ and then subtracting the bare silica sample spectrum from that of the silica with adsorbed fluorobenzene spectrum at each temperature. This is shown in figure 61.

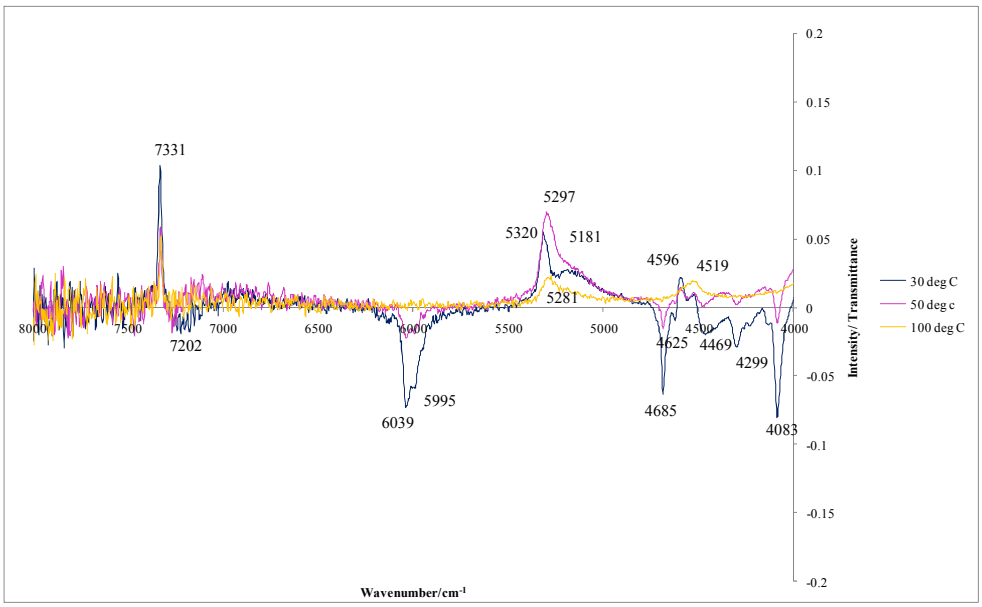


**Figure 61: Near-IR subtraction spectra showing the changes after fluorobenzene adsorption onto silica K60 700˚C activation followed by heating under 100ml/min $N_2$ up 100˚C**

From figure 61 it is possible to see that the 1st overtone of the isolated SiO-H stretching band becomes negative and is not fully restored at 100˚C. This indicates that fluorobenzene is adsorbed onto these groups. Next to it a positive band develops at around 7202cm$^{-1}$ corresponding to the 2νSiO-H band of hydrogen-bonded silanols. This shift between the 2νSiO-H bands for free and hydrogen-bonded silanols of 129cm$^{-1}$, is somewhat smaller than that seen for diethylamine at 270cm$^{-1}$ (shown in figure 53). This is to be expected as diethylamine is a much stronger base than fluorobenzene and the shift in the overtone region mirrors that in the fundamental bands.

Other positive peaks that can be observed in figure 61 are the 2νC-H bands for fluorobenzene at 6039 and 5995cm$^{-1}$ and a variety of fluorobenzene combination bands in the 4690-4000cm$^{-1}$region.

Of more interest is formation and splitting of negative peaks corresponding to adsorbed water combination bands at around 5300cm$^{-1}$ and the silanol

stretch in combination with framework modes at 4600-4500cm$^{-1}$. Various authors have assigned peaks in these regions to different modes but it appears that there may well be more than one mode present. At high coverage of fluorobenzene (30˚C) there are two peaks present in the water combination band region at 5320cm$^{-1}$ and 5181cm$^{-1}$. These are assigned to the ν2+ ν3 modes of asymmetrically perturbed adsorbed water and the ν2+ν3 modes of symmetrically perturbed water present in inner surfaces by Burneau *et al*.[29] Alternative assignments are given by Cannas *et al* as the νOH + ν2 bending mode monomeric and hydrogen-bonded water respectively.[110] It is interesting to note that the band at 5320cm$^{-1}$ shifts to 5297cm$^{-1}$ and becomes increasingly negative as the temperature is increased from 30˚C to 50˚C and even at 100˚C it still tails to the low-frequency side. Fluorobenzene seems to be removed from the species absorbing at low frequency initially but remains associated with a species absorbing at 5281cm$^{-1}$. The shift of the band from 5320cm$^{-1}$ to 5281cm$^{-1}$ may be due to the remaining fluorobenzene interacting more strongly with the water molecules.

It was a little unexpected to see two bands at 4596cm$^{-1}$ and 4519cm$^{-1}$. What is more usual is the broad band at around 4520cm$^{-1}$ seen after heating the sample to 100˚C. However, by comparison with figure 60, it is not certain whether these are genuine bands or merely an artefact from the subtraction. All that can really be gleaned from this is that there is little change in intensity of the νSiO-H combination band at 4546cm$^{-1}$ in figure 60 judging by the lack of bands in this region in the subtraction spectra. It is possible however that an element contributing to this relatively broad band corresponds to that in figure 61 at 4520cm$^{-1}$.

There is relatively little information that can be obtained from the infrared spectra of fluorobenzene adsorbed on high temperature activated silica, despite the great number of bands that are observed, of the probe molecules studied so far, it is the least effective.

## Deuterated Acetonitrile Adsorbed on Three Different 700˚C Activated Silica Samples to Compare Their Acidities

Nitriles are weak Lewis bases and can interact via σ-charge release from the nitrogen lone-pair with any kind of charge withdrawing sites. Interaction with a surface acid group (either Lewis or Brönsted) is observed by an increase in the spectral frequency of the νC≡N vibration (ΔνCN). This ΔνCN depends on the degree of donor-acceptor transfer. To prevent complications from splitting due to Fermi resonance effects $CD_3CN$ is preferred to $CH_3CN$.[44a] In liquid $CD_3CN$ the νCN band is observed at $2262cm^{-1}$, this is slightly different to the νCN band of gaseous $CD_3CN$, which is at $2252cm^{-1}$.[111]

In this study, a sample made up of a mass ratio of 1 part acetonitrile-d3 to 10 parts silica (700˚C activated) was placed undiluted in the environmental chamber of the Brüker Equinox 55 IR and heated under flowing nitrogen up to 120˚C. The 3 different silica samples were, the commercial sample of silica K60, the HMS amine template silica as described previously and a sample of SBA-15 kindly donated by James Comerford and manufactured according to the procedure of Wang *et al*.[86]

The changes after acetonitrile- d3 adsorption onto the silica surface followed by desorption under flowing nitrogen are shown as subtraction spectra for the HMS sample as an example in figure 62. The three samples are compared in figure 64 as the original spectra.

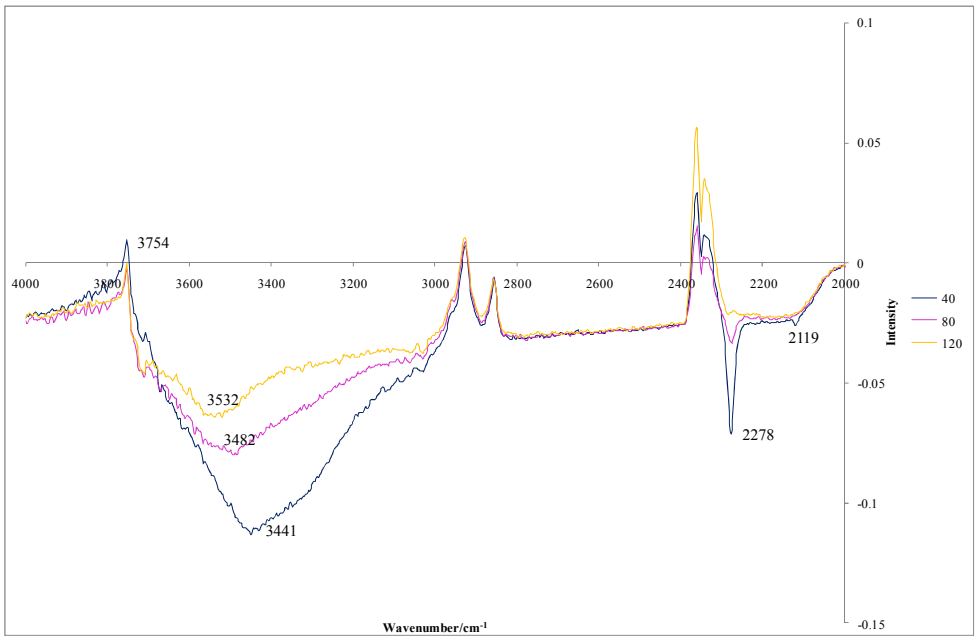


**Figure 62: Infrared subtraction spectra showing the changes after adsorption of acetonitrile-d3 onto 700˚C activated HMS followed by desorption under 100ml/min $N_2$ up to 120˚C**

In figure 62, the νCN band is found at 2278 $cm^{-1}$, this peak position has been found to be characteristic of $CD_3CN$ adsorbed on silanol groups.[112] It can be observed that the terminal SiO-H stretch at 3754$cm^{-1}$ is not reduced in intensity a great deal (the negative peak is very small). So, as expected, the weakly basic $CD_3CN$ does not interact very strongly with the isolated, terminal SiOH groups. The surfaces of these high-temperature activated silica gels would be expected to be made up of quite widely spaced silanol groups interspersed with siloxane. $CD_3CN$ has very little impact on the OH stretching region of the spectrum. This is shown by the very low intensity of all the features in the subtraction spectra. This is to be expected because on surfaces such as these, there are likely to be very few vicinal silanol groups (those close enough to form hydrogen bonds) and bonding to isolated terminal SiOH groups is an unfavourable interaction.

In the absence of strain, Si-O bonds are inert to attack by water, ammonia etc. However, on silica surfaces treated at ≥700˚C the surface siloxane rings

are under considerable strain. These may be attacked in a nucleophilic type mechanism as shown by the modelling work of Walsh and co-workers. This involves a nucleophilic attack on Si followed by proton transfer. An example of one of the figures produced by Walsh *et al* is shown in figure 63.[113] There is also some experimental evidence for this because the species that might be expected to open siloxane bridges; water, ammonia, methanol and organosilanes are all nucleophiles and are good at proton transfer.[39,114] Nitriles are not so good at this.

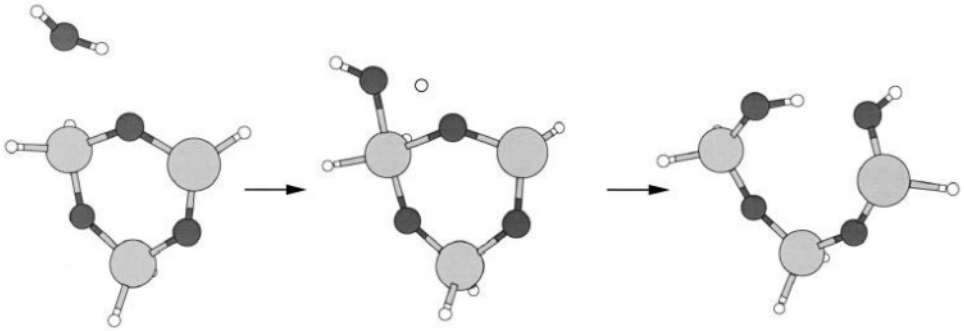

**Figure 63: Hydrolysis of 3-membered siloxane bridge opening as calculated by Walsh *et al*[113]**

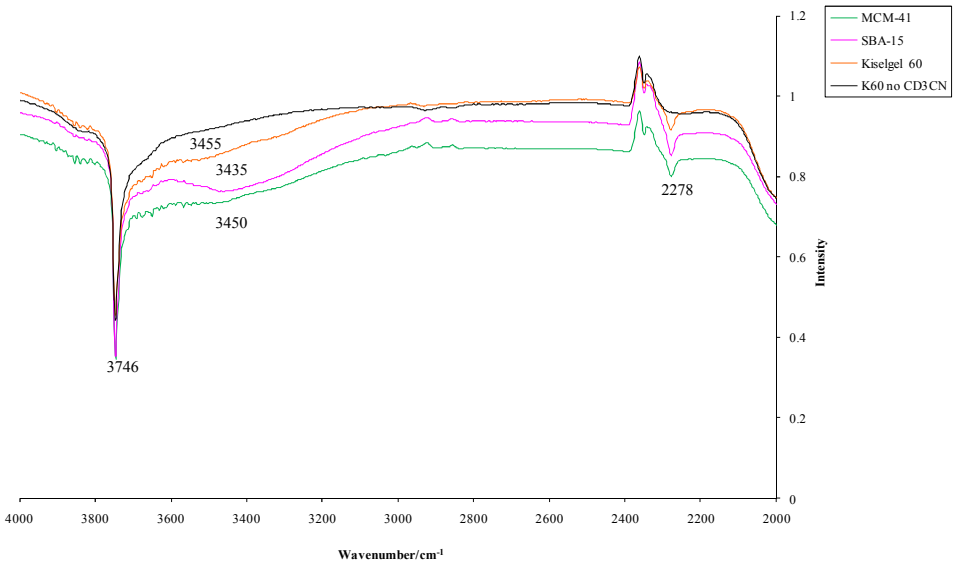


**Figure 64: Infrared Spectra Showing $CD_3CN$ Adsorbed on 3 Silica Samples after heating to 40˚C under flowing $N_2$. The spectrum of the bare Kieselgel 60 (K60) is shown for purposes of comparison**

Despite the relatively weak interactions between acetonitrile-d3 and the silica surfaces, it can be clearly seen that SBA-15 when treated under these conditions has the most hydroxylated surface and is the most acidic. The band in the hydrogen-bonded SiOH region is the most intense of the three and shows the largest shift from the band relating to isolated terminal SiOH. When treated under these conditions Kiselgel 60 and neutral amine templated hexagonal mesoporous silica seem to have similar acidity. The C≡N stretch is not a sensitive enough probe to differentiate between the subtle changes in acidity and the νCN peak position is the same for all three samples.

## 4.2 *In situ* Activation of Samples and Adsorption from the Vapour Phase of Small molecules to Study the Acidity and Hydrophobicity of Silica and the Activity of 3-Aminopropyl Functionalised Silica

The spectra in this section were all recorded at the Polytechnic University of Turin in association with Sonia Fiorelli and Barbara Onida. The equipment available allowed the bare sample to be outgassed under vacuum up to 700˚C whilst in the infrared cell. The sealed cell could then be transferred to the infrared spectrometer and connected to a second vacuum line, where vapours could be adsorbed quantitatively onto the surface or desorbed at room temperature *in situ*. All infrared spectra were recorded as transmission spectra using pressed pellets of the samples. (For further details see Chapter 2.3). In order to provide as fair a possible comparison to those spectra recorded in York, the samples were activated in air up to 700˚C before being pressed into pellets and outgassed in the cell at 120˚Cto remove weakly bound water. This removes the difficulties stated before of samples quickly readsorbing water after the activation and during addition of liquid probe molecules.

Further to the comparison of SBA-15 and HMS using acetonitrile-d3 as the probe. The acidity of each of these silica samples was studied using ammonia and the hydrophobicity by the adsorption of water vapour. Their hydrophobicity was also compared to that of a tri-methylsilyl functionalised HMS (for the preparation of this sample see Chapter 2.1).

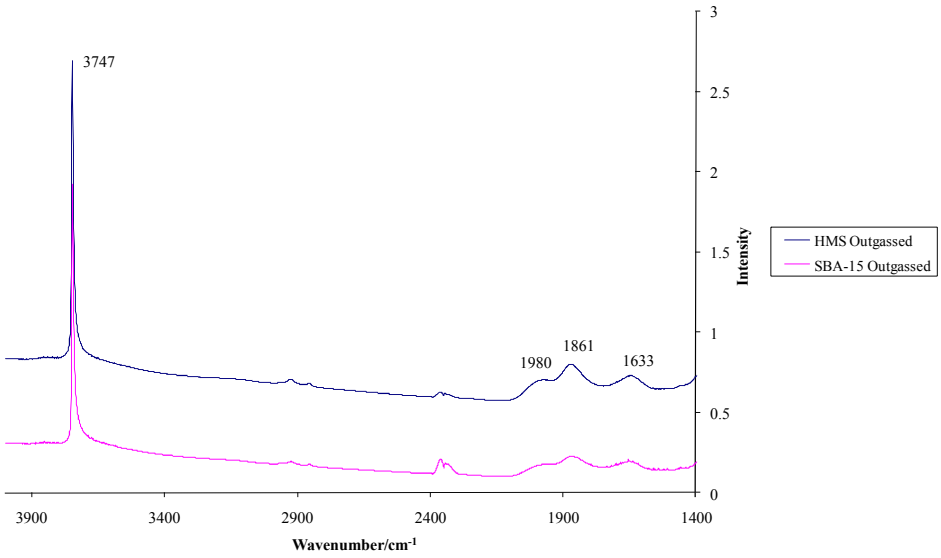


**Figure 65: Infrared spectra of HMS and SBA-15 activated at 700˚C**

After the pre-treatment, the two samples look very similar in the infrared. The bands below 1400 $cm^{-1}$ are not shown because the samples were examined undiluted and the intensity of these bands are off-scale. The only peaks visible in the region of interest are the Si-O-Si and SiOH combination bands (1980-1630 $cm^{-1}$) and the isolated SiOH O-H stretch at 3747 $cm^{-1}$. It is interesting to note that even on these highly dehydroxylated samples, there is still a band at 1633$cm^{-1}$ assigned to a water bending mode,[89] indicating that is still some adsorbed water on the surface.

Many of the spectra showing the changes after adsorption of the probe molecules are given as subtraction spectra. These were calculated by subtracting the spectrum of the outgassed sample from that of the spectrum after each dosage of probe molecule onto the surface. The labels for the different spectra refer to the pressure of gas in the infrared cell.

# Acidity Measurements by $NH_3$ adsorption

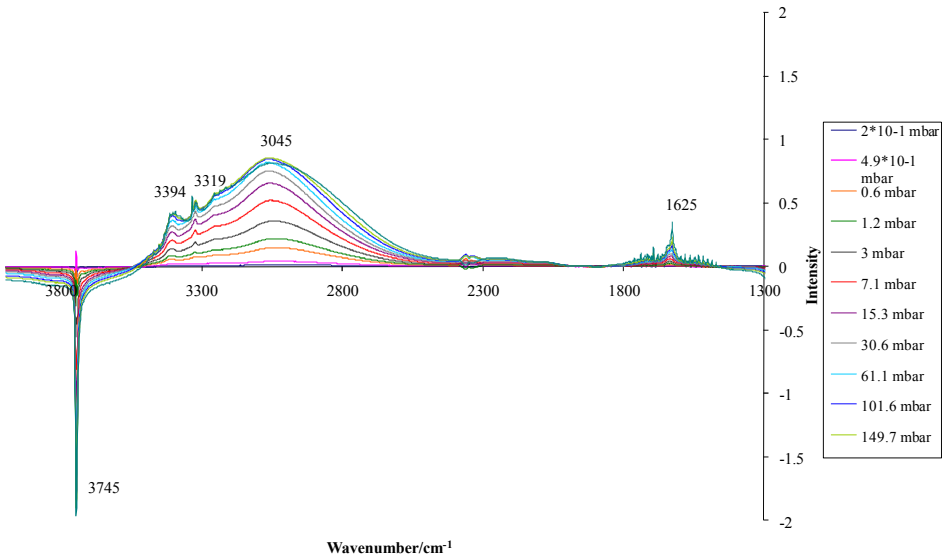


**Figure 66: Difference spectra showing the changes after $NH_3$ adsorption onto HMS activated at 700˚C and then outgassed at 120˚C**

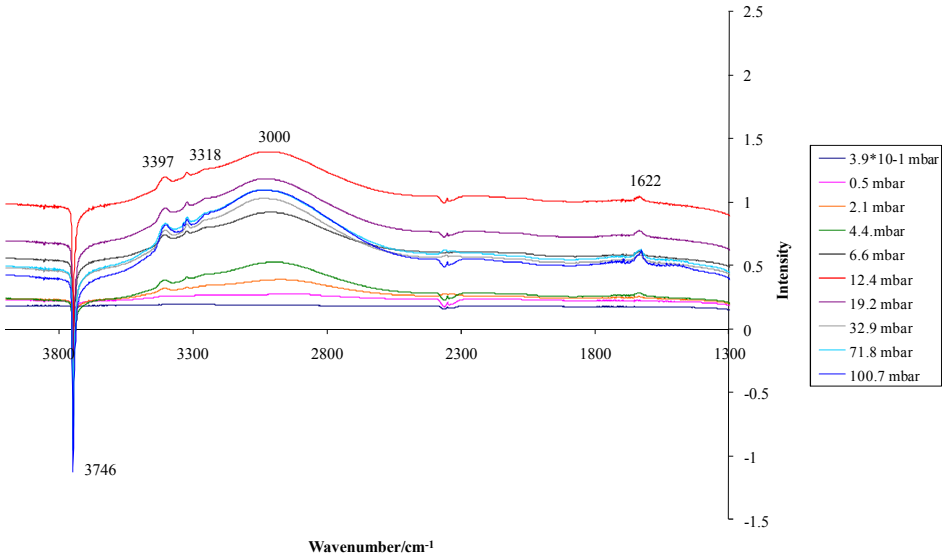


**Figure 67: Infrared difference spectra showing the changes after $NH_3$ adsorption on SBA-15**

The changes in the infrared spectra upon $NH_3$ adsorption are similar for HMS and SBA-15. These are the decrease in the intensity of the isolated SiOH OH stretch peak at 3745 $cm^{-1}$, the appearance of the N-H stretching bands at 3394 $cm^{-1}$ and 3319 $cm^{-1}$ and the N-H deformation at 1625 $cm^{-1}$. This band position does not change on increasing $NH_3$ coverage, demonstrating little or no perturbation of this mode. The major difference between the two samples is in the extent of the shift of the hydrogen bonded SiOH OH stretch from the position of the isolated silanol stretch. At a pressure of 100mbar of $NH_3$, the position of the hydrogen-bonded OH stretch for HMS is 3061$cm^{-1}$ (a difference of 684$cm^{-1}$). For SBA-15 at the same pressure of $NH_3$ the band is at 3032$cm^{-1}$ (a difference of 713$cm^{-1}$). This demonstrates that SBA-15 is more acidic than HMS. The values of around 700 $cm^{-1}$ agree with that found by Cant for a Cabosil silica evacuated at 450°C for 3hrs.[115]

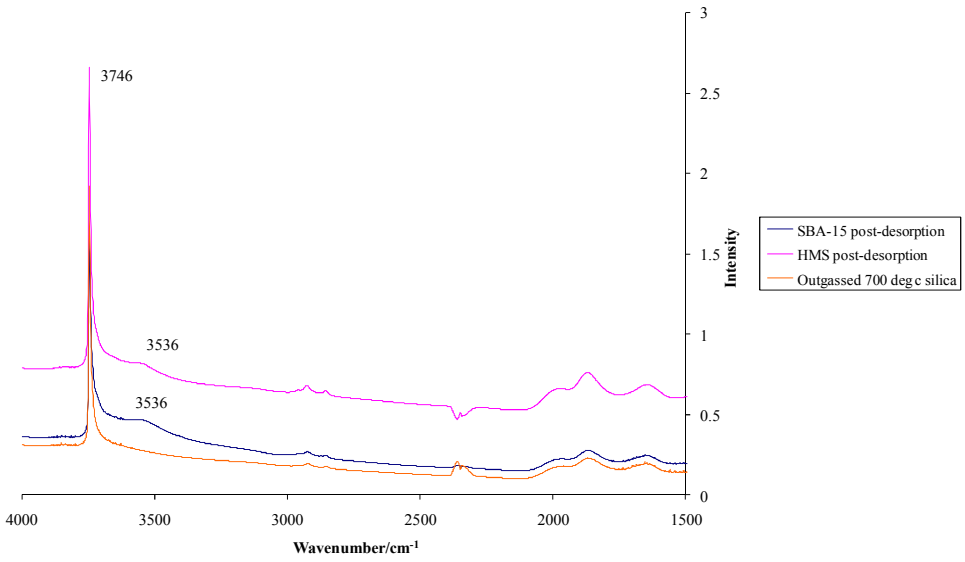


**Figure 68: Infrared spectra comparing the silica samples after desorption of $NH_3$ from the surface with one of the original activated, outgassed samples**

The adsorption/desorption of $NH_3$ on these samples appears to be reversible. As shown by figure 68, all peaks relating to $NH_3$ disappear after the

ammonia is removed from the cell such that vacuum ($10^{-3}$mbar) is again reached. There are also no observable peaks corresponding to chemisorbed $NH_3$ species such as Si-$NH_2$. Si-$NH_2$ has been shown to form on silica gel degassed at 1200°C, either by opening of highly reactive siloxane bridges (reaction scheme 1) or by direct reaction with isolated silanols (reaction scheme 2) shown in figure 69.[39] It was found however in the study by Morrow as in the present study; that the less reactive siloxane bridges present when dehydroxylation occurs under milder conditions do not react with $NH_3$.

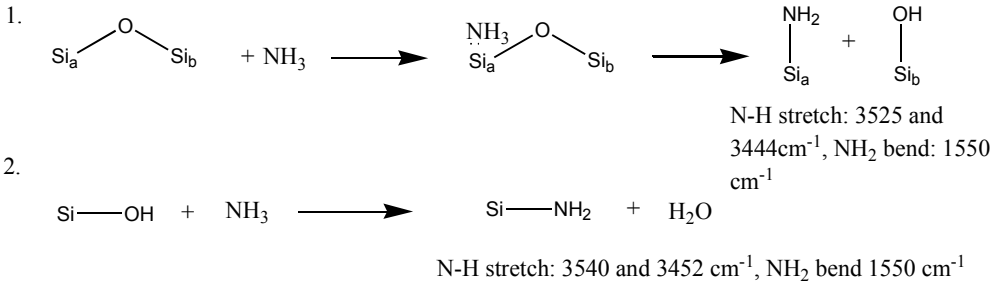


**Figure 69: Possible chemical reactions of $NH_3$ with silica**

However, it can be seen that there is some opening of Si-O-Si bridges, seen from the peak at around 3536 $cm^{-1}$ in figure 68, representing the OH stretch of two interacting SiOH groups. This is thought to be due to trace water present in the sample, this is again in agreement with the literature.[39]

## Hydrophobicity Measurements by $H_2O$ Adsorption

The interaction of silica samples with water vapour was also investigated. The samples being; HMS calcined at 700°C in air and then activated under vacuum at 120°C (denoted HMS 700 °C), SBA-15 treated under the same conditions (SBA-15 700 °C) and a tri-methylsilyl functionalised silica sample produced by co-condensation of TEOS and hexamethyldisiloxane

(HMDS) in a 4:1 molar ratio activated at 120 °C (denoted HMDS silica). The infrared spectra of water adsorption onto and desorption from HMS 700°C are shown as examples in figures 70 and 71.

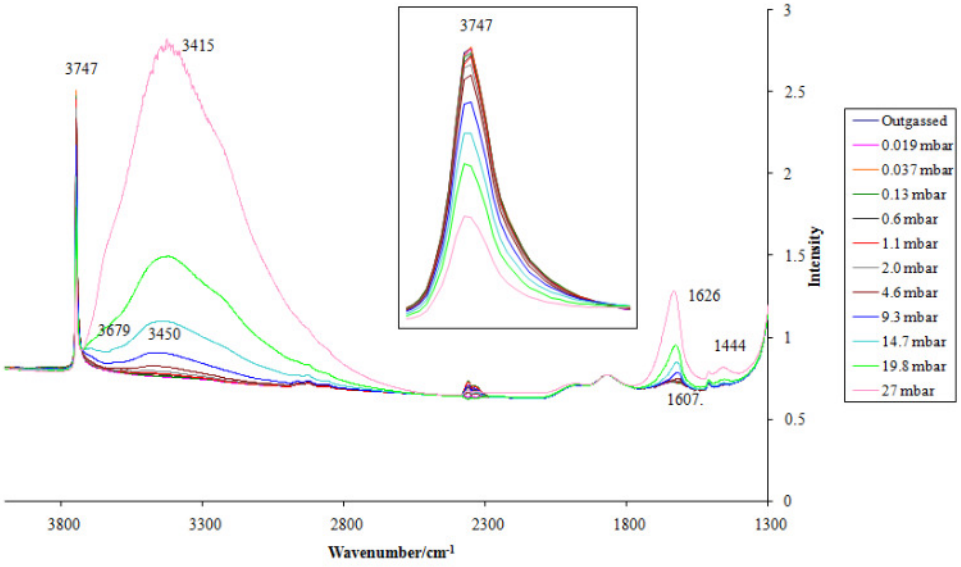


**Figure 70: IR spectra showing the changes during $H_2O$ adsorption on HMS 700˚C (insert shows enlargement of peak at 3747cm$^{-1}$)**

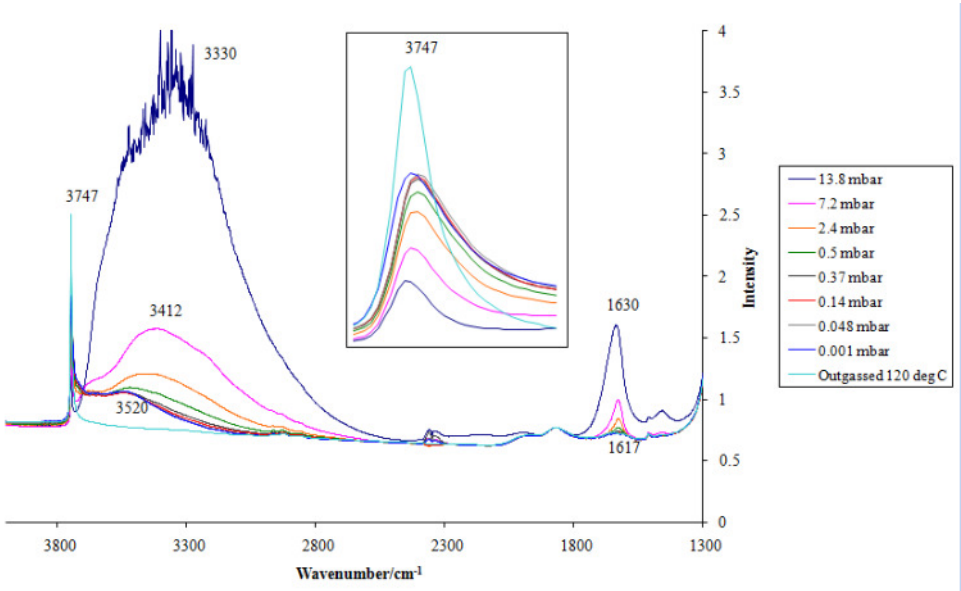


**Figure 71: IR spectra showing the changes during $H_2O$ desorption from HMS 700˚C (insert shows enlargement of peak at 3747cm$^{-1}$)**

In figure 70, it can be seen that the first water species to develop on the surface have bands at around 3679 $cm^{-1}$ and 3450 $cm^{-1}$. The first, corresponds to the OH stretch of hydrogen bonded SiOH.[33] The broad band at 3450 $cm^{-1}$ gradually shifts to around 3410 $cm^{-1}$.This is a combination of the OH stretch of water and a ν1 bend of associated water.[29,33] The water bending mode shifts from 1607 $cm^{-1}$ to 1637 $cm^{-1}$, the first value being close to that of a ν2 bend of an isolated water molecule and the final value representing a perturbed water molecule inside a cluster.[29] The peak at 1444$cm^{-1}$ is thought to be due to trace $NH_3$ in the system because the water vapour study was carried out after the $NH_3$ vapour study.

Figure 71, shows that water adsorption is not reversible. The addition of water opens the siloxane bridges and the broad band at 3520$cm^{-1}$ representing interacting SiOH groups is present even after degassing.

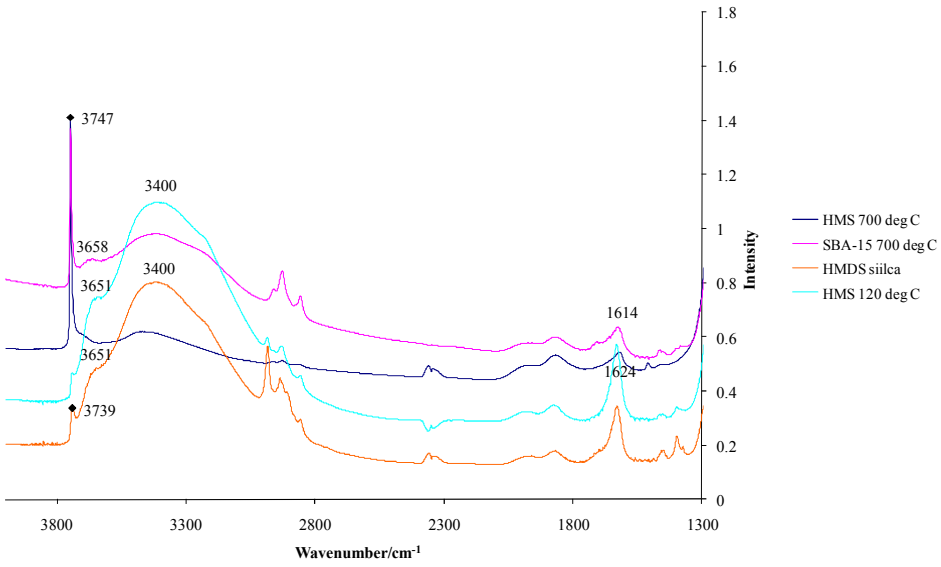


**Figure 72: IR spectra comparing the affects of approximately 7mbar $H_2O$ vapour on different silica samples. HMS 700 deg C= HMS calcined in air at 700˚C, then activated at 120˚C, SBA-15 700deg C= SBA-15 treated as for HMS 700 deg C. HMDS silica= tri-methylfunctionalised silica produced by co-condensation of TEOS and hexamethyldisiloxane in a 4:1 molar ratio and activated at 120˚C under vacuum and HMS 120 deg C= HMS extracted with ethanol under reflux and then activated at 120˚C under vacuum.**

It can be seen from figure 72 that SBA-15 is more hydrophilic than HMS. At this pressure of $H_2O$ vapour, the band relating to hydrogen-bonded silanols (3658 $cm^{-1}$) is present for SBA-15 700˚C but not for HMS 700˚C and the band relating to associated water molecules at around 3450-3400 $cm^{-1}$ is more intense and shifted to lower frequency. The HMS sample that has been extracted with ethanol and activated at 120°C is, as expected, the most hydrophilic sample. It has only a tiny peak representing isolated silanols and a very large and intense band representing associated water. The sample functionalised with tri-methylsilyl groups shows slightly more hydrophobicity but where this hydrophobicity is present in the sample is unclear. These tri-methylsilyl groups may well be present in clusters leaving large areas with free hydroxyl groups. Unlike in a grafted sample, the tri-methylsilyl groups do not cap the active hydroxyl groups on the silica surface.

## 3-Aminopropyl Functionalised HMS

Amine functionalised silica has attracted a great deal of attention as a potential adsorbent for the removal of $CO_2$ from waste gas streams. Current technologies include zeolites, which are water sensitive, limiting their usefulness and liquid amine systems. The liquid amine systems are used aboard space stations and in other closed environments but have been found unsuitable for scale-up and relatively high temperatures are required for the regeneration or the amine.[116] In this study the interactions between 3-aminopropyl functionalised HMS (AMP-HMS) with $CO_2$ and acetone were investigated.

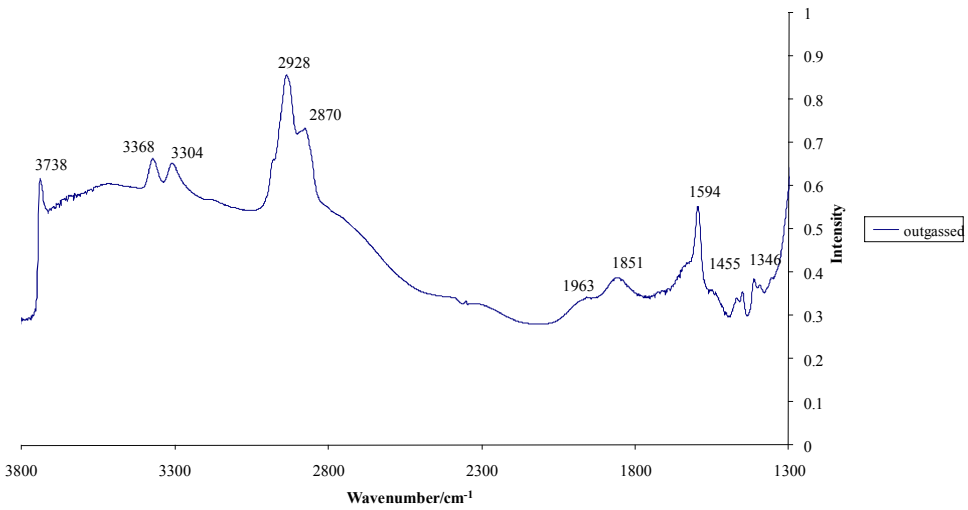


**Figure 73: Infrared spectrum of AMP-HMS outgassed under vacuum at 120˚C**

Figure 73 shows the infrared spectrum of AMP-HMS outgassed under vacuum at 120˚C to remove weakly bound water. As with the other samples, the samples were not diluted so the strong peaks relating to Si-O-Si stretches and Si-OH stretches and bending modes saturate the signal and are not shown. The major peak assignments are given in table 5.

**Table 5: Major peak assignments for AMP-HMS**

| Peak Position/ $cm^{-1}$ | Assignment |
|---|---|
| 3738 | Isolated silanol OH stretch[89] |
| 3520 | v1 or v2 bend associated water molecules[29] |
| 3368 and 3304 | N-H stretch, antisymmetric and symmetric $NH_2$[117] |
| 2928, 2870 | C-H stretch $CH_2$[117] |
| 1963, 1851 | Overtones of Si-O-Si lattice vibrations[118] |
| 1594 | $NH_2$ scissoring |
| 1455 | $CH_2$ scissoring |
| 1346 | $CH_2$ wagging |

## Carbon Dioxide Adsorbed on AMP-HMS

At the high frequency end of the spectra shown in figure 74, the major changes are; a decrease in the intensity of the 3740 $cm^{-1}$ isolated silanol OH stretch, the appearance of a broad band at 3660 $cm^{-1}$ corresponding to the OH stretch of hydrogen bonded silanol groups and a decrease in intensity and shift to lower frequency of the primary amine N-H stretch peaks. This demonstrates that $CO_2$ is adsorbed on both the silanol OH groups and the $NH_2$ groups. The decrease in intensity of the N-H primary amine doublet is accompanied by the formation of a broad, weak band at around 3328 $cm^{-1}$, this corresponds to the N-H stretch of a carbamate species (see figure 76, reaction 1.)[92a] At very high $CO_2$ pressures sharp peaks can be observed in the 3600-3700 $cm^{-1}$ region that seem to relate to rotational-vibrational structure in gaseous $CO_2$.

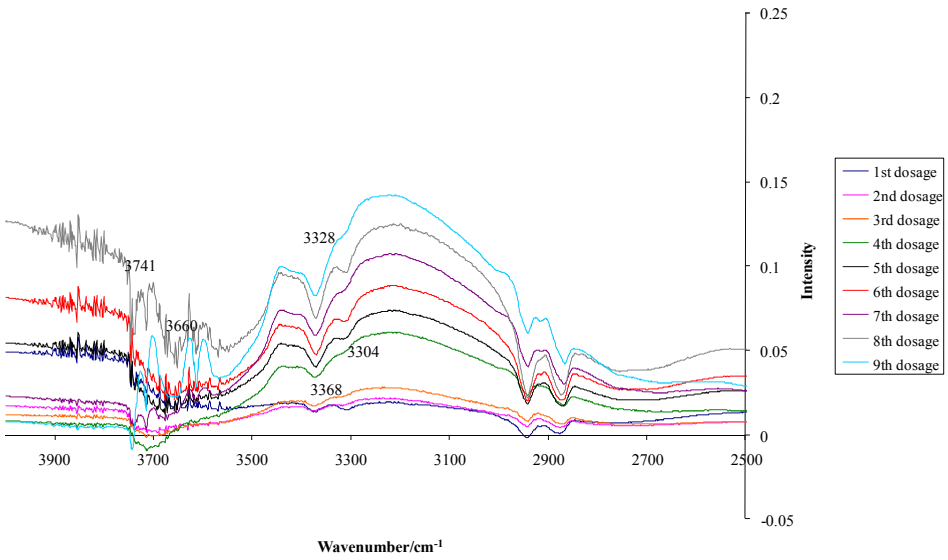


**Figure 74: Difference spectra showing the changes in the high frequency region during $CO_2$ adsorption on AMP-HMS**

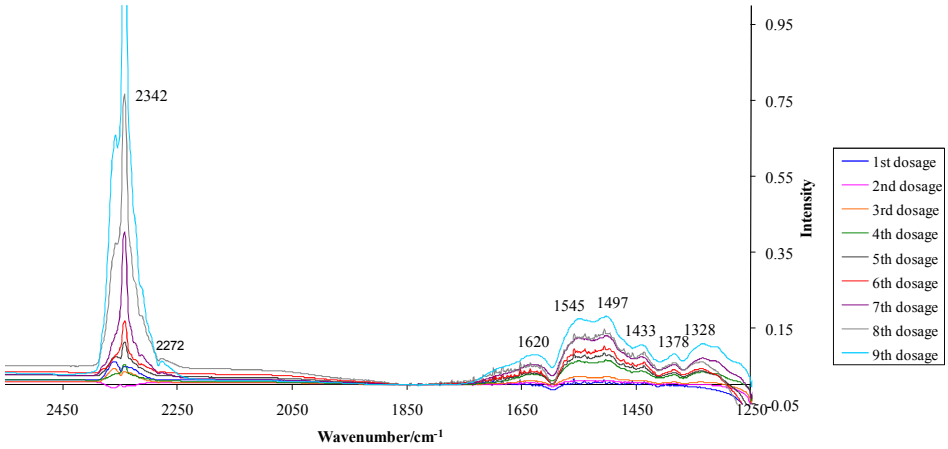


**Figure 75: Infrared spectra showing the changes in the low frequency region during $CO_2$ adsorption on AMP-HMS**

**Table 6: Peak assignments for the low frequency region of $CO_2$ adsorbed on AMP-HMS**

| **Peak Position/ $cm^{-1}$** | **Assignment** |
|---|---|
| 2342 | v3 $CO_2$ adsorbed on $SiO_2$[119] |
| 2272 | v3 $^{13}CO_2$ adsorbed on $SiO_2$[120] |
| 1620 | C=O stretch $NHCO_2^-$ [92a] |
| 1545 | $NHCO_2^-$ + $NH_2$ deformation combination[92a] |
| 1497 | *Monodentate bicarbonate[121] |
| 1433 | *Monodentate bicarbonate[121] |
| 1378 | *Bidentate carbonate[117,121-122] |
| 1328 | *Weakly adsorbed gaseous $CO_2$[117] |

* Tentative assignment

The assignment of bands in the low-frequency region is not straightforward. There is no agreement in the literature as to which species the bands in the 1300-1700$cm^{-1}$ region represent or even as to which species are likely to be present on the surface. The peak assignments given are therefore in some cases tentative.

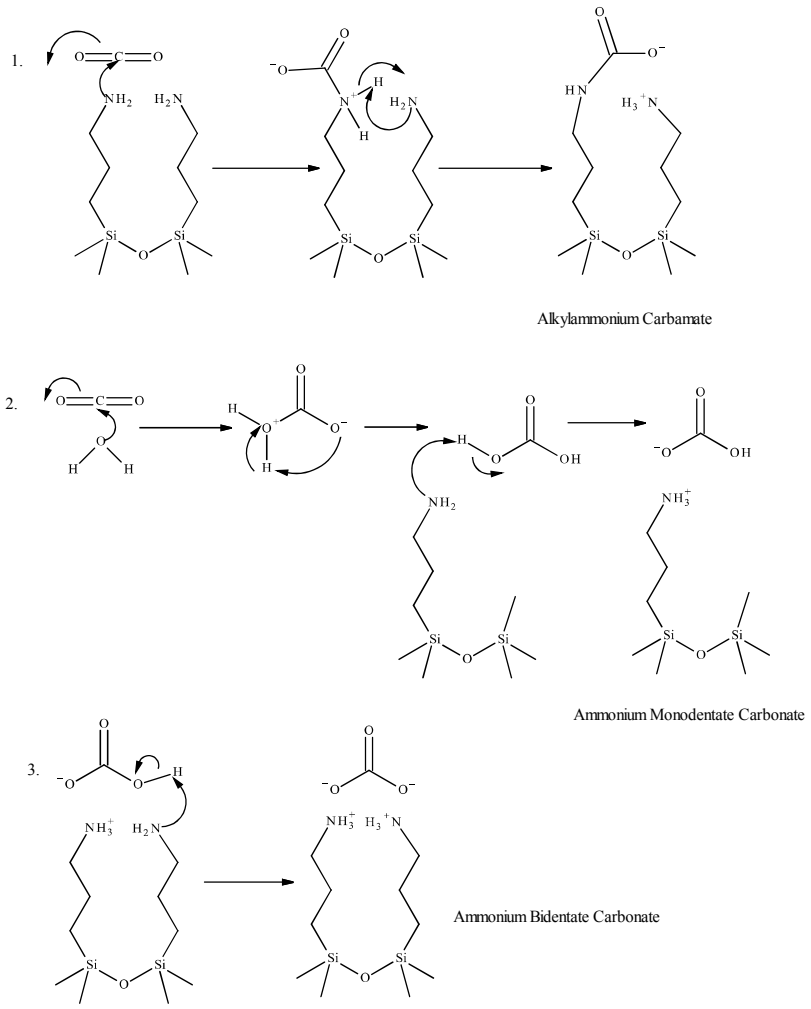


**Figure 76: Scheme showing the reactions of $CO_2$ with AMP-HMS and the species formed**

There is strong evidence in both the N-H stretching region of the spectra and the low frequency region for the formation of carbamate species. This indicates that there must be regions of high amine density on the silica surface. The evidence for the formation of carbonate and bicarbonate species is less strong. In theory, on this sample outgassed at 120°C prior to the measurement there should be no water present. However in the spectrum of the sample before the adsorption of $CO_2$ (figure 73) there is a band in the region corresponding to the bending modes of associated water molecules. It is therefore possible that bicarbonate and carbonate species will form. There are contradictory reports even on this point; in work by Battjes *et al* on

reactions of aminated silane coupling agents with $CO_2$ they assigned all the bands in the 1600-1300 $cm^{-1}$ region to carbamate species, stating that any bicarbonate peaks were in the same region as carbamate peaks and the carbamate peaks masked them.[92a] As did Hiyoshi *et al* in their work on $CO_2$ on aminosilane functionalised SBA-15 even when water vapour was present. It should be noted however, that in the work by this group, the highest concentration of aminosilane (17vol% aminosilane in toluene) was used for the grafting of amine groups onto silica surfaces of any of the literature studies found.[118] So, perhaps this high amine loading had an impact on the species formed after $CO_2$ adsorption.

In other studies, such as those by Huang[117] on amine functionalised MCM-48 and Leal[122a] on amine grafted Davison grade 62 silica gel an enhanced (doubled) uptake of $CO_2$ was observed when water vapour was added to the system consistent with the proposed reaction mechanism 2 in figure 76. However, Harlick and Sayari, in their work on triamine grafted pore-expanded MCM-41 found only about an 8% increase in $CO_2$ adsorption capacity when the material was exposed to a moist vapour stream compared to a dry stream.[123] In order to help identify the species formed Khatri *et al*[121] adsorbed $CO_2$ with $D_2O$ vapour onto amine-grafted SBA-15 and proposed the species shown in figure 77.

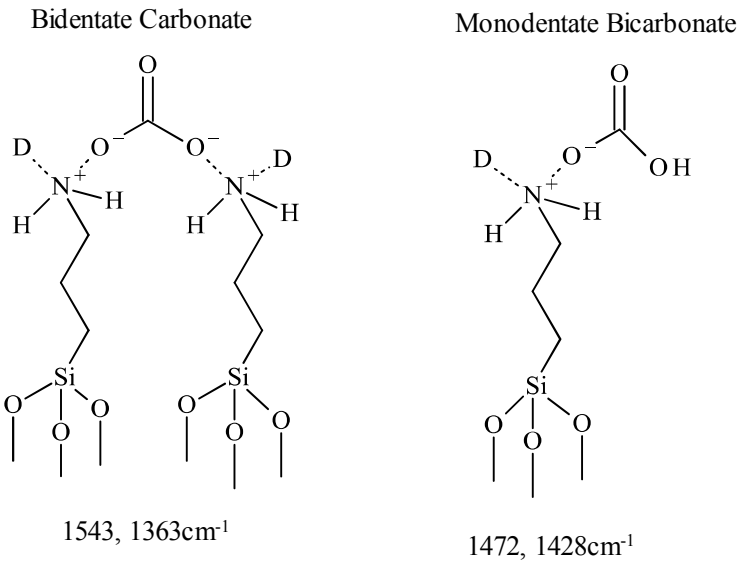


**Figure 77: Species formed by adsorption of $CO_2$ onto amine –grafted SBA-15 in the presence of $D_2O$ as proposed by Khatri[121]**

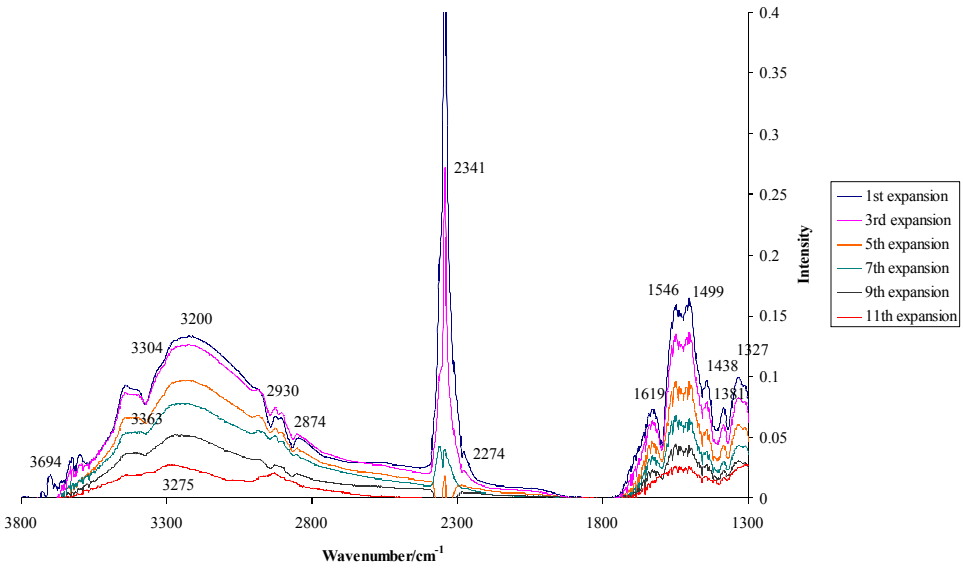


**Figure 78: Infrared difference spectra showing the changes during $CO_2$ desorption from AMP-HMS**

It can be seen from figure 78 that the adsorption/desorption of $CO_2$ on AMP-HMS appears to be reversible even at room temperature. Evidence for this is scarce in the literature. In the majority of studies $CO_2$ is removed from the amine-functionalised surface at raised temperature (70-150°C).[116-118,121-122,122c,123-124] In work by Wang on polyethylenimine functionalised SBA-15, it was found that $CO_2$ was difficult to remove from the surface at room temperature. However, in that study it was also found that the adsorption of $CO_2$ was much more efficient at 75°C due to increased movement of the polymer chains.[125]

There are a great many differences in the literature between the methods used for preparing amine-grafted silica gels and the conditions under which $CO_2$ is adsorbed onto the surfaces. These include; differences in the nature of the support material, the most popular materials are SBA-15,[116,118,121,122c] MCM-41[123,126] and MCM-48.[117,124a] Also whether the surface was dried or not before the grafting or if water was included in the grafting reaction mixture. In the majority of studies monoamine silanes were used [117-118,121-122,122c,124a] but in other cases diamine silanes or[116] triamine silanes[123] were used. The concentrations of aminosilanes used in the grafting reaction also varied from 2% amino silane/g silica[123] to 10% amino silane/g silica.[117]

A higher surface amine concentration does not necessarily lead to a higher $CO_2$ uptake. After a certain point is reached, steric hindrances and/or overloading phenomena leading to inefficiencies in the $CO_2$-amine have been employed as explanations for the experimentally observed plateaus in surface amine concentration/ $CO_2$ uptake plots.[123] The addition of water when grafting amine groups onto silica surfaces has been shown to increase the concentration of amine groups that can be grafted onto a silica surface. This is for two reasons, firstly that it increases the number of surface SiOH groups and secondly that it initiated the hydrolysis of the alkoxy groups. Proposed surface structures for grafting with and without the presence of water are shown in figure 79.

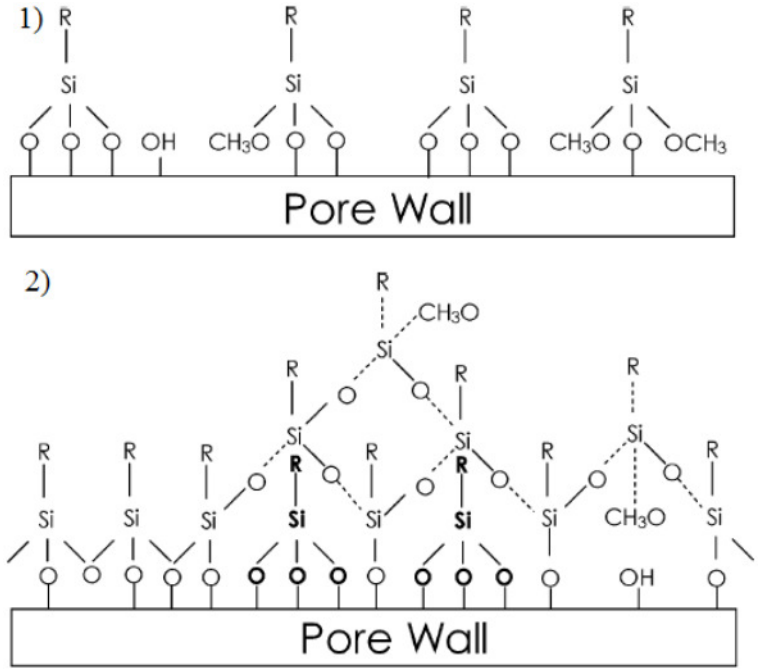


**Figure 79: Proposed surface structures for silica surfaces grated with aminosilanes, where "R" represents the amino groups and the bulk silica is represented by "pore wall". 1) represents grafting under anhydrous conditions and 2) when water is added to the reaction mixture**

Other differences include the temperatures at which $CO_2$ was adsorbed, the extent to which pre-adsorbed $H_2O$ and $CO_2$ were removed prior to $CO_2$ adsorption experiments and whether or not the $CO_2$ was adsorbed under anhydrous conditions or in the presence of water vapour. With all these experimental differences it is not particularly surprising that there should be disagreement regarding the concentration of $CO_2$ that may be adsorbed and the species that are formed.

The major difference between all of the experiments reported in the literature on $CO_2$ adsorbed on amine functionalised silica and the present study is that all of the previous samples were produced by manufacturing the silica support and then adding the amine, either by impregnation[127] or as in the majority of cases, by grafting. In this study however, the amine functionalisation was added during synthesis of the HMS by co-condensation of 3-aminopropyl trimethoxysilane and tetraethyl orthosilicate

in a water/ethanol solution in the presence of n-dodecylamine as a template (see Chapter 2.1). This means that under the mild drying conditions employed; room temperature for drying of the extraction solvent and then activation at 120˚C under vacuum prior to the IR measurements, that there will still be a great number of surface silanol groups present as well as surface amine groups. From infrared spectroscopy and elemental analysis data, Macquarrie *et al* also found around 1.5 unreacted ethoxy groups per amino-propyl chain in similar co-condensed amino-propyl functionalised HMS.[7] From the current infrared data there also seems to be some surface water still present despite the drying (figure 73). Also, the amine groups do not necessarily have to be present at the surface, some will most likely form part of the bulk silica and be inaccessible to $CO_2$. So, it would be difficult to make any correlation between the concentration of 3-aminopropyl trimethoxysilane used in the mixture and the level of $CO_2$ uptake by the resulting adsorbent. It is likely that grafted samples will have a much greater concentration of amine groups accessible to $CO_2$ and permit a greater level of control over the surface hydration.

Though amine functionalised silicas have attracted a great deal of attention as $CO_2$ adsorbents, this particular sample produced by co-condensation does not seem to adsorb a great deal of $CO_2$. After the 4$^{th}$ dosage (which corresponds to a pressure of 5 mbar of $CO_2$) there is not really any change in the 1800-1300 cm$^{-1}$ region of the spectrum up to the 9$^{th}$ dosage (200 mbar).

## Acetone Adsorbed on AMP-HMS

Acetone was adsorbed by increments onto the surface of the amine functionalised HMS and after the last adsorption the sample was heated to 120°C under vacuum for 30 mins before the desorption spectra were recorded.

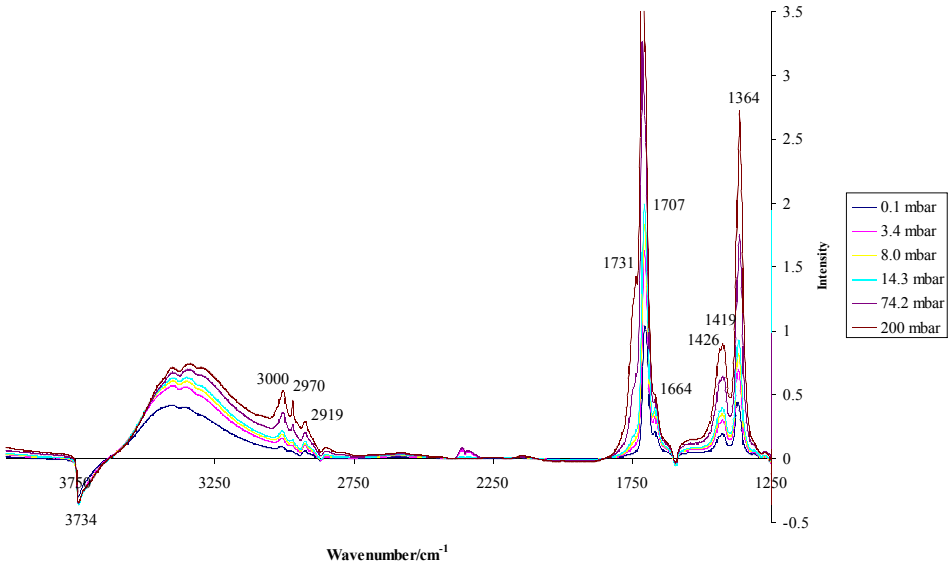


**Figure 80: Infrared difference spectra showing acetone adsorption onto AMP-HMS**

The infrared spectra of acetone adsorbed on AMP-HMS shown in figure 80 demonstrate two different frequencies for the C=O stretch of acetone. The main C=O stretch corresponds to that of liquid acetone, a much less intense band at 1730 $cm^{-1}$ only really observed at higher acetone pressures corresponds to gaseous acetone. This seems to suggest that not all the acetone present is adsorbed on the surface. The bands between 1430 $cm^{-1}$ and 1360 $cm^{-1}$ represent CH deformation modes. A particularly interesting feature is the formation of an imine. This is slightly unexpected because it is generally assumed that acetone is not particularly reactive with amine

functionalised silica at room temperature. The peak assignments are given in table 7

Also in the work by Macquarrie and co-workers on amine-functionalised HMS samples formed by co-condensation; the catalytic activity of the materials was tested by the rate at which the amine group reacted with benzaldehyde at room temperature to give the imine and their ability as catalysts for the Knoevenagel condensation. They found significant differences in the properties if the materials depending on the ethanol:water ratio used in the reaction mixture. It was found that those materials formed in a 50:50 ethanol:water mixture like the material used in the present study showed anomalous behaviour in both their structural properties and catalytic activity. They had some large irregular particles as well as the normal spherical particles and were extremely sluggish in the test reactions.[7] This indicates that the mechanism of formation of a co-condensed amino propyl-HMS is somewhat different to the normal behaviour of HMS systems.

In this study however, the formation of an imine when the AMP-HMS was reacted with acetone suggests a high level of activity. Although it was not published, efforts by S. Taverner and D.Macquarrie to adsorb Reichardt's dye onto silica using acetone as a solvent produced inconsistent results, not observed when DCM was used as the solvent.[93] This lead to speculation that acetone may react with silica surfaces. So, it is possible that the activity with acetone is an anomaly and other ketones would not show the same behaviour.

**Table 7: Peak assignments for acetone adsorbed on AMP-HMS**

| Peak Position/cm$^{-1}$ | Assignment |
|---|---|
| 3734 | Isolated silanol OH stretch |
| 3000 | C-H stretch |
| 2970 | $CH_2$ C-H stretch |
| 2919 | $CH_2$ C-H stretch |
| 1731 | C=O acetone gaseous[124b] |
| 1707 | C=O acetone liquid[124b] |
| 1664 | Imine C=N |
| 1426 | CH deformation |
| 1419 | CH deformation |
| 1364 | CH deformation |

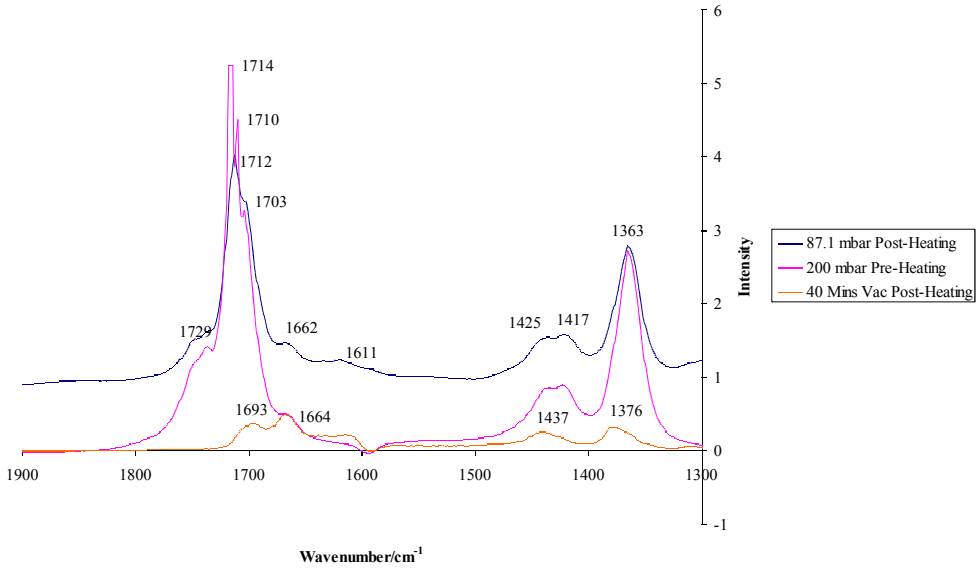


**Figure 81: Difference spectra showing the changes after heating at 120°C -acetone adsorbed on AMP-HMS**

The main points to note from the infrared spectra of acetone adsorbed on AMP-HMS post-heating (figure 81) are the number of different frequencies for the C=O stretch. As in figure 75 for $CO_2$, figure 81 shows bands relating to liquid and gaseous acetone. Also observable are bands relating to hydrogen bonded acetone, most likely on silanol groups, both weakly bonded on isolated silanols and more strongly adsorbed on hydrogen bonded or paired silanols.[128] It can also be seen that some acetone is irreversibly adsorbed, the imine band does not disappear, nor do the CH deformation peaks and the strongly hydrogen bonded C=O peak after evacuation of acetone from the cell. The peak assignments are given in table 8.

**Table 8: Peak assignments of the changes after heating and acetone desorption from AMP-HMS**

| **Peak Position/cm$^{-1}$** | **Assignment** |
|---|---|
| 1729 | C=O acetone gaseous[124b] |
| 1714-1712 | C=O acetone liquid[124b] |
| 1703 | C=O acetone hydrogen bonded on isolated SiOH (weak)[128] bonding |
| 1693 | C=O acetone hydrogen bonded on SiOH (strong)[128] |
| 1662-1664 | Imine C=N |
| 1611 | Conjugated C=C or C=O[129] |
| 1437 | CH deformation[130] |

| | |
|---|---|
| 1425 | CH deformation[130] |
| 1417 | CH deformation[130] |
| 1376 | CH deformation[130] |
| 1363 | CH deformation[130] |

The weak band that appears at 1611cm$^{-1}$ in figure 81 after heating of the sample is in the correct position for either a conjugated C=C or C=O stretching vibration. This may indicate either the formation of a closely interacting layer of acetone on the surface or possible conversion to other species. Zaki and co-workers found that acetone was converted to mesityl oxide on alumina and silica-alumina but not silica via a series of reaction steps. These were a keto-enol conversion to the enolate, followed by addition to another acetone molecule to give diactone alcohol and finally a dehydration to give mesityl oxide. Mesityl oxide does have a νC=O band at around 1615cm$^{-1}$. Their mechanism to reach this species required $Al^{3+}$ and vacancy sites[124b] but it may be possible that the amine and hydroxyl group sites may together be sufficiently active to convert the acetone into a silyl enol ether or a stabilised enolate species.

Since in practically all of the work carries out in the literature on amine-functionalised silica samples different conditions are used every time, it is difficult to make comparisons between the current work and that reported in the literature. This AMP-HMS clearly reacts with both $CO_2$ and acetone to produce a number of different surface species. It would be interesting to study the adsorption of $CO_2$ and acetone on AMP-HMS samples prepared with different ethanol:water ratios to see if greater adsorption and higher or different reactivity could be observed.

# 4.3 Variable Temperature DRIFTs Studies on Metal Oxides using Deuterated Acetonitrile and Benzonitrile as Probes

As covered briefly in section 4.1, nitriles are popular infrared probes for surface acidity. They are weak Lewis bases and can interact via σ-charge release from the nitrogen lone-pair with any kind of charge withdrawing sites. Interaction with a surface acid group (either Lewis or Brönsted) is observed by an increase in the spectral frequency of the νC≡N vibration (ΔνCN). This ΔνCN depends on the degree of donor-acceptor transfer. To prevent complications from splitting due to Fermi resonance effects $CD_3CN$ is preferred to $CH_3CN$.[44a] In liquid $CD_3CN$ the νCN band is observed at 2262 $cm^{-1}$, this is slightly different to the νCN band of gaseous $CD_3CN$, which is at 2252 $cm^{-1}$.[111]

Unlike many of the other probes used in section 4.1, nitriles do not show strong, broad peaks that overlap with the hydrogen-bonded SiOH stretching band in the 3600-3000$cm^{-1}$ region. They can also be added to the sample easily from the liquid phase, an important consideration for carrying out the experiments at York without the equipment available in Turin. These features coupled with the ability of acetonitrile-d3 to distinguish between silica samples of different acidity prompted the investigation of acetonitrile-d3 adsorption on other metal oxides. However, on surfaces more active than silica, acetonitrile and its deuterated equivalent can undergo a number of reactions depending on the properties of the surface, these were discussed by Morterra *et al* and are shown in figure 82.[44]

For this reason, benzonitrile was also used as a probe on the zeolite surfaces studied, which showed the most complex behaviour.

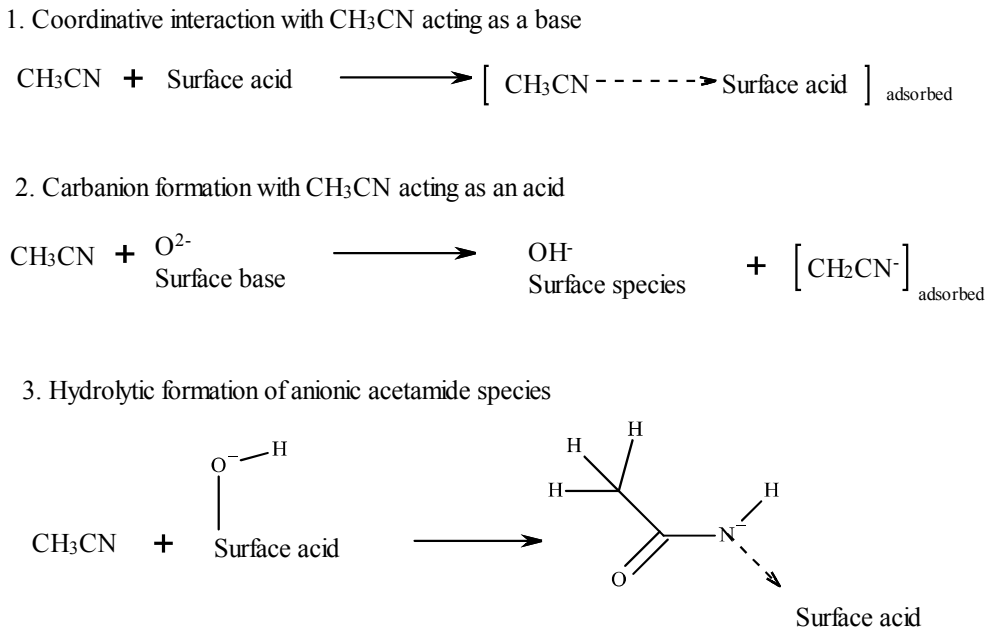


**Figure 82: Possible reactions of acetonitrile adsorbed on a surface**

In this study, $CD_3CN$ was adsorbed onto the surfaces of, basic activated Brockmann alumina, zirconia + 13% alumina, ZSM-5 $SiO_2$:$Al_2O_3$ = 280, ZSM-5 $SiO_2$:$Al_2O_3$ = 30 and 13x molecular sieve in a weight ratio of 10 parts metal oxide to 1 part $CD_3CN$. Prior to the adsorption, the metal oxides were activated at 700˚C for 4 hours. Each sample was then placed undiluted into the environmental chamber of the Brüker Equinox 55 FT-IR, sealed and placed under a 100ml/min flow of nitrogen and heated *in situ*. The bare metal oxide was run as a blank sample to determine the effect of the drying process on the surface before the sample with adsorbed $CD_3CN$ was run. For further details see Chapter 2.3.

In this section the spectra showing the changes after $CD_3CN$ and benzonitrile adsorption are shown as subtraction spectra. The bare metal oxide was placed in the sample chamber and heated under 100ml/min $N_2$ up to around 300˚C and infrared spectra were recorded every 30˚C.The sample with the adsorbed probe was then studied under the same conditions and the

spectrum of the bare metal oxide was subtracted from that of the metal oxide with the probe at each temperature.

## Basic Activated Brockmann Alumina

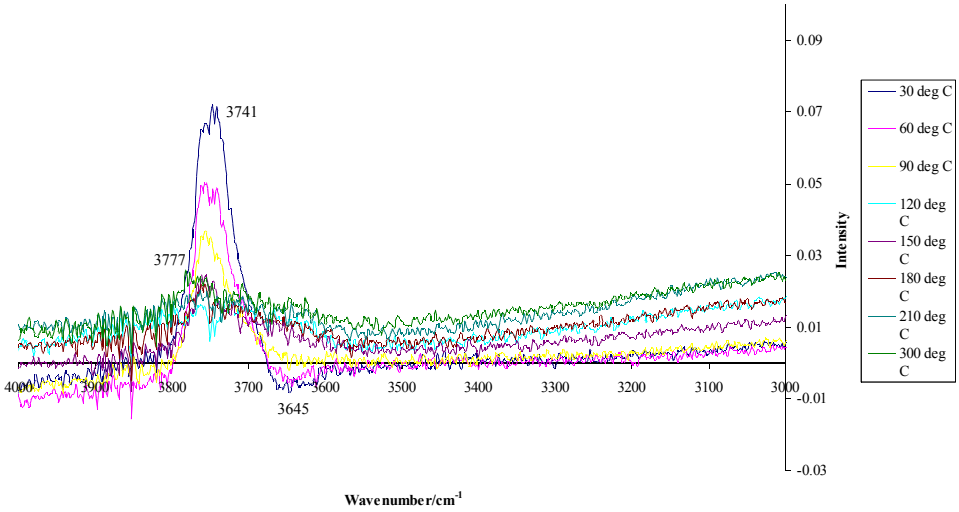


**Figure 83: Infrared subtraction spectra showing the OH stretch region of $CD_3CN$ adsorption onto activated basic Brockmann alumina and then desorption under flowing $N_2$ up to 300˚C**

Due to the almost complete saturation of the infrared signal it is difficult to determine the impact of the adsorption of $CD_3CN$ on the OH stretching region. Diluting the sample with KBr in various ratios was tried but it was not possible to strike a proper balance between being able to observe the weak C≡N bands and the OH stretch region in detail. The undiluted sample was therefore chosen to ensure fair comparison between the different metal oxides under study and to remove any possible interaction with the KBr diluent. So, the changes shown in the OH stretch region in figure 83 may not provide the entire picture.

In the OH stretch region (3800-3000 $cm^{-1}$) in figure 83, after the adsorption of $CD_3CN$ the negative band at 3741$cm^{-1}$ assigned to surface OH groups free from hydrogen bonding.[131] This is gradually restored as the $CD_3CN$ is

desorbed. A positive band at 3645cm$^{-1}$ is observed at high $CD_3CN$ coverage. This corresponds to hydroxyl groups undergoing relatively weak hydrogen bonding. At high desorption temperatures a second, rather indistinct negative band is observed that at 300°C shifts to around 3777cm$^{-1}$. This is assigned to so-called "basic" OH species. These are thought to be terminal OH groups in the coordination sphere of an $Al^{3+}$ ion with tetrahedral coordination carrying a coordinative vacancy.[132] As can be seen this is not fully restored even at 300°C indicating strong adsorption on this site.

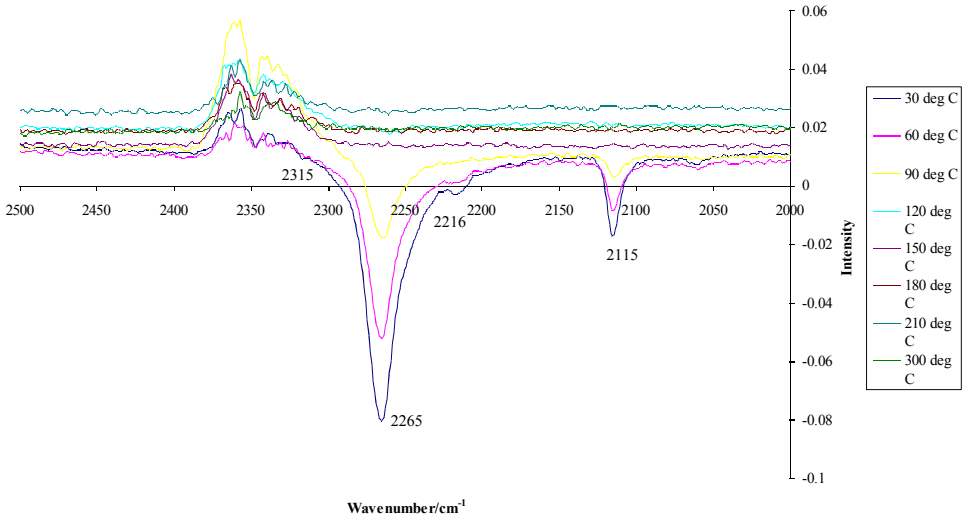


**Figure 84: Infrared subtraction spectra showing the νCN region of $CD_3CN$ adsorbed on basic Brockmann alumina**

The position of the νCN band on this basic alumina sample shown in figure 84 is 2265 cm$^{-1}$, a ΔνCN of only 3 cm$^{-1}$ from the liquid $CD_3CN$ position. [44b] A second slight feature is observable at high coverage at 2315cm$^{-1}$, unfortunately it is somewhat masked by the bands due to $CO_2$ in the beam path. This was assigned to the νCN mode of $CD_3CN$ interacting through the nitrogen lone pair with Lewis acid sites (coordinatively unsaturated surface $Al^{3+}$ ions. Also observable in figure 84 is a second band at 2117 cm$^{-1}$. This is the $\nu_S(CD_3)$ band position for either hydrogen bonded $CD_3CN$ or a

physisorbed liquid-like state.[45]. The feature observable at 2216cm$^{-1}$ at high coverage may be due to the νCN of a polymeric carbanion species, formed by reaction 2 in figure 82. However, this is only a tentative assignment.

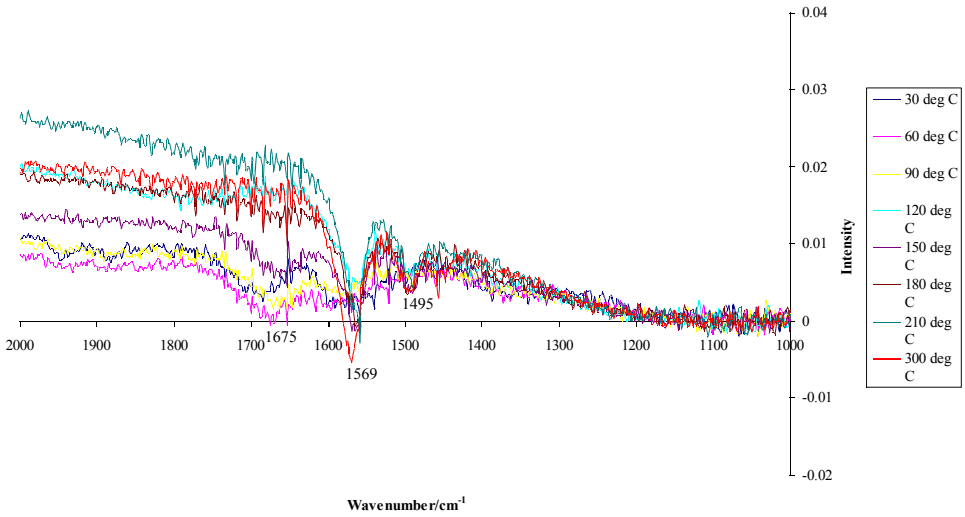


**Figure 85: Infrared subtraction spectra showing the region characteristic of acetamide formation after $CD_3CN$ adsorption onto basic activated Brockmann alumina**

Figure 85 shows three weak bands, those at 1495cm$^{-1}$ and 1569cm$^{-1}$ visible even after desorption at 300°C are characteristic of acetamide species. These are most likely formed by a hydrolytic process catalysed by the "basic" OH species absorbing at 3777cm$^{-1}$.[131] At high coverage (low temperatures) these terminal OH groups are trapped by Lewis coordination of $CD_3CN$. The formation of this acetamide species explains why this band is not restored after heating. The third band at 1675cm$^{-1}$, shifting to 1663cm$^{-1}$ at 150°C is most likely due to a secondary species resulting from the solvation by water of acetamide-like anions.[133] The fact that this peak disappears above 150°C provides some corroboration for this assignment.

## Zirconia +13% Alumina

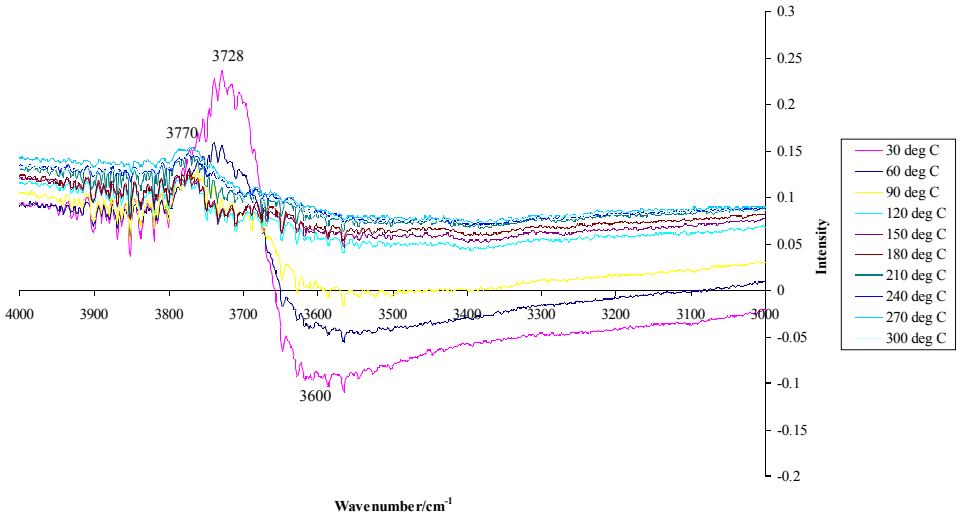


**Figure 86: Infrared subtraction spectra showing the OH stretch region of $CD_3CN$ adsorbed on zirconia + 13% $Al_2O_3$**

In figure 86 the negative bands at 3770 $cm^{-1}$ and 3728$cm^{-1}$ are assigned to hydrogen-bonding free terminal hydroxyl and di-bridged hydroxyl groups respectively. Another peak that may appear in this region is that assigned to tri-bridged hydroxyl groups at ~3685$cm^{-1}$.[134] The band for di-bridged hydroxyl groups is restored by the time that the temperature reaches 90°C, however that for terminal hydroxyl groups is not restored even at 300°C. At high coverage of $CD_3CN$ a broad positive band centred at around 3600$cm^{-1}$ is formed due to hydrogen-bonded hydroxyl groups.

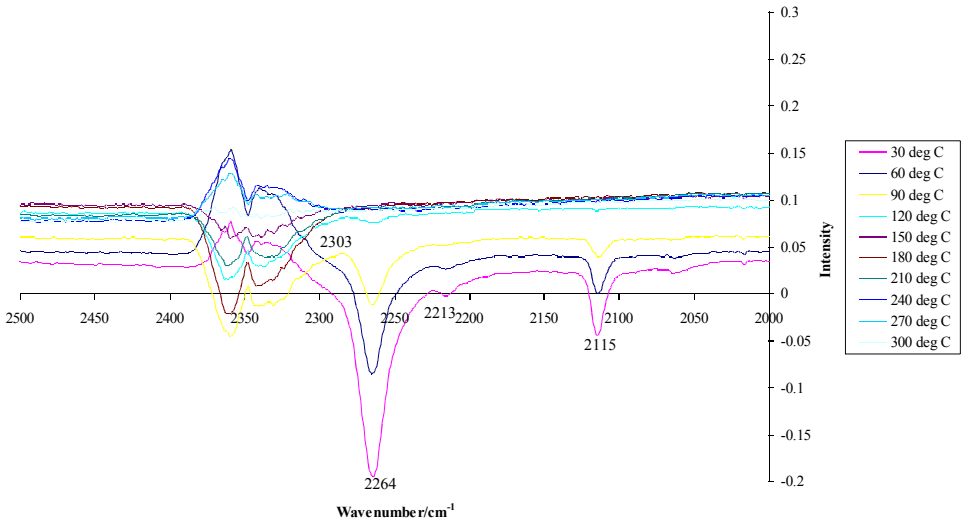


**Figure 87: Infrared subtraction spectra showing the νCN region of $CD_3CN$ adsorbed on zirconia + 13% $Al_2O_3$**

As shown in figure 87, at high $CD_3CN$ coverage, as on alumina, the main peak is at 2264cm$^{-1}$ representing the νCN for hydrogen-bonded or liquid like $CD_3CN$. This is accompanied by a shoulder to high frequency at about 2303cm$^{-1}$. This is assigned to Lewis coordinated $CD_3CN$ (the surface Lewis sites being coordinatively unsaturated $Zr^{4+}$ ions).[44b] The $\nu CD_3$ peak is again visible at 2115cm$^{-1}$ as well as the peak at 2213cm$^{-1}$ attributed to polymeric carbanion species formed on the surface as before.

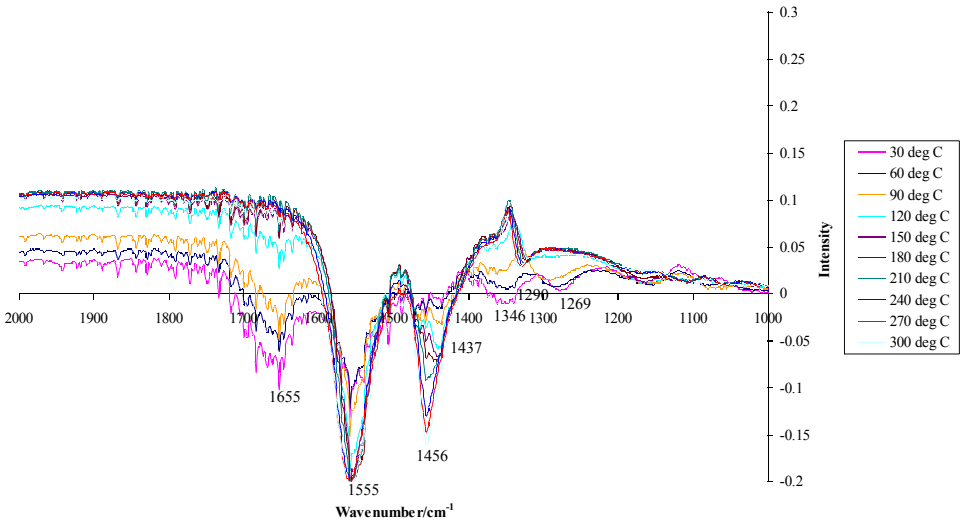


**Figure 88: Infrared subtraction spectra showing the 1000-2000cm$^{-1}$ region of $CD_3CN$ adsorbed on zirconia + 13% $Al_2O_3$**

Figure 88 shows the characteristic peaks for acetamide species forming on a zirconia surface.[44,135]

Aboulayt *et al* postulated the existence of two different acetamide species forming on a zirconia surface. The first designated α, is independent of the surface hydroxyl concentration or type. The second, β, was initially postulated to be formed by the slow reaction of coordinated water with Lewis coordinated acetonitrile.[135] Morterra *et al* refined this hypothesis in light of their data and stated that the formation of β type acetamide species requires the presence of free "basic" terminal OH species, those that absorb at around 3775cm$^{-1}$.[44b]

As on the alumina sample, the band at 1650cm$^{-1}$ is assigned to solvation by water of acetamide-type anions, this band is eliminated by 150˚C. The bands at 1555cm$^{-1}$ and 1456cm$^{-1}$ however grow in intensity up until the final temperature reached in this experiment. These are assigned to β type acetamide species. The fact that these species grow as the experiment progresses corroborates the hypothesis that these are produced by a

relatively slow reaction. The band at 1437cm$^{-1}$, which is masked at higher temperatures by that for the β acetamide is due to α acetamide species. The bands at 1346cm$^{-1}$, 1290cm$^{-1}$ and 1269cm$^{-1}$seem to be due to some surface carbonate species.[44b]

## Zeolite ZSM-5 $SiO_2$:$Al_2O_3$=280

There are a larger number of different surface groups on zeolites than on the single metal oxides shown previously. These include silanol groups, bridging Si-OH-Al groups (Brönsted sites) and Lewis sites. This makes the infrared spectra of $CD_3CN$ adsorbed on zeolite surfaces even more complex to interpret. Figure 89 shows the OH stretch region after $CD_3CN$ adsorption on zeolite ZSM-5 $SiO_2$:$Al_2O_3$= 280 (hereafter referred to as ZSM-5 280).

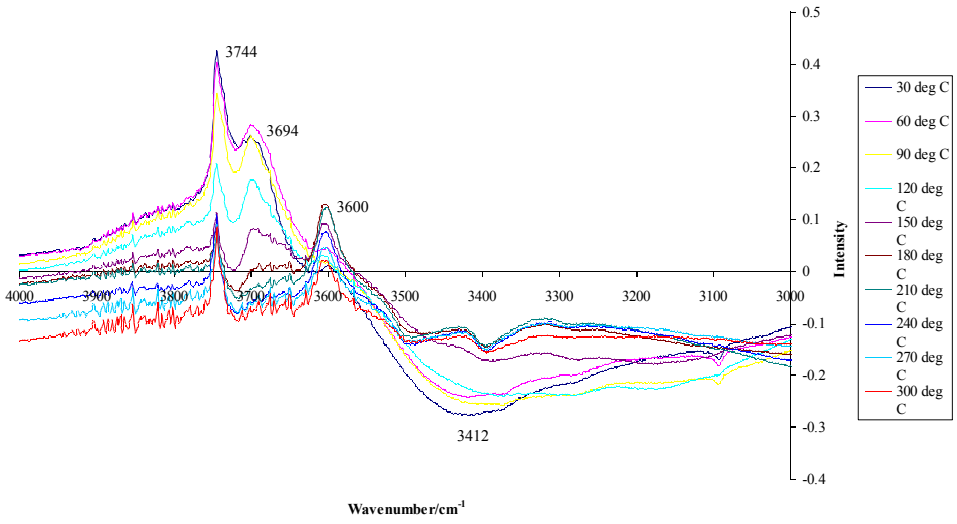


**Figure 89: Infrared subtraction spectra showing the vOH region of $CD_3CN$ adsorbed on ZSM-5 280 and desorption under flowing $N_2$**

The negative bands at 3744cm$^{-1}$ and 3694cm$^{-1}$ represent terminal SiOH groups and OH groups on Al species respectively. The band at 3600cm$^{-1}$ that becomes increasingly negative as the band relating to Al-OH groups is

restored, is assigned to Brönsted sites (Si-OH-Al) species.[41] The band at 3744cm$^{-1}$ is not entirely restored even at 300°C indicating that some species remain associated with it. The band relating to AlOH groups is restored by about 210°C. It is at about this temperature that the Brönsted site band is at its most negative. This perhaps indicates that as species are desorbed from the AlOH groups, they are readsorbed onto the Brönsted sites. The major positive feature is a broad band centred at around 3410 cm$^{-1}$ relating to hydrogen bonded OH groups. The splitting of this band in the higher temperature samples may well be due to Fermi resonance and associated Evans windows rather than different OH species.

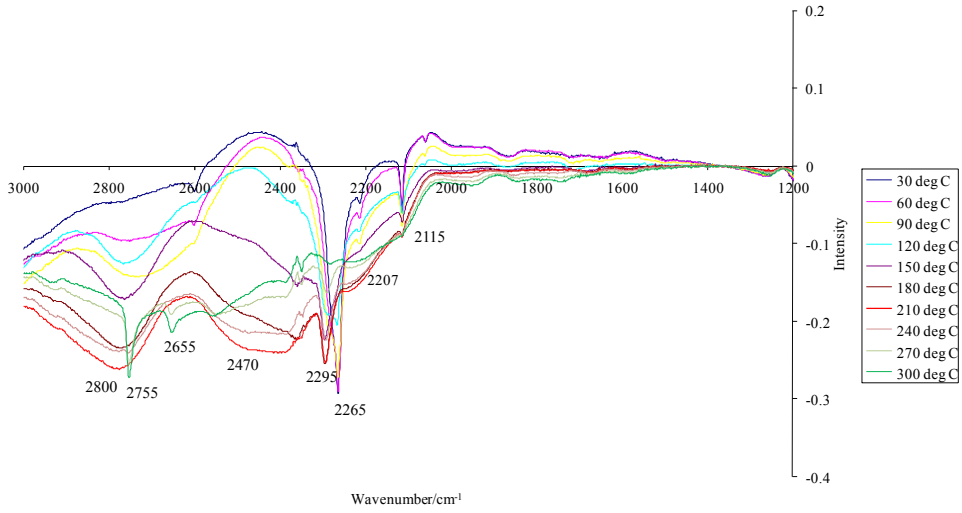


**Figure 90: Infrared subtraction spectra showing the low frequency region for $CD_3CN$ adsorption onto ZSM-5 280 and then desorption up to 300°C**

As can be seen in figure 90, there are two bands associated with C≡N stretching vibrations. The strongest at high coverage (low temperature) at 2263cm$^{-1}$ is characteristic of hydrogen-bonded or liquid-like $CD_3CN$. The band at 2291 cm$^{-1}$ increases in intensity at higher temperatures as the band at 3600cm$^{-1}$ becomes increasing negative and corresponds to $CD_3CN$

adsorbed on Brönsted sites. The broad bands at around 2800cm$^{-1}$ and 2470cm$^{-1}$ are associated with the formation of strongly hydrogen-bonded acetonitrile complexes. They arise due to Fermi resonances (and corresponding Evans transmission window) between OH overtones and $\nu$(OH)±k$\nu$(OH···N) modes. The position of these bands is highly variable.[136] As in the case of alumina and zirconia, the $\nu CD_3$ band is visible at 2115cm$^{-1}$. There is again a tiny peak visible at 2207cm$^{-1}$ at high $CD_3CN$ coverage assigned to polymeric carbanion species. However unlike the zirconia sample, no bands are observed in the region characteristic of acetamide groups.

## Zeolite ZSM-5 $SiO_2$:$Al_2O_3$= 30

The hydroxyl stretch region after adsorption of $CD_3CN$ onto zeolite ZSM-5 $SiO_2$:$Al_2O_3$= 30 (ZSM-5 30) shown in figure 91, appears broadly similar to that for ZSM-5 280 shown in figure 89.

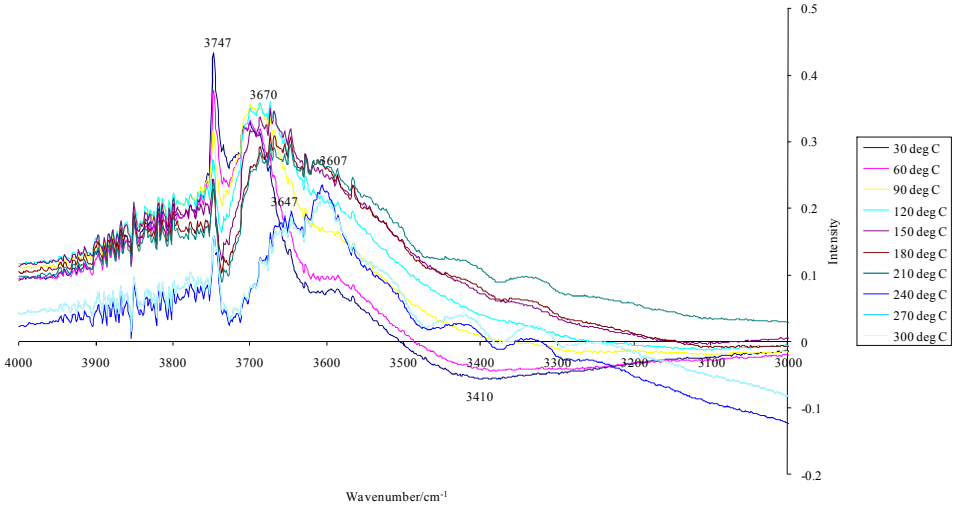


**Figure 91: Infrared subtraction spectra showing the OH stretch region of $CD_3CN$ adsorbed on ZSM-5 30 and then desorbed under flowing nitrogen up to 300˚C**

However, there are some differences in the two samples. The band at around 3607cm$^{-1}$ assigned to the Brönsted sites at all but the lowest and highest temperatures, appears as a broad shoulder on the side of the band relating to AlOH groups. The band for AlOH groups remains as a negative band right up to 300˚C. However, at low temperatures it is present at 3670cm$^{-1}$ and shifts down to around 3647cm$^{-1}$ by 270˚C. This may indicate the presence of a number of different groups of different acidity. Once again, the isolated silanol peak at 3747cm$^{-1}$ is not restored even at 300˚C and there is a broad band centred at around 3410cm$^{-1}$ corresponding to hydrogen bonded silanol groups.

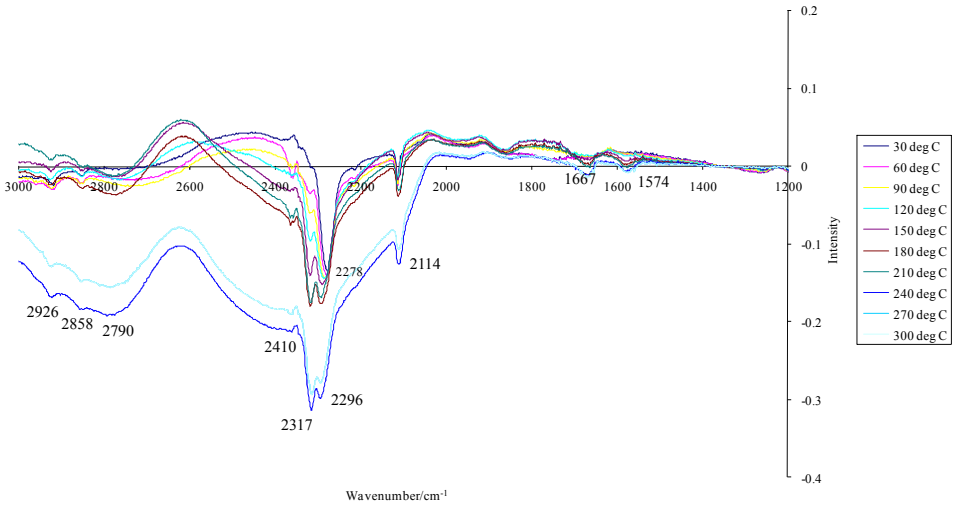


**Figure 92: Infrared subtraction spectra showing the low frequency region for $CD_3CN$ adsorbed on ZSM-5 30, then desorption under flowing nitrogen up to 300˚C**

Comparing figures 90 and 92, significant differences can be seen between the two different zeolite samples. As shown in both, at high coverage, the main νCN band is that at 2278cm$^{-1}$ representing hydrogen-bonded $CD_3CN$. However in figure 92 for ZSM-5 30, by about 120˚C, this band has shifted to 2296cm$^{-1}$, the position for $CD_3CN$ adsorbed on Brönsted sites. Observable by 60˚C and rising in intensity to become the dominant species is a band at 2317cm$^{-1}$, this represents $CD_3CN$ adsorbed onto $Al^{3+}$ Lewis acid species. It is only in this sample with the higher aluminium content that these species are present.

In figure 92 there is possible evidence for acetamide formation. However, the band at 1667cm$^{-1}$ should be assigned to a solvated acetamide anion intermediate and would be expected to disappear at higher temperature. The band at 1574cm$^{-1}$, follows that pattern that would be expected for a β-type acetamide species. These bands are very weak and it can safely be

concluded that any acetamide species, if any are formed are at a much lower concentration than on zirconia.

## 13x Zeolite $SiO_2$:$Al_2O_3$=2.8

The infrared spectra of $CD_3CN$ adsorbed on 13x molecular sieve are quite different from those of the two ZSM-5 samples.

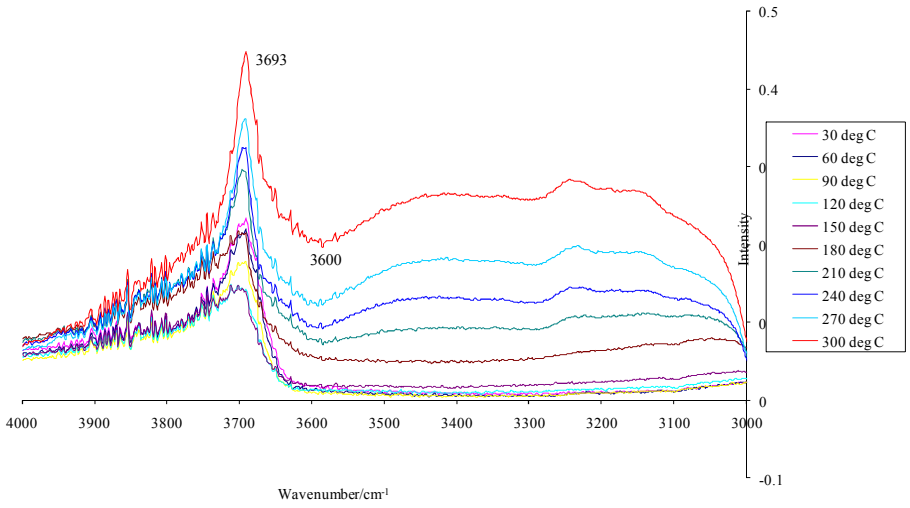


**Figure 93: Infrared subtraction spectra showing the OH stretch region for CD3CN adsorbed on 13x molecular sieve**

The main feature in figure 93 is a νOH band at 3692$cm^{-1}$ that becomes increasingly negative with increasing temperature. This band is assigned to AlOH groups. Above 120˚C the band at 3600$cm^{-1}$ representing Si-OH-Al Brönsted species is restored.

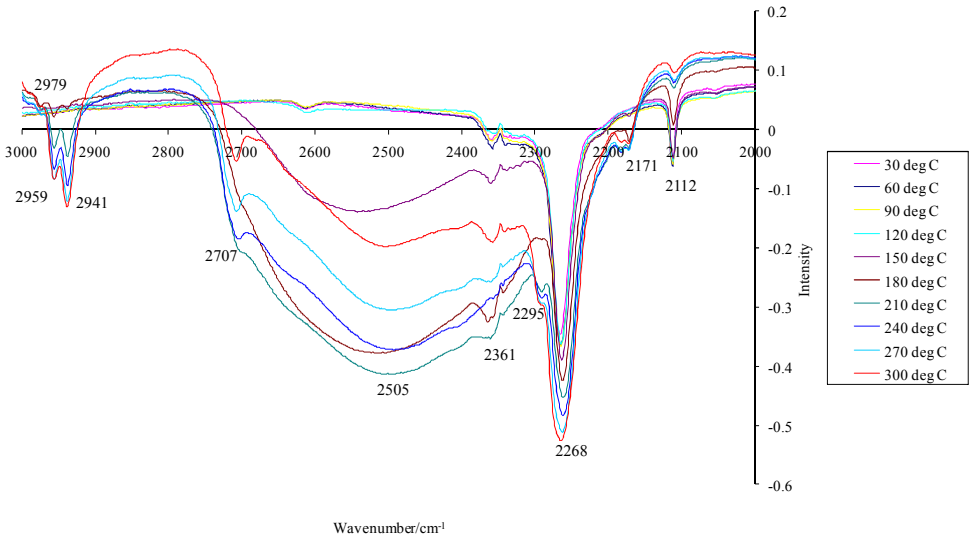


**Figure 94: Infrared subtraction spectra showing νCN region of $CD_3CN$ adsorbed on 13x zeolite and then desorbed up to 300˚C under flowing nitrogen**

The main features shown in figure 94 at high $CD_3CN$ coverage (up to about 120˚C) are, the νCN band corresponding to hydrogen bonded $CD_3CN$ at 2268$cm^{-1}$ and the $\nu CD_3$ band at 2112$cm^{-1}$. Unlike with the other samples both of these bands are present even at 300˚C. In fact the band at 2268$cm^{-1}$ continues to grow during the heating process. Above 180˚C this band is accompanied by the νCN band for $CD_3CN$ adsorbed onto S-OH-Al bridging species at 2295$cm^{-1}$. The small feature at 2361$cm^{-1}$ does not change in intensity and is most likely due to $CO_2$ in the beam path. The peak at 2171$cm^{-1}$ that develops at high temperature is due to polymeric carbanion species. The broad band centred at around 2505$cm^{-1}$ and accompanied by the sharper feature at 2707$cm^{-1}$ correspond to the broad features seen in the previous spectra characteristic of strongly hydrogen-bonded $CD_3CN$. Above 180˚C there is a triplet of bands visible at 2979$cm^{-1}$, 2959$cm^{-1}$ and 2941$cm^{-1}$. These bands are in the appropriate region for C-H stretching vibrations. This suggests more strongly than in the previous cases that deuterium exchange with the surface is taking place. This would form species such as $CD_2HCN$, $CDH_2CN$ and $CH_3CN$.

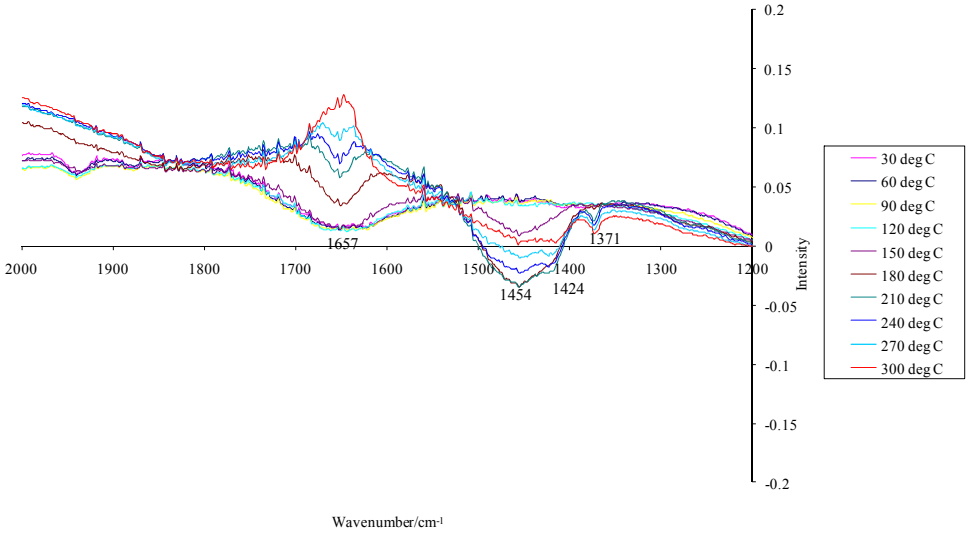


**Figure 95: Infrared subtraction spectra showing the region characteristic of acetamide formation of $CD_3CN$ adsorbed on 13x zeolite and the desorbed up to 300˚C under flowing $N_2$**

As with the alumina and zirconia samples, there are significant bands in this region. At low temperatures, the solvated acetamide ion species is observed at 1657cm$^{-1}$. At higher temperatures, there is a broad band centred at around 1454cm$^{-1}$ with a shoulder at 1424cm$^{-1}$. These represent α and β acetamide species respectively. The peak at 1371cm$^{-1}$ is not due to acetamide groups and may well correspond to a C-H deformation band brought about by deuterium exchange between $CD_3CN$ and the surface OH groups.

The adsorption of acetonitrile-d3 on metal oxide surfaces shows many complex effects. These however provide useful information about the activity of the surfaces. By this study the order of activity for the formation of acetamide species is zirconia followed by alumina, 13x zeolite, ZSM-5 30 and then ZSM-5 280. However, 13x zeolite appears to have the greatest concentration of highly basic sites based of the possible formation of a number of different nitrile species by deuterium exchange.

## Benzonitrile Adsorption on Zeolites

The multiple reactions that take place when $CD_3CN$ is adsorbed on surfaces more active than silica, such as alumina or zirconia lead to complicated infrared spectra. This is particularly true in the case of zeolites, where the surface contains a number of different adsorption sites. So, in order to simplify the assignments, the deuterated acetonitrile experiment was repeated using benzonitrile as the probe molecule. For further details see Chapter 2.3.

### ZSM-5 $SiO_2$:$Al_2O_3$= 280

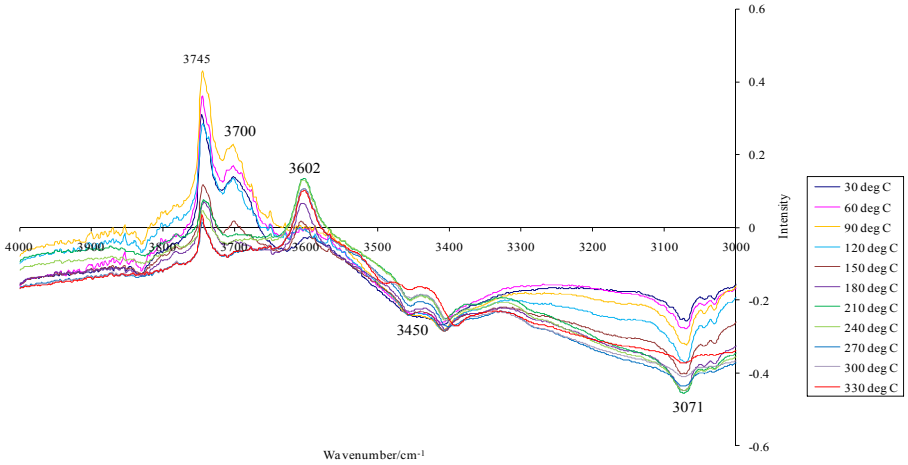


**Figure 96: Infrared subtraction spectra showing the νOH region for benzonitrile adsorbed on ZSM-5 280 then desorbed under flowing $N_2$ up to 330˚C**

As can be seen in figure 96, the changes in the νOH region after benzonitrile adsorption on ZSM-5 280 are practically the same as those after deuterated acetonitrile adsorption. As before, the isolated SiOH stretch remains negative right up to the highest temperatures, the AlOH stretch is restored by about 210˚C and the Si-OH-Al stretch band becomes increasingly

negative. Also there is a broad positive band due to hydrogen bonded hydroxyl groups centred at around 3450cm$^{-1}$ accompanied by the Fermi windows at higher temperature.

Differing from $CD_3CN$, in this region at 3070cm$^{-1}$, is a positive band corresponding to the aromatic C-H stretching vibrations, which is much weaker though still present by 300˚C. This band is shifted to higher frequency than in liquid benzonitrile at 3040cm$^{-1}$.[137]

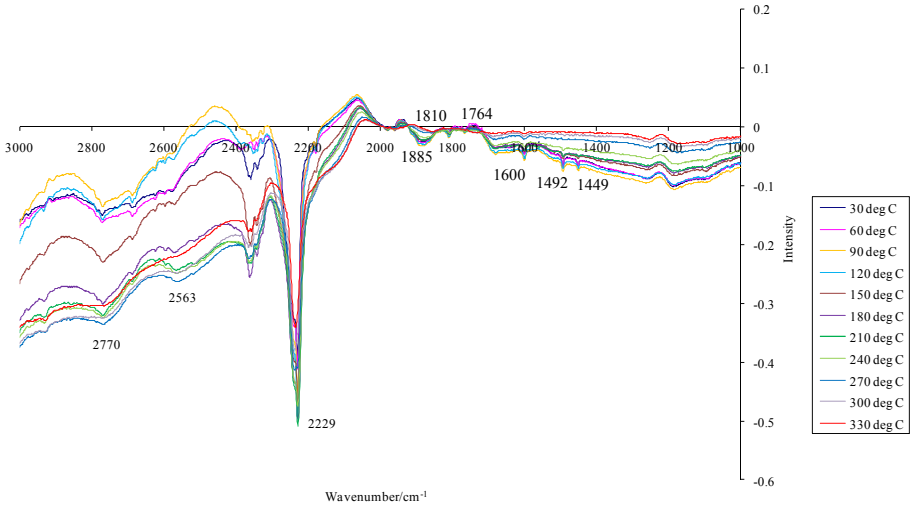


**Figure 97: Infrared subtraction spectra showing the low frequency region of benzonitrile adsorbed on ZSM-5 280 and then desorbed under flowing nitrogen up to 300˚C**

As can be seen in figure 97, the adsorption of benzonitrile onto ZSM-5 280 does not lead to multiple reactions as in the case of deuterated acetonitrile. The major band at low coverage at 2229cm$^{-1}$ corresponds to the νCN band of benzonitrile. This is an upward frequency shift of only 9cm$^{-1}$ from the liquid value,[137] demonstrating that this represents weakly hydrogen bonded benzonitrile, most likely onto silanol groups. Unfortunately, any peaks at higher frequency that would correspond to benzonitrile adsorbed on Brönsted species or AlOH species are masked by peaks in the 2350-

2370cm$^{-1}$ region due to $CO_2$. At higher temperatures, the same broad features can be seen at 2770cm$^{-1}$ and 2563cm$^{-1}$ as can be observed in the acetonitrile spectra. By analogy, these should correspond to a strongly hydrogen bonded benzonitrile system.

The groups of three bands at 1885, 1810 and 1764cm$^{-1}$ most likely represent some sort of surface carbonate species. The bands at 1600, 1492 and 1449cm$^{-1}$ all correspond to νC-C bands of benzonitrile.

**ZSM-5 $SiO_2$: $Al_2O_3$=30**

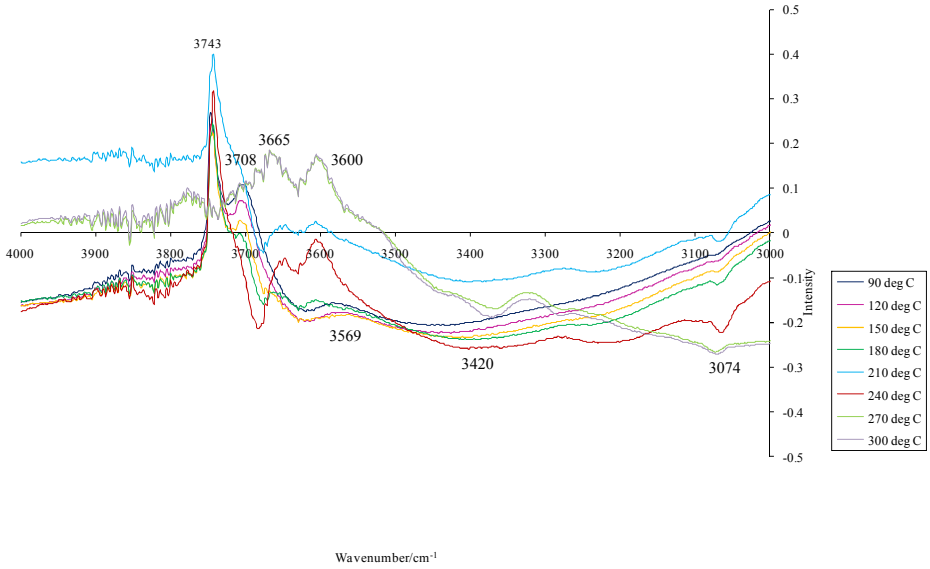


**Figure 98: Infrared subtraction spectra showing the high frequency region of benzonitrile adsorbed on ZSM-5 30**

For this sample, the spectra recorded at 30 and 60˚C showed a somewhat weaker signal than the others. They may have been recorded as the MCT detector was becoming too warm. They have been removed from the spectrum. As is seen in figures 96 and 97 for ZSM-5 280, major changes in the spectra cannot be observed until the temperatures reaches about 150˚C. So, the absence of the 1$^{st}$ two readings from the spectra is unlikely to matter.

In figure 98, at low temperatures (up to 150˚C) the negative peaks are; the isolated terminal SiOH stretch at 3743cm$^{-1}$, the AlOH stretch at 3708cm$^{-1}$ and the bridging Si-OH-Al stretch at 3570cm$^{-1}$. The positive band relating to hydrogen bonded OH species is centred at around 3420cm$^{-1}$. As the temperature increases however, the band at 3708cm$^{-1}$ becomes a shoulder on the side of the 3743cm$^{-1}$ band, a new band develops at 3665cm$^{-1}$and the Brönsted site band shifts to 3600cm$^{-1}$. Unlike in the case of ZSM-5 280 or any of the zeolites with deuterated acetonitrile, the isolated SiOH stretch is restored by 300˚C.This seems to indicate that there a number of different AlOH and Brönsted sites, some of which have a stronger affinity for benzonitrile than others. Also the lack of formation of surface acetamide species allows complete desorption from the isolated silanol species. In ZSM-5 30, there will be far fewer isolated SiOH groups than in ZSM-5 280 and these are only weakly acidic sites, so desorption from them will occur first. It is however clear that a much longer desorption time or higher temperature would be necessary to completely remove the benzonitrile from the surface. This is due to the higher boiling point of benzonitrile compared to acetonitrile-d3 (191˚C compared to 81˚C).

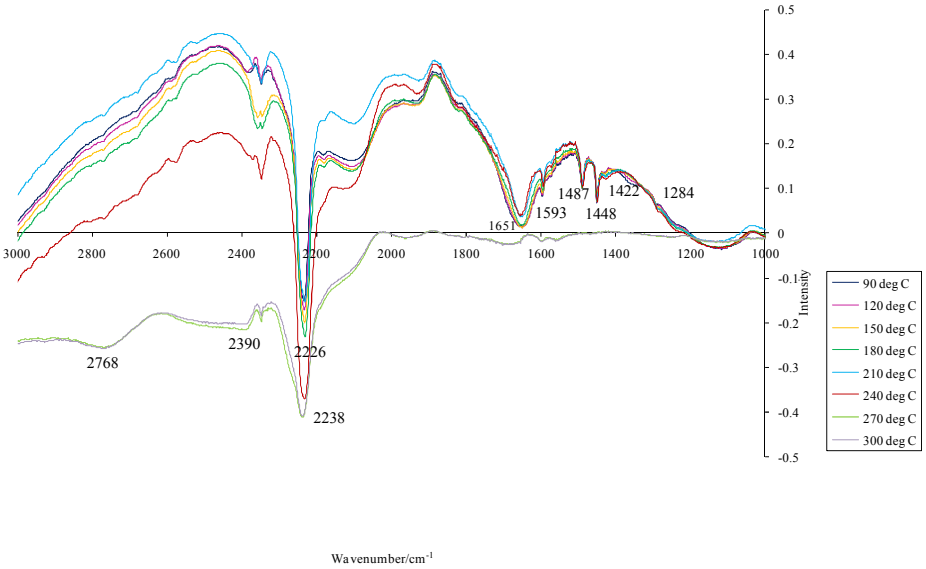


**Figure 99: Infrared subtraction spectra showing the low frequency region of benzonitrile adsorbed on ZSM-5 30 then desorbed under flowing nitrogen up to 300˚C**

In figure 99 as with ZSM-5 280 in figure 97, the main feature that can be observed at low temperatures is the νCN band for weakly hydrogen bonded or liquid-like benzonitrile at 2226cm$^{-1}$. In this case however, this band can be seen to shift to 2238cm$^{-1}$ indicating adsorption onto stronger sites, possibly the Brönsted sites. The broad band at 1652cm$^{-1}$ is also new to this sample. It may represent some sort of solvated species as it disappears at high temperatures. The other bands are much the same as those seen in figure 97 except that two extra bands relating to benzonitrile can be observed at 1422 and 1284cm$^{-1}$. These are assigned to a C-C stretching band and a C-H deformation band respectively.

## 13x Zeolite

The νOH region of the infrared spectra of benzonitrile adsorbed on 13x zeolite shows very similar features to that of $CD_3CN$ adsorbed on 13x zeolite.

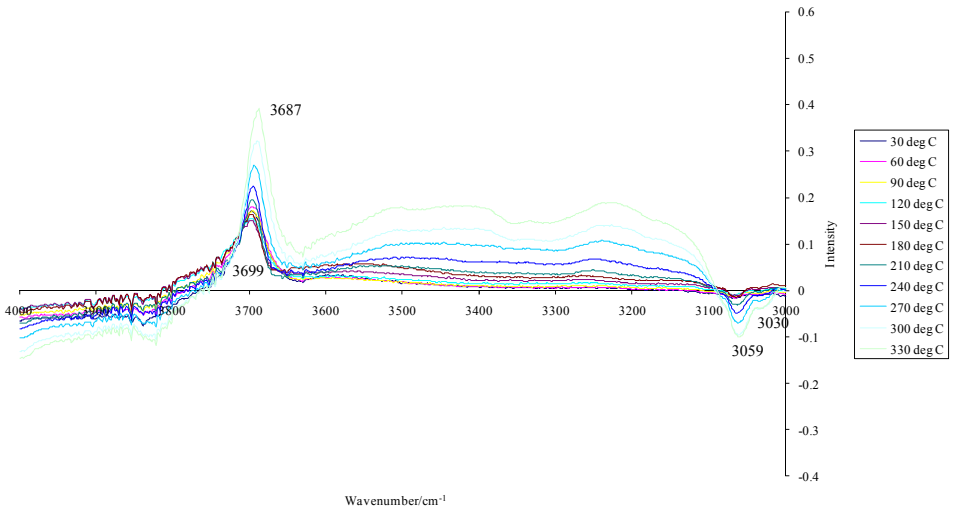


**Figure 100: Infrared subtraction spectra showing the high frequency region of benzonitrile adsorbed on 13x zeolite and then desorbed under flowing nitrogen up to 300˚C**

In figure 100 the negative band at 3699cm$^{-1}$ shifts to 3687cm$^{-1}$ and becomes increasingly negative as the temperature increases. This band is in the region for AlOH groups. The fact that it shifts as the temperature increases demonstrates that there are at least two different sites present and the groups absorbing at 3687cm$^{-1}$ adsorb benzonitrile strongly. The other feature of note is a positive band at 3059cm$^{-1}$, representing the aromatic C-H stretch for benzonitrile. This is a lower frequency than that found for benzonitrile adsorbed on either of the two ZSM-5 samples. This is joined by a second band at 3030cm$^{-1}$ at high temperatures. This suggests adsorption on two different sites as corroborated by the peak shift in the νOH region.

Another possible explanation is that the differences represent adsorption via the aromatic ring as well as adsorption via the C≡N bond. This is unlikely however, by comparison with benzene adsorbed on X-type zeolites the C-H stretching vibrations only shift to lower frequency by 1-2cm$^{-1}$ from the liquid value.[138]

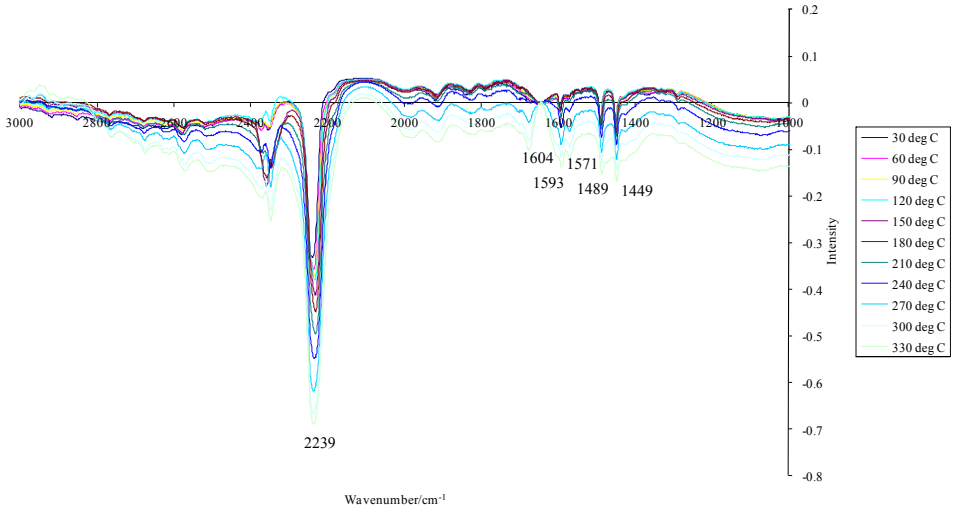


**Figure 101: Infrared subtraction spectra showing the low frequency region of benzonitrile adsorbed on 13x and then desorbed under flowing nitrogen up to 330°C**

In the low frequency region, the subtraction spectra of benzonitrile adsorbed on 13x zeolite (figure 101) show similar features to those for the two ZSM-5 samples. The major differences are; the νCN band is at 2239cm$^{-1}$ right from the low temperatures. This is the position of the upward shifted band seen in figure 99 after heating of ZSM-5 30 under nitrogen. This may indicate that 13x zeolite is more acidic than the ZSM-5 samples. Another difference is the lack of the broad bands at around 2800 and 2400cm$^{-1}$. This suggests a different surface benzonitrile distribution to that found on the two ZSM-5 samples. More peaks can be seen in 1610-1440cm$^{-1}$ region corresponding to

benzonitrile stretching and deformation modes because all the band intensities are greater.

The adsorption of benzonitrile onto the 3 zeolite samples shows the same pattern of activity as that seen for the adsorption of acetonitrile-d3. It can be seen that there are a number of different adsorption sites present with different acidities. These seem to be accessible to both the nitrile species, which is not surprising as they are both small molecules. The differences between external and internal sites could be investigated by the use of a larger nitrile such as adamantane-carbonitrile as used by Areán and co-workers.[136]

## 4.4 Conclusions

The popularity of infrared probing techniques is understandable given the wealth of information about surface activity that can be obtained relatively quickly and easily. From the adsorption of basic probe molecules such as ammonia and acetonitrile-d3 it is possible to distinguish between the surface acidity of even very weakly acidic and quite similar materials such as HMS and SBA-15 silica gel samples. The adsorption of water onto the tri-methylsilyl functionalised silica gel revealed that the tri-methylsilyl groups are not evenly distributed on the surface but are instead present in clusters leaving other areas of the silica surface free to adsorb water. The adsorption of acetone onto 3-aminopropyl functionalised silica gel showed in unusually high level of reactivity for this system.

Also by the adsorption and heating of acetonitrile-d3 on alumina, zirconia and different zeolites, several different sites were revealed, some acidic and some basic. Some of the acidic sites, particularly on zirconia and 13x zeolite were active enough to convert acetonitrile to surface acetamide species. In addition, 13x zeolite showed evidence of deuterium exchange between the

surface and the acetonitrile-d3 providing firm indication of the presence of $O_2^-$ basic surface sites. The level of formation of acetamide species allows the acidity of the samples to be ranked in the order zirconia > alumina > 13x zeolite > ZSM-5 30 > ZSM-5 280 > silica.

However, as can be seen from these studies, the data is not always straight-forward to interpret. This accounts for much of the disagreement in the literature regarding exact assignments of certain bands, such as the carbonate/carbamate bands present in the spectra of $CO_2$ adsorbed on amino-functionalised silica surfaces. It also must be taken into account the fact that these are empirical methods for studying the activity of surfaces and they are only really useful when there is other similar data available to compare the results to.

In the cases where the infrared samples were diluted with KBr before being heated, it would be useful to see what, if any affect the KBr has on the probe molecule. In the experiments discussed in this chapter, the KBr has been assumed to be inert and indeed no unexpected bands were seen in the spectra recorded using KBr as a diluents. Nevertheless, it would be useful to adsorb the probe molecule onto pure KBr and again carry out the variable temperature infrared measurements.

Some more recent studies in the literature have attempt to model spectra of probe molecules adsorbed on surfaces in attempt to remove some of the difficulties associated with peak assignments.[139] These modelling techniques are likely to become increasingly valuable as models increase in sophistication.

# Chapter 5: UV-Visible Probing of Surface Chemistry

As detailed in the introduction, UV-visible probing techniques developed for ascertaining the acid-base properties of solutions have successfully been extended to the characterisation of surface properties.[58,140] It was decided that since much of the work on infrared probing (discussed in Chapter 4) concerned the acid properties of surfaces that the study of a UV-visible probe for the basic properties of surfaces would be interesting. Based on the work by Choi[69] and Doskocil[75] on determining the donor strengths of basic sites on zeolites and the work by Camarota[74] on periodic mesoporous organosilicas, iodine was selected as a potentially interesting probe molecule for the surface properties of inorganic, organic and hybrid materials surfaces. The relevant bands in the UV-visible spectrum of iodine are detailed in Chapter 1.4.

In order to test the sensitivity of iodine as a probe for surface electron donating ability, the $\lambda_{max}$ values for the $\pi^*$-$\sigma^*$ band of iodine adsorbed on silica Kieselgel 60 (K60) surfaces after pretreatment at different temperatures were compared with those of the well established probe molecule for hydrogen-bond donating ability and polarity- Reichardt's dye.[58b,58e] As the silica surface becomes more dehydroxylated with increasing pre-treatment temperature and becomes increasingly composed of siloxane bridges, it would be expected that both the number of hydrogen-bond donating and electron-donating sites would decrease. This is because it is the silanol groups that are the adsorption sites on a silica surface.

# 5.1 Comparison of Reichardt's Dye and Iodine as UV-Visible Probes for Silica

Adsorption of the Reichardt's dye onto the silica surfaces was carried out as detailed in Chapter 2.4. For the data series labelled "post-vac" in figure 102, after solvent removal on the rotary evaporator, the silica sample with the adsorbed dye was put through an additional drying process on a high-vacuum line at room temperature until equilibrium vacuum was reached. This extra step was taken because it was found that the $\lambda_{max}$ value varied with the drying time.

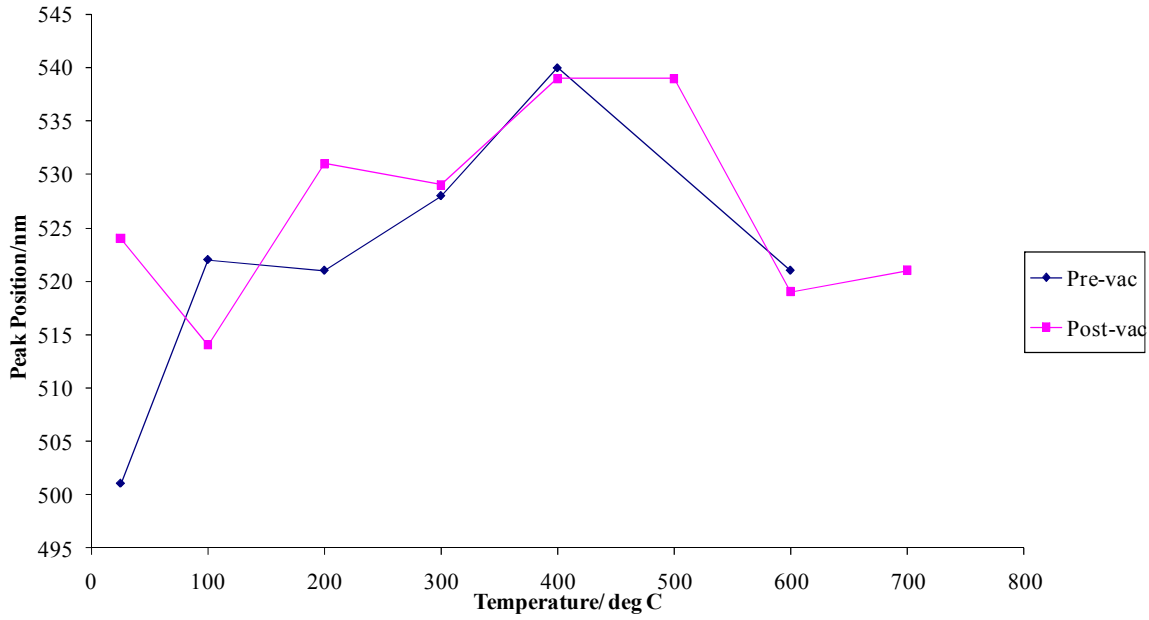


**Figure 102: The $\lambda_{max}$ values for Reichardt's dye adsorbed on silica $K_{60}$ samples with increasing pre-treatment temperature**

With decreasing surface hydrogen-bond donating ability and polarity, the π-π* transition of Reichardt's dye shifts to longer wavelength. As seen in figure 102 and in the work by Tavener and co-workers,[36,68] increasing the

temperature of thermal treatment on silica causes a decrease in surface hydrogen-bond donating ability and polarity. However, from figure 102 it can be seen that the $\lambda_{max}$ value reached the longest wavelength on a silica heated to between 400 and 500˚C before the $\lambda_{max}$ shifts to shorter wavelength at higher temperatures. This is a little surprising, it would be expected that the surface would continue to be dehydroxylated above 500˚C. Some surface restructuring may take place above 700˚C but an apparent increase in hydrogen-bond donating ability below that temperature in not expected. In the work by Tavener; the silica was heated to 800˚C and loss of surface area was observed between 700˚C and 800˚C related to condensation of adjacent particles. This was accompanied by a slight increase in surface polarity attributed to surface restructuring.[68]

The effect of different drying times on the $\lambda_{max}$ values is seen by comparing the "pre-vac" and "post-vac" data sets in figure 102. As might be expected, the differences are most pronounced for the untreated (25˚C) and low-temperature treated samples. After low-temperature treatment the silica surface will re-adsorb water much more quickly than a highly dehydroxylated surface produced by high temperature treatment. This effect cannot be used to explain why the hydrogen-bond donating ability of the surface apparently increases above 500˚C but since the "post-vac" data set shows a fair amount of data scatter; the unexpected results may not reflect real surface effects and repeating the experiment may give different values.

For the adsorption of iodine onto the surface; the initial procedure followed was similar to that used for the adsorption of infrared probes from the liquid state onto a surface. A known mass of silica (or other solid) was placed inside a glass sample vial with a known mass of iodine. The sample vial was then sealed and placed in an oven at 120˚C to sublime the iodine. However much of the iodine was found to adsorb on the lid and the sides of the vial and some solid iodine remained. In some cases, the plastic lid of the vial melted. So a new method was devised, in which the iodine was adsorbed

onto the surfaces under vacuum and is detailed in Chapter 2.4. The second method was used for the majority of the samples shown.

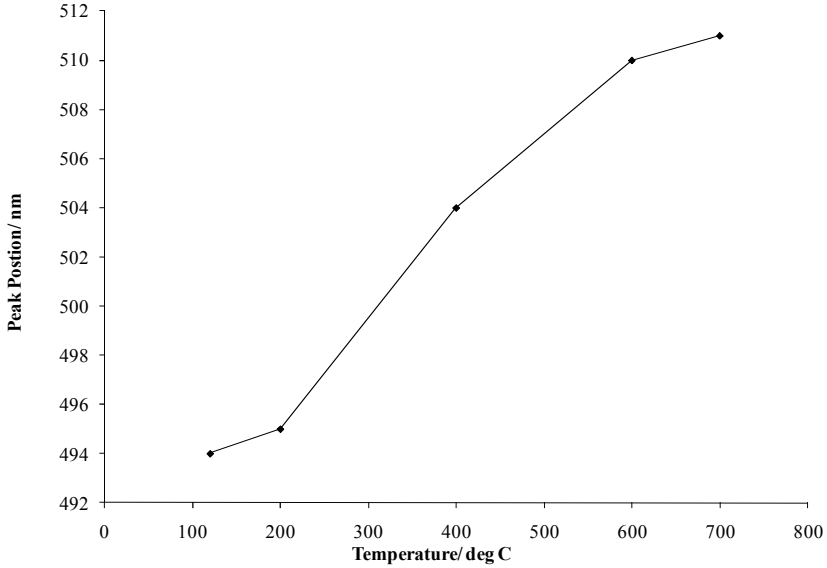


**Figure 103: The $\lambda_{max}$ values for the $\pi^*$-$\sigma^*$transition of iodine adsorbed on silica $K_{60}$ after heating the silica to different temperatures.**

As discussed in Chapter 1, an increase in electron-donating ability of the environment that iodine is in contact with causes an increase in the energy of the $\pi^*$-$\sigma^*$ transition. This is the band in the visible region in the UV-visible spectrum of iodine and in the gas phase is at about 520nm.[74] Interaction with a more electron-donating environment causes this value to shift to shorter wavelengths. Therefore the increase in the $\lambda_{max}$ value from 494 to 511nm shown in figure 103 when the silica is heated from 120-700˚C indicates a decrease in electron-donating ability of the surface. Though the shift in the $\lambda_{max}$ for iodine is not as large as for Reichardt's dye, it still seems to be sensitive to the changes in the surface of silica, which compared to many other metal oxides is relatively unreactive. The shift in $\lambda_{max}$ also follows a systematic trend, this is also essential if the probe is to be used to make meaningful comparisons between different surfaces.

A decrease in the number of electron-donating sites on the silica surface can be seen by the decrease in the concentration of iodine that may be adsorbed on the surface. This is shown by the decrease in the intensity for all the bands associated with iodine in the UV-visible spectra of selected silica $K_{60}$ samples in figure 104. Attempts were made to determine the mass of iodine adsorbed by surfaces gravimetrically but the silica surfaces are highly hydroscopic so it was impossible to exclude water. The adsorption of water and the effect on iodine adsorption was briefly studied by the use of controlled humidity chambers and discussed in section 5.4.

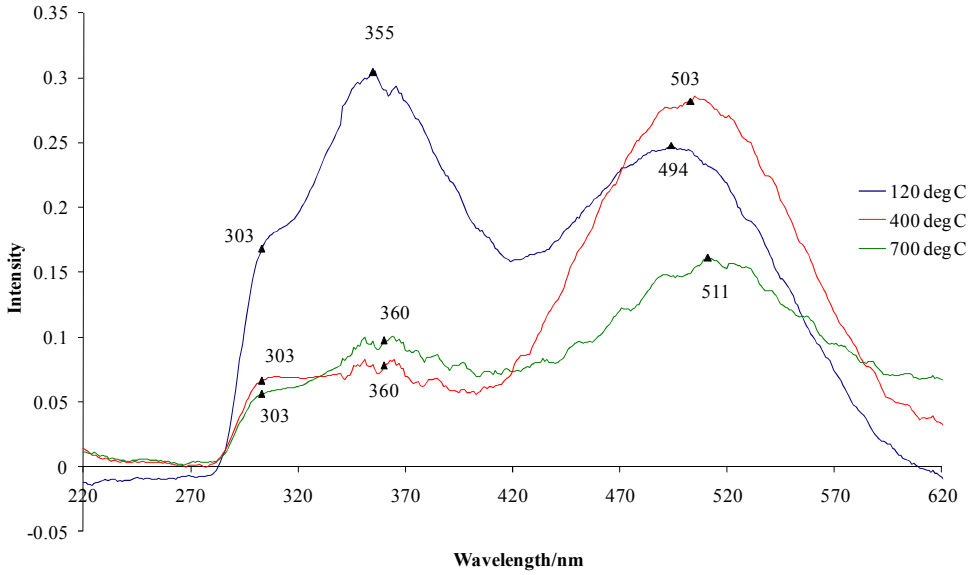


**Figure 104: UV-visible spectra of iodine adsorbed on silica surfaces after heating to different temperatures. These spectra were obtained by subtracting the UV-visible spectra of the bare silica from that with adsorbed iodine**

The bands at around 360nm and 303nm are characteristic of $I_3^-$, this indicates the presence of some sites of the surface basic enough to dissociate $I_2$. These sites may not be very numerous despite the high intensity of these bands. The molar extinction coefficients for $I_3^-$ are larger than those for $I_2$. For instance in water, $\varepsilon I_3^-$ (300nm) = 40000, $\varepsilon I_3^-$ (360nm) = 264000, $\varepsilon I_2$ ($\pi^*$-$\sigma^*$) = 978.[141] The 120˚C shows the highest concentration of $I_3^-$. This is most

likely due to solvation of the $I^+$ and $I_3^-$ by residual water stabilising the ions. By 400˚C, the surface water has been removed and at this temperature the band relating to $I_2$ is at its most intense, possibly indicating the creation of more sites for $I_2$ adsorption; these sites disappear by the time the sample is heated to 700˚C. Another band that may be present but not observable due to the limits of the wavelength range accessible using the diffuse reflectance mode on the UV-Visible spectrometer; is the $I_2$ charge transfer band which absorbs at around 200nm.

The success of iodine adsorption on silica prompted the decision to try adsorbing iodine on a wide variety of solid surfaces, metal oxides, carbonates, organically functionalised silicas and polysaccharides. See table 9 for a complete list of band positions and intensities.

## 5.2 Review of Iodine as a Probe Molecule for a Range of Solid Surfaces

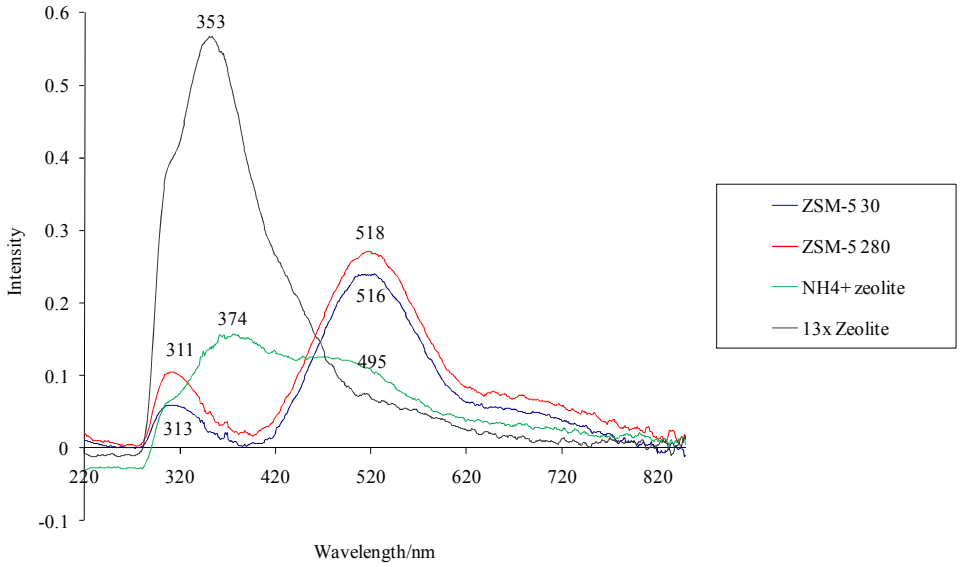


**Figure 105: UV-visible spectra showing iodine adsorption on Zeolites ZSM-5 $SiO_2$:$Al_2O_3$= 30, ZSM-5 $SiO_2$:$Al_2O_3$=280, ammonium Y zeolite and 13x zeolite all pretreated at 600˚C**

It can be seen from figure 105, that iodine shows markedly different behaviour on the different zeolite samples examined. The two ZSM-5 samples ($H^+$ cations) show similar behaviour to the silica K60 samples treated at the same temperature. There is a slight difference in the $\lambda_{max}$ of the long wavelength band, with the higher silica/alumina ratio zeolite showing a slightly lower electron-donating ability. This is consistent with the behaviour observed by Choi *et al* in their work on evaluating the donor strengths of different zeolites using $I_2$.[69] Based on their observations they found that the adsorption sites for iodine on a zeolite are the framework oxygens located away from the cation. The decrease in aluminium content accordingly decreases the donor strength of these oxygen atoms. The assignment of the weak band at around 311nm is not so certain but it may well represent a small amount of $I_3^-$ formation. Iodine charge transfer bands have been observed at this position but generally only when iodine is in contact with aromatic groups so this is a less likely explanation.

The decreased basicity of lower alumina concentration zeolites has also been demonstrated by the use of pyrrole as an infrared and NMR probe on alkali metal exchanged zeolites. Barthomeuf[142] and Huang[143] in separate studies used the shift in the IR N-H stretching frequency to characterise the basicity of zeolites of the faujasite type; X, Y and L. The Al(Si+Al) ratio increases in the order L<Y<X and the N-H stretching vibration shifts to lower wavenumber in the same order. Sánchez-Sánchez and Blasco studied the $^1H$ NMR of pyrrole adsorbed on X and Y type zeolites and found a shift to higher field of the N-H group when pyrrole was adsorbed on alkali zeolites from the liquid value of $\delta$ 7.1. A greater upwards shift was observed when pyrrole was adsorbed on X-type rather than Y-type zeolites.[144]

The other two zeolite samples show quite different behaviour, 13x zeolite with $Na^+$ cations shows a much greater conversion of $I_2$ to $I_3^-$. In fact the presence of $I_2$ is only demonstrated by a shoulder to the low energy side of the band at 353nm. The position of this band is similar to that for the silica

K60 after 120˚C heating. This particular sample seems to have a high concentration of strongly basic sites. It was also found to be more reactive with deuterated acetonitrile than the ZSM-5 $SiO_2$:$Al_2O_3$= 30 or 280 samples as seen in Chapter 4.3. There was some evidence for the presence of basic $O^{2-}$ species as seen in the formation of bands due to polymeric carbanion species and surface OD groups.

The behaviour of iodine adsorbed on ammonium Y zeolite is more easily explained. At the pretreatment temperature used it is expected that much of the $NH_4^+$ will have dissociated to $NH_3$ and $H^+$, so the cation should be comparable with the H-ZSM-5 zeolites. The shift of the $I_2$ band to 495nm is in the same region as found by Doskocil and co-workers for iodine adsorbed on Y zeolites and reflects a much lower Si/Al ratio than in the ZSM-5 zeolites.

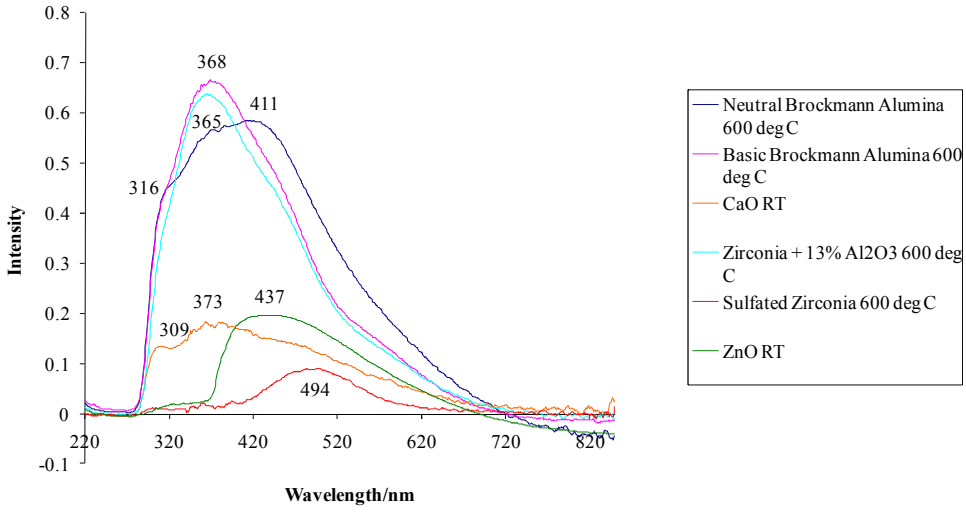


**Figure 106: UV-Visible spectra showing iodine adsorbed on a variety of single metal oxides after pretreatment at the temperatures indicated.**

It can be seen from figure 106 that iodine as a probe molecule can distinguish between neutral and basic activated Brockmann aluminas.

Neutral Brockmann alumina shows 3 bands in the 316 to 411nm region, indicating the presence of a number of sites of different activity. When iodine is adsorbed on acidic Brockmann alumina however, the band at 411nm is eroded and the main band is at 368nm instead. The zirconia + 13% $Al_2O_3$ sample also shows a relatively high concentration of sites capable of producing $I_3^-$. These may well correspond to the basic sites capable of forming the polymeric carbanion species when $d_3$-acetonitrile was adsorbed on the surface in Chapter 4.3.

Unsurprisingly, the calcium oxide is strongly electron donating; only peaks relating to $I_3^-$ can be distinguished. The zinc oxide is much less basic and the $\lambda_{max}$ is at 437nm. The only sample in this series to show a band that is definitely in the region for $I_2$ and also shows no sign of $I_3^-$ formation is sulfated zirconia. This would be expected to be an acidic sample, so this is not surprising.

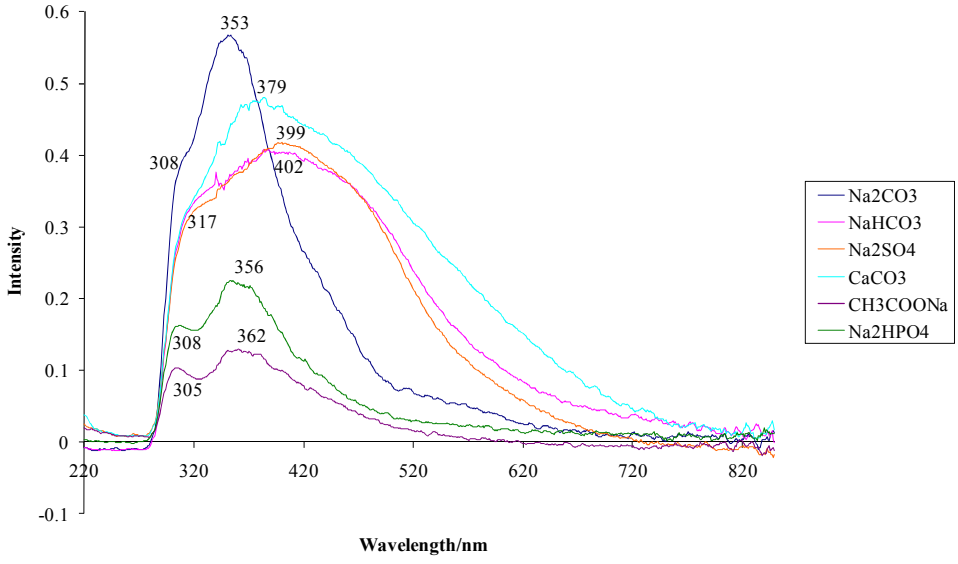


**Figure 107: UV-Visible spectra showing iodine adsorbed on a variety of basic solid metal salts**

Figure 107 shows that iodine is more or less entirely converted to $I_3^-$ on these metal salts as on the metal oxides. One thing that can be observed

from them however is the number of adsorption sites for iodine. The sodium acetate and sodium hydrogen phosphate for instance, show much less intense bands for iodine than the other solids shown in the same figure. This is not likely to be just due to lower surface area as these are all non-porous solids in powder form.

The uptake of iodine on alumina cement mixed with calcium sulfate has been investigated for the potential of this material to adsorb radioactive iodine ($^{129}I$).[145] This adsorption was carried out from sodium iodide solution. The authors found that $I^-$ was able to displace the $OH^-$ and $SO_4^-$ ions in the material to give new hydrates of the form $CaO.Al_2O_3.CaI_2.12H_2O$. It cannot be known however, in the present study whether any ion displacement occurs. Clearly there is formation of $I^-$ from the bands relating to $I_3^-$ in the spectra and on all but the sodium acetate and sodium hydrogen phosphate there is a high iodine uptake so maybe some sort of exchange could take place. This is perhaps unlikely however in the solid state.

From the preceding spectra, it can be seen that UV-visible spectra of iodine adsorbed on these solids shows discernable differences even between solids that are otherwise difficult to analyse such as sodium acetate and sodium sulphate. Although these differences have not as yet been correlated to any known properties of the surfaces.

As iodine is known to undergo strong interactions with many organic moieties, it was thought that the study of organically functionalised silica samples and silica-polysaccharide hybrids might yield interesting results. These results are shown in the following spectra.

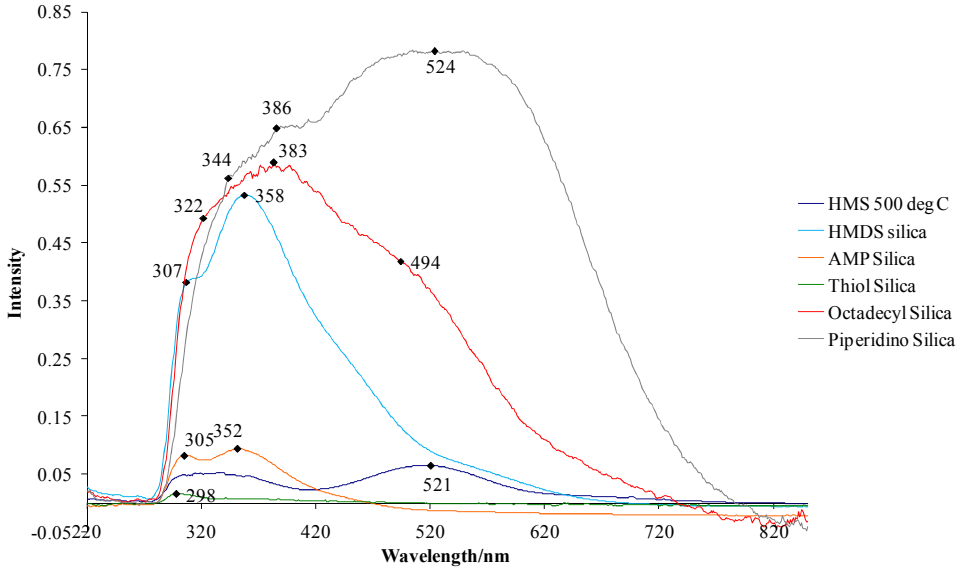


**Figure 108: UV-visible spectra showing iodine adsorbed on a variety of organically functionalised silica samples with a calcined hexagonal mesoporous silica shown for the purposes of comparison**

The abbreviations used in figure 108 are: HMS= hexagonal mesoporous silica (amine-templated), HMDS silica= trimethylsilyl functionalised HMS (see Chapter 2.1), AMP silica= 3-aminopropyl functionalised HMS (see Chapter 2.1), thiol silica= 3-mercaptopropyl functionalised HMS (see Chapter 2.1), octadecyl silica = commercial sample of octadecyl functionalised silica gel and piperidino silica= commercial sample of (1-piperidino)propyl functionalised silica gel.

As in the case of the metal salts in figure 107, there is a great variation in the loading of iodine that is adsorbed onto the organically functionalised silica surfaces. The commercial samples adsorbed a great deal of iodine. The (1-piperidino)propyl functionalised silica gel in particular, became a very deep red colour after iodine adsorption. This shows a very broad structure, with the centre of the band relating to $I_2$ being difficult to pinpoint exactly. The peak relating to $I_3^-$ is present as a broad shoulder on the side of this. It does seem to be less basic than the 3-aminopropyl silica. From comparison of the pKa values for the corresponding conjugate acids for the

n-propylpiperidine and propylamine groups at 10.48[146]and 10.53[147] respectively, it seems unlikely that it would be possible to differentiate between them. However, it should be reiterated as in the previous Chapter, that pKa values are measured in solution (usually water) and don't necessarily correlate with the behaviour observed in the vapour phase. The very strong adsorption of iodine on the piperidino silica surface may indicate that a specific interaction is taking place. The difference between the iodine adsorption on the primary amine and the tertiary amine therefore most likely indicates a change in reactivity rather than simply a change in basicity.

The octadecyl silica seems to be a stronger donor to iodine than the equivalent aliphatic solvent; iodine in alkane solutions gives a $\lambda_{max}$ value of about 520nm.[148] Also, no $I_3^-$ would be expected to be produced in an aliphatic solvent. It is not known what may cause this effect. It is expected that the octadecyl groups would keep the iodine away from the silica surface; that is after all their purpose. So, it cannot be due to interaction between the iodine and the silica. Perhaps the tethering of the octadecyl groups produces a different interaction with iodine than the free solvent.

The high apparent basicity of the trimethylsilyl functionalised silica (similar to the 3-aminopropyl functionalised silica) looks like an anomaly caused by some of the dodecylamine template remaining in the silica gel structure. The lack of visible iodine on the surface of the 3-mercaptopropyl functionalised HMS is most likely caused by the iodine oxidising the thiol groups to form S-S bonds and HI, according to the mechanism shown in figure 110.[149]

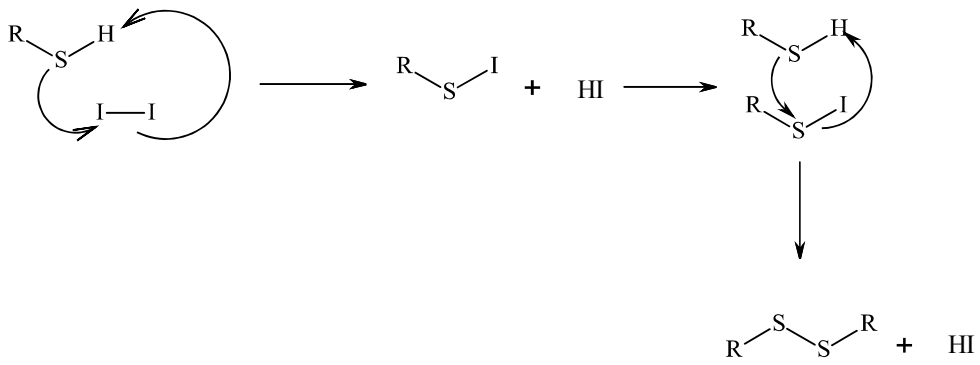


**Figure 109: Mechanism of thiol oxidation by iodine**

It is interesting that a much lower concentration of iodine is adsorbed on the silica samples prepared in the laboratory than the commercial silica samples. These differences are unlikely to be due to differences in surface area because all the samples have a surface area of at least 500 $m^2g^{-1}$ as measured by nitrogen porosimetry and also they all have similar porosity with a high proportion of mesopores allowing good diffusion.[7,10]

The effect of incorporation of polysaccharides into silica gels was also studied by iodine adsorption (see Chapter 2.2 for their preparation). Figure 110 shows the UV-visible spectra of iodine adsorbed on the pure polysaccharides and figure 110 shows iodine adsorption on the hybrid materials.

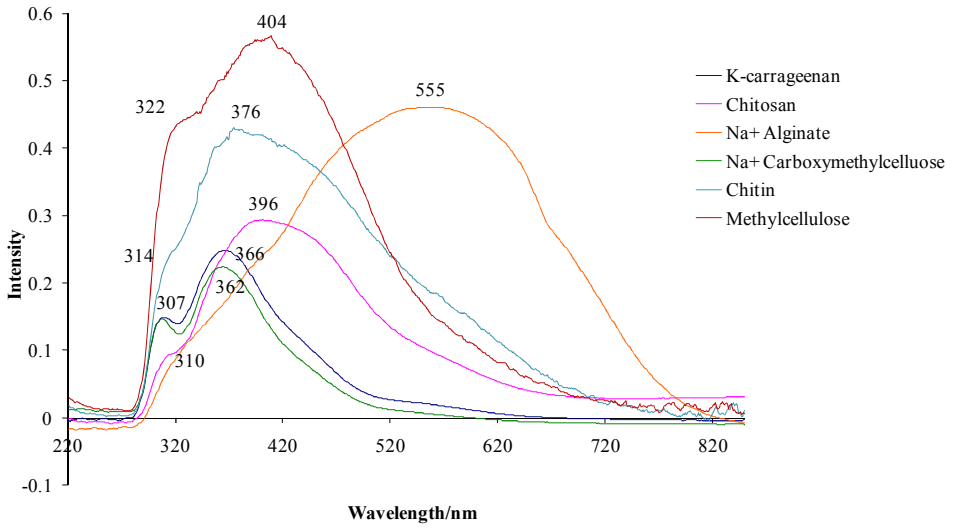


**Figure 110: UV-visible spectra showing iodine adsorption on polysaccharides**

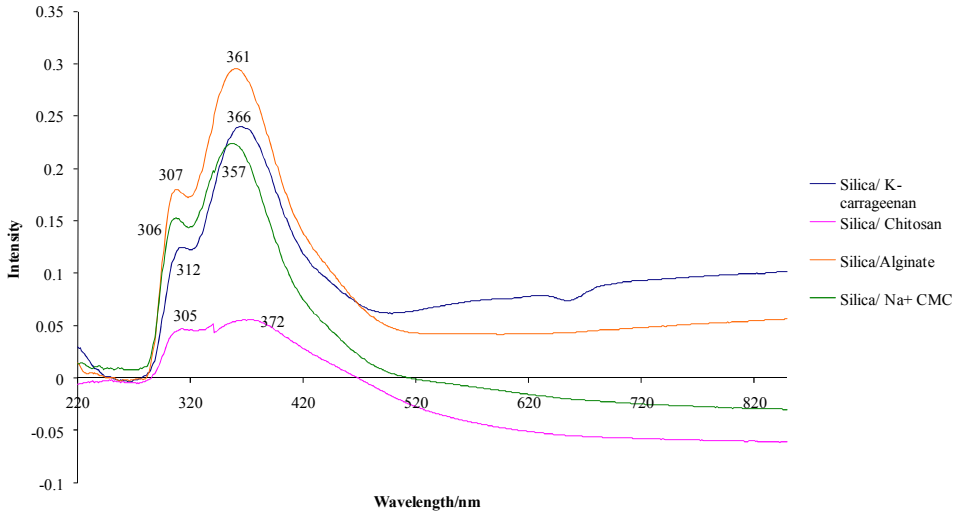


**Figure 111: UV-visible spectra showing iodine adsorbed on silica-polysaccharide composite materials**

The polysaccharide structures are shown in figure 112.

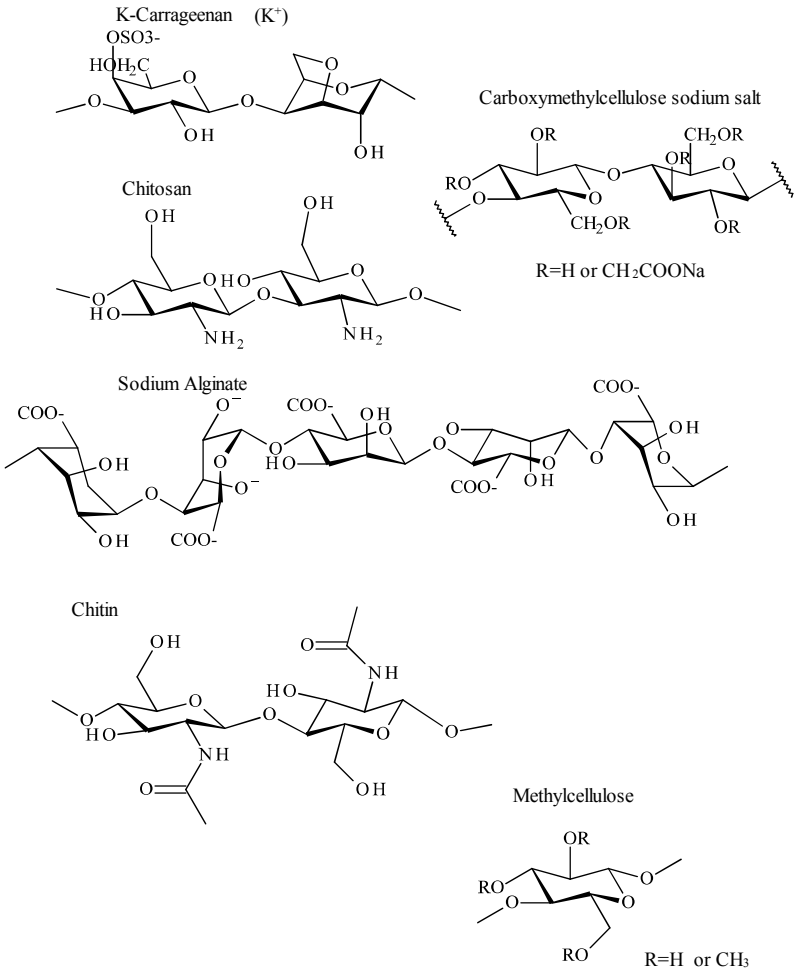


**Figure 112: The structures of the polysaccharides that iodine was adsorbed onto**

Interactions of iodine with various polysaccharides have been well studied in the literature. For, example, the blue-black coloured complex that forms when iodine is added to starch is a classic test for the presence of starch and the configuration of iodine within this complex has thoroughly investigated.[150] When iodine (or iodide) is added in solution to amylose, the iodine molecules/ triiodide position themselves inside the amylose helices with the long axis of the iodine molecule parallel to helix axis.[151]

Iodine also forms an inclusion complex with chitosan. As seen in figure 112, chitosan is an N-deacetylated derivative of chitin. The characteristics of chitosan have been found to vary with the degree of deacetylation, the

distribution of acetyl groups, chain length and molecular weight distribution.[152] In the solid state, chitosan chains have been reported to assume an extended two-fold helical conformation, stabilised by the O3···O5 hydrogen bond or an extended left-handed 8/5 helical conformation.[153] The chitosan-iodine complex on the other hand, has been shown by the X-ray diffraction studies carried out by Hanafusa *et al* to adopt a 4/1 helical conformation.[154] Iodine adsorption on chitosan was studied by Shigeno and co-workers, who concluded that the adsorption was caused by the formation of charge-transfer complexes between the amino groups of chitosan and the iodine molecules.[155] However, this is contradicted by $^{13}C$ NMR studies carried out by Yajima *et al*; who found that in the chitosan-iodine complex only the signals corresponding to carbon atoms adjacent to OH groups or glycosidic oxygen atoms were shifted to a higher field due to the effect of the heavy iodine atoms. The signal corresponding to the C2 atom bonded to nitrogen was not shifted. They concluded that the binding sites for iodine were the OH groups rather than the amine. [152]

Yajima *et al*, also found that the absorption maximum for the chitosan-iodine complex in solution was at 500nm. This absorption band and the circular dichroism bands decreased sharply in intensity above 30˚C and disappeared entirely above 60˚C. They were not restored even after cooling to 4˚C. However, when the solution was frozen and then thawed, the bands were completely restored. They concluded that the formation of the chitosan-iodine complex was irreversible. In another part of this investigation, they studied the Raman spectra of the chitosan-iodine complex and found bands that were assigned to $I_3^-$ and $I_5^-$ ions and concluded that these were the main species responsible for the colour of the complex.[152] The basic amino groups on chitosan could certainly cause the dissociation of $I_2$. The irreversible adsorption of $I_3^-$ has also been shown in other systems, such as caesium exchanged zeolites.[75] So, this is entirely plausible.

In figure 110 however, the absorption maximum for iodine on chitosan is at 396nm, not 500nm. This band position is indicative of $I_3^-$ whereas a band position of 500nm is suggestive of $I_2$. The most likely reason for the differences between the value obtained here and that found in the literature is due to the method of adsorbing iodine onto the polysaccharide. In all the literature studies found, the iodine is added in the form of a KI-$I_2$ solution. In this work, all the materials are solids. In solution, there is a much greater degree of freedom for the conformation of the polysaccharides to change and incorporate the iodine in the lowest energy conformation. This is unlikely to occur in the solid state.

Chitin is also known to form a complex with iodine, but since it seems to be mainly used as a starting material to make chitosan and adsorbing media such as the amino-acid substituted glucans,[156] it appears to have been studied in less depth. X-ray diffraction has identified three polymorphs of chitin, α-, β- and γ-chitin. Of these α-chitin appears to be the most stable form and consists of a series of two-fold chains.[157] Under the conditions used in the present study, in which there is little opportunity for conformational change in the adsorbent, the similarity in the behaviour of iodine on the surface of chitin and chitosan is perhaps not surprising. On both polysaccharides, the main absorbing species appears to be $I_3^-$.

A difference, though a much less dramatic one, is also seen when comparing the $\lambda_{max}$ for the alginate-iodine system at 555nm and the literature value of 587nm.[158] The literature value was recorded on a film under highly acidic conditions. Under these conditions sodium alginate is converted to the form of alginic acid with the appearance of helicoidal structures.[159] A literature value for the $\lambda_{max}$ for an iodine-sodium alginate complex could not be found. However, the very strong absorbance by iodine on the sodium alginate indicates a large take-up of iodine and hence most likely the formation of some sort of inclusion complex. Unlike on the other polysaccharides shown in figure 110, the main absorbing species would appear to be $I_2$.

The uptake of iodine is used as a measure of the degree of accessibility of cellulose in different forms, it was originally proposed as an empirical test by Schwertassek.[160] Though, as appears to be the case for all the studies on polysaccharide-iodine complexes, the iodine is adsorbed from a KI-$I_2$ solution. The iodine adsorbed was calculated by titration of the supernatant solution with $Na_2SO_4.H_2O$ solution after standing the cellulose fibres in the KI-$I_2$ solution for a period of time.[161]

It would appear from figure 110, that when adsorbed under these conditions, methylcellulose has a much greater accessibility to iodine than the carboxymethylcellulose sodium salt. It is possible that the sodium ions in the salt block some of the potential binding sites for iodine.

A search of the literature did not reveal any work carried out on the spectroscopic properties of iodine adsorbed on carrageenans. However, because of its ability to form a closely bound and elastic solid containing excess water (this caused some difficulties when manufacturing the silica-κ-carrageenan hybrid as discussed in Chapter 2.2) κ-carrageenan has been used as a medium to manufacture a solid version of the dye-sensitised solar cell, known as Graetzel's cell.[162] In this cell, a nanoparticulate $TiO_2$ film and Pt coated glass are the working electrode and counter-electrode respectively and the redox ion pair is $I^-/I_3^-$. The aqueous κ-carrageenan gel was exchanged with an $I^-/I_3^-$ redox solution and then electrodes were put in contact with this gel. This cell was found to be just as effective as that with the redox solution in liquid form. It is obvious from this that a swollen κ-carrageenan gel is capable of sorbing iodine. However, since it does not appear to interfere with the action of the electrodes this indicates that the iodine species are not tightly bound to the surface. This may indicate why very little iodine is adsorbed onto the dry (and therefore not swollen) gel surface.

For chitosan and sodium alginate, that form strong complexes with iodine, the concentration of iodine adsorbed on the surface of the silica-polysaccharide hybrid as shown in figure 111 is a lot lower than that adsorbed on the pure polysaccharide. However, for κ-carrageenan and sodium carboxymethylcellulose, the spectra of iodine adsorbed on the hybrids are almost identical to that of the pure polysaccharides. The concentration of polysaccharides in each of the hybrids should be approximately the same. It is also interesting to note that unlike in the spectrum of iodine adsorbed on HMS 500 (figure 108) in which the band corresponding to $I_2$ can clearly be observed despite a low up-take of iodine, it is not possible to observe a band relating to $I_2$ for any of the silica-polysaccharide hybrids. This suggests quite different properties for these materials which seem to entirely dissociate adsorbed $I_2$. As discussed in Chapter 1.4, in the work by Camarota *et al* on iodine adsorption on phenylene-bridged periodic mesoporous organosilicas,[74] it was found that the phenyl moieties were the preferred sites for iodine adsorption onto the surface. Thus the incorporation of the organic species into the silica framework affected the surface chemistry. A similar affect seems to be occurring here, with the incorporation of the polysaccharides affecting the surface properties of the silica.

It is also interesting to note how the incorporation of the polysaccharide into silica affects the polysaccharide. Sodium alginate for instance, produces a strong complex with iodine. However, its corresponding hybrid material does not. This means that the sodium alginate chains are certainly not sitting on the surface of the silica and may provide some evidence to corroborate the mechanism of formation proposed by Shchipunov[84a,b] and discussed in Chapter 7.1, in which, the polysaccharide provides a template for the silica structure to form around it.

## 5.3 Summary

**Table 9: The band positions and intensities for iodine adsorbed on all the materials in this investigation**

| **Material** | **$I_3^-$ HF[a] position/nm** | **Intensity** | **$I_3^-$ main position/nm** | **Intensity** | **$I_2$ position/nm** | **Intensity** |
|---|---|---|---|---|---|---|
| Silica $K_{60}$ 120˚C | 303 | 0.168 | 355 | 0.304 | 494 | 0.248 |
| Silica $K_{60}$ 400˚C | 303 | 0.066 | 360 | 0.078 | 503 | 0.282 |
| Silica $K_{60}$ 700˚C | 303 | 0.056 | 360 | 0.098 | 511 | 0.161 |
| ZSM-5 $SiO_2$:$Al_2O_3$=30 | 313 | 0.068 | | | 516 | 0.238 |
| ZSM-5 $SiO_2$:$Al_2O3$=280 | 311 | 0.104 | | | 518 | 0.27 |
| Ammonium Y Zeolite | | | 374 | 0.154 | 495 | 0.121 |
| 13x Zeolite | 309 | 0.391 | 353 | 0.566 | | |
| Neutral Brockmann Alumina | 316 | 0.445 | 411 | 0.578 | | |
| Basic Brockmann Alumina | 316 | 0.445 | 368 | 0.664 | | |
| Calcium Oxide RT | 309 | 0.133 | 373 | 0.172 | | |

| | | | | | | |
|---|---|---|---|---|---|---|
| Zirconia + 13% $Al_2O_3$ 600˚C | | | 365 | 0.637 | | |
| Sulfated Zirconia 600˚C | | | | | 494 | 0.09 |
| Zinc Oxide[b] | | | 437 | 0.196 | | |
| Sodium Carbonate | 308 | 0.388 | 352 | 0.566 | | |
| Sodium Hydrogen Carbonate | 311 | 0.314 | 402 | 0.404 | | |
| Sodium Sulfate | 311 | 0.314 | 399 | 0.416 | | |
| Calcium Carbonate | 311 | 0.314 | 379 | 0.473 | | |
| Sodium Acetate | 305 | 0.103 | 362 | 0.128 | | |
| Sodium Hydrogen Phosphate | 308 | 0.162 | 356 | 0.225 | | |
| HMS 500˚C[c] | 307 | 0.047 | 345 | 0.049 | 521 | 0.064 |
| HMDS Silica | 307 | 0.382 | 358 | 0.532 | | |
| AMP Silica | 305 | 0.081 | 352 | 0.093 | | |
| Thiol Silica | 298 | 0.015 | | | | |
| Octadecyl Silica | 322 | 0.493 | 383 | 0.589 | | |

| | | | | | | |
|---|---|---|---|---|---|---|
| Piperidino Silica | 344 | 0.562 | 386 | 0.649 | 524 | 0.782 |
| K-carrageenan | 307 | 0.146 | 366 | 0.244 | | |
| Chitosan | 315 | 0.093 | 396 | 0.292 | | |
| $Na^+$ Alginate | | | | | 555 | 0.46 |
| $Na^+$ Carboxymethylcellulose | 307 | 0.146 | 362 | 0.223 | | |
| Silica/K-carrageenan | 312 | 0.124 | 366 | 0.239 | | |
| Silica/Chitosan | 305 | 0.043 | 372 | 0.056 | | |
| Silica/ $Na^+$ Alginate | 307 | 0.18 | 361 | 0.295 | | |
| Silica/ $Na^+$ CMC | 306 | 0.152 | 357 | 0.224 | | |

[a] HF refers to the highest energy band. [b] The absorption band for $I_2$ on zinc oxide is broad and asymmetric and most likely involves bands for both $I_2$ and $I_3^-$, [c] The bands for $I_3^-$ on HMS are not separated and the $\lambda_{max}$ values are only an estimate.

Table 9 highlights several trends in the behaviour of iodine on the wide variety of solid surfaces tested. It can be noted that when used as a probe molecule, iodine (at least in forms detectable by UV-visible spectroscopy) sometimes is only adsorbed in low concentrations. This seemed particularly pronounced in this study on the some of the organically functionalised silica samples, such as the thiol silica, AMP silica and silica/chitosan. This is surprising because iodine is expected to form strong interactions with amines, indeed the ammonium Y zeolite and the commercial sample of piperidino functionalised silica show very high uptake of iodine. The low concentration of visible iodine on the thiol silica has already been accounted for by the reduction of $I_2$ and associated formation of S-S bonds and HI.

Low concentrations of visible iodine on the organically functionalised silica samples (with amines groups) was also unexpected because the silica samples show a good deal of mesoporosity and iodine molecules have a van der Waals radius of 4.3Å.[163] So, iodine should have no difficulty in accessing the pores, besides iodine has been shown to adsorb into the channels of zeolites[164] and microporous silicas.[165]

As can be seen from table 9, iodine shows different behaviour on all of the surfaces. On the majority of the surfaces studied, some or all of the $I_2$ is converted to $I_3^-$. These bands for $I_3^-$ show large shifts between the different surfaces. However, it is difficult to correlate these shifts to the surface properties. On those surfaces where both $I_2$ and $I_3^-$ are present such as the silica samples, the ZSM-5 zeolites and the ammonium Y zeolite although the bands for both $I_2$ and $I_3^-$ show significant shifts, there does not seem to be any pattern to the direction or size of the peak shifts. For example, on silica K60 treated at 120˚C, iodine bands are observed at 494nm for $I_2$ and 355 and 303nm for $I_3^-$. For ammonium Y zeolite, which shows a band for $I_2$ at approximately the same position at 494nm, the main band relating to $I_3^-$ is found at 374nm and the high energy transition is not observed. For sodium carbonate and sodium hydrogen carbonate, which would be expected to

have relatively similar properties, the main $I_3^-$ band is found at completely different positions, 352nm for sodium carbonate and 402nm for sodium hydrogen carbonate. This makes it very difficult to assess, except in general terms, the surface basicity of those surfaces upon which $I_2$ is converted entirely to $I_3^-$.

## 5.4 Impact of Humidity of the Atmosphere on the Behaviour of Iodine Adsorbed on Solid Surfaces

It was considered that some of the anomalous behaviour as discussed in section 5.3 could be explained to some extent by varying degrees of water adsorption by the surfaces. Although the solids in many cases were dried before addition of the iodine and the iodine was added to the surface in a closed vessel. It was thought that these conditions were not rigorous enough to entirely eliminate water. Also, as soon as the samples were removed from the dessicator, even with the lids on the vials they would adsorb water in the fairly humid environment of the laboratory.

Therefore, iodine adsorption on a selection of the solids was carried out under conditions of a 10% humidity atmosphere and a 50% humidity atmosphere. The atmospheric humidity was controlled by the use of sulphuric acid solutions as detailed in Chapter 2.4. The solids chosen were 13x zeolite, silica K60, calcium oxide, basic activated Brockmann alumina and zeolite ZSM-5 $SiO_2$:$Al_2O_3$= 80.

Initially the solid samples were placed in the controlled humidity chamber without iodine to measure the mass change. Table 10 shows the levels of mass increase in the different levels of humidity. It can be seen that even in a very dry environment; a small increase in mass can be noted. This is perhaps surprising because the atmosphere in the laboratory would be expected to be much more humid than this and the samples were not dried

before being placed into the controlled humidity chamber. However, the 13x zeolite did not increase in mass. As expected, contact with the 50% humidity atmosphere resulted in a much larger mass increase.

**Table 10: The mass change of the solid samples after exposure to different levels of humidity for around 3 hours**

| **Solid** | **Mass change after 10% humidity treatment/g** | **Mass change after 50% humidity treatment/g** |
|---|---|---|
| 13x zeolite | 0.00 | +0.0124 |
| Silica K60 | +0.053 | +0.1365 |
| Calcium oxide | +0.0898 | +0.1797 |
| ZSM-5 $SiO_2$:$Al_2O_3$= 80 | +0.0082 | +0.0172 |
| Basic activated Brockmann alumina | +0.0816 | +0.1512 |

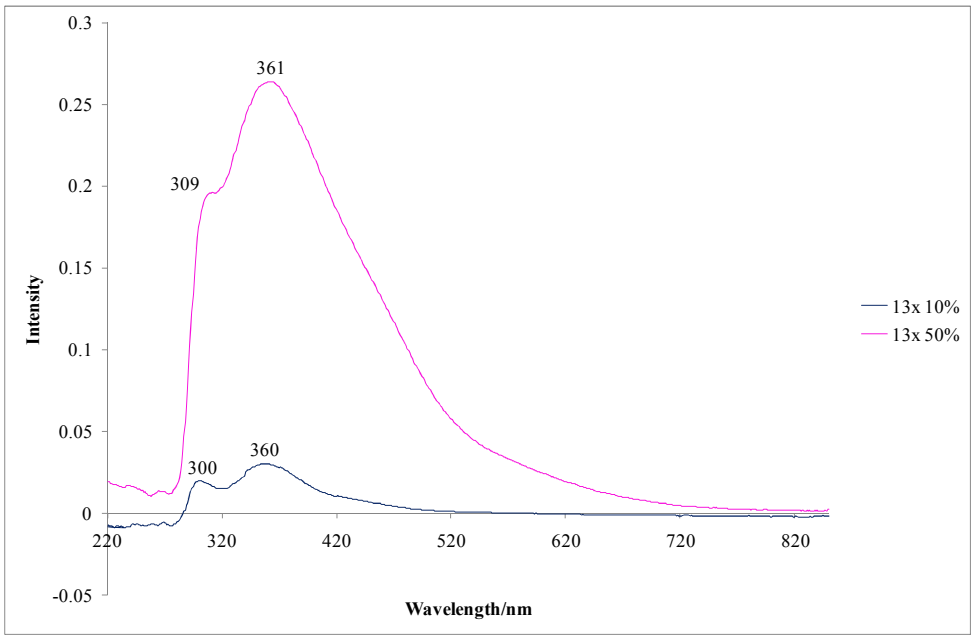


**Figure 113: UV-Visible spectra showing iodine adsorbed on 13x zeolite under different atmospheric humidity conditions**

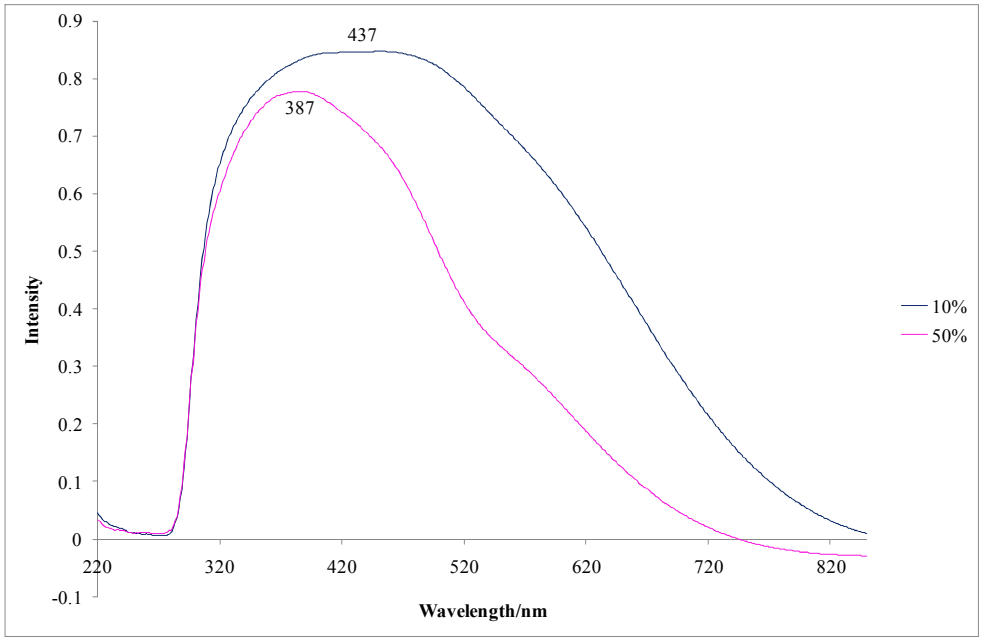


**Figure 114: UV-Visible spectra showing iodine adsorbed on basic activated Brockmann alumina under different atmospheric humidity conditions**

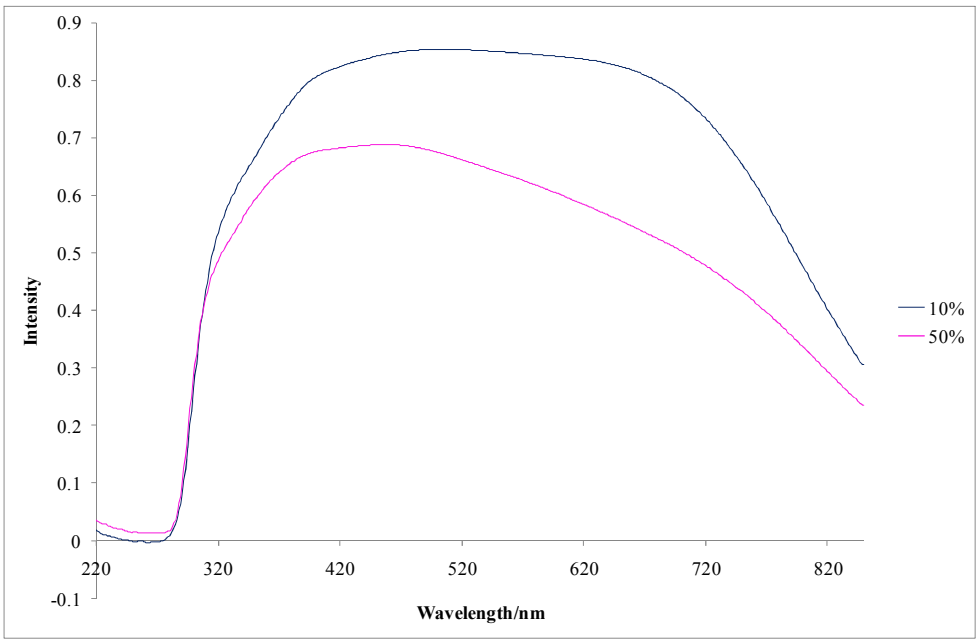


**Figure 115: UV-Visible spectra showing iodine adsorbed on calcium oxide under different atmospheric humidity conditions**

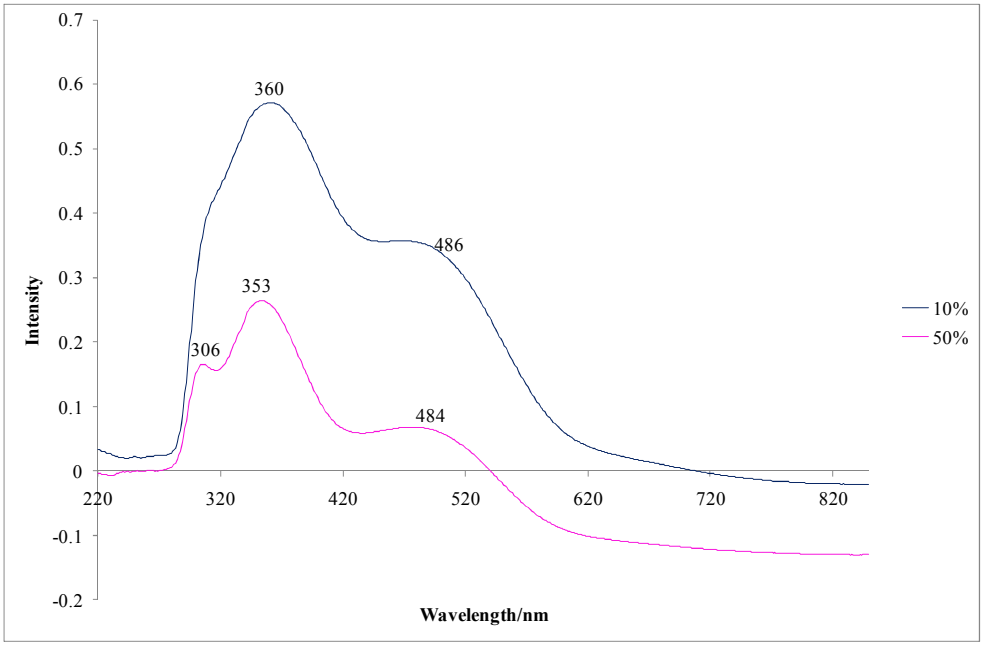


**Figure 116: UV-Visible spectra showing iodine adsorbed on silica K60 under different atmospheric humidity conditions**

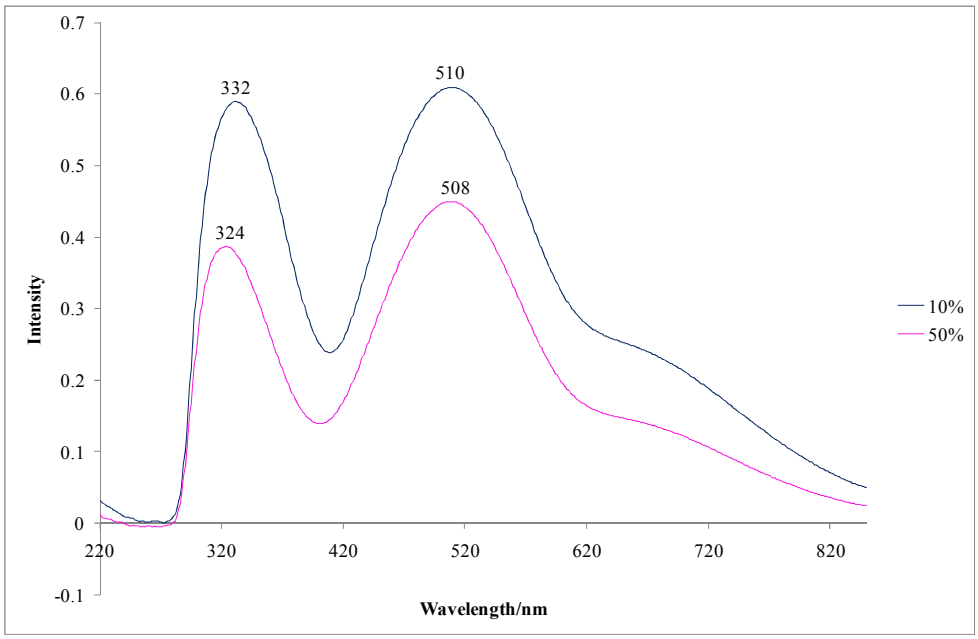


**Figure 117: UV-Visible spectra showing iodine adsorbed on ZSM-5 $SiO_2$:$Al_2O_3$=80 under different atmospheric humidity conditions**

Apart from the 13x zeolite shown in figure 113, it can be seen that a greater concentration of iodine is adsorbed on the surfaces in the lower humidity atmosphere. The higher humidity atmosphere also leads to a shift in the bands to a shorter wavelength. The adsorption of a greater concentration of iodine in a less humid atmosphere makes sense because water molecules would be expected to compete for the adsorption sites. The behaviour shown by 13x zeolite is somewhat unexpected but the higher iodine concentration in a higher humidity atmosphere is corroborated by the intensity of the iodine bands shown in figure 105 where no efforts to control or determine the levels atmospheric humidity were made. It may be that the solvation effects of the surface water create a more favourable environment for iodine adsorption than the dry surface.

As expected, for the majority of the surfaces used in this humidity study the behaviour of iodine on the surfaces when adsorbed in a 50% humidity environment matched that seen in the previous comparison of different surfaces in section 5.3. This is not true in the case of calcium oxide. In

figure 115, the intensity and broadness of the iodine bands are much greater than that shown in figure 106. One possible explanation is that several bottles of calcium oxide were present in the laboratory and a sample with a different level of hydration was used in the humidity study.

The blue-shift of the bands when iodine is adsorbed onto the surfaces in a more humid environment is the same as that shown in figure 104 when silica K60 is dried under increasingly rigorous conditions. From this it appears that surface molecular water has a significant impact on the chemistry of these surfaces. This seems to be particularly true for those surfaces on which the iodine is converted to $I_3^-$. It may be hypothesised that the water solvates and stabilises the $I^+$ and $I_3^-$ ions.

The most important outcome from this investigation is the knowledge that the atmospheric humidity has a significant impact on the behaviour of iodine as a probe molecule and in future investigations steps should be taken to control this.

## 5.5 The Behaviour of Iodine in Solution

For the purposes of comparison the UV-visible spectra of iodine dissolved in a number of different solvents were recorded. The solvents chosen were those with boiling points of 120˚C or above so that they could be used for the Knoevenagel condensation model reactions in Chapter 6. The spectra are shown in figure 118 and the peak positions and intensities are given in table 11.

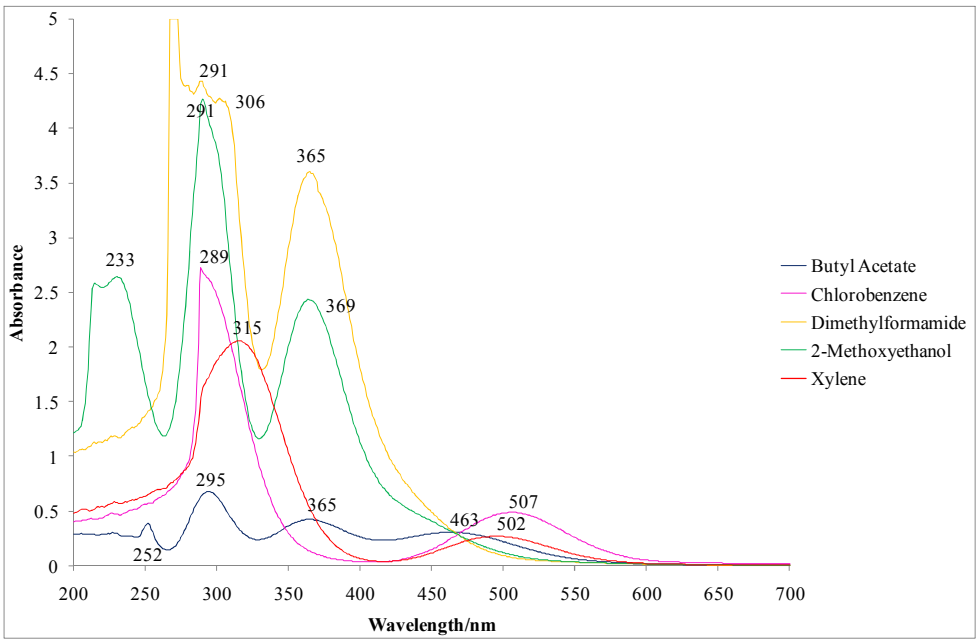


**Figure 118: UV-Visible Spectra of iodine dissolved in various solvents**

When iodine is dissolved in solution, as well as the bands relating to $I_2$ and $I_3^-$, it is also possible to observe bands relating to the charge transfer transition between the solvent and iodine. This band is observed in all of the solvents apart from dimethylformamide. In DMF $I_2$ seems to be entirely converted to $I_3^-$. In DMF the band for $I_3^-$ saturated the signal, so $\lambda_{max}$ cannot be determined accurately.

The band positions for $I_3^-$ in DMF and 2-methoxyethanol are quite similar to those of fairly basic solids such as calcium oxide and basic Brockmann alumina. The $I_2$ band position in xylene and chlorobenzene is similar to that for weakly basic solids such as silica.

**Table 11: Band positions and intensities for the UV-visible spectra of iodine dissolved in a series of solvents[74]**

| Solvent | Charge Transfer position/nm | Intensity | $I_3^-$ position/nm | Intensity | $I_3^-$ Position/nm | Intensity | $I_2$ Position/nm | Intensity |
|---|---|---|---|---|---|---|---|---|
| Xylene | 315 | 2.05 | | | | | 502 | 0.265 |
| Chlorobenzene | 289 | 2.72 | | | | | 507 | 0.485 |
| Butyl Acetate | 252 | 0.389 | 295 | 0.677 | 365 | 0.422 | 463 | 0.307 |
| 2-Methoxyethanol | 233 | 2.62 | 291 | 4.26 | 369 | 2.39 | | |
| Dimethylformamide | | | 290 | 4.43 | 365 | 3.6 | | |

## 5.6 Conclusions

Iodine as a UV-visible probe of surface basicity shows the ability to distinguish between otherwise difficult to analyse surfaces such as sodium acetate and zinc oxide. The conversion of $I_2$ to $I_3^-$ seems, as well as being a measure of surface basicity, to be a measure of the surface hydration. The behaviour of iodine on organically functionalised surfaces and organic-inorganic hybrid materials was also very interesting.

For more detailed analysis of the spectra of iodine adsorbed on surfaces, the intensity of the $I_2$ and $I_3^-$ bands may be normalised using knowledge of their extinction coefficients. This would allow the concentration of sites capable of converting $I_2$ to $I_3^-$ to be estimated.

As with all probe molecules, there are certain factors that have to be taken into account when interpreting the spectra. In the case of iodine it has been observed that surfaces do not adsorb iodine at equal concentrations and it is known that the position of the $I_2$ band is dependent on the iodine concentration.[69] Also, as discussed in section 5.4, the atmospheric humidity and hence the levels of surface hydration have an impact on the band position and intensity. Thirdly, as has been discussed previously, it is not yet known what causes the shifts in the $I_3^-$ band position.

.

# Chapter 6: The Knoevenagel Condensation Reaction as a Test for Surface Basicity

## 6.1 Introduction

As covered in Chapter 1.5 on the use of model reactions as a method for characterising acid-base catalysis, one reaction studied is the Knoevenagel condensation of benzaldehyde with compounds such as malononitrile, ethyl cyanoacetate and ethyl acetoacetate.[5,79c,166] This particular model reaction was selected for this study because unlike the majority of the others it can be run as liquid phase batch reactions rather than as high temperature gas phase reactions using flow-through apparatus. This made it easier to carry out using the equipment available in the laboratory.

This model reaction was used as another test for basicity for a group of the solid catalysts studied by iodine adsorption and UV-visible spectroscopy measurements in chapter 5. As can be seen from the results and discussion, the outcome was not necessarily as expected. So the model reaction was also carried out in a range of solvents of different basicities to exclude specific surface effects.

It was found that out of ethyl cyanoacetate and ethyl acetoacetate only the latter was sufficiently active with benzaldehyde to permit following the reaction over the course of a day with the chosen solid catalysts and the temperatures used (120-140˚C). Malononitrile was also investigated but the melting point of this reactant (32˚C) meant that it was more difficult to work with and so ethyl acetoacetate was selected as the reactant.

After some initially unsuccessful trials, it was decided that the higher temperature (140˚C ) using xylene rather than toluene as a solvent were the

most appropriate conditions. As detailed in the Chapter 2.5, the solids tested ranged from inorganic oxides and carbonates to organic polymers such as chitin and included the silica/polysaccharide hybrid materials that were synthesised. The two bench mark reactions were; the mixture with no catalyst and 3-aminopropyl silica (designated AMP silica) as a catalyst. The formation of the Knoevenagel product was confirmed by GC-MS.

## 6.2 Testing of Different Solid Catalysts

### Results

**Table 12: GC Retention Times of the Starting Materials, Internal Standard and Product in the Knoevenagel Condensation Model Reaction**

| Molecule | Retention Time/mins |
|---|---|
| Ethyl acetoacetate | 3.44 |
| Benzaldehyde | 3.65 |
| Dodecane (internal standard) | 5.69 |
| Product (Ethyl 2-benzylideneacetoacetate) | 9.7 |

The GC peak areas were all normalised by dividing the area of the peak in question by that of the area of the dodecane peak for each sample taken. Literature values for the response factors could only be found for benzaldehyde and dodecane. Attempts were made to predict response factors using the effective carbon number (ECN) method of Scanlon and Willis[167] using the calculation given in the paper by Katritzky[168](RF=[(MW

compound/ECN standard)/(MW standard/ECN compound)] with dodecane as the standard. However, values for the effective carbon numbers for ethyl acetoacetate and ethyl 2-benzylideneacetoacetate could not be found either and attempts to estimate them based on the functional groups according to work by Jorgensen[169] gave rather strange results (values of 0.33 (ECN=6.6) for benzaldehyde 0.25 (ECN= 3.95) for ethyl acetoacetate and 1.13(ECN=10.9) for the product, using an ECN value of 12.34 for dodecane. Although it would have been possible to determine experimentally response factors for the reactants by the use of calibration curves, insufficient quantities of the product were obtained for this. Since, in this study only relative values were of interest, response factors were not considered further.

As can be seen from figures 119 and 120, it was not possible to obtain quantitative kinetic or thermodynamic information about the reactions because the rate of consumption of the reactants differed very little between all the reactions. However, it was possible to compare the rate of product formation between the different catalysts.

In all of the following graphs "Normalised GC peak area" refers to the area of the peak for the relevant reactant or product divided by the area of the peak for dodecane (internal standard).

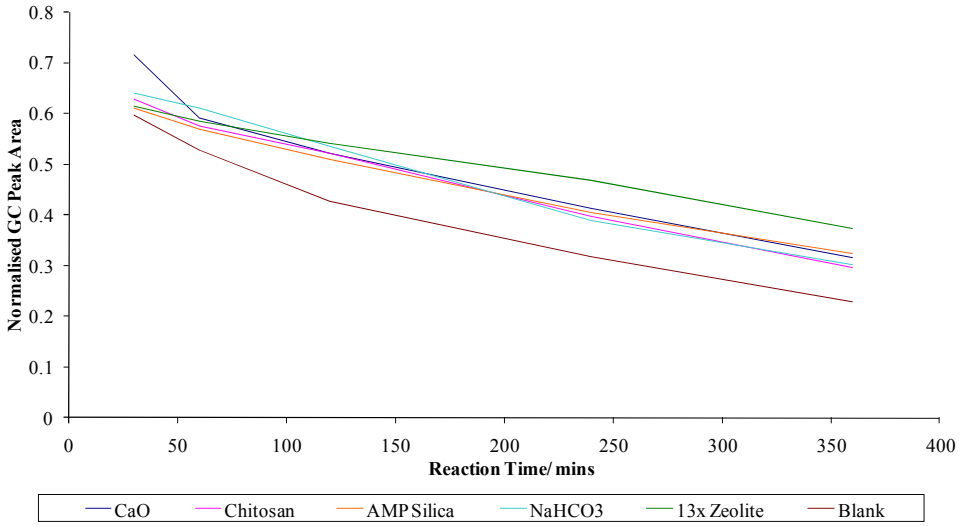


**Figure 119: Graph showing the rate of consumption of ethyl acetoacetate during the Knoevenagel condensation for a selection of the catalysts tested**

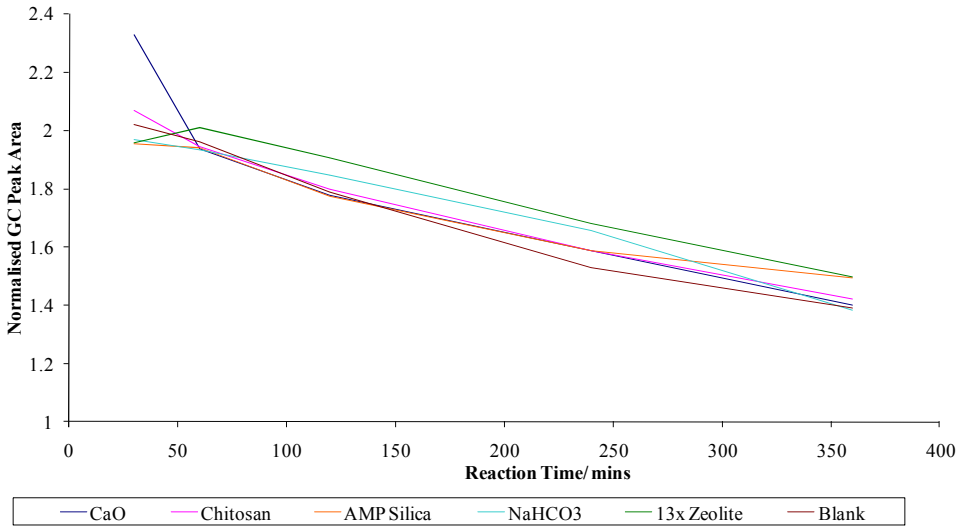


**Figure 120: Graph showing the rate of benzaldehyde consumption during the Knoevenagel condensation for a selection of the catalysts tested**

The rate of product formation is shown for all the catalysts tested in figures 121 and 122, they are separated into two groups for the purpose of clarity.

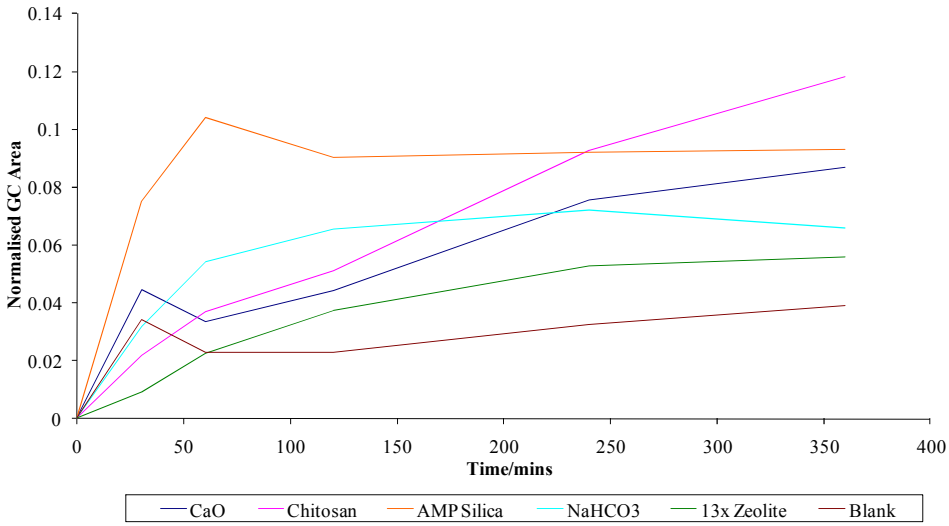


**Figure 121: Graph Showing the Rate of Product Formation during the Knoevenagel Condensation for a Selection of the Catalysts Tested**

For the catalysts shown in figures 119-121, the reactions were repeated and the values shown at each time are an average value for the two runs, however due to shortage of time, a second run was not carried out for the reactions shown in figure 122.

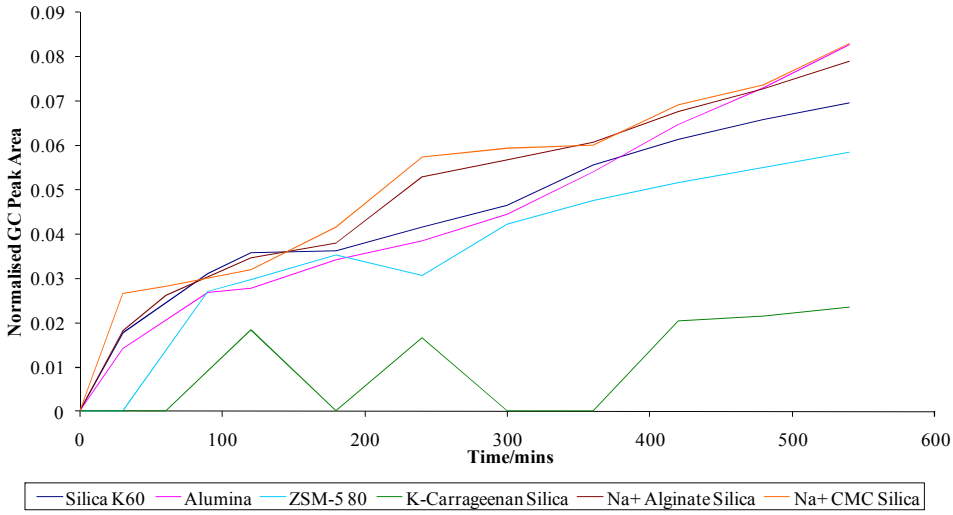


**Figure 122: Graph showing the rate of product formation during the Knoevenagel condensation for the rest of the catalysts tested**

Due to the fact that at the end of the reaction time some benzaldehyde and ethyl acetoacetate remain in the reaction mixture it can be seen that the reactions have not gone to completion. Though they do seem to have reached a plateau where the normalized benzaldehyde peak areas have decreased in intensity by 31-40% and normalized ethyl acetoacetate peak areas by 68-86%.

It was decided that the measure of basicity for the different catalysts should be taken as the gradient of the normalised GC peak area plotted against time for the initial stages of the reaction. Figures 123 and 124 show the initial rates of product formation for the Knoevenagel test reactions and table 13 summarises the results.

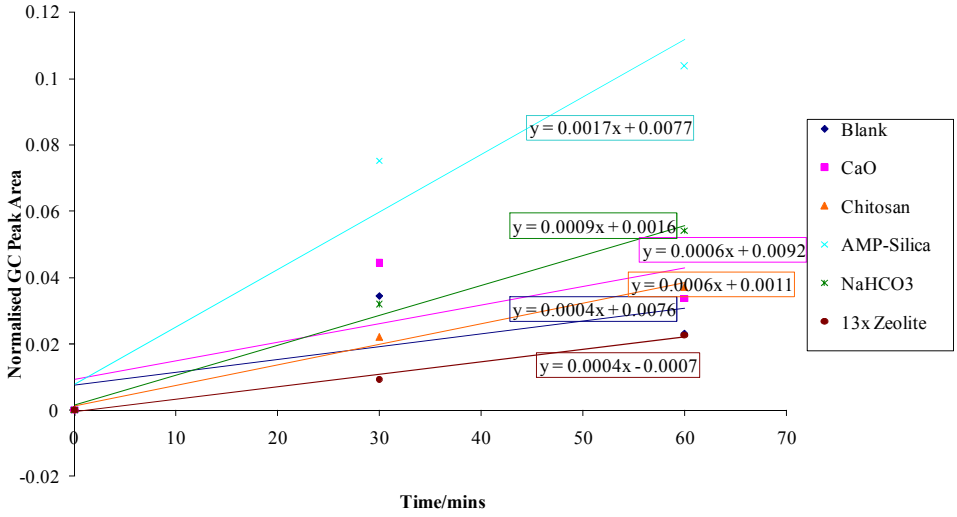


**Figure 123: Initial Rates of Product Formation Graph 1**

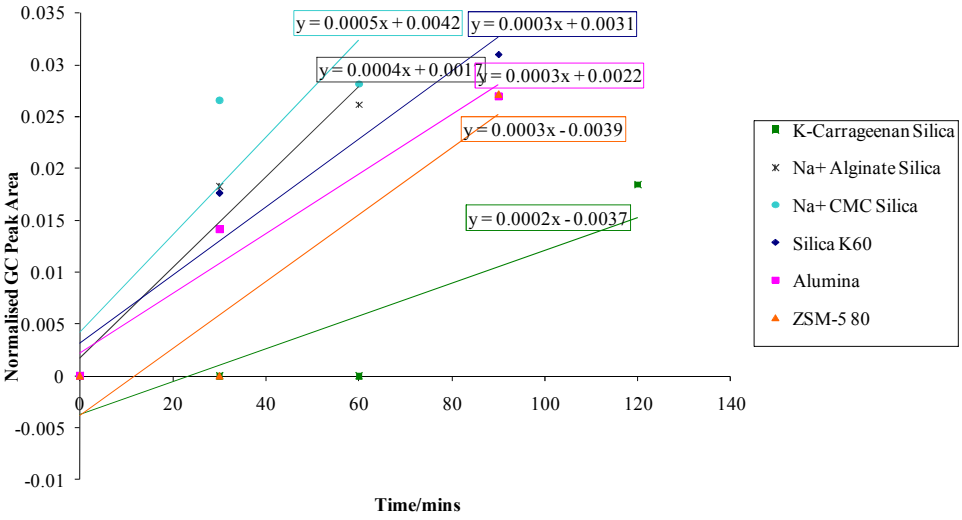


**Figure 124: Initial Rates of Product Formation Graph 2**

It is unfortunate that there was insufficient time to repeat the experiments that produced the graph shown in figure 124 as there is a good deal of scatter in the data points. It is quite difficult to draw firm conclusions from

the data plotted here. The data points from these experiments used in subsequent tables should therefore be treated with some caution.

**Table 13: Summary of the Results of the Knoevenagel Model Reactions with Solid Catalysts**

| Catalyst | Gradient | Intercept |
|---|---|---|
| AMP Silica | 0.0017 | 0.0077 |
| $NaHCO_3$ | 0.0009 | 0.0016 |
| CaO | 0.0006 | 0.0092 |
| Chitosan | 0.0006 | 0.0011 |
| [1.] Sodium carboxymethylcelluose/silica ($Na^+$CMC silica) | 0.0005 | 0.0042 |
| Blank (no catalyst) | 0.0004 | 0.0076 |
| [1.] Sodium Alginate/ Silica | 0.0004 | 0.0017 |
| 13x Zeolite | 0.0004 | -0.0007 |
| [1.] Silica K60 | 0.0003 | 0.0031 |
| [1.] Neutral Activated Brockmann Alumina (Alumina) | 0.0003 | 0.0022 |
| [1.] Zeolite ZSM-5 Silica: Alumina Ratio =80 (ZSM-5 80) | 0.0003 | -0.0039 |
| [1.] K-Carrageenan /Silica | 0.0002 | -0.0037 |

1. Only 1 experimental run was carried out for these catalysts so the results should be treated with caution
2. A chitosan/silica hybrid material was also manufactured but there were difficulties in getting a gel to form and so there was not enough

of the material to carry out these tests with. However there are results from the iodine adsorption studies shown in chapter 5.

The results in table 13 are given in order of decreasing basicity as measured by the initial rate of product formation for the Knoevenagel condensation. Where the gradient for the initial rate of product formation is the same, those with the most positive intercept values are taken to be the most basic of that group. The reason for this is that if the line of best fit was forced through the origin, the gradient would be steeper.

## Discussion

The use of the Knoevenagel condensation as a test reaction is slightly complicated by the fact there are two possible mechanisms by which the reaction can occur. One is known as the ion-pair mechanism, shown in figure 125. This is the mechanism that operates on inorganic catalysts such as zeolites and on tertiary amine groups. The reaction also occurs via this mechanism when uncatalysed in protic solvents.[79a]

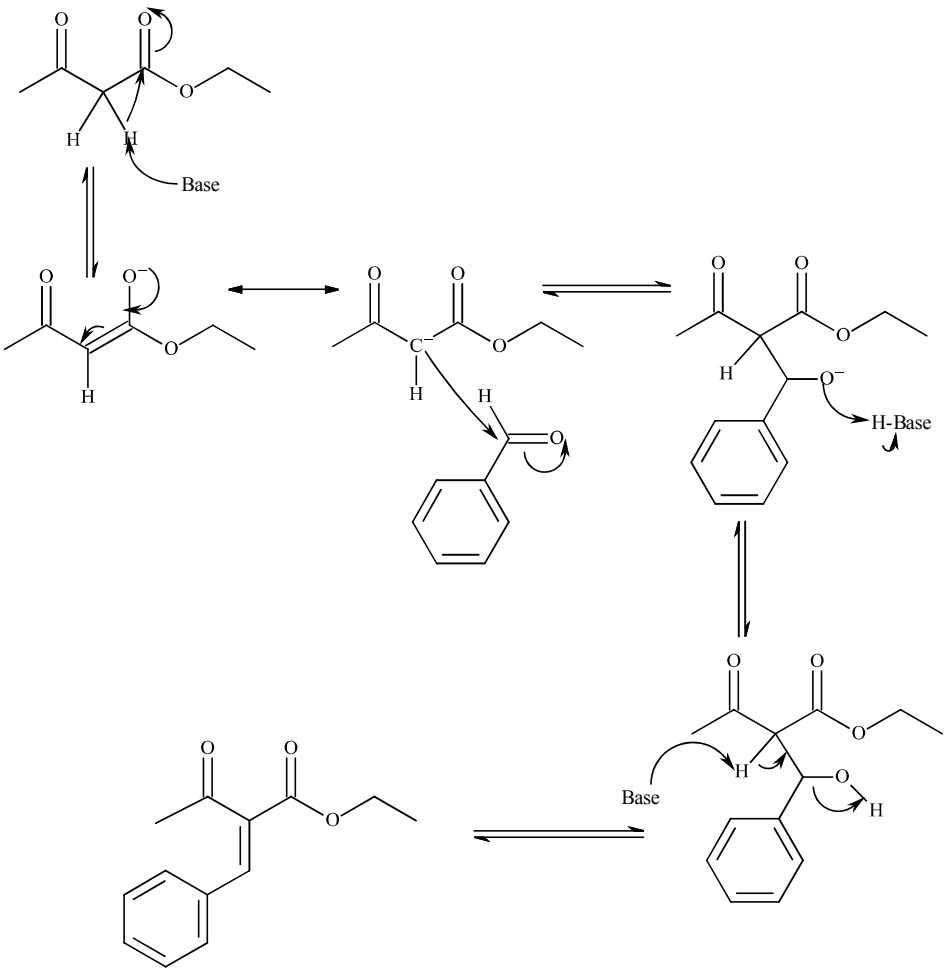


**Figure 125: The ion-pair mechanism for the Knoevenagel condensation**

The Knoevenagel condensation using a primary amine functionalized catalyst is thought to occur via an imine intermediate. Some evidence for this comes from the observation that imines are formed when benzaldehyde is reacted with 3-aminopropyl functionalised silica. [7]The imine mechanism proposed by Brunel is shown in figure 126.[170]

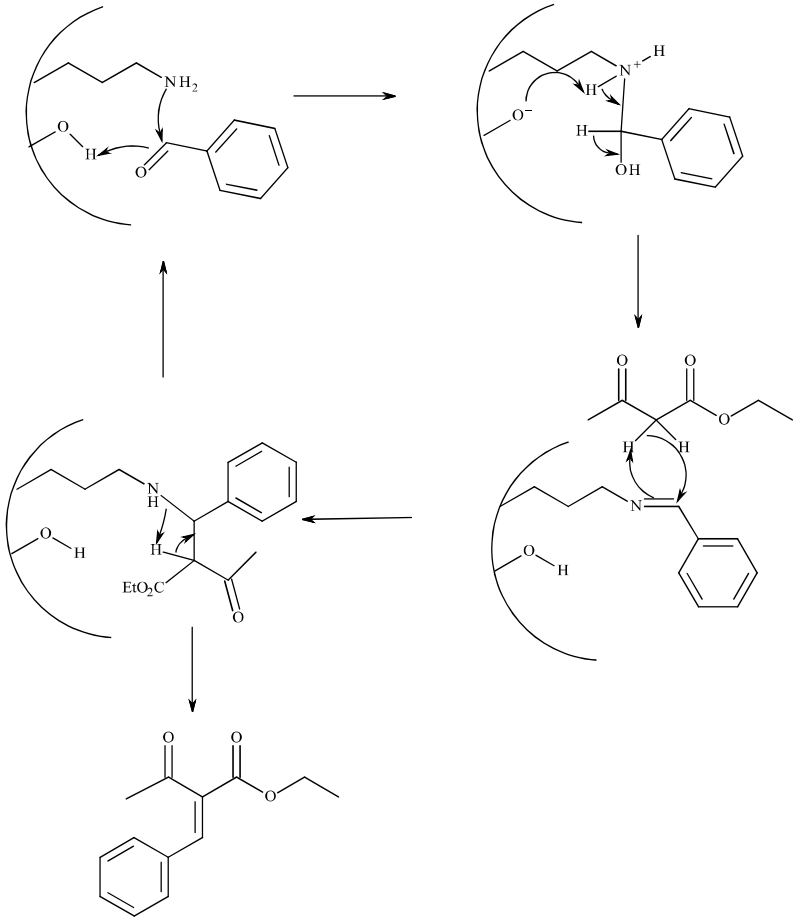

**Figure 126: The primary amine mechanism for the Knoevenagel condensation**

This second mechanism explains why the reaction occurs much more efficiently on those catalysts that incorporate primary amine groups, in this study those are 3-aminopropyl functionalized silica and chitosan. In the literature it was found that the turnover rate for the Knoevenagel condensation of benzaldehyde and ethyl cyanoacetate for primary and tertiary amine sites was 3.4 and $0.61^{-1}$min$^{-1}$ respectively.[171]

The fact that the rate of reaction is initially slow on chitosan but increases towards the end of the reaction time can be attributed to swelling of the chitosan and hence increasing the accessibility of the active sites. As with all the catalysts, the chitosan was put in dry but at the end of the reaction it had visibly swollen. Pre-swelling of chitosan would therefore most likely

improve the rate of reaction. However, the rate of reaction is initially fast on the 3-aminopropyl silica and then levels off; this is not due to complete consumption of the reactants as shown by figures 119 and 120. It has been suggested that the amine group may form an amide with the ester group of the ethyl acetoacetate which may not turn-over.[172]

It is interesting to note that on many of the surfaces tested, the reaction occurs more slowly than when there is no catalyst. It appears that many of these materials actually inhibit the reaction. With reference to the ion pair mechanism shown in figure 125, the reaction requires the presence of sites capable of removing a proton from ethyl acetoacetate. Ethyl acetoacetate has a $pK_a$ of 10.7, the pKa of a silanol groups for instance is around 7.[106] It seems that the ethyl acetoacetate may adsorb on the silica surface but preferentially in its protonated form, stabilization of the anion would be disfavoured.

The incorporation of sodium carboxymethyl cellulose and sodium alginate into silica increases the basicity; however, addition of κ-carrageenan decreases the basicity. This shows that the polysaccharides do have an impact upon the surface chemistry of the hybrid materials.

It was thought that perhaps the results from the UV-visible spectroscopy and the Knoevenagel condensation test reactions may show some correlation however as seen from table 14, there is little evidence of such correlation.

**Table 14: Comparison of the results from the Knoevenagel condensation test reactions and the iodine adsorption experiments**

| Catalyst | Gradient | Intercept | $I_3^-$ HF position/nm | Intensity | $I_3^-$ main position/nm | Intensity | $I_2$ position/nm | Intensity |
|---|---|---|---|---|---|---|---|---|
| AMP Silica | 0.0017 | 0.0077 | 305 | 0.081 | 352 | 0.093 | | |
| $NaHCO_3$ | 0.0009 | 0.0016 | 311 | 0.314 | 402 | 0.404 | | |
| CaO | 0.0006 | 0.0092 | 309 | 0.133 | 373 | 0.172 | | |
| Chitosan | 0.0006 | 0.0011 | 315 | 0.093 | 396 | 0.292 | | |
| Sodium Carboxymethylcellulose/ Silica | 0.0005 | 0.0042 | 306 | 0.152 | 357 | 0.224 | | |
| Blank (no catalyst) | 0.0004 | 0.0076 | | | | | | |

| | | | | | | | | |
|---|---|---|---|---|---|---|---|---|
| Sodium Alginate/ Silica | 0.0004 | 0.0017 | 307 | 0.18 | 361 | 0.295 | | |
| 13x Zeolite | 0.0004 | -0.0007 | 309 | 0.391 | 353 | 0.566 | | |
| Silica $K_{60}$ | 0.0003 | 0.0031 | 303 | 0.168 | 355 | 0.304 | 494 | 0.248 |
| Neutral Activated Brockmann Alumina (Alumina) | 0.0003 | 0.0022 | 316 | 0.445 | 411 | 0.578 | | |
| Zeolite ZSM-5 Silica: Alumina Ratio =80 (ZSM-5 80) | 0.0003 | -0.0039 | 302 | 0.008 | | | 521 | 0.043 |
| K-Carrageenan /Silica | 0.0002 | -0.0037 | 312 | 0.124 | 366 | 0.239 | | |

It is unfortunate that on almost all of the catalysts tested, $I_2$ was converted to $I_3^-$ by the time the spectrum was recorded. Whether perhaps this might not have been the case if a quicker method of adsorbing iodine onto the surface had been used and therefore the iodine was not in contact with the surface for so long is unknown. For the two surfaces where the iodine is present as $I_2$ on the surface- the silica K60 and the ZSM-5 80, the red-shift of the $I_2$ band for ZSM-5 80, indicating lower electron-donating basicity does appear at least to follow the pattern of reduced activity for the Knoevenagel condensation reaction. As discussed in Chapter 5, the $\lambda_{max}$ of the main $I_3^-$ band at around 350-360nm shows quite extensive shifts however these have not been reliably correlated to surface properties. From table 14, it appears that they do not correlate with the surface basicity as measured by the catalytic activity of the surfaces in the Knoevenagel condensation.

## 6.3 Testing of Different Solvents

In order to eliminate the possibility of specific surface effects in interactions with iodine or in the Knoevenagel condensation reaction, the reaction was carried out without a catalyst and with $NaHCO_3$ as a catalyst in a number of different solvents. These results were compared to the iodine bands in the solvents and the Kamlet and Taft parameters for the solvents.

The solvents were selected for a variety of properties and a boiling point above 120˚C, at which temperature the reactions were carried out. The solvents chosen were butyl acetate, dimethylformamide (DMF), xylene, chlorobenzene and 2-methoxyethanol.

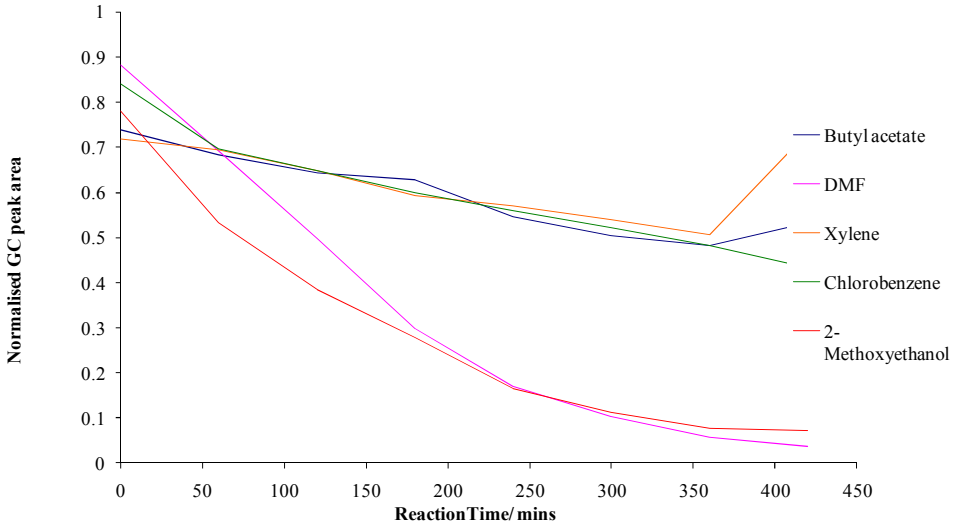


**Figure 127: Rate of ethyl acetoacetate consumption in Knoevenagel test reactions in different solvents without catalyst**

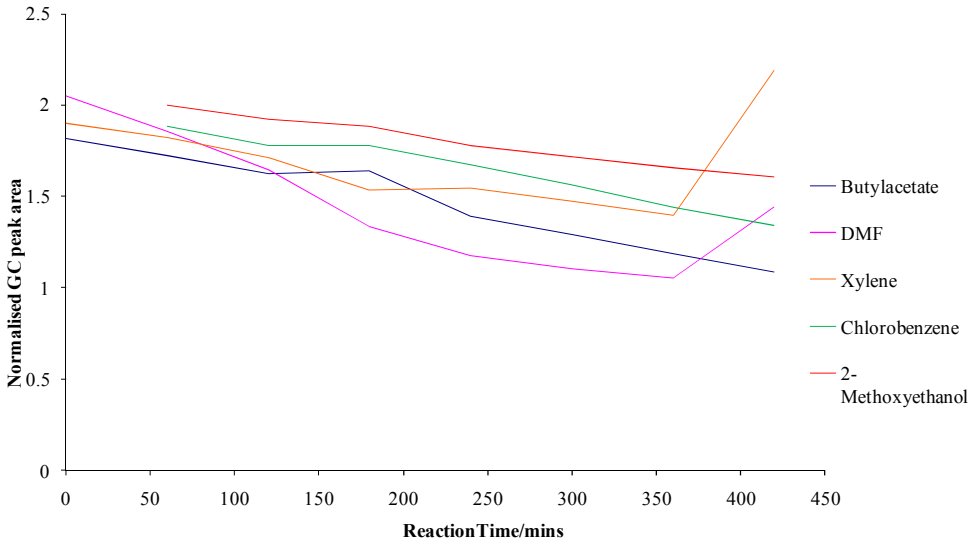


**Figure 128: Rate of benzaldehyde consumption in Knoevenagel test reactions in different solvents without catalyst**

As with many of the test reactions for solid catalysts, the values shown in figures 127-129 are the average of two runs of the reaction in each solvent.

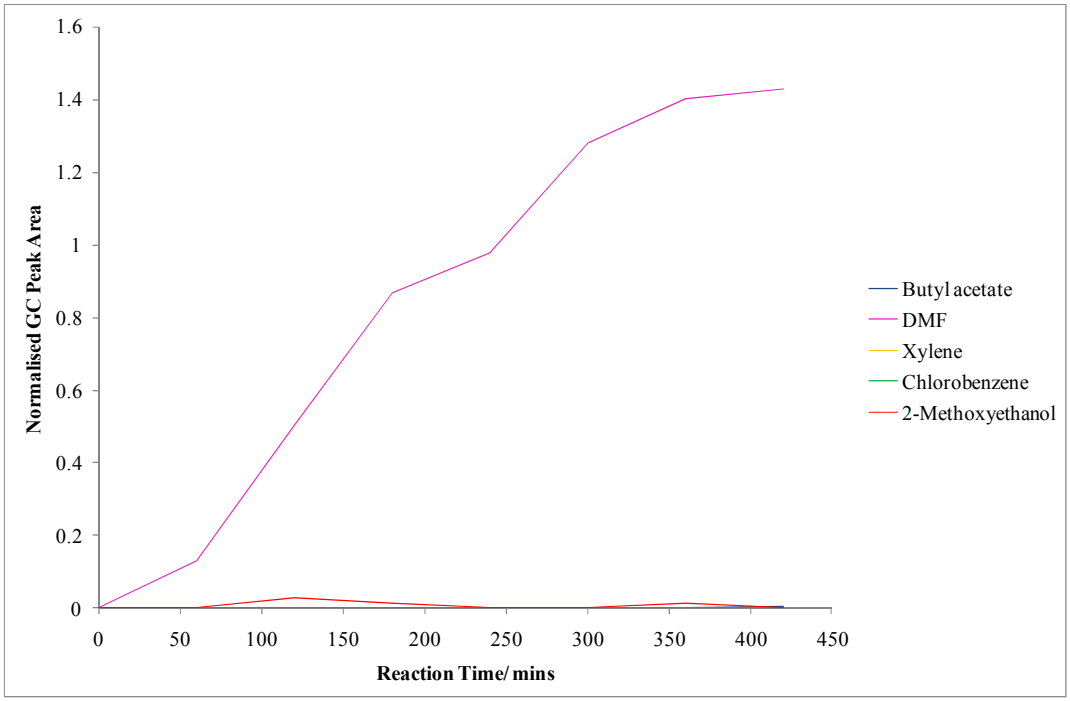


**Figure 129: The rate of product formation in Knoevenagel test reactions in different solvents without catalyst**

As can be seen from figure 129, only in the most active solvent did any significant product formation occur. Therefore the basicity was characterized by the initial slope for the ethyl acetoacetate consumption.

**Table 15: Initial rate of ethyl acetoacetate consumption compared with the Kamlet and Taft parameters for the solvents tested**

| | Kamlet and Taft Parameters[59] | | | |
|---|---|---|---|---|
| **Solvent** | **Ethyl acetoacetate gradient** | **π*** | **β** | **α** |
| Xylene | -0.0006 | 0.43 (p) 0.47 (m) | | |
| Chlorobenzene | -0.0008 | 0.71 | 0.07 | 0 |
| Butyl Acetate | -0.0016 | 0.46 | | 0 |
| 2-Methoxyethanol | -0.0033 | 0.71 | | |
| Dimethylformamide | -0.0032 | 0.88 | 0.69 | 0 |

**Table 16: The band positions and intensities for iodine dissolved in the solvents**

| | **Bands observed for iodine dissolved in the solvents**[a] | | | | | | | |
|---|---|---|---|---|---|---|---|---|
| **Solvent** | **Charge Transfer** | **Intensity** | **$I_3^-$ position/ nm** | **Intensity** | **$I_3^-$ Position/ nm** | **Intensity** | **$I_2$ Position/ nm** | **Intensity** |
| Xylene | 315 | 2.05 | | | | | 502 | 0.265 |
| Chlorobenzene | 289 | 2.72 | | | | | 507 | 0.485 |
| Butyl Acetate | 252 | 0.389 | 295 | 0.677 | 365 | 0.422 | 463 | 0.307 |
| 2-Methoxyethanol | 233 | 2.62 | 291 | 4.26 | 369 | 2.39 | | |
| Dimethyl-formamide | | | 290 | 4.43 | 365 | 3.6 | | |

[a]The assignments are based on those of Camarota *et al*.[74]

As can be seen from the Kamlet and Taft parameters in table 15, none of the solvents chosen show α (hydrogen bond donating acidities). Unfortunately the β (hydrogen bond accepting basicities) are not available for many of them. Unlike in the case of the solids however there is reasonably good correlation between the rate of ethyl acetoacetate consumption and the $\lambda_{max}$ values for iodine dissolved in the solvents. In xylene and chlorobenzene, which show similar rates of reaction in the Knoevenagel condensation, the $I_2$ $\lambda_{max}$ values are close together. Based on the differences in the gradients of ethyl acetoacetate consumption, it would be expected that the $I_2$ $\lambda_{max}$ value for chlorobenzene would be blue-shifted rather than red-shifted in comparison to that for xylene. However, since the difference in the gradients is so small and the $I_2$ peaks are relatively broad (see Chapter 5) the disagreement between the two techniques could well be due to experimental error.

The correlation can be clearly seen when going from the aromatic solvents to butyl acetate, which shows a more rapid consumption of ethyl acetoacetate and a large blue-shift in the $I_2$ $\lambda_{max}$ value. In the two most active solvents for the Knoevenagel condensation, iodine is dissociated to give $I_3^-$. Both tests for basicity therefore indicate a highly basic environment. It can also be observed from table 16 that the position of the charge transfer band is also blue-shifted down the table. This is not correlated simply with the basicity of the solvent but studies on various electron/donor acceptor systems show that the energy of the charge transfer band is correlated with donor ionization potential.[72]

In an attempt to produce a larger difference in the rate of the Knoevenagel condensation reaction in different solvents a catalyst was added. Sodium hydrogen carbonate was chosen as a catalyst that showed some activity in this reaction but was not the most efficient so that solvent effects might be observed. However as will be discussed later, the results were quite surprising.

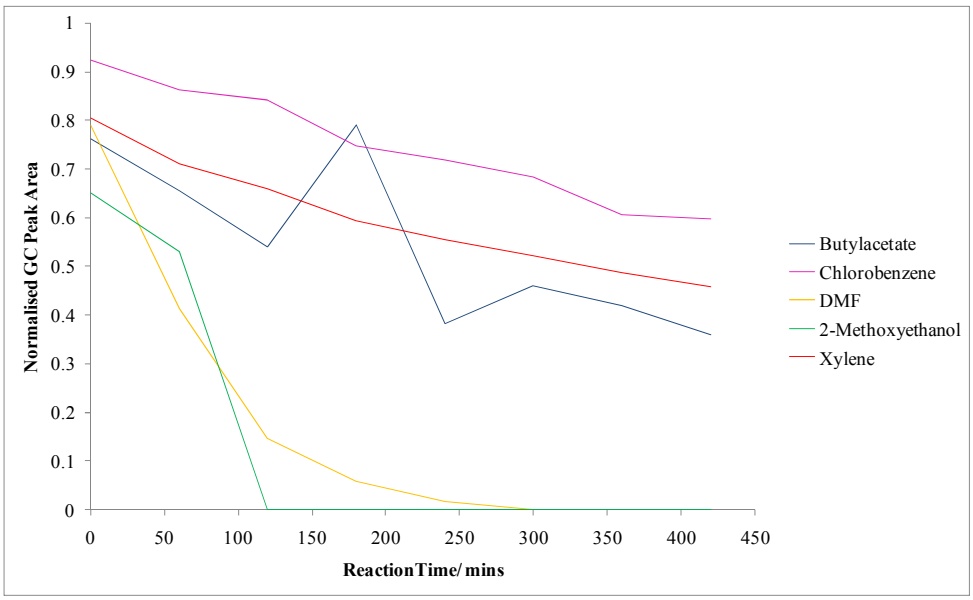


**Figure 130: Rate of ethyl acetoacetate consumption in the Knoevenagel condensation test reactions in different solvents with $NaHCO_3$ catalyst**

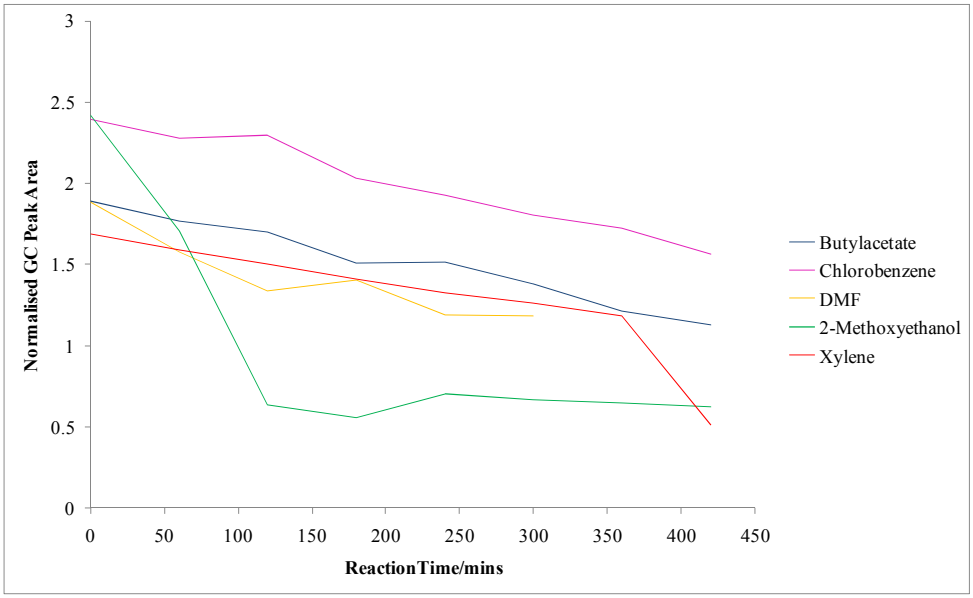


**Figure 131: Rate of benzaldehyde consumption in the Knoevenagel condensation test reactions in different solvents with $NaHCO_3$ catalyst**

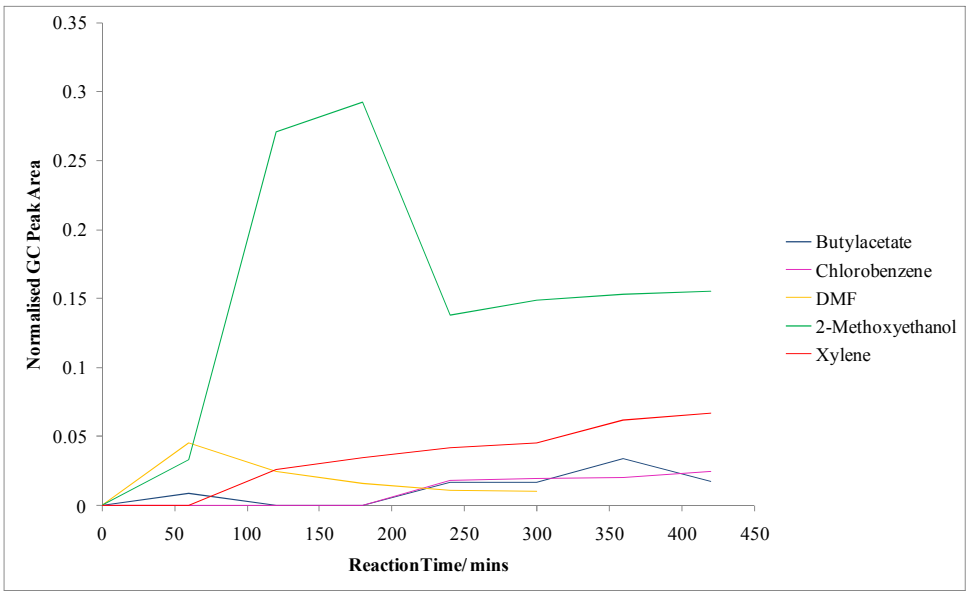


**Figure 132: Rate of product formation in the Knoevenagel condensation test reactions in different solvents with $NaHCO_3$ catalyst**

Again, the initial rate of ethyl acetate consumption was used as a measure of the basicity of the solvent. These are reported in table 17.

**Table 17: The initial gradient for ethyl acetoacetate consumption during the Knoevenagel condensation in different solvents with $NaHCO_3$ catalyst**

| **Solvent** | **Ethyl acetoacetate gradient** |
|---|---|
| Xylene | -0.0012 |
| Chlorobenzene | -0.0007 |
| Butyl Acetate | -0.0018 |
| 2-Methoxyethanol | -0.0054 |
| Dimethylformamide | -0.0054 |

As can be seen by comparison of tables 15 and 17, the trend for the rate of ethyl acetoacetate consumption is the same both with and without the $NaHCO_3$ catalyst. However in this case, the most efficient reaction system was $NaHCO_3$ in 2-methoxyethanol. As can be seen from figure 131, the reaction in dimethylformamide did not proceed as expected. Initially, the Knoevenagel product formed but this was rapidly converted to several different unknown products. These products seem to incorporate ethyl acetoacetate since this is entirely consumed. Several of the products would also appear to incorporate nitrogen containing groups. No evidence for reactions of this nature has been found in the literature. The GC and GC-MS data is shown in the appendix.

## 6.3 Conclusions

The Knoevenagel condensation reaction would appear to be a useful test for the basicity of both solid surfaces and solvents. For the solvents at least, the results are fairly consistent with those obtained from spectroscopic measurements of iodine dissolved in the solvents. However, for the solid surfaces tested, there is very little correlation. The behavior of iodine on the majority of these surfaces is quite complex and the most useful band (the $I_2$ $\pi^*$-$\sigma^*$band) is not observed. In the only two cases where this band is observed (on silica K60 and ZSM-5 80), the shift in the $\lambda_{max}$ value is in the expected direction based on the initial rate of product formation in the Knoevenagel condensation reaction. So it would seem that on weakly basic surfaces with no special interactions with iodine (such as that occurring with many polysaccharides) the two techniques might be correlated. However, with only two points, this cannot be stated for certain.

When using the Knoevenagel condensation as a test reaction, the possibility of it occurring by two different mechanisms must be taken into account. So, it would not be a suitable method for testing a completely unknown

material. Some knowledge of whether or not primary amine groups are present is necessary.

On the whole however, this is a useful technique and it has the advantage over many of the techniques used in previous chapters that the results are easily interpreted.

# Chapter 7: Preparation of Silica/Polysaccharide Hybrid Materials

## 7.1 Introduction

Nanocomposite materials based on silica prepared by the sol-gel technique in aqueous solutions have attracted attention because of their biocompatibility. One particular potential application is the entrapment of enzymes without having to covalently bond them to the surrounding matrix.[84c] However, the most commonly used precursors tetramethylorthosilicate (TMOS) and tetraethylorthosilicate (TEOS) are poorly water soluble. Solvents such as ethanol or acetonitrile are added to improve the solubility. In these solvents biopolymers may be less soluble and in some cases they can have a denaturing effect on the biopolymers.[173]

A new precursor has been developed, tetrakis(2-hydroxyethyl) orthosilicate (THEOS), from TEOS (or TMOS) and ethanediol[174] The structure of this is shown in figure 133. THEOS is completely water soluble and so no organic solvents are required in the reaction mixture. Shchipunov and co-workers used this precursor with a variety of biopolymers in order to create hybrid materials.[84] They found that these materials could be formed by the use of cationic, anionic or neutral polysaccharides. The properties of the materials changed with the charge on the polysaccharide. Anionic or neutral polysaccharides produced turbid or opaque hydrogels and cationic polysaccharides produced transparent or opalescent hydrogels.

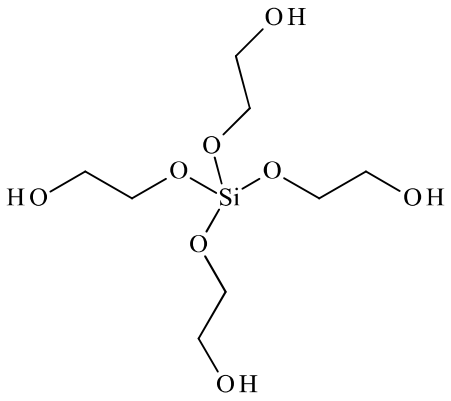


**Figure 133: The structure of tetrakis(2-hydroxyethyl)orthosilicate (THEOS)**

The polysaccharides were found to act as both a catalyst for the reaction and a template for the silica gel formation. In their first study they used carrageenans as the polysaccharides in the hybrid materials as these are known to form aqueous gels on their own. They found that addition of carrageenan to THEOS induced sol-gel formation without the need for any additional catalysts such as acids.[84a] They hypothesised that it was the large number of hydroxyl groups in these polysaccharides that catalysed the reaction and to test this they compared the catalytic activity polyvinyl alcohol, which has one OH for each repeating unit and polyethylene oxide which only has terminal OH groups. They found that polyvinyl alcohol catalysed the reaction but polyethylene oxide did not.[84b]

It was decided that any covalent bond formation between the polysaccharides and the silanol monomers was very slight and of minor importance in the reaction. On the basis of SEM images, DSC data indicating that when incorporated into these silicate materials κ-carrageenan did not lose its reversible helix-coil transition and evidence on the role of hydrogen bonding in biomineralization[175] Shchipunov and co-workers suggested that hydrogen bonding was the main interaction between the silica and polysaccharides in these systems.[84a]

The acceleration of the silica-gel formation by the polysaccharides is therefore believed to be caused by hydrogen-bonding between the Si-OH groups produced by hydrolysis of THEOS. These form hydrogen-bonded units that provide nucleation centres for the formation of the silicate.[84b]

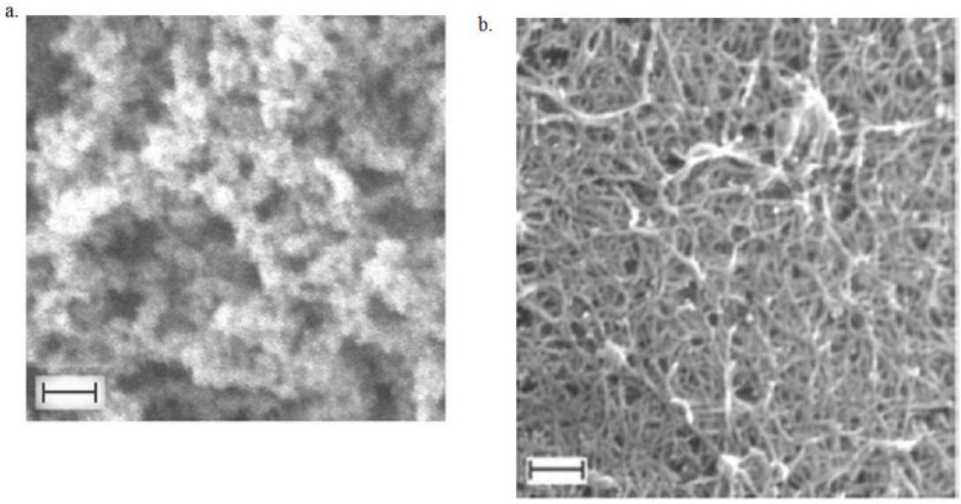


**Figure 134: SEM micrographs showing aerogels synthesised in an aqueous solution containing a) 50 wt%, 0.2 wt% *N*-[(trimethoxysilyl) propyl]-*N,N,N*-trimethylammonium chloride and 1M sulphuric acid, b) 10wt% THEOS and 0.5 wt% κ-carrageenan[84a]**

In the absence of the polysaccharide, the addition of N-[(trimethoxysilyl) propyl]-N,N,N-trimethlammonium chloride and sulphuric acid is required to form the gel. In this material solid particles are observable, connected to each other to form a 3-dimensional network. In the material containing κ-carrageenan a 3-dimensional network is also visible but made up of crossed fibres and the spherical particles are absent. This provides some evidence that the silica formed in situ by the sol-gel process is linked with the polysaccharide at the molecular level. It may also indicate that the structural organisation of the silica is directed by the carrageenan.

In the present study the THEOS precursor was synthesised simply by heating TEOS with a slight excess of ethanediol at reflux followed by distillation to remove the ethanol as detailed in the Chapter 2.2. The

polysaccharides chosen for incorporation into the hybrid materials were chitosan (75-85% deacetylated), κ-carrageenan, sodium carboxymethylcellulose and sodium alginate. Chitosan, κ-carrageenan and sodium alginate have all been shown to form these composite materials[84b] and sodium carboxymethylcellulose is similar in structure to hydroxethylcellulose which has also been shown to react successfully.[84b] These polysaccharides show a few different groups that could produce hybrid materials with interesting surface properties.

Their structures are shown in figure 135 below

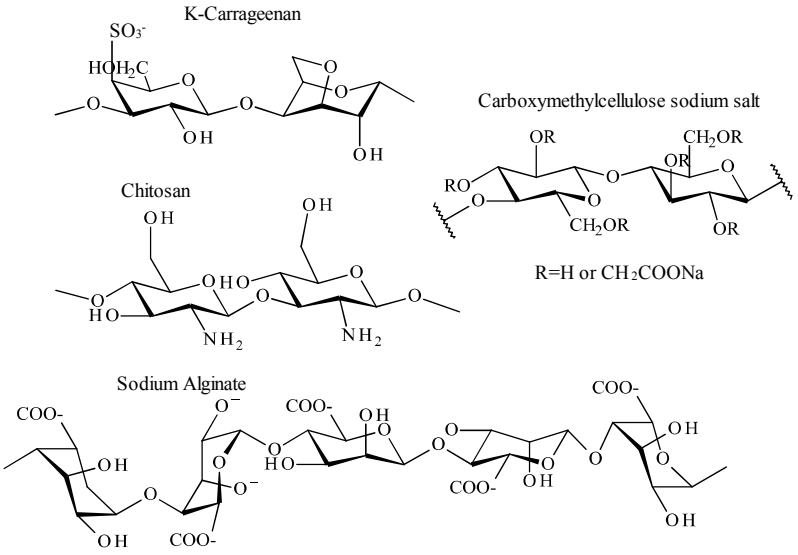


**Figure 135: The structures of the polysaccharides incorporated into the hybrid materials**

# 7.2 Results

The silica/polysaccharide materials were dried by exchanging the water for acetone and then drying under super-critical $CO_2$. When the hydrogels or acetone exchanged wet-gels were just allowed to air-dry, the samples formed shrank considerably and became very dense. Supercritical $CO_2$

drying in this case is a form of solvent replacement drying. The water was exchanged with acetone, which is more miscible with $CO_2$ and then the acetone is exchanged with the supercritical $CO_2$. This removes the problem of surface tension breaking up the structures.[176]

## Analysis of the Thermal Properties of Polysaccharides and Silica/Polysaccharide Hybrid Materials

The thermal properties of polysaccharides[177] and their blends with proteins[178] and other polymers such as polyethylene oxide[179] have previously been reported in the literature. Since such data has already been published only a qualitative comparison between the thermogravimetric and DSC traces of the polysaccharides and their equivalent hybrids was attempted.

Simultaneous thermal analysis combining thermogravimetric analysis (TGA) and differential scanning calorimetry (DSC) was used to study the thermal properties of the polysaccharides: chitosan, sodium alginate, K-carrageenan and sodium carboxymethyl cellulose both in their pure forms and incorporated into silica/polysaccharide hybrid materials. The decomposition was studied under a 50mls/min flow of nitrogen and oxidation processes studied under a 50mls/min flow of air. In both cases the heating rate was 10˚C/min.

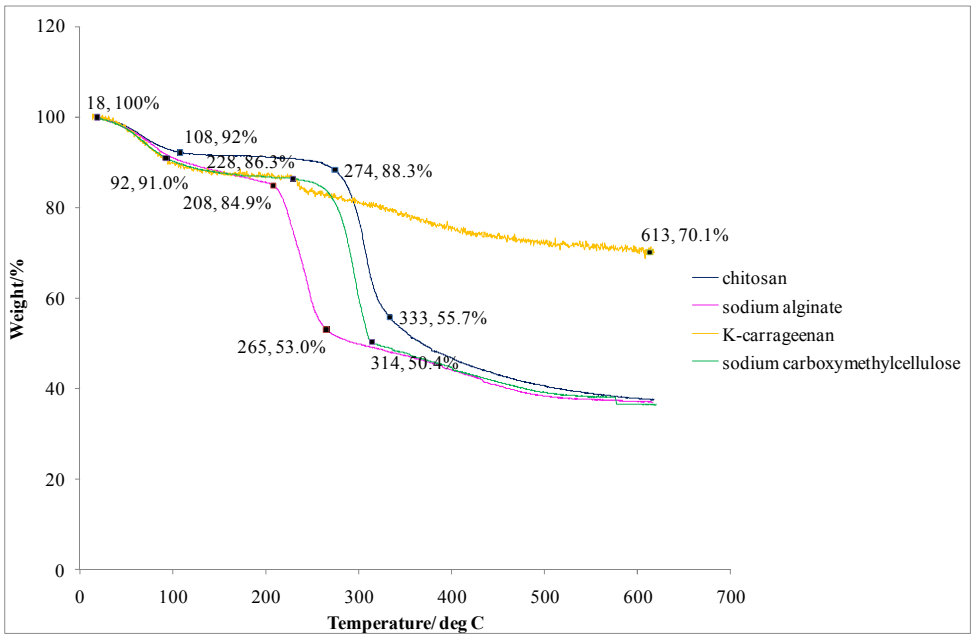


**Figure 136: TGA curves for the pure polysaccharides heating at 10˚C/min under 50 ml/min $N_2$**

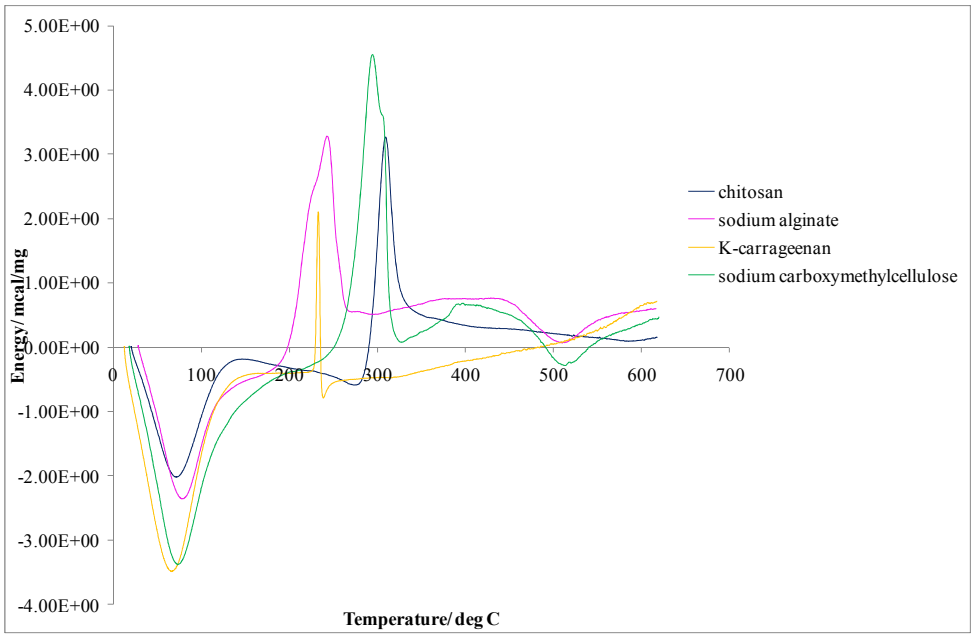


**Figure 137: DSC traces for pure polysaccharides heated at 10˚C/min under 50ml/min $N_2$**

The DSC traces shown in figure 137 are similar in form to those published by Zohuriaan et al in their paper on the thermal analysis of polysaccharide

gums.[177c] As can be seen from figure 136, there are two major regions of weight loss when the polysaccharides are heated. The first is associated with the loss of water and involves an 8-9% mass loss for all the samples. This mass loss represents the amount of bound water in the samples and can vary between 2 and 10%.[177c] In the solid state polysaccharides may have disordered structures that are easily hydrated. The extent of hydration depends on both the primary structure (e.g. the hydrophilicity of the functional groups) and the supramolecular structure.[177a]

The second transition is the first stage of decomposition, occurring above 200˚C for all of the polymers studied. Chitosan is particularly stable with decomposition not commencing until the temperature reaches 274˚C. This particular chitosan sample has been deacetylated 75-85%. The thermal properties depend on the degree of deacetylation. The DSC trace for this sample shows the same form as those published by Kittur *et al* for chitosan with around 79% deacetylation.[177a]. The main differences observable with increasing deacetylation are, increased peak areas for both the endothermic and exothermic transitions and a decreased temperature for the onset of the exotherm. This indicates that the deacetylation process increases the number of hydrophilic centres and decreases the thermal stability of the polymer.[177a]

For chitosan and κ-carrageenan there is only one exothermic transition but both sodium alginate and sodium carboxymethyl cellulose show a second exotherm and a second endotherm. For both of these materials the second exotherm occurs at around 400˚C and the second endotherm at around 510˚C. The high temperature transitions in general represent dehydration, depolymerisation and pyrolytic decomposition processes involving the formation of $H_2O$, CO, $CH_4$ and in the case of chitosan, $NH_3$. The different functional groups on the polysaccharide will change either the degradation routes or the resulting fragments. The sodium alginate and sodium carboxymethyl cellulose contain carboxylate functional groups and their decomposition may occur via thermal scission of the carboxylate groups and

evolution of $CO_2$ from the carbohydrate backbone.[177c] Undoubtedly different mechanisms of decomposition operate on the carboxylate containing polysaccharides compared to the others in this study.

The sharp, single exothermic transition during the decomposition of κ-carrageenan is in accordance with the results of Raemy *et al*.[180] The very small mass loss for κ-carrageenan shown in figure 136 is very surprising. All the other polysaccharides show similar mass losses and κ-carrageenan would be expected to lose a greater mass due to the heavy sulphur atoms being present. This small mass loss is not in agreement with the results of Lii *et al*.[181] This particular measurement would ideally be repeated to see if it is genuine or if something went wrong during the run.

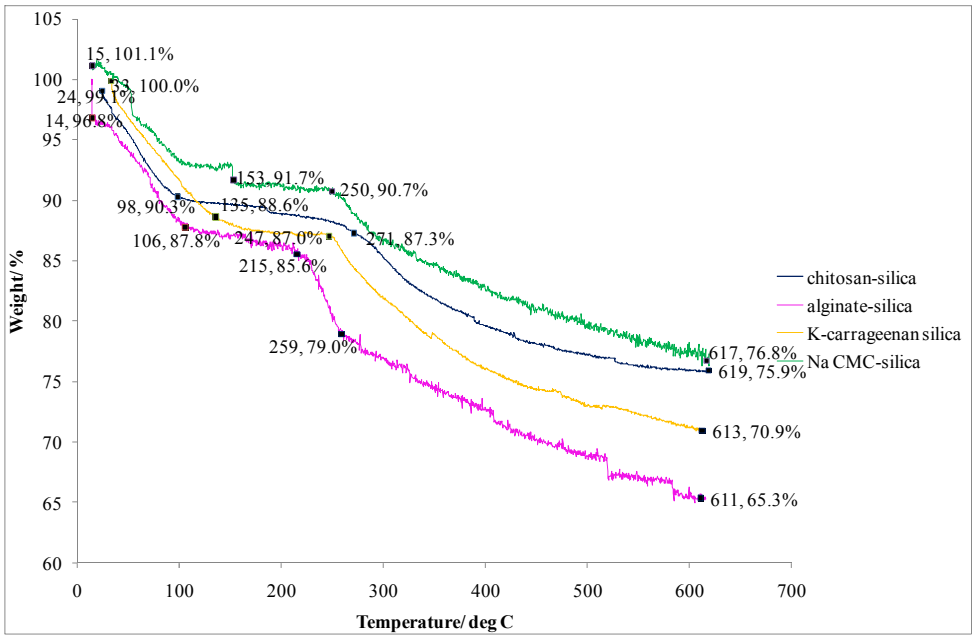


**Figure 138: TGA curves for the silica-polysaccharide hybrids heated in nitrogen**

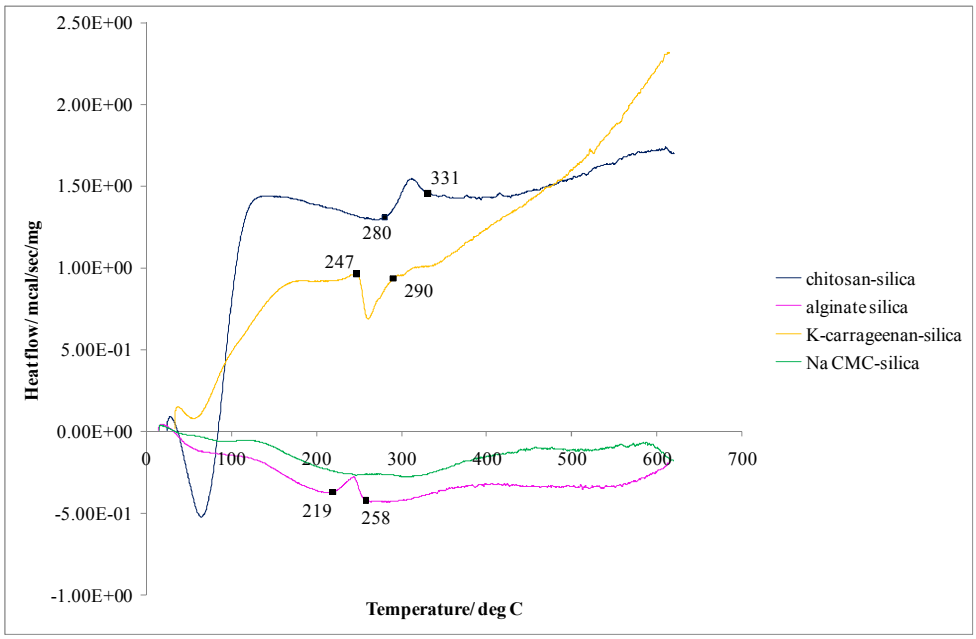


**Figure 139: DSC curves for the silica-polysaccharide hybrids heated in nitrogen**

The thermal properties of the silica-polysaccharide composites are quite different from those of the pure polysaccharides as can be seen from figures 138 and 139. The weight loss due to water evaporation is slightly larger at around 11%. This figure contains contributions from water adsorbed on both the silica and the polysaccharide. Silica gels may contain up to about 10% water especially if they are only gently heated as in this experiment.[29] Pure silica will only show surface dehydration and some dehydroxylation during heating up to 625˚C. So, sharp transitions are not expected for the silica. It is interesting to note that the instead of the consistent exotherm seen at the onset of decomposition above 200˚C in figure 137 for the polysaccharides, the next transition in figure 139 after the loss of water may be either an endotherm or an exotherm depending on the material. For the silica-sodium carboxymethyl cellulose composite no definite peaks at all can be seen in the DSC trace. In the hybrid materials the second transition occurs at approximately the same temperature as in the polysaccharides. Obviously these peaks are smaller due to the lower mass of polysaccharide being present in the hybrids.

The oxidation of the polysaccharides and their hybrids was also measured.

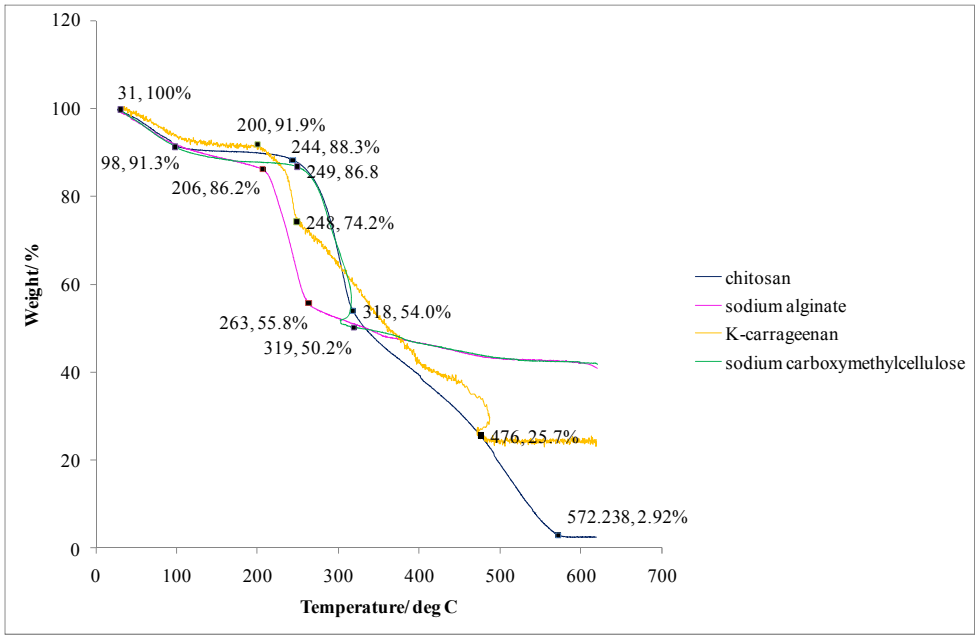


**Figure 140: TGA curves for the polysaccharides heated in air**

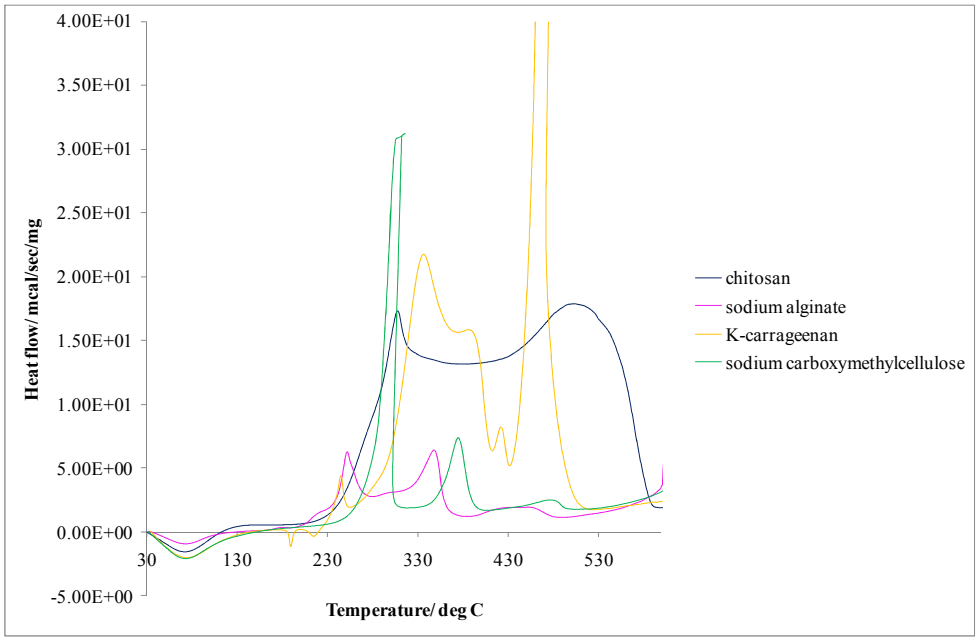


**Figure 141: DSC traces for the polysaccharides heated in air**

As can be seen from figure 140, the overall mass loss when the samples are heated in air is much greater than that when the samples are heated in nitrogen. Chitosan in particular, leaves very little residue after oxidation. This much greater mass loss is expected due to oxidative process breaking down the carbohydrates to a much greater degree than the thermal decomposition alone. The residual mass in the polysaccharides used as the sodium salts must be due mostly to the metal because these show a smaller mass loss than those without sodium.

The DSC curves shown in figure 141 are much more complex than those shown in figure 137. Obviously a number of different oxidative processes take place. Interestingly, the onset of the processes that occur above 200˚C all take place at much the same temperature unlike when the polysaccharides were heated in nitrogen. The peak that went off scale in the κ-carrageenan trace seems to be due to the machine being knocked or some other artefact.

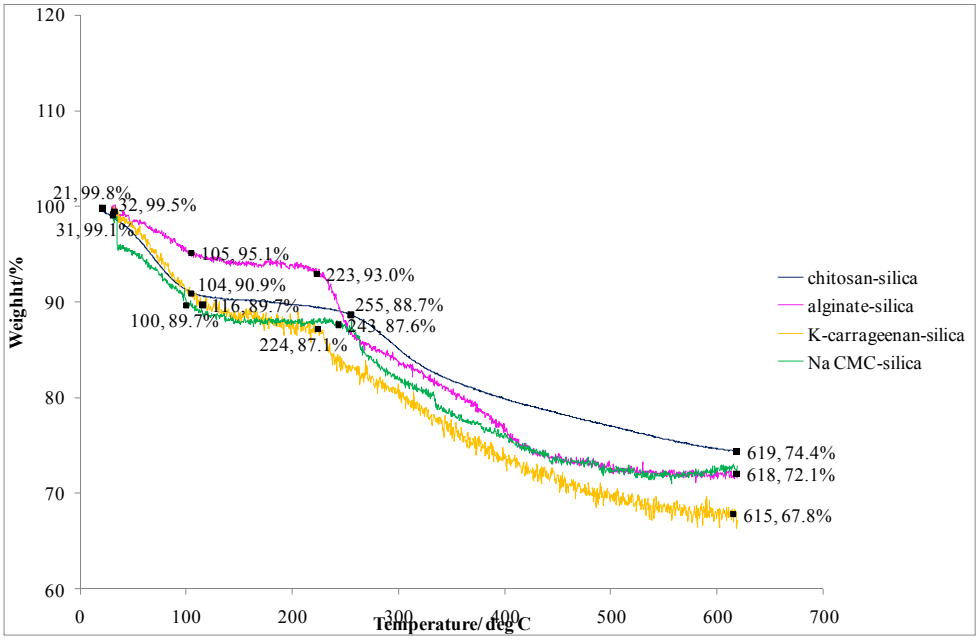


**Figure 142: TGA curves for the silica-polysaccharide composites heated in air**

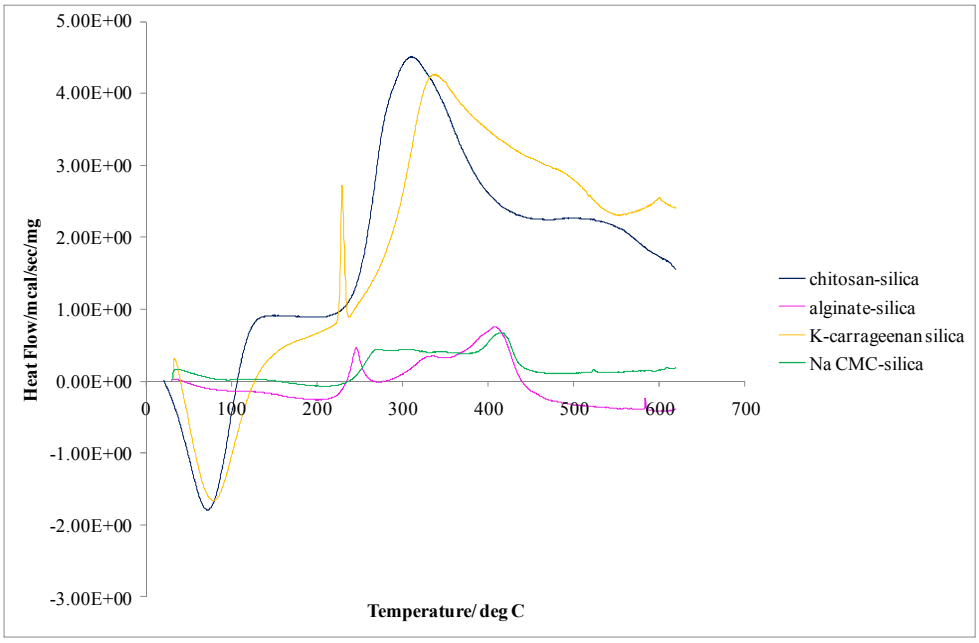


**Figure 143: DSC curves for the silica-polysaccharide composites heated in air**

It seems from the TGA curves in figure 142 that the remaining material in the silica-polysaccharide composites is just silica (and the sodium ions in the salts) due to the fact that a similar residual mass is present in each case. The most interesting points to note in comparing the DSC curves for the polysaccharides and composites when they are heated in air (figures 141 and 143) are that for sodium alginate and sodium carboxymethyl cellulose the peak pattern is very similar in both cases just at lower intensity in the hybrid. However, for chitosan and κ-carrageenan the DSC curves appear quite different in the polysaccharide and the hybrid. Although, these changes could simply be due to a loss of resolution because the peaks are so much smaller and the structure particularly in the case of κ-carrageenan is quite complex in the pure polysaccharide. This suggests that the polysaccharides structures are maintained in the hybrid material, corroborating the infrared evidence collected and the literature reports.

## Porosimetry Results

**Table 18: BET surface areas and pore diameters for the silica/polysaccharide hybrids obtained by nitrogen porosimetry**

| **Material** | **BET Surface Area/$m^2$ $g^{-1}$** | **BET Average Pore diameter/nm** |
|---|---|---|
| Silica/ κ-carrageenan | 850 | 11.4 |
| Silica/ sodium alginate | 730 | 13.3 |
| Silica/ sodium carboxymethylcellulose | 700 | 13.5 |
| Silica/ chitosan | 390 | 4.9 |

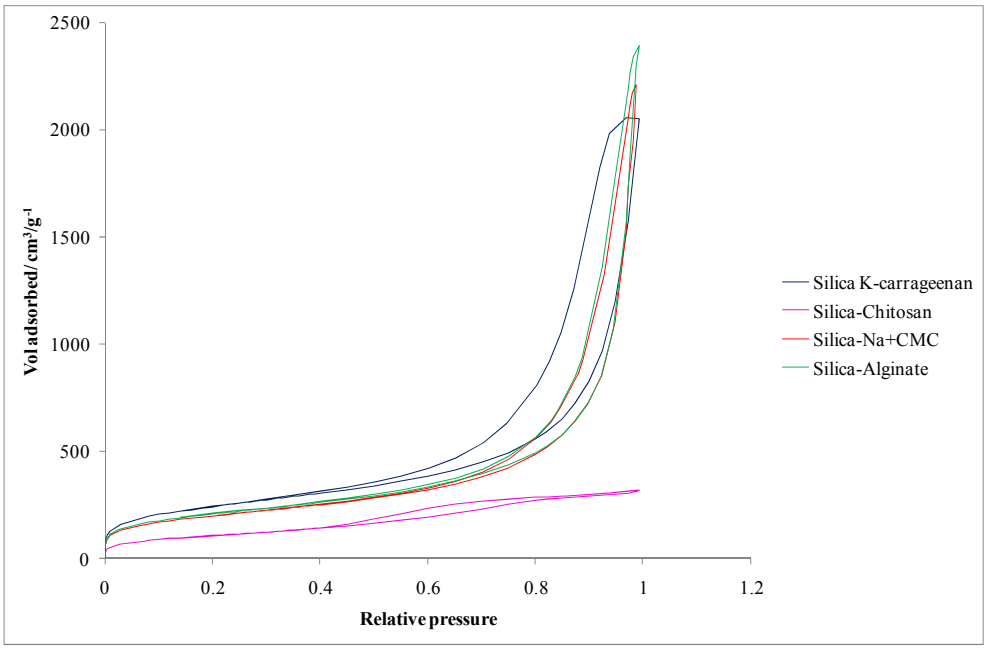


**Figure 144: BET Isotherms of silica/polysaccharide hybrids**

It can be seen from table 18 that the surface areas of the all the silica hybrid materials (except the silica/chitosan hybrid) are very high compared to typical values for silica gels (Kieselgel 100 typically has a surface area of around $400 m^2 g^{-1}$)[10]. Silica/chitosan has a much lower value than that of the other hybrid materials. This is most likely due to the difficulties encountered in forming a gel in the THEOS and chitosan solution discussed in Chapter 2.2 and in the previous section. Differences are also seen in the BET isotherms in figure 144. The volume of nitrogen adsorbed by this material is much smaller than that adsorbed by the others.

The BET isotherms shown are closest in form to the type IV isotherm characteristic mesoporous adsorbents. The hysteresis loops are difficult to assign to a particular type but are most similar to type H1. These are usually associated with porous materials with a regular array of agglomerates or uniform spheres and hence have a fairly narrow pore size distribution. From the electron micrographs recorded by Shchipunov it was observed that the κ-carrageenan-silica composites were constructed of a 3-dimensional

network of crossed fibres. This is in contrast to the silica sample manufactured from THEOS with *N*-[(trimethoxysilyl) propyl]-*N,N,N*-trimethylammonium chloride and sulphuric acid, which was made up of spherical particles.[84a] The interpretation of the BET isotherm shape may well be a regular array of fibres rather than a regular array of agglomerates.

## Infrared Spectra

Figures 145 and 146 show the infrared spectra of the silica/polysaccharide composite materials. They were recorded on the Brüker equinox 55 IR operating in DRIFT mode and the samples were diluted with an accurately weighed mass of KBr in a ratio of 1:20 sample:KBr.

Unsurprisingly, due to the fact that these materials are mostly made up of silica (based on the thermal analysis data), the infrared spectra of the silica/polysaccharide hybrid materials are very similar to those of pure silica, examples of which can be seen in Chapter 4. The peaks characteristic of silica are those at 810, 975, 1220-1090, 1633, 1871, 1990, 3000, 3640.and 5214cm$^{-1}$. In silica these bands are assigned to the Si-O-Si symmetric stretch, the Si-OH stretch, the Si-O-Si antisymmetric stretch, the bending mode of associated water, two silica framework combination bands, OH stretch hydrogen-bonded water, OH stretch hydrogen-bonded SiOH and an OH+ ν2 bending mode combination band of water respectively. The assignment of bands for the hybrid materials is complicated by the fact that several bands relating to polysaccharides and silica occur in the same region. C-O-C vibrations occur in the 1030-1150cm$^{-1}$ region,[182] the same as Si-O-Si and it is impossible to distinguish between hydrogen bonded SiOH and COH based on the OH stretch region.

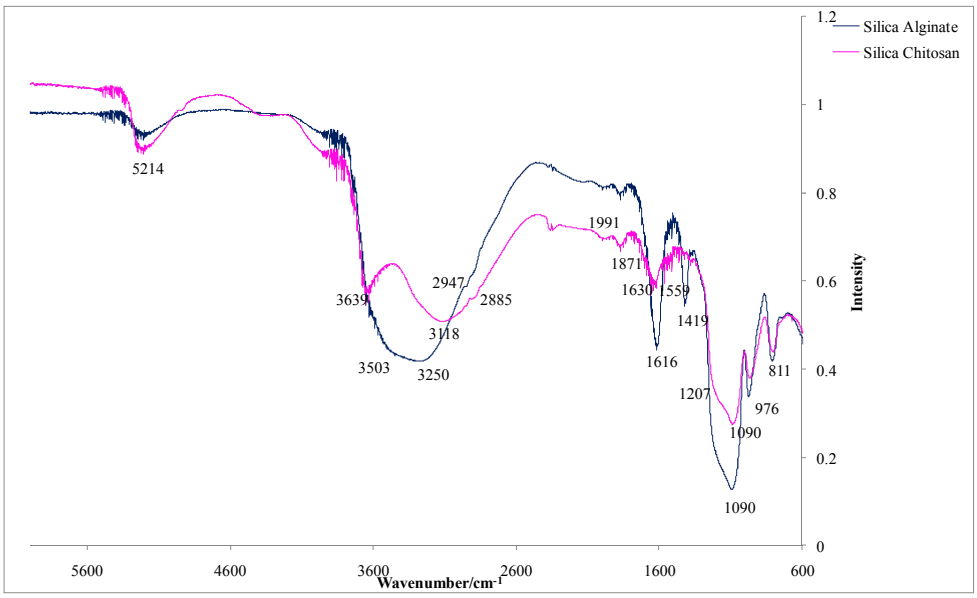


**Figure 145: Infrared spectra showing the silica composite materials containing sodium alginate and chitosan**

**Table 19: Infrared peak assignments for sodium alginate[182]**

| **Band Position/cm$^{-1}$** | **Assignment** |
|---|---|
| 3700-3000 (broad) | O-H stretch |
| 3000-2850 | C-H stretch |
| 1596 | Antisymmetric $CO_2^-$ stretch |
| 1412 | Symmetric $CO_2^-$ stretch |
| 1297 | Skeletal vibration |
| 1081-1027 | C-O-C antisymmetric stretch |

The bands in the infrared spectrum of the silica/sodium alginate composite appear to be a mixture of the infrared spectra of silica and sodium alginate. There are no particularly significant differences between the literature values for characteristic bands of sodium alginate and those in the measured spectrum of the hybrid material. There is a slight shift to higher

wavenumber of the antisymmetric stretch of $CO_2^-$ from 1596cm$^{-1}$ in sodium alginate to 1616cm$^{-1}$ in the composite material. This is most likely due symmetry perturbation of the $CO_2^-$ group caused by interaction with the silica.

**Table 20: Infrared peak assignments for chitosan[182]**

| **Band Position/cm$^{-1}$** | **Assignment** |
|---|---|
| 3290 | O-H and N-H stretch |
| 2864 | C-H stretch |
| 1645 | Amide |
| 1584 | N-H bend from amine and amide |
| 1414 | -$CH_2$ bending |
| 1375 | $CH_3$ symmetrical deformation |
| 1150 | C-O-C antisymmetric stretch and C-N stretch |
| 1026 | Skeletal vibration of C-O stretching |

A similar situation is seen in the spectrum of the silica/chitosan hybrid; the spectrum for the most part appears to be simply a mixture of the spectra of silica and of chitosan based on the literature assignments above. But again there are two bands that are shifted compared to the literature values, the band characteristic of amides and the N-H bending vibration. This time there is a downward shift from 1584cm$^{-1}$ in pure chitosan to 1559cm$^{-1}$ in the composite material. This might be caused by hydrogen bonding between the amine/amide groups and the SiOH groups. Or again may be as a result or perturbation of the symmetry of the groups.

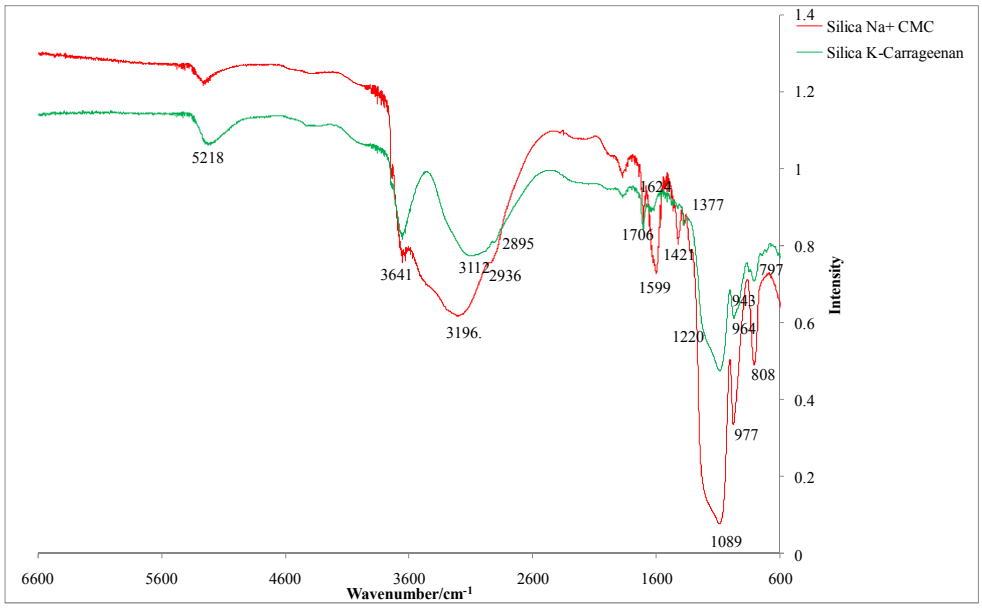


**Figure 146: Infrared spectra showing the silica composites containing sodium carboxymethylcellulose and κ-carrageenan**

**Table 21: Infrared peak assignments for sodium carboxymethyl cellulose[183]**

| **Band Position/cm$^{-1}$** | **Assignment** |
|---|---|
| 3432 | O-H stretch |
| 2909 | C-H stretch |
| 1603 | Antisymmetric $CO_2^-$ stretch |
| 1423 | -$CH_2$ scissoring |
| 1325 | -OH bending |
| 1061 | >CH-O-$CH_2$ |

As far as it is possible to tell by comparison of figure 146 and table 21 the infrared spectrum of the silica/sodium carboxymethyl cellulose composite appears to be just a mixture of the spectra of pure silica and sodium carboxymethyl cellulose.

**Table 22: Infrared peak assignments for κ-carrageenan[184]**

| **Band Position/cm$^{-1}$** | **Assignment** |
|---|---|
| 3700-3500 | O-H stretch free |
| 3500-3100 | O-H stretch hydrogen-bonded |
| 2900-2700 | C-H stretch |
| 1240 | O=S=O antisymmetric stretch |
| 930 | C-O 3,6-anhydrogalactose |
| 845 | C-O-S of axial secondary sulfate on C4 of galactose |

The infrared studies carried out on carrageenans reported in the literature focus on the bands relating to the sulfate groups as these can be used to distinguish between the different forms of carrageenan; κ, λ and β.[184a] These bands are unfortunately quite weak in the spectrum of the silica/κ-carrageenan composite in figure 144 and to some extent overlap with silica bands. However, the bands at 964cm$^{-1}$ and 797cm$^{-1}$ have shoulders on the low-frequency side and high-frequency side respectively that must correspond to the sulfate groups since they are not present in any of the other spectra. Beyond that, it is difficult to make any further comments.

The lack of difference in the positions of the peaks characteristic of the polysaccharides between the measure spectra and the literature values is in agreement with the mechanism for the formation of these materials proposed by Shchipunov; which states that the main interaction between the silica and the polysaccharide is hydrogen-bonding rather than strong covalent bonds.

## 7.3 Conclusions

Silica-polysaccharide hybrid materials have been successfully synthesised and they show interesting morphological and thermal properties. They all show a similar pore diameter and except for the chitosan hybrid, where difficulties in forming a gel were encountered, very similar, high surface area values were obtained by nitrogen porosimetry.

It is difficult to gain information about the interaction between the polysaccharides and silica by infrared spectroscopy; the spectra appear to be in most cases a mixture of the characteristic features of silica and the polysaccharides. There are slight shifts for some of the bands but these are most likely due to symmetry perturbations.

The DSC data shows some changes when the polysaccharides are incorporated into the hybrid materials but the stronger peaks obtained during the oxidations suggest that the changes may well simply be due to the peaks being so much smaller for the hybrids.

The morphology of the materials has not been investigated by either porosimetry or electron microscopy after calcination to remove the polysaccharide. It would be interesting to see whether this structure is maintained. Also it would be interesting to investigate the acid-base properties of these materials by infrared probing techniques as well as the

iodine probing and Knoevenagel condensation test reactions used in Chapters 5 and 6.

# Chapter 8: Conclusions and Future Work

The main aims of this study were to review some of the current methods for evaluating the surface properties of materials, if possible to develop new methods and to test the properties of some novel materials. These aims have been met to a large extent. Infrared probing techniques with a variety of different probes have been used to test the acid-base properties of a number of metal oxides including silica, zeolites, zirconia and alumina as well as organically functionalised silica samples. Iodine had only been investigated by very few workers in the literature as a probe for surface basicity and here the advantages and limitations of this method have been discussed for a wide variety of surfaces. The Knoevenagel condensation has been established as a useful model reaction for the testing of surface basicity. Some novel silica-polysaccharide hybrid materials have been synthesised and their surface properties tested by several methods.

## 8.1 Infrared Examination of Silica and Silica-Polysaccharide Hybrid Structures

Little information was obtained about the mechanism of silica gel formation or the bonding between the silica and polysaccharides in the hybrid materials by direct infrared measurements. All that could be confidently identified by observing silica gel formation in Chapter 3 was that for the microporous silica gel made by acidification of "water-glass" the gel-forming reaction did not stop until the silica was dried. Also for the neutral-amine templated HMS that the gel-forming reaction appeared to have completed by 7 hours reaction time, so overnight gelation times were unnecessary.

Infrared examination of the silica-polysaccharide materials for the most part simply showed peaks relating to both the silica and the relevant polysaccharide. This however is consistent with the mechanism proposed for their formation, in which the silica and polysaccharide interact through hydrogen-bonds and not covalent-bonding.[84a,b]

## 8.2 Infrared Probing Techniques

In Chapter 4 a number of classic infrared probes; ammonia, carbon dioxide, $d_3$-acetonitrile and water were reviewed along with a few less commonly used ones such as aniline, propanoic acid and fluorobenzene to establish what information can be obtained by their use. Information was obtained about the acidity, basicity and hydrophobicity of silicas and other metal oxides. A lot of work has already been done in this area and these techniques have long been established as successful.

Difficulties with some of the infrared probe molecules arose due to overlap between the bands associated with the probe molecule and the surface. This was particularly pronounced for propanoic acid on silica, since the interacting groups on both species were OH groups. However, the main disadvantage of these techniques is the length of time and depth of research needed in many cases to interpret the spectra obtained. One specific example is the adsorption of $d_3$-acetonitrile on zeolites, zirconia and alumina and then desorption under flowing nitrogen at elevated temperatures. This caused reactions between the $d_3$-acetonitrile and the surfaces, which whilst providing valuable information about the surface interactions greatly complicated the spectral analysis.

The vast amount of data available in the literature however, on the behaviour of various infrared probes makes these techniques potentially very useful for studying the surface chemistry of new and novel materials,

such as the metal-organic framework materials[185] and other inorganic-organic hybrid materials[186] that are currently attracting so much attention in the literature. They have been proposed as potential adsorbents for $CO_2$ capture and hydrogen purification,[187] separation of acetylene and ethylene[188] and hydrogen storage[189] as well as potential catalysts, particularly for enantioselective reactions,[190] amongst many other possible applications. It would be possible to compare these materials to the behaviour of currently used materials, identify active sites and possibly predict their reactivity.

## 8.3 UV-Visible Probing Methods

Compared to infrared, UV-visible probing methods have been less frequently studied in the literature for solids. However, these probes have been shown to be sensitive both to the surface and the environment surrounding the surface. Therefore they provide a more realistic model of the true surface activity under reaction conditions. It was seen that the $\lambda_{max}$ values for both Reichardt's dye and iodine changed with the level of surface hydration. It also appeared that solvation by surface water stabilised the $I^+$ and $I_3^-$ species formed from $I_2$. With the appropriate control it therefore may be possible to characterise a bare surface and the surface in the presence of solvents or reagents. This would be technically challenging but if it could be successfully accomplished would provide a wealth of valuable information.

The use of iodine as a probe molecule allowed distinctions to be made between otherwise apparently very similar solids such as neutral and basic activated Brockmann alumina and sodium carbonate and sodium hydrogen carbonate. However, on all of these solids, significant concentrations of $I_3^-$ were observed and more work is needed on what properties the shifts in the $I_3^-$ band relate to. Also, for the majority of surfaces, very little is known about the preferred adsorption sites for iodine. Some work has been done by Basch using Raman, UV-visible and X-ray absorption spectroscopy to

characterise iodine sorbed into the pores of zeolite A samples exchanged with different cations.[164a] Detailed work has also been carried out on the structures of some polysaccharide-iodine complexes[150,152]and preferred adsorption sites iodine on two different periodic mesoporous organosilicas have been ascertained by Camarota *et al*[74] but other detailed studies on the exact iodine-surface interactions have not been published for the vast majority of surfaces.

One difficulty with the use of iodine as a probe is that some solids only adsorb a very low concentration. Further work to try and determine the surface features that result in low-iodine uptake and to experiment with different techniques for adsorbing the iodine onto the surface may help to resolve this. One possible technique for adsorbing iodine onto surfaces that may result in higher uptake is to dissolve iodine in supercritical $CO_2$ and use it to carry the iodine into the pores of the material. This has been used to dope conductive poly(3-undecylbithiophene) and its composites with porous, cross-linked polystyrene by Abbett and co-workers.[191]

Interesting results were obtained when iodine was used as a probe molecule to compare the surface properties of the organic-inorganic hybrid materials such as the organically functionalised silica samples and the silica-polysaccharide hybrid materials. For the latter materials, it was seen that they differed in electron-donating ability from both pure silica and the pure polysaccharides.

## 8.4 Knoevenagel Condensation as a Test Reaction for Surface Basicity

The Knoevenagel condensation reaction seems to be a successful method for establishing the basicity of surfaces. Differences can clearly be observed between the different surfaces and analysis and interpretation of the results

is straight-forward. The main problems associated with this technique are; firstly that it is relatively time consuming- the reactions have to be run for a number of hours, monitored periodically and repeated to improve confidence in the values. Secondly, there are two possible mechanisms by which the reaction can occur depending on whether or not primary amine groups are present, so this technique could not be used to test a completely unknown material.

It was a little unfortunate the results did not correlate well with the UV-visible probing results, except when different solvents were compared. It seems that for surfaces at least, the two techniques were measuring different surface properties. It is possible that iodine adsorbed on different sites to those that catalysed the Knoevenagel condensation. Also, in many cases the $I_2$ was converted to $I_3^-$ and as has been stated repeatedly, it is not yet known what the shifts in these bands correlate to.

This technique is not ideal as a method for testing the properties of new materials unless of course they are being screened as potential catalysts for the Knoevenagel condensation. Other test reactions have been successfully used to test the acid-base properties of surfaces[76-77,192] but again these methods are best used when screening catalysts for these reactions.

## 8.5 Techniques for the Future

It was originally intended that the focus of this study would be on the use of fluorinated probe molecules and $^{19}F$ NMR to characterise surfaces according to properties such as surface shielding, polarizability and hydrogen-bonding as in the work carried out by Budarin *et al*.[10] The idea was to find a small set of molecules that showed changes in the chemical shift values when adsorbed on different surfaces that could be used to quantify the surface properties of any solid. This would produce values similar to the Kamlet and

Taft parameters that use UV-visible active dyes to compare surfaces.[58] However, serious failure of the NMR equipment prevented this work from ever being carried out. This is still a potentially useful study. The measurement of Kamlet and Taft parameters is made difficult by a lack of useful probe molecules, particularly for the measurement of surface hydrogen-bond donating ability. Also, obviously this cannot be used for active carbons or other materials that are dark or highly coloured. NMR probing has the advantage that it is nucleus specific, for instance if there are no fluorine atoms in the solid, only in the probe molecule then changes in the NMR shift using a detector tuned to fluorine must be due to the probe. So, there is no confusion caused by overlap between peaks of the probe molecule and the surface as can occur with infrared probing. A further advantage is that, unlike with UV-visible probing techniques, there is almost a limitless range of potential probe molecules. All that is required is that they incorporate at least one fluorine atom.

Computer modelling has become increasingly important in the characterisation of surface activity. Modelling techniques have been used to characterise the surface hydroxyl groups on silica[34,193] alumina[194] and to explore the effect of thermal dehydration on silica surfaces.[195] Computational techniques have also been used to model adsorbate-surface interactions on heterogeneous catalysts.[139] Much work has already been carried out in this area but as computer models are improved and new ones developed such techniques may well become a standard method for the characterisation of surface properties.

Despite the large volume of work that has already been carried out on the use of probing techniques to characterise surface properties, the rapid development of new materials and the ever expanding market for industrial heterogeneous catalysts and adsorbents mean that there will still be a great deal of work to be carried out in the future.

# Appendix: GC and GC-MS Traces

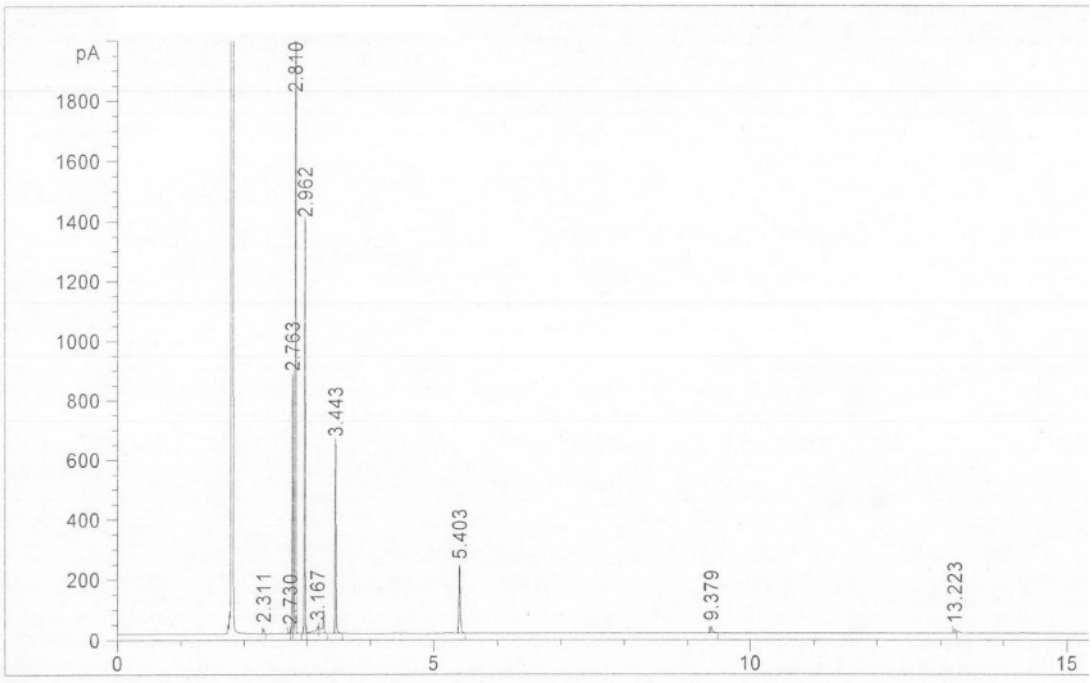


**Figure 147: GC Trace of a typical Knoevenagel condensation reaction using 3-aminopropyl functionalised silica as the catalyst (recorded on the Varian 3800 GC)**

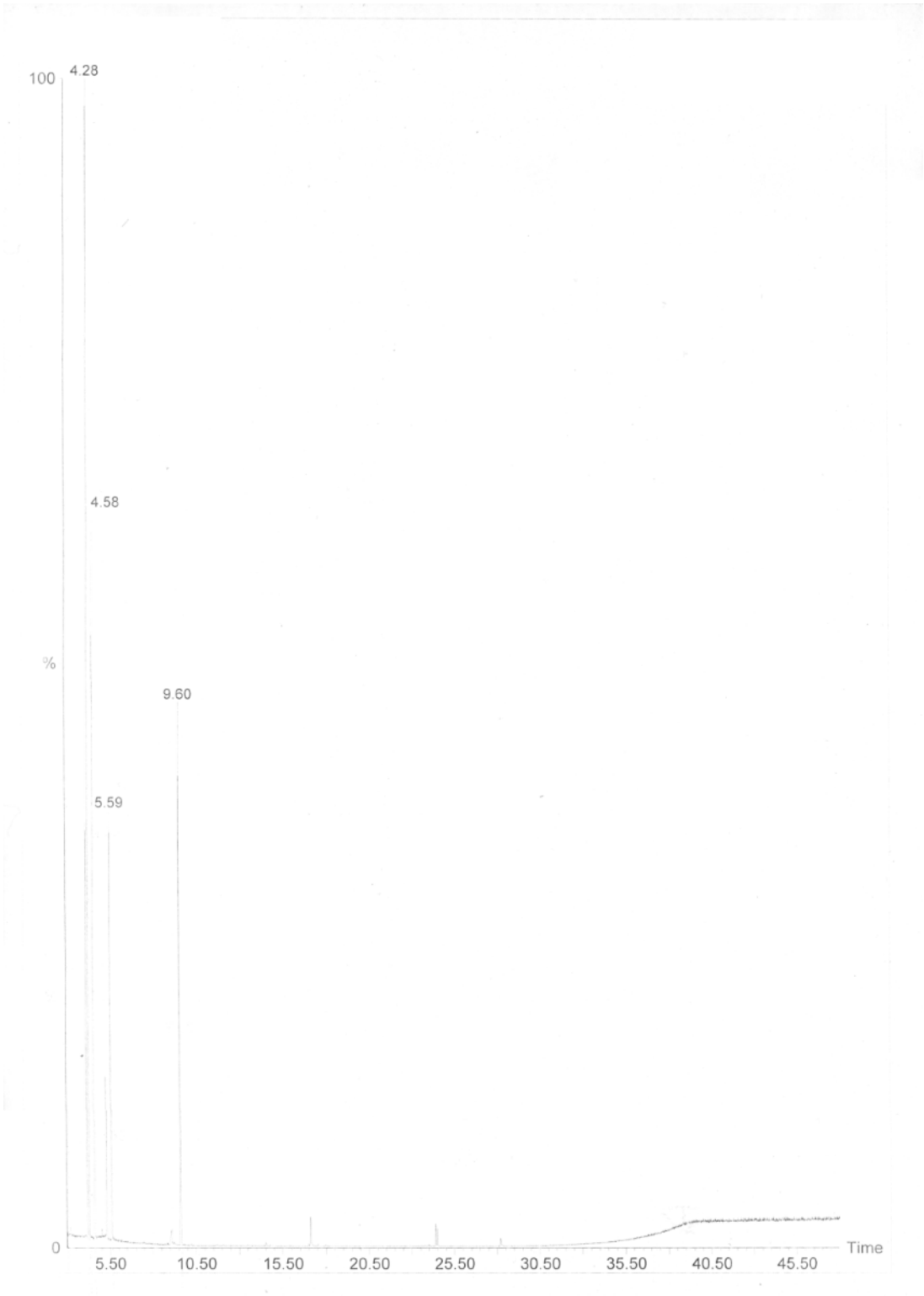


**Figure 148: GC Trace of a typical Knoevenagel condensation reaction using 3-aminopropyl functionalised silica as the catalyst (recorded on the Perkin Elmer Claus 500 GC)**

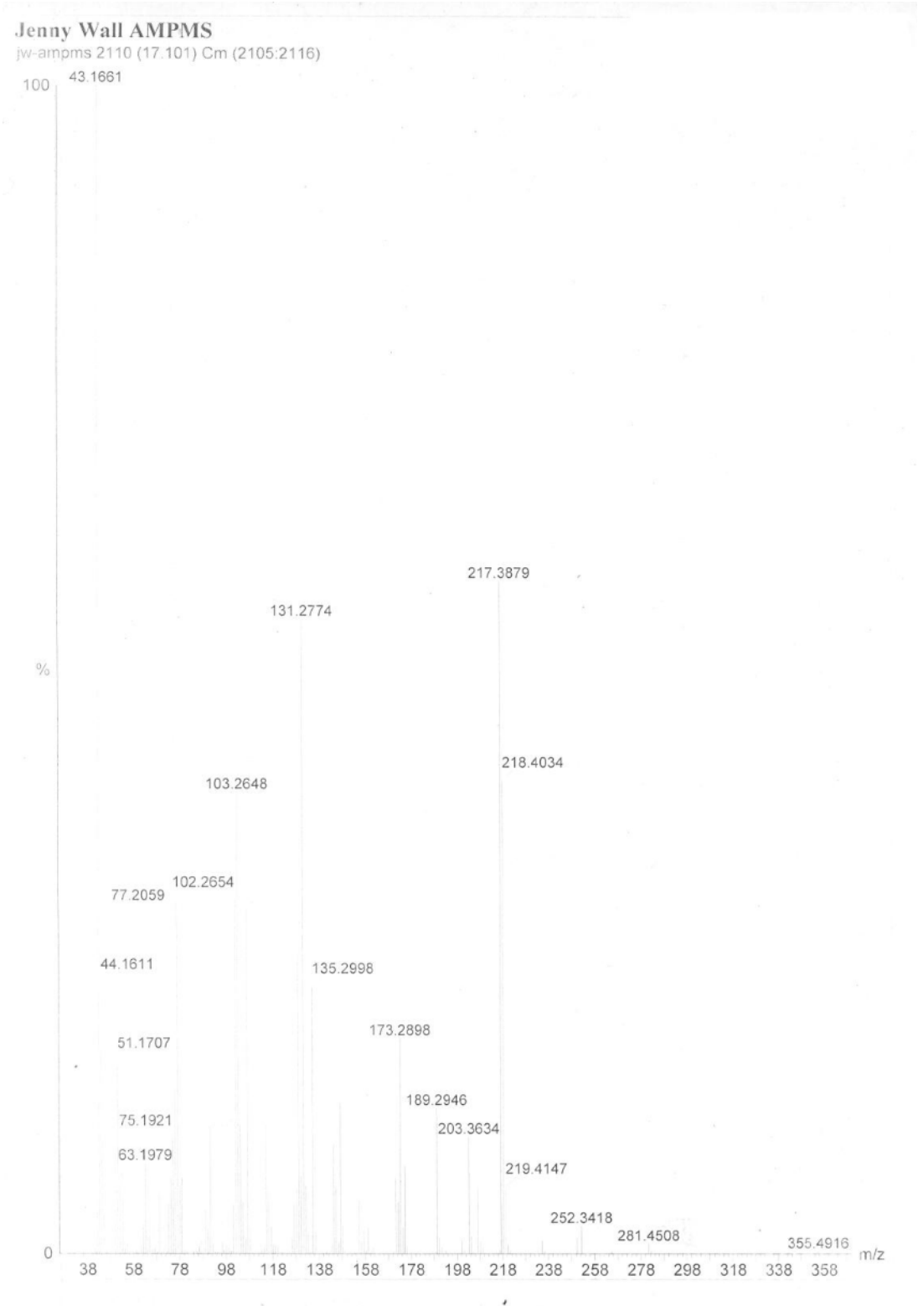


**Figure 149: Mass Spectrometry trace of the product of the Knoevenagel condensation reaction using 3-aminopropyl functionalised silica as the catalyst (peak at 17.01 minutes in figure 2).**

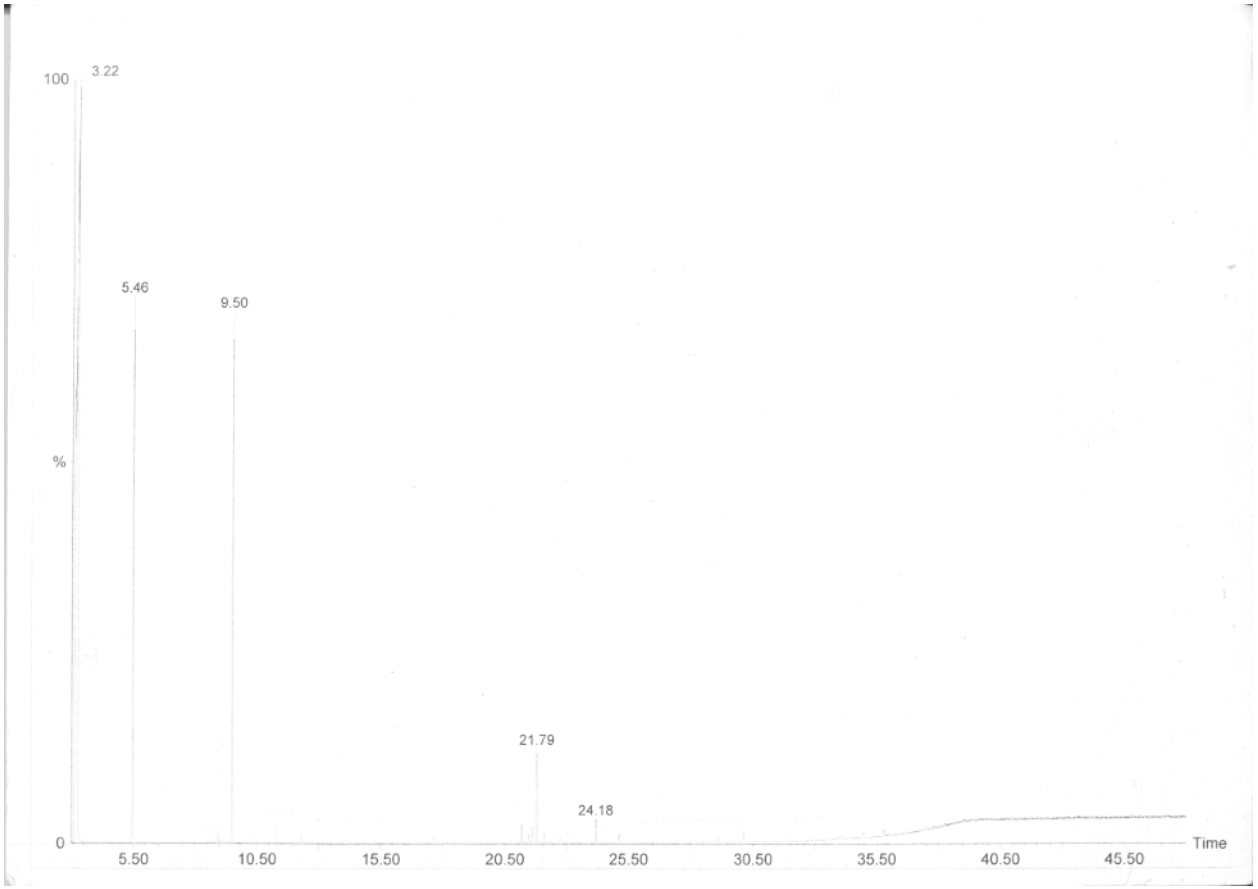


**Figure 150: GC trace of the products of reaction in DMF with $NaHCO_3$ as a catalyst (recorded on the Perkin Elmer Claus 500 GC)**

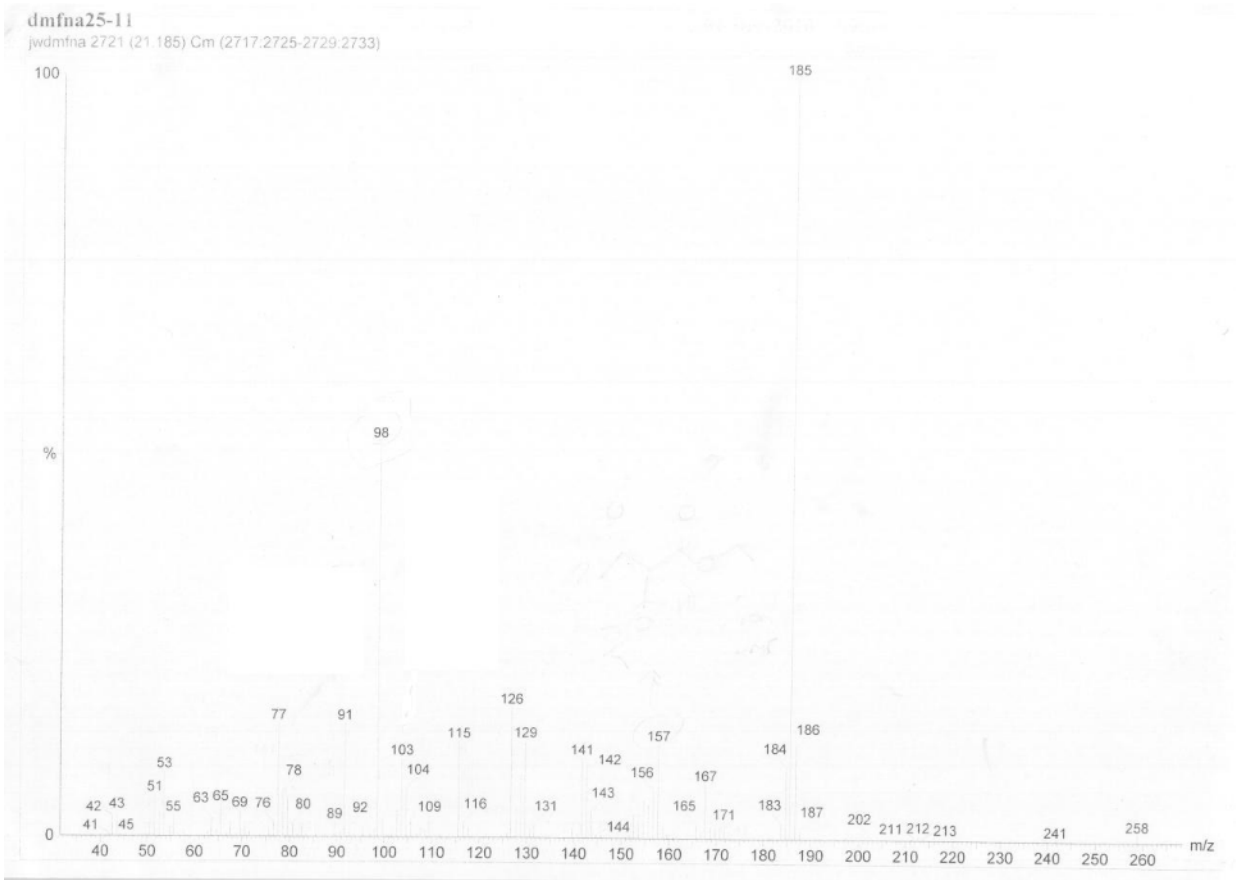


**Figure 151: Mass Spectrometry trace of the peak at 21.185 minutes from the reaction in DMF with $NaHCO_3$ as a catalyst**

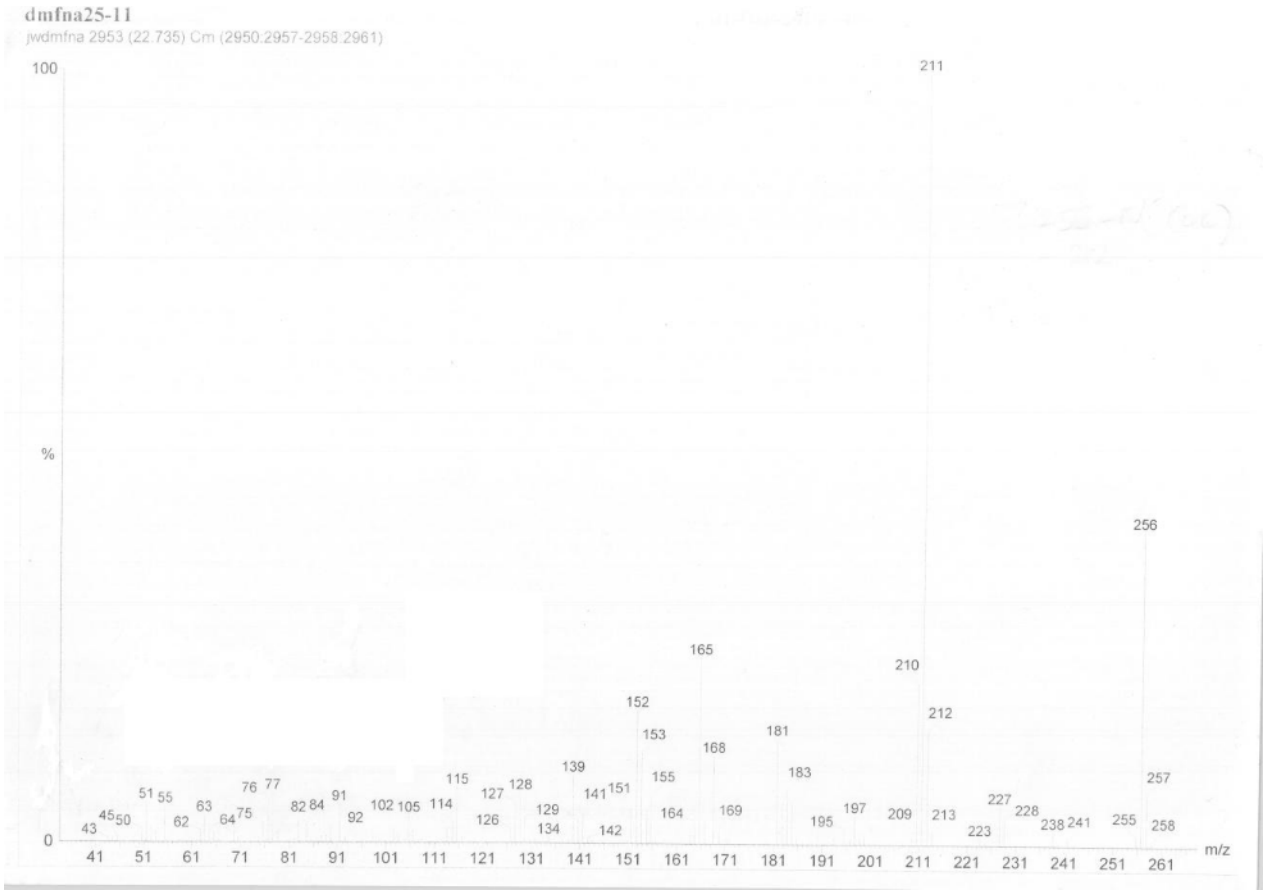


**Figure 152: Mass spectrometry trace of the peak at 22.735 minutes from the reaction in DMF with $NaHCO_3$ as a catalyst**

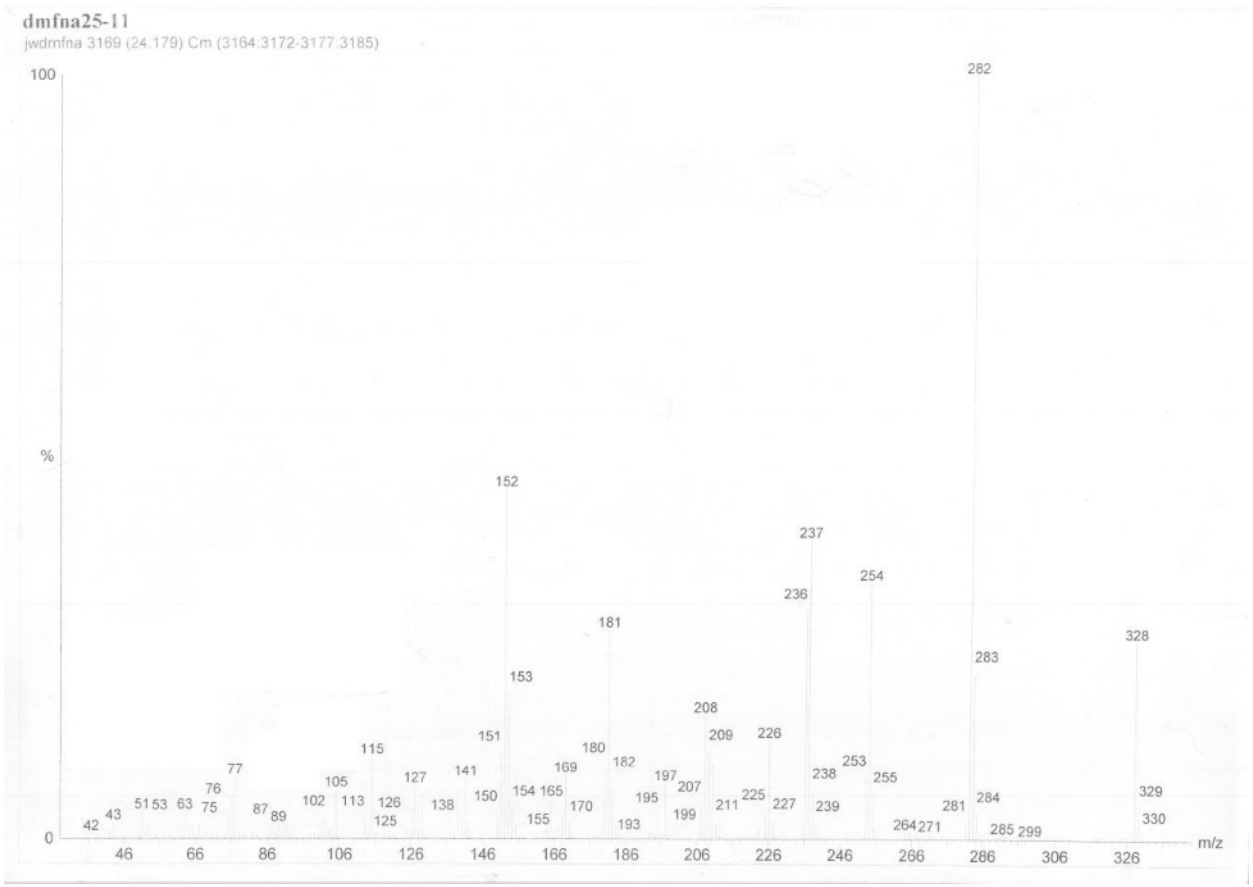


**Figure 153: Mass spectrometry trace of the peak at 24.179 minutes from the reaction in DMF with $NaHCO_3$ as a catalyst**

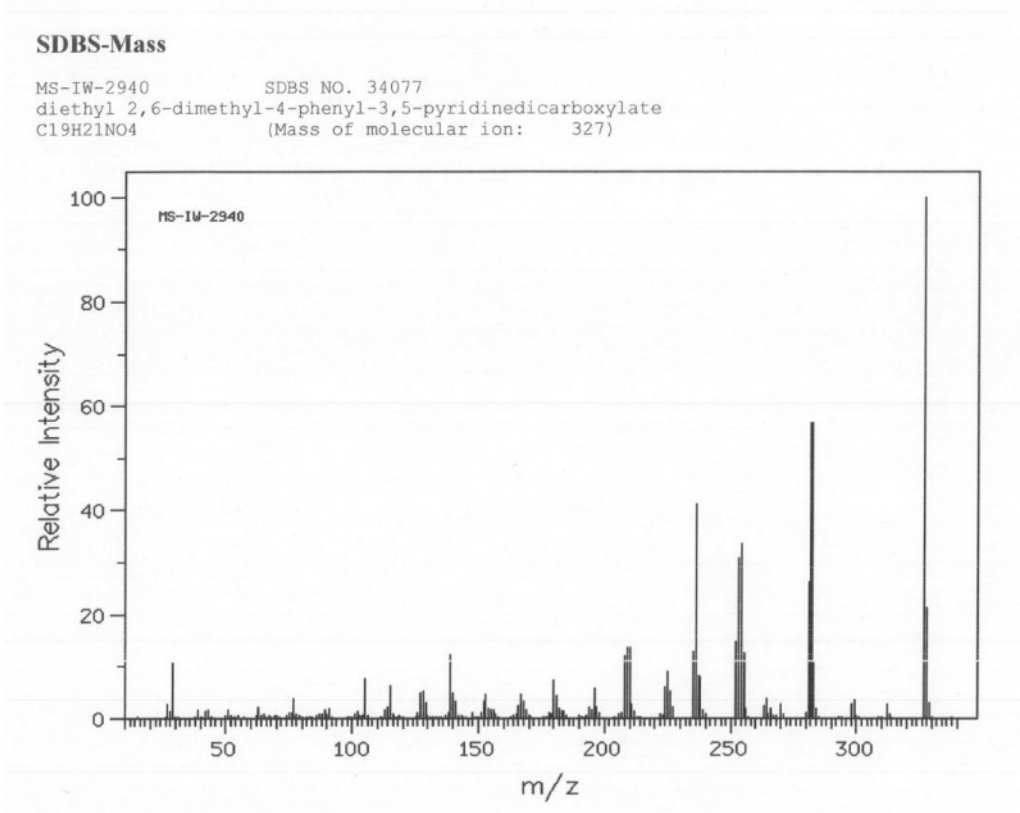


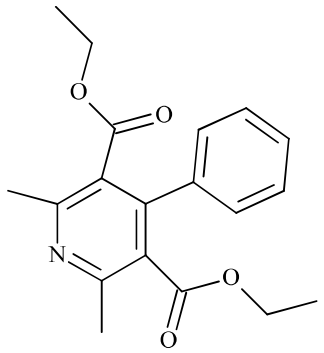


**Figure 154: Possible library match for the peak at 24.179 minutes in figure 5**

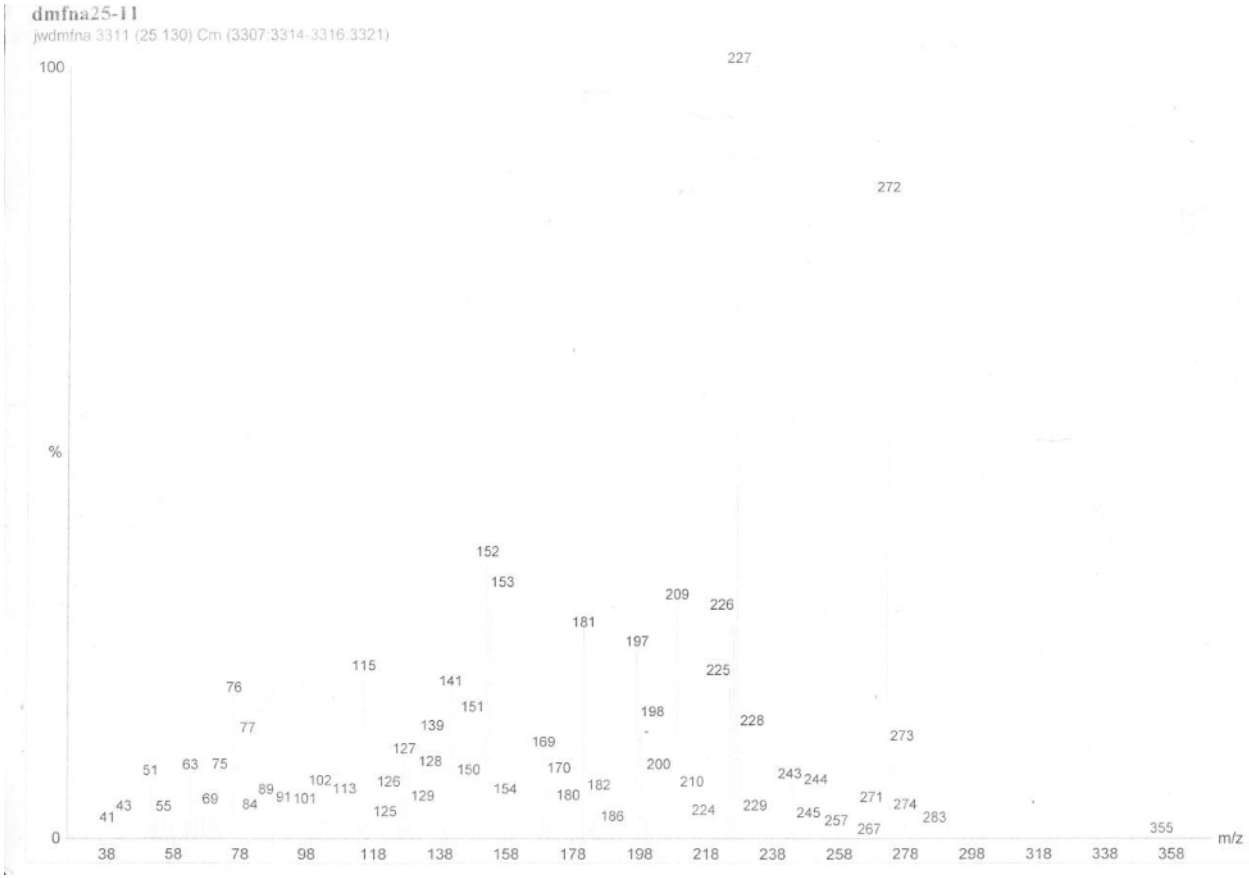


**Figure 155: Mass spectrometry trace of the peak at 25.130 minutes from the reaction in DMF with $NaHCO_3$ as a catalyst**

# Acronyms and Abbreviations

AMP-silica or AMP-HMS: 3-aminopropyl functionalised hexagonal mesoporous silica produced by co-condensation of 3-aminopropyl trimethoxysilane and tetraethyl orthosilicate

ATR: Attenuated total reflectance

BET: Brunauer, Emmett and Teller

CMC: Critical micelle concentration

DMF: Dimethylformamide

DRIFT: Diffuse reflectance infrared Fourier transform

DSC: Differential scanning calorimetry

DTA: Differential thermal analysis

EPR: Electron paramagnetic resonance

FTIR: Fourier-transform infrared

GC: Gas chromatography

GC-MS: Gas chromatography-mass spectrometry

HMS: Hexagonal mesoporous silica

HMDS-silica: Tri-methylsiyl functionalised hexagonal mesoporous silica produced by co-condensation of hexamethyldisiloxane and tetraethyl orthosilicate

IR: Infrared

K60: Kieselgel 60

NMR: Nuclear magnetic resonance

PMO: Periodic mesoporous organosilica

REACH: Registration, evaluation, authorisation & restriction of chemicals

RT: Room temperature

SEM: Scanning electron microscopy

STA: Simultaneous thermal analysis

TEM: Transmission electron microscopy

TEOS: Tetraethyl orthosilicate

TG: Thermogravimetry

THEOS: Tetrakis(2-hydroxyethyl)orthosilicate

Thiol-silica: 3-mercaptopropyl functionalised HMS produced by co-condensation of (3-mercapto) trimethoxysilane and tetraethyl orthosilicate

UV: Ultra-violet

XRD: X-ray diffraction

ZSM-5 30: ZSM-5 type zeolite with $H^+$ cations and an $Al_2O_3$:$SiO_2$ ratio of 30

ZSM-5 280: ZSM-5 type zeolite with $H^+$ cations and an $Al_2O_3$:$SiO_2$ ratio of 2800

# References


(1) Wood, L. "Global Refinery Catalyst Market - Fcc, Htc, Hcc By Units, Geography, Ingredients & Applications (2010-2015) ", 2011.

(2) Hoag, H. *Chemical Heritage Magazine* **2010**, *28*.

(3) (a) Brinker, C. J. *Curr. Opin. Solid State Mater. Sci.* **1996**, *1*, 798(b) Lavalley, J. C. *Catal. Today* **1996**, *27*, 377.

(4) (a) Barkhuizen, D.; Mabaso, I.; Viljoen, E.; Welker, C.; Claeys, M.; van Steen, E.; Fletcher, J. C. Q. *Pure Appl. Chem.* **2006**, *78*, 1759(b) Basagiannis, A. C., Verykios, X.E., *Applied Catalysis B: Environmental* **2008**, *82*, 77(c) Bolis, V.; Maggiorini, S.; Meda, L.; D'Acapito, F.; Palomino, G. T.; Bordiga, S.; Lamberti, C. *J. Chem. Phys.* **2000**, *113*, 9248(d) Magnacca, G.; Cerrato, G.; Morterra, C.; Signoretto, M.; Somma, F.; Pinna, F. *Chem. Mater.* **2003**, *15*, 675 (e) Morterra, C.; Cerrato, G.; Pinna, F.; Signoretto, M. *J. Catal.* **1995**, *157*, 109.

(5) Delsarte, S.; Auroux, A.; Grange, P. *Phys. Chem. Chem. Phys.* **2000**, *2*, 2821.

(6) Stein, A., Melde, B.J., Schroden, R.C *Adv. Mater.* **2000**, *12*, 1403.

(7) Macquarrie, D. J.; Jackson, D. B.; Tailland, S.; Utting, K. A. *J. Mater. Chem.* **2001**, *11*, 1843.

(8) Rowsell, J. L. C.; Yaghi, O. M. *Microporous Mesoporous Mater.* **2004**, *73*, 3.

(9) Goto, Y.; Inagaki, S. *Chem. Commun.* **2002**, 2410

(10) Budarin, V. L.; Clark, J. H.; Deswarte, F. E. I.; Mueller, K. T.; Taverner, S. J. *Phys. Chem. Chem. Phys.* **2007**, *9*, 2274.

(11) Liu, G.; Xin, Z. *Chromatographia* **1996**, *42*, 290.

(12) Sing, K. S. W. *Colloids Surf., A* **2004**, *241*, 3.

(13) Knözinger, H. In *Elementary Reaction Steps in Heterogeneous Catalysis*; Joyner, R. W., van Santen, R.A, Ed.; Kluwer: Dordrecht, 1993.

(14) Paukshtis, E. A.; Yurchenko, E. N. *Russ. Chem. Rev.* **1983**, *52*, 242.

(15) (a) Beck, J. S.; Vartuli, J. C.; Roth, W. J.; Leonowicz, M. E.; Kresge, C. T.; Schmitt, K. D.; Chu, C. T.-W.; Olson, D. H.; Sheppard, E. W.; McCullen, S. B.; Higgins, J. B.; Schlenker, J. L. *J. Am. Chem. Soc.* **1992**, *114*, 10834(b) Beck, J. S.; Mobil Oil Corp.: US Patent 5 057 296, 1991(c) Kresge, C. T.; Leonowicz, M. E.; Roth, W. J.; Vartuli, J. C.; Beck, J. S. *Nature* **1992**, *359*, 710

(16) Zhao, X. S., Lu, G.Q., Millar, G.J *Ind. Eng. Chem. Res.* **1996**, *35*, 2075

(17) Wilson, S. T.; Lok, B. M.; Messina, C. A.; Cannan, T. R.; Flanigen, E. M. *J. Am. Chem. Soc.* **1982**, *104*, 1146.

(18) Dessau, R. M.; Schlenker, J. L.; Higgins, J. B. *Zeolites* **1990**, *10*, 522.

(19) Davis, M. E.; Saldarriaga, C.; Montes, C.; Garces, J.; Crowder, C. *Nature* **1988**, *331*, 698.
(20) Estermann, M.; Mccusker, L. B.; Baerlocher, C.; Merrouche, A.; Kessler, H. *Nature* **1991**, *352*, 320.
(21) (a) Tanev, P. T., Pinnavaia, T.J *Science* **1995**, *267*, 865(b) Tanev, P. T., Pinnavaia, T.J *Chem. Mater.* **1996**, *8*, 2068
(22) (a) Chen, C.-Y.; Xiao, S.-Q.; Davis, M. E. *Microporous Mater.* **1993**, *4*, 1(b) O'Brien, S.; Francis, R. J.; Price, S. J.; O'Hare, D.; Clark, S. M.; Okazaki, N.; Kuroda, K. *J. Chem. Soc., Chem. Commun.* **1995**, 2423.
(23) (a) Caldararu, H.; Caragheorgheopol, A.; Savonea, F.; Macquarrie, D. J.; Gilbert, B. C. *J. Phys. Chem. B* **2003**, *107*, 6032(b) Zhang, J.; Luz, Z.; Goldfarb, D. *J. Phys. Chem. B* **1997**, *101*, 7087.
(24) (a) Steel, A., Carr, S.W., Anderson, M.W. *Chem. Mater.* **1995**, *7*, 1829 (b) Steel, A.; Carr, S. W.; Anderson, M. W. *J. Chem. Soc. Chem. Commun.* **1994**, 1571.
(25) (a) Holmes, S. M.; Zholobenko, V. L.; Thursfield, A.; Plaisted, R. J.; Cundy, C. S.; Dwyer, J. *J. Chem. Soc., Faraday Trans.* **1998**, *94*, 2025 (b) Zholobenko, V. L.; Holmes, S. M.; Cundy, C. S.; Dwyer, J. *Microporous Mater.* **1997**, *11*, 83.
(26) Galarneau, A.; Di Renzo, F.; Fajula, F.; Mollo, L.; Fubini, B.; Ottaviani, M. F. *J. Colloid Interface Sci.* **1998**, *201*, 105.
(27) Monnier, A.; Schüth, F.; Huo, Q.; Kumar, D.; Margolese, D.; Maxwell, R. S.; Stucky, G. D.; Krishnamurty, M.; Petroff, P.; Firouzi, A.; Janicke, M.; Chmelka, B. F. *Science* **1993**, *261*, 1299.
(28) Lercher, J. A.; Gründling, C.; Eder-Mirth, G. *Catal. Today* **1996**, *27*, 353.
(29) Burneau, A.; Barres, O. *Langmuir* **1990**, *6*, 1364.
(30) Davis, K. M.; Tomozawa, M. *J. Non-Cryst. Solids* **1996**, *201*, 177.
(31) Takeia, T., Katoa, K., Meguroa A., Chikazawa, M. *Colloid. Surface. A* **1998**, *150*, 77.
(32) Van Roosmalen, A. J.; Mol, J. C. *J. Phys. Chem.* **1979**, *83*, 2485.
(33) Perry, C. C.; Li, X. *J. Chem. Soc., Faraday Trans.* **1991**, *87*, 3857.
(34) Burneau, A.; Carteret, C. *Phys. Chem. Chem. Phys.* **2000**, *2*, 3217.
(35) Zarubin, D. P. *J. Non-Cryst. Solids* **2001**, *286*, 80.
(36) Tavener, S. J., Clark, J.H., Gray, G.W., Heath, P.A., Maquarrie, D.J *Chem. Commun.* **1997**, 1147.
(37) (a) Tsuchiya, I. *J. Phys. Chem.* **1982**, *86*, 4107(b) Benesi, H. A.; Jones, A. C. *Phys. Rev.* **1959**, *62*, 179.
(38) Barthos, R.; Lónyi, F.; Onyestyák, G.; Valyon, J. *J. Phys. Chem. B* **2000**, *104*, 7311.
(39) Morrow, B. A.; Cody, I. A.; Lee, L. S. M. *J. Phys. Chem.* **1976**, *80*, 2761.
(40) Knözinger, H.; Krietenbrink, H. *J. Chem. Soc., Faraday Trans. 1* **1975**, *71*, 2421
(41) Gil, B.; Zones, S. I.; Hwang, S. J.; Bejblova, M.; Cejka, J. *J. Phys. Chem. C* **2008**, *112*, 2997.

(42) Pazé, C.; Bordiga, S.; Lamberti, C.; Salvalaggio, M.; Zecchina, A. *J. Phys. Chem. B* **1997**, *101*, 4740.
(43) Jia, C.; Massiani, P.; Barthomeuf, D. *J. Chem. Soc. Faraday Trans.* **1993**, *89*, 3659.
(44) (a) Morterra, C., Cerrato, G., Novarino, E., Mentruit, M.P. *Langmuir* **2003**, *19*, 5708 (b) Morterra, C.; Mentruit, M. P.; Cerrato, G. *Phys. Chem. Chem. Phys.* **2002**, *4*, 676.
(45) Escalona Platero, E.; Peñarroya Mentruit, M.; Morterra, C. *Langmuir* **1999**, *15*, 5079.
(46) Camarota, B.; Onida, B.; Goto, Y.; Inagaki, S.; Garrone, A. *Langmuir* **2007**, *23*, 13164
(47) Onida, B., Borello, L., Busco, C., Ugliengo, P., Goto, Y., Inagaki, S., Garrone, E. *J. Phys. Chem. B* **2005**, *109*, 11961.
(48) (a) Ghiotti, G.; Garrone, E.; Morterra, C.; Boccuzzi, F. *J. Phys. Chem.* **1979**, *83*, 2863(b) Hush, N. S.; Williams, M. L. *J. Mol. Spectrosc.* **1974**, *50*, 349.
(49) Burneau, A.; Gallas, J. P. *The Surface Properties of Silicas*; J. Wiley and Sons: New York, 1999.
(50) Busca, G.; Lorenzilli, V. *Mater. Chem.* **1982**, *7*, 89.
(51) Paukshtis, E. A.; Kotsarenko, N. S.; Karakchiev, L. G. *React. Kinet. Catal. Lett.* **1979**, *12*, 315.
(52) Förster, H.; Schumann, M. *J. Chem. Soc. Faraday Trans. 1* **1989**, *85*, 1149.
(53) Jacobs, P. A.; van Cauwelaert, F. H.; Vansant, E. F. *J. Chem. Soc. Faraday Trans. 1* **1973**, *69*, 2130.
(54) Morterra, C.; Zecchina, A.; Coluccia, S.; Chiorino, A. *J. Chem. Soc. Faraday Trans. 1* **1977**, *73*, 1544.
(55) Pearson, M. J. *Ind. Eng. Chem. Prod. Res. Dev* **1977**, *16*, 154.
(56) Lavalley, J. C.; Janin, A.; Preud'homme, J. *React. Kinet. Catal. Lett.* **1981**, *18*, 85.
(57) Mohammed Saad, A. B.; Saur, O.; Wang, Y.; Tripp, C. P.; Morrow, B. A.; Lavalley, J. C. *J. Phys. Chem.* **1995**, *99*, 4620.
(58) (a) Spange, S.; Prause, S.; Vilsmeier, E.; Thiel, W. R. *J. Phys. Chem. B* **2005**, *109*, 7280 (b) Spange, S.; Reuter, A. *Langmuir* **1999**, *15*, 141(c) Spange, S.; Reuter, A.; Vilsmeir, E. *Colloid. Polym. Sci.* **1996**, *274*, 59(d) Spange, S.; Sens, R.; Zimmermann, Y.; Seifert, A.; Roth, I.; Anders, S.; Hofmann, K. *New J. Chem.* **2003**, *27*, 520(e) Spange, S.; Vilsmeier, E.; Zimmermann, Y. *J. Phys. Chem. B* **2000**, *104*, 6417 (f) Spange, S.; Zimmerman, Y.; Graeser, A. *Chem. Mater.* **1999**, *11*, 3245
(59) Kamlet, M. J.; Abboud, J. L. M.; Abraham, M. H.; Taft, R. W. *J. Org. Chem.* **1983**, *48*, 2877
(60) Reichardt, C. *Chem. Rev.* **1994**, *94*, 2319.
(61) Hildebrand, J. H. *Science* **1965**, *150*, 441.
(62) Taft, R. W.; Kamlet, M. J. *J. Am. Chem. Soc.* **1976**, *98*, 2886.
(63) Kamlet, M. J.; Taft, R. W. *J. Am. Chem. Soc.* **1976**, *98*, 377.

(64) Kamlet, M. J.; Abboud, J. L.; Taft, R. W. *J. Am. Chem. Soc.* **1977**, *99*, 6027.
(65) Dimroth, K.; Reichardt, C.; Siepmann, T.; Bohlmann, F. *Justus Liebigs Ann. Chem.* **1963**, *661*, 1.
(66) Marcus, Y. *J. Solution. Chem.* **1991**, *20*, 929.
(67) Spange, S., Lauterbach, H.M., Gyra, A.K., Reichardt, C. *Liebigs Annalen der Chemie* **1991**, 323.
(68) Macquarrie, D. J.; Tavener, S. J.; Gray, G. W.; Heath, P. A.; Rafelt, J. S.; Saulzet, S. I.; Hardy, J. J. E.; Clark, J. H.; Sutra, P.; Brunel, D.; di Renzo, F.; Fajulab, F. *New J. Chem.* **1999**, *23*, 725.
(69) Choi, S. Y.; Park, Y. S.; Hong, S. B.; Yoon, K. B. *J. Am. Chem. Soc.* **1996**, *118*, 9377.
(70) (a) Benesi, H. A.; Hildebrand, J. H. *J. Am. Chem. Soc.* **1948**, *70*, 2832(b) Benesi, H. A.; Hildebrand, J. H. *J. Am. Chem. Soc.* **1949**, *71*, 2703(c) Benesi, H. A.; Hildebrand, J. H. *J. Am. Chem. Soc.* **1950**, *72*, 2273(d) Hastings, S. H.; Franklin, J. L.; Schiller, J. C.; Matsen, F. A. *J. Am. Chem. Soc.* **1953**, *75*, 2900(e) Keefer, R. M.; Andrews, L. J. *J. Am. Chem. Soc.* **1952**, *74*, 1891(f) Voigt, E. M. *J. Phys. Chem.* **1968**, *72*, 3300(g) Walkley, J.; Glew, D. N.; Hildebrand, J. H. *J. Chem. Phys.* **1960**, *33*, 621.
(71) Mulliken, R. S. *J. Am. Chem. Soc.* **1952**, *74*, 811
(72) Mebel, A. M.; Lin, H. L.; Lin, S. H. *Int. J. Quantum Chem.* **1999**, *72*, 307.
(73) Kebede, Z.; Lindquist, S.-E. *Sol. Energy Mater. Sol. Cells* **1999**, *57*, 259.
(74) Camarota, B.; Goto, Y.; Inagaki, S.; Garrone, E.; Onida, B. *J. Phys. Chem. C* **2009**, *113*, 20396.
(75) Doskocil, E. J.; Bordawekar, S. V.; Kaye, B. G.; Davis, R. J. *J. Phys. Chem. B* **1999**, *103*, 22903.
(76) Aramendía, M. A.; Boráu, V.; Jiménez, C.; Marinas, J. M.; Porras, A.; Urbano, F. J. *React. Kinet. Catal. Lett.* **1998**, *65*, 25.
(77) Aramendía, M. A.; Borau, V.; Jiménez, C.; Marinas, J. M.; Porras, A.; Urbano, F. J. *J. Catal.* **1996**, *161*, 829.
(78) Martin, D.; Duprez, D. *J. Mol. Catal. A: Chem.* **1997**, *118*, 113.
(79) (a) Hruby, S. L.; Shanks, B. H. *J. Catal.* **2009**, *263*, 181(b) Kantam, L. M.; Choudary, B. M.; Reddy, C. V.; Rao, K. K.; Figueras, F. *Chem. Commun.* **1998**, 1033(c) López-González, J. D. D.; López-Peinado, A.; Martín-Aranda, R. M.; Rojas-cervantes, M. L. *Carbon* **1993**, *31*, 1231.
(80) (a) Díez, V. K.; Apesteguía, C. R.; Di Cosimo, J. I. *J. Catal.* **2003**, *215*, 220(b) Di Cosimo, J. I.; Diez, V. K.; Xu, M.; Iglesia, E.; Apesteguia, C. R. *J. Catal.* **1998**, *178*, 499(c) Di Cosimo, J. I.; Apesteguia, C. R.; Ginés, M. J. L.; Iglesia, E. *J. Catal.* **2000**, *190*, 261.
(81) Gervasini, A.; Fenyvesi, J.; Auroux, A. *Catal. Lett.* **1997**, *43*, 219.
(82) Bordawekar, S. V.; Doskocil, E. J.; Davis, R. J. *Catal. Lett.* **1997**, *44*, 193.

(83) Shen, W.; Li, Z.; Liu, Y. *Recent Pat. Chem. Eng.* **2008**, *1*, 27.
(84) (a) Shchipunov, Y. A. *J. Colloid Interface Sci.* **2003**, *268*, 68(b) Shchipunov, Y. A.; Karpenko, T. U. *Langmuir* **2004**, *20*, 3882(c) Shchipunov, Y. A.; Karpenko, T. U.; Bakunina, I. Y.; Burtseva, Y. V.; Zvyagintseva, T. N. *J. Biochem. Biophys. Methods* **2004**, *58*, 25.
(85) Munoz-Aguado, M. J.; M, G. *J. Colloid Interface Sci.* **1997**, *185*, 459.
(86) Wang, Y.; Noguchi, M.; Takahashi, Y.; Ohtsuka, Y. *Catal. Today* **2001**, *68*, 3.
(87) Wilson, R. E. *Ind. Eng. Chem.* **1921**, *13*, 326.
(88) (a) Matos, M. C.; Illharco, L. M.; Almeida, R. M. *J. Non-Cryst. Solids* **1992**, *147-148*, 232(b) Rubio, F.; Rubio, J.; Oteo, J. L. *Spectrosc. Lett.* **1998**, *31*, 199.
(89) Perry, C. C.; Li, X. *J. Chem. Soc., Faraday Trans.* **1991**, *87*, 761.
(90) Rubio, F.; Rubioa, J.; Oteo, J. L. *Spectrosc. Lett.* **1998**, *31*, 199
(91) Matos, M. C.; Ilharco, L. M.; Almeida, R. M. *J. Non-Cryst. Solids* **1992**, *147-148*, 232.
(92) (a) Battjes, K. P.; Barolo, A. M.; Dreyfuss, P. *J. Adhesion Sci. Technol.* **1991**, *5*, 785(b) Nakamoto, K.; Sarma, Y. A.; Ogoshi, H. *J. Chem. Phys.* **1965**, *43*, 1177.
(93) Taverner, S. J., Clark, J.H., Gray, G.W., Heath, P.A., Macquarrie, D.J *Chemical Communications* **1997**, 1147.
(94) Gruenloh, C. J.; Florio, G. M.; Carney, J. R.; Hagemeister, F. C.; Zwier, T. S. *J. Phys. Chem. A* **1999**, *103*, 496.
(95) Michniewicz, N.; Muszyński, A. S.; Wrzeszcz, W.; Czarnecki, M. A.; Golec, B.; Hawranek, J. P.; Mielke, Z. *J. Mol. Struct.* **2008**, *887*, 180.
(96) Dobrowolski, J. C.; Ostrowski, S.; Kołos, R.; Jamróz, M. H. *Vib. Spectrosc.* **2008**, *48*, 82.
(97) Kaloyeros, A. E.; Zheng, B.; Lou, I.; Lau, J.; Hellgeth, J. W. *Thin Solid Films* **1995**, *262*, 20.
(98) Richardson, H. H. *J. Phys. Chem.* **1992**, *96*, 5898.
(99) Sethna, P. P.; Williams, D. *J. Phys. Chem.* **1979**, *83*, 405.
(100) Osterholtz, F. D.; Pohl, E. R. *J. Adhesion Sci. Technol.* **1992**, *6*, 127.
(101) Chrzczonowicz, S.; Lasocki, Z. *Rocz. Chem.* **1962**, *36*, 275.
(102) Macquarrie, D. J., Gilbert, B.C., Gilbey, L.J., Caragheorgheopol, A., Savonea, F., Jackson, D.B., Onida, B., Garrone, E., Luque, R. *Journal of Materials Chemistry* **2005**, *15*, 3946
(103) Onida, B., Geobaldo, F., Testa, F., Aiello, R., Garrone, E. *The Journal of Physical Chemistry B* **2002**, *106*, 1684.
(104) (a) Morimoto, T.; Imai, J.; Nagao, J. *J. Phys. Chem.* **1974**, *78*, 704(b) Clark-Monks, C.; Ellis, B. *Can. J. Chem.* **1972**, *50*, 907.
(105) Heacock, R. A.; Marion, L. *Can. J. Chem.* **1956**, *34*, 1782.
(106) Noller, H.; Mayerböck, B.; Zundel, G. *Surf. Sci.* **1972**, *33*, 82.
(107) Stewart, J. E. *J. Chem. Phys.* **1959**, *30*, 1259.
(108) Wojciechowski, P. M.; Zierkiewicz, W.; Michalska, D.; Hobza, P. *J. Chem. Phys.* **2003**, *118*, 10900.

(109) Young, R. P. *Can. J. Chem.* **1969**, *47*, 2237.
(110) Cannas, C.; Casu, M.; Musinu, A.; Piccaluga, G. *J. Non-Cryst. Solids* **2005**, *351*, 3476.
(111) Kosower, E. M.; Markovich, G.; Borz, G. *ChemPhysChem* **2007**, *8*, 2513
(112) Jänchen, J.; Stach, H.; Busio, M.; van Wolput, J. H. M. C. *Thermochim. Acta* **1998**, *312*, 33.
(113) Walsh, T. R.; Wilson, M.; Sutton, A. P. *J. Chem. Phys.* **2000**, *113*, 9191.
(114) Van Roosmalen, A. J., Mol, J.C. *The Journal of Physical Chemistry* **1978**, *82*, 2748
(115) Cant, N. W.; Little, L. H. *Can. J. Chem.* **1965**, *43*, 1252.
(116) Zheng, F.; Tran, D. N.; Busche, B. J.; Fryxell, G. E.; Addleman, R. S.; Zemanian, T. S.; Aardahl, C. L. *Ind. Eng. Chem. Res.* **2005**, *44*, 3099.
(117) Huang, H. Y.; Yang, R. T. *Ind. Eng. Chem. Res.* **2003**, *42*, 2427.
(118) Hiyoshi, N.; Yogo, K.; Yashima, T. *Microporous Mesoporous Mater.* **2005**, *84*, 357.
(119) Goodman, A. L. *Energy Fuels* **2009**, *23*, 1101.
(120) Bonelli, B.; Onida, B.; Fubini, B.; Otero Areán, C.; Garrone, E. *Langmuir* **2000**, *16*, 4976.
(121) Khatri, R. A.; Chuang, S. S. C.; Soong, Y.; Gray, M. *Energy Fuels* **2006**, *20*, 1514.
(122) (a) Leal, O.; Bolívar, C.; Ovalles, C.; García, J. J.; Espidel, Y. *Inorg. Chim. Acta* **1995**, *240*, 183(b) Srivastava, R.; Srinivas, D.; Ratnasamy, P. *Microporous Mesoporous Mater.* **2006**, *90*, 314(c) Chang, A. C. C.; Chuang, S.S.C; Gray, M.; Soong, Y. *Energy Fuels* **2003**, *17*, 468.
(123) Harlick, P. J. E.; Sayari, A. *Ind. Eng. Chem. Res.* **2007**, *46*, 446.
(124) (a) Kim, S.; Vadim, J. I.; Guliants, V.; Lin, J. Y. S. *J. Phys. Chem. B* **2005**, *109*, 6287(b) Zaki, M. I.; Hasan, M. A.; Al-Sagheer, F. A.; Pasupulety, L. *Langmuir* **2000**, *16*, 430.
(125) Wang, X.; Schwartz, V.; Clark, J. C.; Ma, X.; Overbury, S. H.; Xu, X.; Song, C. *J. Phys. Chem. C* **2009**, *113*, 7260.
(126) Franchi, R. S.; Harlick, P. J. E.; Sayari, A. *Industrial & Engineering Chemistry Research* **2005**, *44*, 8007.
(127) Franchi, R. S.; Harlick, P. J. E.; Sayari, A. *Ind. Eng. Chem. Res.* **2005**, *44*, 8007.
(128) Okunev, A. G.; Paukshtis, E. A.; Aristov, Y. L. *React. Kinet. Catal.* **1998**, *65*, 161.
(129) Bellamy, L. J. *The Infra-Red Spectra of Complex Molecules*; 3 ed.; Chapman and Hall: London, 1975.
(130) Panov, A.; Fripiat, J. J. *Langmuir* **1998**, *14*, 3788.
(131) Platero, E. E.; Mentruit, M. P.; Morterra, C. *Langmuir* **1999**, *15*, 5079
(132) Morterra, C., Magnacca, G. *Catalysis Today* **1996**, *27*, 497.

(133) Aboulayt, A.; Binet, C.; Lavalley, J. C. *J. Chem. Soc. Faraday Trans.* **1995**, *91*, 2913.
(134) Tsyganenko, A. A.; Filimonov, V. N. *J. Mol. Struct.* **1973**, *19*, 579.
(135) Aboulayt, A.; Binet, C.; Lavalley, J. C. *J. Chem. Soc. Faraday Trans.* **1995**, *91*, 2913.
(136) Areán, C. O.; Platero, E. E.; Mentruit, M. P.; Delgado, M. R.; Xamena, F. X. L. I.; Garcia-Raso, A.; Morterra, C. *Microporous Mesoporous Mater.* **2000**, *34*, 55.
(137) Wilson, H. W.; Bloor, J. E. *Spectrochim. Acta* **1965**, *21*, 45.
(138) de Mallmann, A.; Barthomeu, D. *Zeolites* **1988**, *8*, 292.
(139) Neyman, K. M.; Illas, F. *Catal. Today* **2005**, *105*, 2.
(140) Prause, S.; S, S. *J. Phys. Chem. B* **2004**, *108*, 5734.
(141) Awtrey, A. D.; Connick, R. E. *J. Am. Chem. Soc.* **1951**, *73*, 1842.
(142) Barthomeuf, D. *J. Phys. Chem.* **1984**, *88*, 42.
(143) Huang, M.; Kaliaguine, S. *J. Chem. Soc. Faraday Trans.* **1992**, *88*, 751.
(144) (a) Sánchez-Sánchez, M., Blasco, T. *J. Am. Chem. Soc.* **2002**, *124*, 3443 (b) Sánchez-Sánchez, M.; Blasco, T. *Chem. Commun.* **2000**, 491.
(145) Toyohara, M.; Kaneko, M.; Mitsusuka, N.; Fujihara, H.; Saito, N.; Murase, T. *J. Nucl. Sci. Technol.* **2002**, *39*, 950.
(146) Adams, R.; Mahan, J. E. *J. Am. Chem. Soc.* **1942**, *64*, 2588.
(147) Hall Jr, H. K. *J. Am. Chem. Soc.* **1957**, *79*, 5441.
(148) Voigt, E. M. *J. Phys. Chem.* **1968**, *73*, 3300.
(149) (a) Danehy, J. P.; Doherty, B. T.; Egan, C. P. *J. Org. Chem.* **1971**, *36*, 2525(b) Danehy, J. P.; Egan, C. P.; Switalski, J. *J. Org. Chem.* **1971**, *36*, 2530.
(150) Rundle, R. E.; Foster, J. F.; Baldwin, R. R. *J. Am. Chem. Soc.* **1944**, *65*, 2116.
(151) Rundle, R. E.; Edwards, F. C. *J. Am. Chem. Soc.* **1943**, *65*, 2200.
(152) Yajima, H.; Morita, M.; Hashimoto, M.; Sashiwa, H.; Kikuchi, T.; Ishii, T. *Int. J. Thermophys.* **2001**, *22*, 1265.
(153) Ogawa, K.; Yui, T.; Okuyama, K. *Int. J. Biol. Macromol.* **2004**, *34*, 1.
(154) (a) Hanafusa, Y.; Osawa, K.; Noguchi, K.; Okuyama, K.; Ogawa, K. *Polym. Prep. Jpn.* **1999**, *48*, 3853(b) Hanafusa, Y.; Osawa, K.; Noguchi, K.; Okuyama, K.; Ogawa, K. *Polym. Prep. Jpn.* **2000**, *49*, 404.
(155) (a) Shigeno, Y.; Kondo, K.; Takemoto, K. *Angew. Makromol. Chem.* **1980**, *91*, 55(b) Shigeno, Y.; Kondo, K.; Takemoto, K. *J. Appl. Polym. Sci.* **1980**, *25*, 731.
(156) Muzzarelli, R. A. A.; Tanfani, E.; Emanuelli, M.; Bolognini, L. *Biotech. Bioeng.* **1985**, *27*, 1115.
(157) Carlstron, D. *J. Biophys. Biochem. Cytol.* **1957**, *3*, 669.
(158) Takahashi, Y. *J. Inclusion Phenom.* **1984**, *2*, 399.
(159) Takahashi, Y. *J. Inclusion Phenom.* **1987**, *5*, 525.
(160) Schwertassek, K. *Melliand Textilber.* **1931**, *12*, 457.

(161) Nelson, M. L.; Rouselle, M.-A.; Cangemi, S. J.; Trouard, P. *Text. Res. J.* **1970**, *40*, 872.
(162) (a) Kaneko, M.; Hoshi, T.; Kaburagi, Y.; Ueno, H. *J. Electroanal. Chem.* **2004**, *572*, 21(b) Nemoto, J.; Sakata, M.; Hoshi, T.; Ueno, H.; Kaneko, M. *J. Electroanal. Chem.* **2007**, *599*, 23.
(163) Takemura, K.; Minomura, S.; Shimomura, O.; Fuji, Y.; Axe, J. D. *Phys. Rev. B: Condens. Matter* **1982**, *26*, 998.
(164) (a) Basch, A.; Hartl, M.; Behrens, P. *Microporous Mesoporous Mater.* **2007**, *99*, 244(b) Seff, K.; Shoemaker, D. P. *Acta Crystallogr.* **1967**, *22*(c) Song, M. K.; Choi, E. Y.; Kim, Y. *J. Phys. Chem. B* **2003**, *107*, 10709.
(165) Wirnsberger, G.; Fritzer, H. P.; Popitsch, A.; Van de Groor, G.; Berens, P. *Angew. Chem. Int. Ed.* **1996**, *35*, 2777.
(166) Corma, A.; Fornes, V.; Martin-Aranda, R. M.; Garcia, H.; Primo, J. *Appl. Catal.* **1990**, *59*, 237.
(167) Scanlon, J. T.; Willis, D. E. *J. Chromatogr. Sci.* **1985**, *23*, 333.
(168) Katritzky, A. R.; Ignatchenko, E. S.; Barcock, R. A.; Lobanov, V. S. *Anal. Chem.* **1994**, *66*, 1799.
(169) Jorgensen, A. D.; Picel, K. C.; Stamoudis, V. C. *Anal. Chem.* **1990**, *62*, 683.
(170) Brunel, D. *Microporous Mesoporous Mater.* **1999**, *27*, Functionalized micelle.
(171) Brunel, D. *Microporous Mesoporous Mater.* **1999**, *27*, 329.
(172) Clark, J. H.; Macquarrie, D. J. *Chem. Commun.* **1998**, 853.
(173) Gill, I.; Ballesteros, A. *J. Am. Chem. Soc.* **1998**, *120*.
(174) Meyer, M.; Fischer, A.; Hoffmann, H. *J. Phys. Chem. B* **2002**, *106*, 1528.
(175) (a) Livage, J.; Coradin, T.; Roux, C. *J. Phys. Condens. Matter* **2001**, *13*, R673(b) Zaremba, C. M.; Stucky, G. D. *Curr. Opin. Solid State Mater. Sci.* **1996**, *1*, 425.
(176) Wang, B.; Zhang, W.; Zhang, W. *Drying Technol.* **2005**, *23*, 7.
(177) (a) Kittur, F. S.; Harish Prashanth, K. V.; Udaya Sankar, K.; Tharanathan, R. N. *Carbohyd. Polym.* **2002**, *49*, 185(b) Nieto, J. M.; Peniche-Covas, C.; Padro´n, G. *Thermochim. Acta* **1991**, *176*, 63(c) Zohuriaan, M. J.; Shokrolahi, F. *Polym. Test.* **2004**, *23*, 575.
(178) Imeson, A. P.; Ledward, D. A.; Mitchell, J. R. *J. Sci. Food Agric.* **1977**, *288*, 661.
(179) Çaykara, T.; Demirci, S.; Eroğlu, M. S.; Güven, O. *Polymer* **2005**, *46*, 10750.
(180) Raemy, A.; Schweizer, T. F. *J. Therm. Anal.* **1983**, *28*, 95.
(181) Lii, C.-Y.; Chen, H.-H.; Lu, S.; Tomasik, P. *J. Polym. Environ.* **2003**, *11*, 115.
(182) Lawrie, G.; Keen, I.; Drew, B.; Chandler-Temple, A.; Rintoul, L.; Fredericks, P.; Grøndahl, L. *Biomacromolecules* **2007**, *8*, 2533.
(183) Biswal, D. R.; Singh, R. P. *Carbohyd. Polym.* **2004**, *57*, 379.
(184) (a) Chopin, T.; Whalen, E. *Carbohyd. Res.* **1993**, *246*, 51(b) Sekkal, M.; Legrand, P. *Spectrochim. Acta A* **1993**, *49*, 209.

(185) Meek, S. T.; Greathouse, J. A.; Allendor, M. D. *Adv. Mater.* **2011**, *23*, 141.
(186) Sanchez, C.; Belleville, P.; Popall, M.; Nicole, L. *Chem. Soc. Rev.* **2011**, *40*, 696.
(187) Herm, Z. R.; Swisher, J. A.; Smit, B.; Krishna, R.; Long, J. R. *J. Am. Chem. Soc.* **2011**, *133*, 5664.
(188) Xiang, S.-C.; Zhang, Z.; Zhao, C.-G.; Hong, K.; Zhao, X. S.; Ding, D. R.; Xie, M.-H.; Wu, C.-D.; Das, M. C.; Gill, R.; Thomas, K. M.; Chen, B. *Nat. Commun.* **2011**, *2*, 877.
(189) Hirsher, M. *Angew. Chem. Int. Ed.* **2011**, *50*, 581.
(190) Jeong, K. S.; Go, Y. B.; Shin, S. M.; Lee, S. J.; Kim, J.; Yaghi, O. M.; Jeong, N. *Chem. Sci.* **2011**, *2*, 877.
(191) Abbett, K. F.; Teja , A. S.; Kowalik, J.; Tolbert, L. *J. Appl. Polym. Sci.* **2003**, *90*, 3876
(192) (a) Aramendía, M. A.; Boráu, V.; García, I. M.; Jiménez, C.; Marinas, A.; Marinas, J. M.; Porras, A.; Urbano, F. J. *Appl. Catal., A*. **1999**, *184*, 115(b) Béres, A.; Hannus, I.; Kiricsi, I. *React. Kinet. Catal. Lett.* **1995**, *56*, 55.
(193) (a) Chuang, I.-S.; Maciel, G. E. *J. Phys. Chem. B* **1997**, *101*, 3052(b) Dijkstra, T. W.; Duchateau, R.; van Santen, R. A.; Meetsma, A.; Yap, G. P. A. *J. Am. Chem. Soc.* **2002**, *124*, 9856.
(194) (a) Digne, M., Sauteta, P., Raybaud, P., Euzen, P., Toulhoat, H. *J. Catal.* **2004**, *226*, 54(b) Digne, M.; Sautetb, P.; Raybaudc, P.; Euzend, P.; Toulhoate, H. *J. Catal.* **2002**, *211*, 1.
(195) (a) Branda, M. M.; Montani, R. A.; Castellani, N. J. *Surf. Sci.* **1995**, *341*, 295(b) HoIysz, L. *Colloids Surf., A* **1998**, *134*, 321.